Grain Structure Development During Casting, Reheating and Deformation of Nb-Microalloyed Steel

By

Amrita Kundu

A thesis submitted to

The University of Birmingham

For the degree of

DOCTOR OF PHILOSOPHY

School of Metallurgy and Materials
College of Engineering and Physical Sciences
The University of Birmingham (UK)
March 2011

Contents

ABSTRACT

An as continuously cast slab (Slab 1) containing 0.045 wt % Nb has been characterised in terms of secondary dendritic arm spacing, second phase volume fraction using optical microscopy and high resolution SEM. SEM investigation has been carried out to measure the Nb content in the dendritic and in the interdendritic regions. In the present study equilibrium thermodynamics has been used to predict the amount of microsegregation. This agrees well with the measured amount of segregated material present in the structure determined after quantifying the second phases present in the as-cast condition. The reheat temperatures were selected based on Thermo-Calc predicted precipitate stability in solute-rich and solute-depleted regions. In the present study reheating carried out on Slab 1 to two different reheat temperatures, 1225 and 1150 °C to generate unimodal and bimodal grain size distribution respectively. The as-cast slab was homogenised to 1225 °C for 4 days to remove Nb segregation. The mode grain size after reheating and homogenisation and the available Nb in the solution has been used as an input to Dutta-Sellars model, most frequently used to predict recrystallisation, precipitation and the interaction of recrystallisation and precipitation.

Dutta-Sellars model has been reviewed to check the limits of validity across the wide range of grain size, composition and strain. The other recent models in the literature have also been reviewed to check their validity using the literature data. Deformation simulations have been carried out for range of strain and temperature on homogenised 0.045 and 0.094 wt % Nb steel. It has been found out that Dutta-Sellars equations based on individual grain size class i.e. taking into account entire starting grain size distribution gives better agreement to the results from the present study and literature data at 0.3 strain compared to the original Dutta-Sellars model using mode or average grain size. Some discrepancy present after deformation in steels containing

0.094 wt % Nb is due to deformation-induced precipitates of Nb(C,N) slowing down recrystallisation. This has been verified after quantifying deformation-induced Nb(C,N) on both the steel using thin foil TEM study. This method also allowed prediction of the grain size distributions after deformation at 0.3 strain, which is important for subsequent toughness prediction. The original Dutta-Sellars equations does not predict the amount of recrystallisation well over a large strain range (0.1 - 0.6) using the literature data (both under- and over-predictions are seen). When the starting grain size distribution is taken into account the greater discrepancy was seen for higher strain range (i.e. strain > 0.3) compared to that in the lower strain range (i.e. strain < 0.3). Some of the over-prediction of recrystallisation can be accounted for by strain-induced precipitates reducing the recrystallised fraction, particularly for high Nb steels (literature data and result from the present study) and at high strains (results presented here).

The present thesis also examines the applicability of the Dutta-Sellars equations in predicting the recrystallised grain sizes following deformation for a 0.045 wt % Nb-bearing, commercially produced steel with a segregated solute content (from continuous casting). The investigation considered initial unimodal and bimodal grain size distributions before deformation that were generated by reheating the steel to 1225 and 1150 ºC respectively. It was found that the reheated grain size distribution (separated into grain size classes) could be related to the solute-rich (smaller grain size classes) and solute-depleted (larger grain size classes) regions. The use of these relationships and a simple halving of the grain size within the distribution on recrystallisation (used previously for homogenised samples of this steel) was found to be appropriate in the grain size class-based use of the Dutta-Sellars equations in predicting the mode and maximum grain sizes after hot deformation and holding. This approach successfully predicted (confirmed by experiment) the formation of a bimodal grain structure from an initially

unimodal one, but did not fully predict the proportions of recrystallised grains – underestimating the fraction of solute-rich grains that recrystallised at the highest deformation temperatures, whilst overestimating the fraction of solute-depleted grains recrystallised at lower deformation temperatures. An analysis of the factors used indicated that the discrepancies can be most readily accounted for by invoking strain partition between different sized grains along with a greater temperature dependence of solute drag than currently in the model.

It has been shown in the literature that the use of Nb(C,N) to pin prior austenite grains during thermomechanical processing can give rise to bimodal grain structures after reheating linked to Nb segregation and subsequent variation in precipitate distribution and stability on reheating and deformation. In the present study a steel stab containing 0.057 wt % Al was investigated as the segregation tendency of Al is much less compared with Nb so that AlN may provide grain boundary pinning in regions of reduced Nb(C,N) volume fraction and stability. Quantification of precipitate and prior austenite grain size distributions after reheating has confirmed the governing mechanisms of precipitate dissolution / coarsening whilst identifying grain boundary pinning by AlN at temperature below 1125 ^{o}C, but controlled by Nb(C,N) at higher temperatures.

Acknowledgements

It has been my proud privilege to work with Prof. Claire Davis, who has given me ample opportunity to meet the objectives of the present work. I cannot adequately express my deep sense of gratitude to Claire. I will always remember her constant support, encouragement, important suggestions and valuable comments; in every aspect of the work she has played a great role that has sustained me and allowed me to present this research work in the present form. She took time to keep me focused and motivated with regular grilling and basting. Claire not only supported me in my academic pursuit but also helped immensely to settle and work in a different culture.

I like to thank Dr. Martin Strangwood for his academic guidance all the time and his support with the experimental work, particularly for metallography, Thermo-Calc and fundamentals of TEM diffraction pattern analysis.

I gratefully acknowledge The Universities of UK, and the School of Metallurgy and Materials, The University of Birmingham, for funding my research work with an Overseas Research Scholarship, ORS, and a Departmental Scholarship, respectively and Tata Steel, UK for providing the materials for this research. I thank The Worshipful Company of Armourers and Brasiers, the Institute of Materials, Minerals and Mining, IOM3 and The Royal Academy of Engineering for awarding me travel grants for presenting my work at conferences; SIMPRO 2008, PTM 2010 and REX-GG-2010.

I am indebted to Prof. Paul Bowen, Head, School of Metallurgy and Materials, The University of Birmingham, UK for the provision of research facilities. Thanks are due to Drs. Sally Parker, Andy Howe, Winfried Kranendonk and Roger Beaverstock, all from Tata Steel for valuable discussions and Dr. Zul Husain and Mr Gary Claxton from Swinden Technology Centre for their help during some of the Gleeble experiments.

I am grateful to Prof. John Knott for his comments on my literature review and Prof. Ian Jones and Dr. Yu Lung Chiu for their encouragement and help on the TEM.

I would like to thank Anne Cabezas, Dr. Tim Doel (initial Gleeble experiments), Paul Stanley (SEM), Dr. Ming Chu (TEM), Dr. Rengen Ding (TEM sample preparation), Jeff Sutton (sealing the samples and XRD), John Lane, Dave Price and Jasbinder Singh. Massive thanks to Mick Cunningham and Avril Rogers for providing help readily. Thanks are also due to the inhabitants of N206, and past and present members of Phase Transformation and Microstructural Modelling Group, especially Anca (for my orientation to the department and to Birmingham, drinks and being my dinner host on innumerable times), Heiko (for help with image analysis) and Dan (for help with excel) and my friends in the department.

My sincere gratitude to Dr. Sukanta Biswas and his family, Dr. Sharada Sugirtharaja and her family and Mr. T. Chanda and his family for their help in settling down in a new country. Thanks to Asbury community especially Rene, Vennesa, Lehlyn, Saira, Nathalie, Swati and Barbara for providing much needed distractions.

I sincerely thank Prof. Pravash Ch. Chakraborti, Jadavpur University, India. Without his help, encouragement and unfailing support it would not have happened for me to reach Birmingham and complete my research here. His mentoring and constant enthusiasm helped me overcome the hard times and directed me towards the right decisions. I am indebted to Prof. Dinabondhu Ghosh (Jadavpur University, India), Dr. Debdutta Lahiri (BARC, India), Dr. Soumitra Tarafder (NML, India), Prof. Indradev Samajder (IIT Mumbai, India), Prof. Sanat Roy and Prof. K. K. Ray (IIT- Kharagpur, India) for their encouragement to start a PhD, leaving a permanent job at BARC, India.

My foundation of strength has come from my parents and my brother, as it has throughout my life. Especially without the inspiration of my mother it won't have been possible for me to reach this stage. It is she who always has faith in me and has supported me all through and in that note I would like to dedicate my thesis to her.

List of publications from this work

JOURNAL

- Grain structure development during reheating and deformation of Niobium-microalloyed steels: **A. Kundu**, C. L. Davis and M. Strangwood, Materials and Manufacturing Processes, Volume 25, Issue 1-3, January 2010, Pages 125-132.
- Modeling of grain size distributions during single hit deformation of a Nb-containing Steel: **A. Kundu**, C. L. Davis and M. Strangwood, Metallurgical and Material Transaction A. Volume 41, Number 4, April 2010, Pages 994-1002.
- Grain size distributions after single hit deformation of a segregated, commercial Nb-containing steel: prediction and experiment: **A. Kundu**, C. L. Davis and M. Strangwood, Metallurgical and Material Transaction A. Volume 42, Number 9, 2011, Pages 2794-2806.
- Pinning of austenite grain boundaries by mixed AlN and NbCN precipitates: **A. Kundu**, C. L. Davis and M. Strangwood, Solid State Phenomena, Volume 172-174, 2011, Pages 458-463.
- Effect of grain size and strain on recrystallisation kinetics of Nb containing steel; review and a new Approach: **A. Kundu**, C. L. Davis and M. Strangwood, under preparation for Metallurgical and Material Transactions A.
- Effect of Nb on recrystallisation kinetics of Nb containing steel: **A. Kundu**, C. L. Davis and M. Strangwood, under preparation for Metallurgical and Material Transactions A.
- Prediction and quantification of microsegregation in Nb-bearing, low carbon microalloyed steels: **A. Kundu**, C. L. Davis and M. Strangwood, under preparation for Material Science and Technology.
- Effect of AlN on grain boundary pinning during reheating in Nb microalloyed steel: **A. Kundu**, C. L. Davis and M. Strangwood, under preparation for Scripta Materialia.

CONFERENCE PROCEEDINGS

- Grain Structure Development During Deformation In Segregated Nb Microalloyed Steels: **A. Kundu**, C. L. Davis and M. Strangwood, TATA Academia Symposium, Cardiff, UK, 14-15th July 2011. This poster won the best poster award.
- Effect of strain on recrystallisation during hot deformation in Nb-containing microalloyed steels: **A. Kundu**, C. L. Davis and M. Strangwood, manuscript accepted for the Proceedings of 4th International Conference on Recrystallisation and Grain Growth IV (ReX & GG IV 2010), Sheffield, UK, 4-9 July 2010.
- Grain structure development during deformation of segregated Nb microalloyed steel: **A. Kundu**, C. L. Davis and M. Strangwood, Proceedings of 2nd International Conference on Thermo-Mechanical simulation and Processing of Steels (SIMPRO 2008), Ranchi, India, 9-11 December 2008.
- Grain Structure Development During Deformation In Microalloyed Steels; Effect of Segregation: **A. Kundu**, C. L. Davis and M. Strangwood, CORUS Academia Symposium, Birmingham, UK, 2008.

List of Symbols

Chapter 2 Grain structure development during casting and reheating of Nb microalloyed steel: influence of microsegregation

G_L	Actual temperature gradient in the liquid at the interface
R	Rate of movement of the interface
m_L	Slope of the liquidus line or the equilibrium freezing range of the alloy
C_o	Bulk alloy composition
k_p	Equilibrium partition ratio
D_L	Diffusion coefficient of solute in the liquid
C_α	Bulk liquid composition
C^*_s	Solid composition at the liquid solid interface
f_s	Fraction of solid
C_s	Solute concentration of the solid
C_l	Solute concentration of the liquid
r	Segregation ratio
δ	Delta ferrite
γ	Austenite
L	Liquid
α	Ferrite
T_{DISS}	Equilibrium dissolution temperature
A	Constant
B	Constant
K_S	Solubility product
[M]	Matrix concentration of microalloying element M
X	Interstitial element
$(D_0)_{diff}$	Diffusion constant
Q_{diff}	Activation energies of diffusion for the microalloying elements and important interstitials (C and N)
D_{diff}	Diffusion coefficients
R	Universal gas constant
D	Grain diameter
d	Particle diameter
ξ	Constant in Gladman's model
R_o	Initial matrix grain size
f	The volume fraction of particles
Z	The heterogeneity of the matrix grain size
r*	The maximum particle size that would effectively counteract the driving force for austenite grain coarsening
T_{GC}	Temperature at which abnormal or discontinuous grain growth starts

Chapter 3 Review of grain structure formation during hot deformation of microalloyed steel

T_{NR}	No recrystallisation temperature
$T_{95\%R}$	Recrystallisation limit temperature

$T_{5\%R}$	Recrystallisation stop temperature
A_3	Austenite to ferrite transformation temperature
$\Delta\sigma$	The increase in flow stress caused by work hardening
σ_o	The initial yield strength
α	Constant
μ	Shear modulus
b	Burgers vector
$\Delta\rho$	The difference in dislocation density
F_{RXN}	The driving force for static recrystallisation
$A^{/}$	Constant
Q_{gg}	Constant
D_{rex}	Recrystallised grain size
D	Final grain size
D_o	Initial grain size
ε	Strain
D'	Constant
G	Rate of grain coarsening
γ	Specific grain boundary energy per unit volume
V_M	Molar volume of austenite
n	Isothermal grain coarsening law exponent
t	Coarsening time
λ	Reciprocal of boundary mobility of pure austenite
α	Reciprocal of boundary mobility at unit solute concentration
$C^{/}$	bulk solute concentration
t_{REF}	Recrystallisation starting time of a reference steel
t_y	Recrystallisation starting time of a second steel
p_r	Retarding force per unit area of the boundary
r	Radius of the particles
f	Volume fraction of particles
σ_B	Specific boundary surface energy
σ	Interfacial energy of the austenite grain boundary
N_s	Number of particles per unit area
F^s_{PIN}	Pinning force per unit area
f_v	Volume fraction of particles
l	Sub-grain size
X_v	Fraction recrystallised in time t
t_F	Time for some specified fraction of recrystallisation
$t_{0.5}$	Time for 50% recrystallisation
q	Grain size exponent
p	Strain exponent
T_{sol}	Solution temperature above which Nb-rich precipitates are completely dissolved in the austenite matrix
$T^{/}$	Temperature below which recrystallisation and precipitation compete
T_R	Temperature below which precipitation occurs prior to recrystallisation
R_s	Start of recrystallisation (5 % recrystallisation)
$R_{f,}$	Finish of recrystallisation (85 % recrystallisation)
$R_s^{,}$ and $R_f^{,}$	Start and finish of recrystallisation in plain carbon steels
$P_s^{,}$ and $P_s^{,,}$	Predicted precipitation start times in deformed and undeformed austenite

	respectively
P_s	Strain-induced Nb(C, N) precipitation start time
Z	Zener-Hollomon parameter
$\dot{\varepsilon}$	Strain rate
Q_{def}	Activation energy for deformation
k	Avrami exponent
B'	Constant
ρ_a	Dislocation density in completely recrystallised austenite
X	Recrystallised area fraction
ρ	Dislocation density in unrecrystallised austenite
Q_{rex}	Activation energy for recrystallisation
t_i and T_i	Finite difference in time at which the temperature was T_i
K, m and p	Material dependent constants

Chapter 4 Materials and Experimental Techniques

T_r	Re-heat temperatures
T_d	Deformation temperature
t_h	Holding time in second after deformation
a	Lattice parameter

Chapter 5 Microstructure of as-cast and reheated slab; Prediction and quantification of microsegregation

D	Diffusivity of Nb in austenite
x	Diffusion distance

Chapter 6 Limits of validity of Dutta-Sellars equations at 0.3 strain: Influence of starting grain size and compositions and prediction of grain size distribution after deformation

ρ^G	Geometrically necessary dislocations
ρ^S	Statistically stored dislocations
E_t	Total stored energy
α	Material dependent constant
G	Shear modulus
M	Taylor factor
α_S	Material dependent constant
C	Constant
C_1	Constant
γ	Shear strain

List of Abbreviations

Chapter 1 Introduction

HSLA	High strength low alloy
TMCR	Thermomechanical controlled rolled

Chapter 2 Grain structure development during casting and reheating of Nb microalloyed steel; influence of microsegregation

SDAS	Secondary dendrite arm spacing
CAFD	Cellular automata finite difference
LA-ICP-MS	Laser ablation inductively coupled plasma mass spectrometer
SEM-EDS	Scanning electron microscopy equipped with energy dispersive spectroscopy
WDS	Wavelength dispersive spectroscopy
CM	Concentration mapping
CCT	Continuous cooling transformation

Chapter 3 Review of grain structure formation during hot deformation of microalloyed steel

HR	Hot rolling
RLT	Recrystallisation limit temperature
RST	Recrystallisation stop temperature
SIBM	Strain-induced boundary migration
TSDR	Thin slab direct rolled
SRP	Solute retardation parameter
RPTT	Recrystallisation, precipitation, time and temperature

Chapter 4 Materials and Experimental Techniques

ECD	Equivalent circle diameter
FEG	Field emission gun
TEM	Transmission Electron Microscopy
SADP	Selected area diffraction pattern
XRD	X-ray diffraction

Chapter 6 Limits of validity of Dutta-Sellars equations at 0.3 strain: Influence of starting grain size and compositions and prediction of grain size distribution after deformation

RMS	Root mean square error
JMAK	Johnson–Mehl–Avrami–Kolmogorov
SIP	Strain induced precipitates

Chapter 10 Pinning of austenite grain boundaries by mixed AlN and Nb(C,N) precipitates

BSE	Back scattered electron

List of Tables

Chapter 5

Chapter 6

Chapter 7

Chapter 8

Chapter 9

Chapter 10

List of Figures

Chapter 4

Chapter 5

Chapter 6

Chapter 8

Chapter 9

Chapter 10

CHAPTER – 1

Introduction

Mechanical properties of microalloyed steels are strongly influenced by their ferrite grain structure. It is well established that a fine and uniform distribution of ferrite grains results in high strength coupled with high toughness [1-20]. The evolution of the final ferrite grain structure and any precipitate population are influenced by the processing schedule. A common processing route for high strength low alloy (HSLA) steel plate is shown in Figure 1.1 [16]. After steel making the molten metal is continuously cast. Continuous casting not only improves the casting yield (compared to ingot casting), but also a smaller section size can be cast (smaller billet or bloom sections instead of large ingots). This reduces the amount of hot working required to produce the semi-finished and finished products saving energy, time and cost [1]. The continuous cast slabs are reheated prior to rolling. Reheating reduces the inhomogeneity of the cast structure, makes the steel soft for subsequent deformation and dissolves the majority of microalloy precipitates to achieve the maximum benefit of microalloying. A two or three stage controlled rolling schedule with single or double hold after reheating is quite a common practice to achieve the maximum grain refinement [1, 17, 18, 20].

In some thermomechanical controlled rolled (TMCR) microalloyed steel plate the presence of a bimodal grain size distribution has been observed [7, 19, 21, 22]. A bimodal grain structure is one where there are abnormally large grains in a matrix of smaller grains i.e. two modes in grain size distribution. A typical bimodal ferrite grain structure and the corresponding grain size distribution is shown in Figure 1.2. It should be noted that area % distribution curves, rather than number % curves, show bimodal grain size distributions more clearly [14, 22, 23].

Bimodal grain size distributions have been reported to cause a variation in mechanical properties, and are particularly detrimental for impact fracture toughness (can cause significant scatter) of TMCR microalloyed steel plates [7, 14, 24]. The formation of a bimodal grain size distribution has been associated with microsegregation of microalloying elements, particularly Nb [14, 22, 23]. Niobium (Nb) is known to be the most effective element for grain refinement during rolling but it segregates strongly to the interdendritic regions, along with C and N, during solidification [14, 22, 23]. Preferential Nb segregation in the interdendritic regions results in an inhomogeneous solute and precipitate distribution [14, 22, 23]. This leads to non-uniform grain boundary pinning action during reheating, finally resulting in the development of a bimodal grain structure [14, 22, 23].

After reheating the next stage is deformation. Grain structure development during deformation depends on recrystallisation, precipitation and the interaction of recrystallisation and precipitation [1, 17, 18, 20]. Nb is known to influence recrystallisation by solute drag and forming particles during deformation [1, 5, 6, 12, 13, 17, 25]. Any inhomogenity in Nb content in the microstructure present after casting or reheating would influence recrystallisation kinetics and thus final development of the grain structure in the final product. Therefore, designing an appropriate processing schedule requires understanding microsegregation during solidification and its effect on grain structure development during reheating as these are the pre processing stages before hot rolling. The local solute content after solidification influences the precipitate stability during reheating and that influences the grain structure after reheating and hence recrystallisation during hot rolling. Therefore, the microstructural changes taking place at every processing stage need to be studied as each stage influences the final development of the grain structure in the final rolled plate.

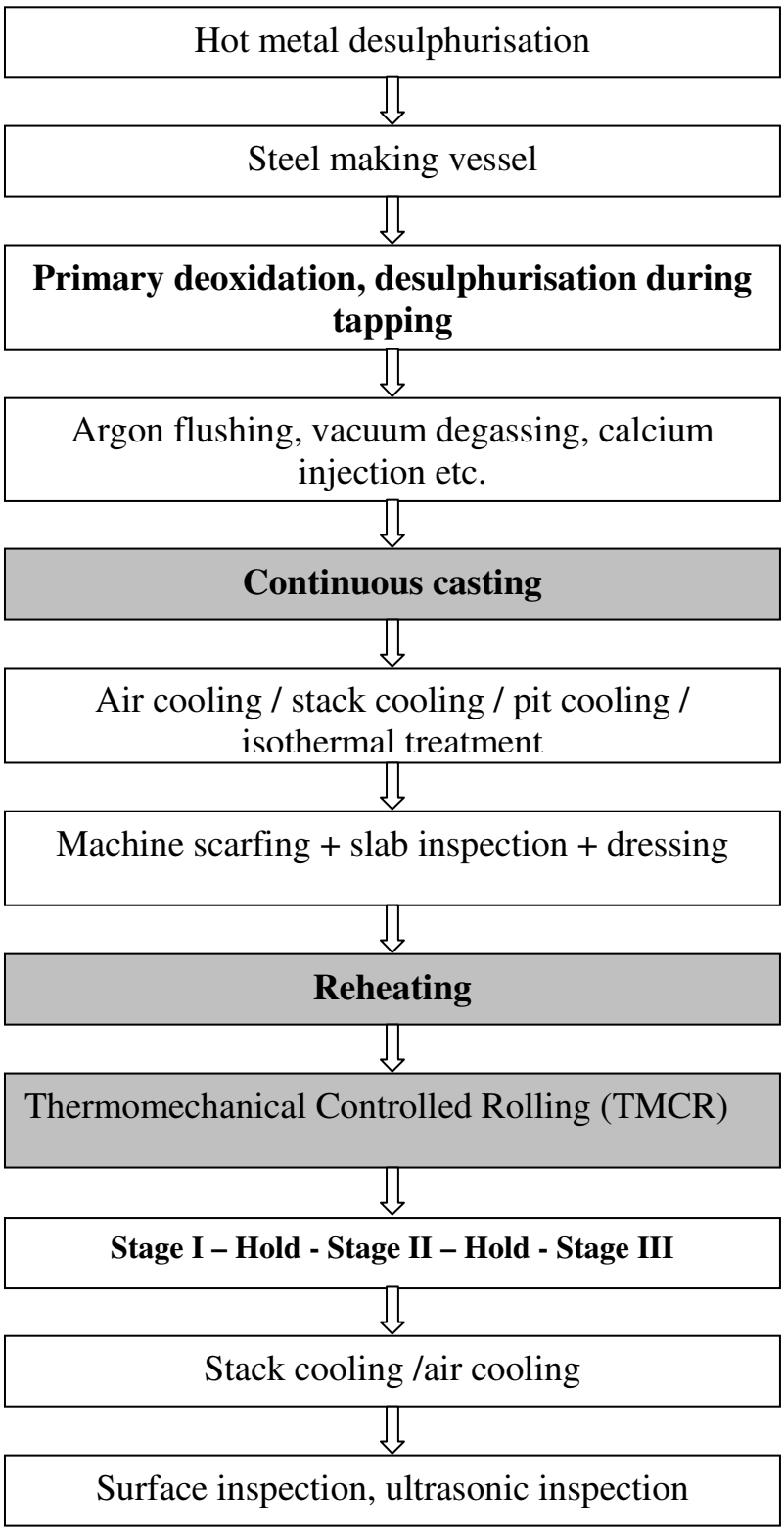

Figure 1.1. Flow chart showing the typical processing route for TMCR-microalloyed-pipeline steels. The dark shaded stages are important from the point of view of grain structure and therefore, are studied in the present investigation.

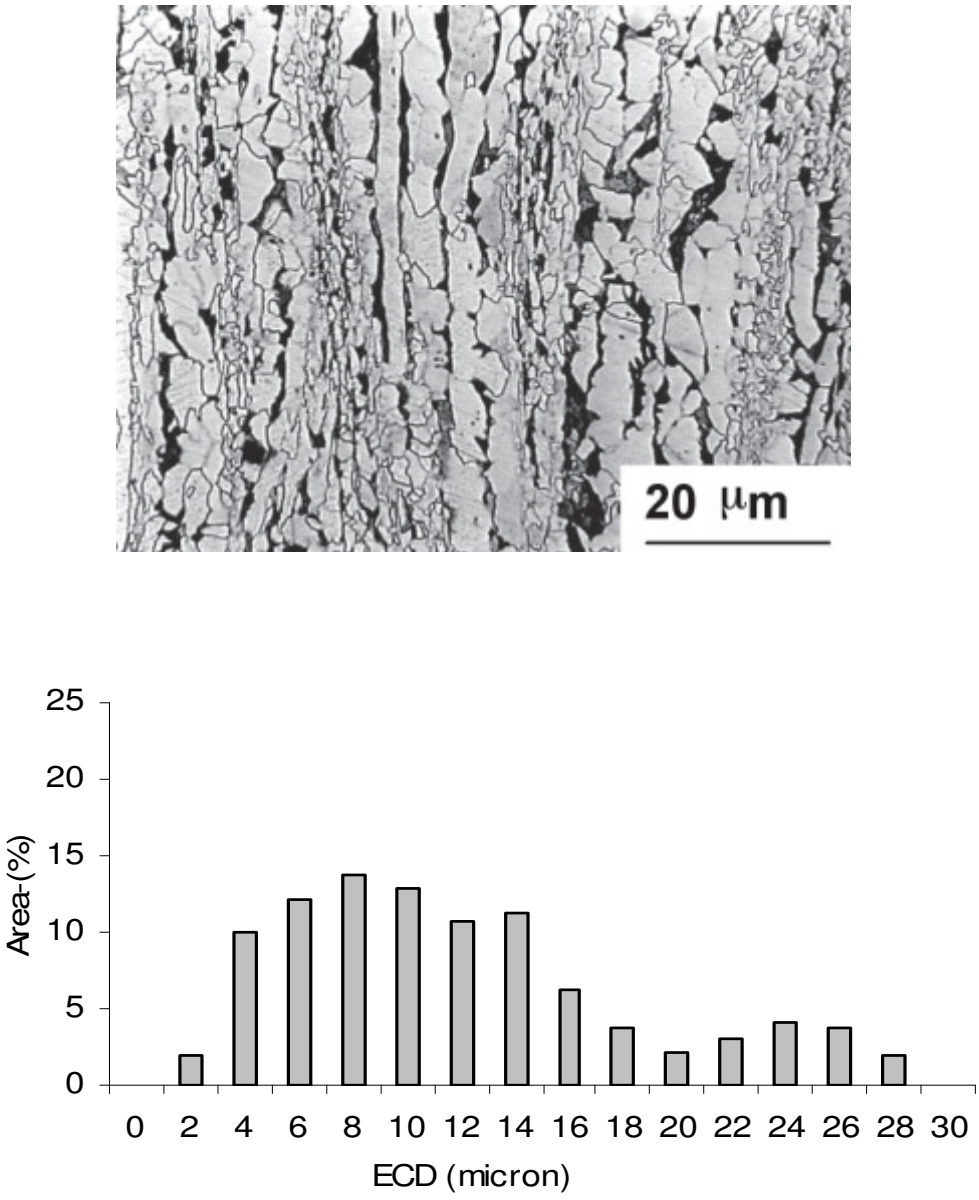

Figure 1.2. Microstructure and ferrite rain size distribution of a TMCR plate showing bimodal grain size distribution [19].

CHAPTER – 2

Grain structure development during casting and reheating of Nb microalloyed steel: influence of microsegregation

2.1. Introduction

As indicated in the introduction continuous casting is the preliminary stage to TMCR. The microstructure, precipitation and segregation that develop during casting have a direct effect on the final microstructure. In order to predict the final microstructure the amount of microsegregation after casting and reheating needs to be quantified. Hence it is necessary to study the development of the solidification structure during casting and how that influences the grain structure development during reheating by influencing the precipitate stability.

2.2. Grain structure development during solidification

Three morphological crystal zones (fine grained chilled zone at the surface followed by a columnar zone and central equiaxed zone) are typically present in the transverse section of a casting or ingot (Figure 2.1). The 'chill zone' lies in a narrow band following the contour of the mould and consists of small equiaxed crystals, which usually have random orientations. Inside this zone the crystals become large in size, elongated in shape, with their length predominantly parallel to the heat flow direction (normal to the mould walls). These grains have a very strong preferred orientation with a direction of dendritic growth parallel to their long axis. Because of the shape of the crystals in this zone it is called the columnar zone. The last zone lies at the centre of the mould and represents the last metal to freeze. In this region the grains are again equiaxed and have random orientation. The chill zone present at the surface is produced

by a high rate of nucleation of fine randomly oriented equiaxed crystals in the highly supercooled liquid adjacent to the mould wall. Further nucleation is stopped adjacent to the 'chill' zone (as supercooling in the liquid is lost by the latent heat of fusion released by the 'chill' zone) and growth of the favourably oriented grains with the preferred crystallographic orientation (<100> in cubic metals) and parallel to the temperature gradient continues due to constitutional supercooling. These grains form the columnar crystals in the columnar zone [26]. As the columnar grains grow in size there is also an increase in their diameter due to the elimination of less favourably oriented grains. Additionally grain coarsening of the castings or ingots can occur from the movement of the grain boundary due to grain boundary surface energy factors.

The central zone of the as-cast shape consists of large equiaxed crystals produced by nucleation in the highly constitutionally supercooled interior liquid, and by broken parts of crystals in the columnar zone swept by convection in the liquid to the central zone [15, 26, 27]. Crystallisation in the central zone, therefore, occurs, through the appearance and growth of new crystals, and not through the continued growth of the elongated crystals of the columnar zone. Overall an increase in as-cast grain size can be expected from the subsurface 'chill' zone towards the slab centre due to the drop in cooling rate, giving a longer residence time in the mushy zone and hence greater growth prior to impingement [28, 29].

Zhang et al. [28] reported a gradual increase in ferrite grain size from subsurface (46-50 μm at 10 mm from the top of the slab) to the quarter thickness (76-93 μm) and to the mid thickness position (88-115 μm) for the three continuously cast slabs (composition, wt %: 0.09-0.10 C, 0.020-0.045 Nb, 0.001-0.009 Ti, 0-0.05 V, 0.008 N; slab thickness: 200 mm).

2.2.1. Cellular and dendritic solidification

Cellular and dendritic solidification is associated with constitutional supercooling. According to constitutional supercooling theory, which arises due to the variation of solute concentration ahead of the solidification front resulting in a variation of equilibrium solidification temperature i.e., liquidus temperature, this supercooling results in the instability of the plane front since any protuberance forming on the interface would find itself in supercooled liquid and therefore would not disappear. The constitutional supercooling criterion is given by equation 2.1 assuming no convection [27].

$$(G_L/R) \geq - [(m_L C_o(1- k_p))/ k_p D_L] \quad (2.1)$$

where, G_L is the actual temperature gradient in the liquid at the interface; R is the rate of movement of the interface; m_L is the slope of the liquidus line or the equilibrium freezing range of the alloy; C_o is the bulk alloy composition, k_p is the equilibrium partition ratio and D_L is the diffusion coefficient of solute in the liquid.

When convection is sufficiently vigorous that, from a solute redistribution standpoint, diffusion in the liquid is complete, then:

$$(G_L/R) \geq - [(m_L C_\alpha(1- k_p))/ k_p D_L] \quad (2.2)$$

where, C_α, the bulk liquid composition, is equal to C_o for a small amount of solidification from a large melt [27].

Clearly planar front solidification is most difficult for alloys with a large solidification range and high rates of solidification. If the temperature gradient ahead of an initially planar interface is gradually reduced below the critical value the first stage in the breakdown of the interface is the formation of a cellular structure. The formation of the first protrusion causes solute to be rejected laterally and pile up at the

root of the protrusion resulting in the lowering of the equilibrium solidification temperature, causing recesses to form, which in turn trigger the formation of other protrusions. Eventually the protrusions develop into long arms or cells growing parallel to the direction of heat flow. The solute rejected from the solidifying liquid concentrates into the cell walls, which solidify at the lowest temperatures. Each cell has virtually the same orientation as its neighbours and together they form a single grain.

Cellular microstructures are only stable for a certain range of temperature gradients. When regular cells form and grow at relatively low rates, they grow perpendicular to the liquid solid interface regardless of the crystal orientation. When, however, the growth rate is increased, crystallographic effects begin to exert an influence. The cell growth direction deviates towards the preferred crystallographic growth direction (<100> for cubic metals). Simultaneously the cross section of the cell begins to deviate from its previously circular geometry owing to the effect of orientation leading to the formation of a dendritic structure. The driving force for the cellular to dendritic transition is associated with the creation of constitutional super-cooling in the liquid between the cells causing interface instabilities in the transverse direction.

2.2.2. Segregation

Segregation refers to any non-uniformity of chemical composition, which occurs during freezing of an alloy. Segregation occurs when the solid has a different (usually lower) solubility for alloying elements compared with the liquid causing the alloying elements to partition preferentially into the solid or liquid [30]. Segregation can occur on the scale of 10s – 100s of μm (micro-segregation) or 1 – 1000 mm (macro-segregation) [27].

2.2.2.1 Segregation during cellular solidification

Cells protrude into the liquid and the intercellular liquid becomes increasingly enriched with distance back from the cell tips. The assumptions associated with the solute redistribution in cellular solidification are [31]:

1. Isotherms are flat perpendicular to the growth direction.
2. The cell spacing adjusts so that constitutional supercooling in the inter cellular region is very small.
3. Cell size is sufficiently coarse that the effect of radius of curvature on melting point can be neglected.
4. Solid state diffusion is negligible.

Assuming that solute flow exists only by diffusion and solid and liquid densities are constant and equal, the local solute redistribution equation can be written as follows [31]:

$$C^*_s=k_pC_o[(a/(k_p-1))+(1-(a\,k_p/(k_p-1))(1-f_s)^{(k_p-1)}] \quad (2.3)$$

Where $C^*_s = k_pC_L$ is the solid composition at the liquid solid interface when f_s fraction of solid has formed in the element. $a = -(D_LG/(m_LRC_o))$.

2.2.2.2 Segregation during dendritic solidification

Micro-segregation results from freezing of solute enriched liquid in the interdendritic spaces. On the other hand macro-segregation is non-uniformity of composition in the cast section on a larger scale. For example a high degree of positive segregation in the central region of a continuously cast section is known as centreline segregation, and poses quality problems [27].

Solidification of steel in continuous casting is predominantly dendritic in the above-mentioned columnar zone due to the constitutional super-cooling and preferred

crystallographic growth. Figure 2.2 shows a schematic diagram that illustrates dendritic solidification [32]. The darker shading in between the dendrites in the diagram shows the increase in solute content in the liquid around the solidifying dendrites and the solute atom redistributes in the liquid and solid based on equilibrium solidus and liquidus temperatures. At any given temperature the solute concentration of the solid can be designated as C_s and that of the liquid as C_l as defined by a tie line at that temperature. If an impure liquid were kept in contact with its solid at the freezing temperature for an appreciable time, equilibrium partitioning of the solutes would be attained between the liquid and the solid.

The redistribution, or the partitioning, of the solute can then be defined as the partitioning ratio, k_p, as [26, 27]:

$$k_p = C_s/C_l \tag{2.4}$$

With this parameter solute distribution in liquid, C_l, as a function of weight fraction of solid, f_s, in the solidifying volume element can be given by the Scheil equation as:

$$C_l = C_o(1-f_s)^{k_p-1} \tag{2.5}$$

where, C_o is the initial alloy composition within the volume element [27] and C_l/C_o is known as the segregation ratio (r), a measure for solute segregation (i.e. enrichment) of the liquid with progressive solidification. The assumptions of the Scheil's equation are negligible under-cooling, complete diffusion of solute in the liquid in the volume element, negligible diffusion of solute in the solid and constant k_p throughout solidification. The Scheil equation has been shown to accurately represent solute enrichment in the solid as solidification proceeds [27, 33].

During solidification the entire mass consists of three regions, solid, liquid and solid liquid mixture; the mushy zone consisting of dendrite and interdendritic liquid.

Positive micro-segregation occurs in the interdendritic liquid due to solute rejection from solidifying dendrites. The composition of the solidifying dendrite is not uniform; this is known as coring. The first solid to solidify, or the first dendrites to grow in steel, has the lowest solute content but as the solidification proceeds, the concentration of solute/solutes in the dendrite increases. However the liquid adjacent to growing dendrites also gets richer in solutes. After significant solidification secondary and tertiary arms of neighbouring primary dendrites impinge each other trapping solute rich liquid in the interdendritic regions.

During solidification the extent of partitioning is represented by the equilibrium partition ratio (as mentioned in equation 2.4), k_p. If k_p is less than 1 then upon solidification the solute would be rejected into the remaining liquid [30]. For a binary alloy of composition C_0 the composition of the first solid to form is k_pC_0. The excess solute will be rejected into the liquid. Very slow cooling will allow extensive solid state diffusion, so that, with continued solidification, the compositions of liquid and solid will always be homogeneous, Figure 2.3(a). Since the solidification is one dimensional, conservation of solute requires the two areas in Figure 2.3 (a) to be equal. The last liquid will have the composition C_0/k_p [30].

A different scenario would be for no solid-state diffusion and perfect mixing in the liquid. In this case, the composition of the first solid would be k_pC_0, with solute rejected into the liquid to raise the composition of the liquid above C_0. With further undercooling the next layer of solid that forms would be slightly richer in solute than the first due to mixing in the liquid; overall the composition of the solid steadily increases with the degree of solidification, Figure 2.3 (b). Under these conditions, the enrichment of the liquid can be very large and may even reach a eutectic composition, Figure 2.3 (c), terminating solidification close to the eutectic temperature [30].

If there is no stirring or convection in the liquid phase then the solute rejected from the solid will only be transported away from the solid - liquid interface by diffusion. Hence, there will be a rapid build up of solute ahead of the solid – liquid interface and a correspondingly rapid increase in the composition of the solid formed. Eventually, with the progress of solidification, the liquid adjacent to the solid then has a composition C_0/k_p and the solid forms with the bulk composition C_0, Figure 2.3 (d) [30]. This is the type of profile noted for most continuously cast low carbon steel slab [33, 34]. Micro-segregation of the type that determines grain size bimodality occurs within the steady-state regime shown in Figure 2.3 (d). The extent of micro-segregation of any solute species will be governed by the partition ratio but also by the diffusivity of the alloying elements present in the alloy.

Micro-segregation behaviour will be different for the various alloying elements found in HSLA steels. A list of k_p values of some elements found in the HSLA steel is given in Table 2.1 [33, 35, 36]. Nb has been shown to be most effective microalloying element to achieve grain refinement during rolling, but has a greater tendency to partition in the interdendritic regions during solidification (Table 2.1) than titanium [13, 22, 23, 33, 37]. Partitioning data for Nb, Ti, Al and V are shown in Figure 2.4 [14]. In this figure partition data corresponds to the ratio of the composition of the element in liquid to the composition of the element in solid i.e. C_l/C_s which is reverse to the equation 2.4, therefore greater than 1. It is observed that the partition ratio for Nb between the liquid and the solid at the final stages of solidification can be as high as 7 (composition in the final liquid compared to the average composition [14] and there is an abrupt change when solidification changes from δ ferrite to mixed δ ferrite and austenite indicating greater partitioning to austenite. Titanium can also be seen to segregate, although less strongly compared to Nb (partition ratio of 5 between the final liquid to solidify and the solid phase) [14]. Vanadium shows limited partitioning

(partition ratio of approximately 1.8 between final liquid to solidify and the solid phase) and aluminium shows a very small tendency to segregate to the solid phase during solidification (either δ ferrite or austenite) with a partition ratio of approximately 0.8 between the final liquid to solidify and the solid phase [14].

The extent of micro-segregation also depends on the size of the dendrites particularly on the secondary dendrite arm spacing (SDAS). A larger SDAS may increase the size of the dendritic area and concentration of solute elements within the interdendritic liquid resulting in an increase in micro-segregation [33]. The SDAS increases with increasing distance from the chill surface; with decreasing cooling rate; and with increasing section size [15, 27, 38]. The effect of cooling rate on the SDAS is shown in Figure 2.5 for a steel containing 0.1 wt % C [27]. An increase in SDAS has been reported by Zhang et al. [28] with the increase in distance from subsurface (SDAS of 80 – 86 µm at 10 mm from surface, 190 – 220 µm at quarter thickness and 230 – 290 µm at mid thickness) corresponding to a decrease in cooling rate. Using the data from Figure 2.5 it can be said that at the subsurface the cooling rate is 12 times (120 ºC/min) greater than at quarter thickness position (10 ºC/min). Figure 2.6 shows the variation of SDAS in a 50 mm thick slab as a function of distance from the surface for a 1020 steel [33]. At the sub surface the SDAS is 60 µm and at mid thickness position it is ~ 120 µm and that leads to more uniform cooling rate (150 ºC/min at subsurface and 100 ºC/min at mid thickness position) compared to the thicker slab reported by Zhang et al. [28]. Although whether there is any change in partition ratio of the alloying element from surface to the centre is not discussed in the paper.

The size of the columnar zone and associated interdendritic segregation and shrinkage porosity can greatly be reduced by the use of in-strand or in-mould

electromagnetic stirring [39]. Stirring fragments the columnar dendrites and increases the size of the equiaxed solidification zone reducing segregation levels. [33].

Apart from interdendritic or microsegregation, macrosegregation (compositional variation over distances much larger than the interdendritic spacing), is also a common phenomenon in continuously cast steel. Various types of segregation, which are often encountered in the longitudinal section of continuously cast slabs, are shown in Figure 2.7 [15, 40]. Centreline segregation (the most common form of macrosegregation) is a positive segregation (local composition higher than average composition) that takes place at the slab-centre, where the last (solute-rich) liquid solidifies. Figure 2.8 shows typical carbon segregation in continuously cast steel slab [41]. Composition variation due to centreline segregation results in higher local hardenability at the centreline and the formation of a greater amount of lower temperature transformation products (i.e. martensite or bainite in ferrite + pearlite steel) during cooling after subsequent hot-rolling. Varying microstructure can cause non-uniformity in the mechanical properties of the finished product [35, 40]. Although there are several parameters governing centreline segregation, the tendency of macrosegregation also depends on the segregation ratio (r), which can be determined primarily by 'k_p' (as listed in Table 2.1) in the same way as microsegregation [33, 41]. For continuously cast slabs, the most successful corrective action for centreline segregation is called 'soft reduction' the principle of which is to mechanically reduce the total thickness of the slab during its cooling and solidification [40].

Analysis of four continuously cast slabs from two different sources showed that the centre-line composition arising from macro-segregation can be predicted by equilibrium thermodynamics when solidification occurs as a single phase for simple casters (no/little soft reduction) [34]. In addition, it was shown that 80 % of the slab

thickness solidified as the bulk average composition and equilibrium thermodynamics applied to the liquid and solid compositions in that region [34]. Hence, for these areas, micro-segregation can be predicted using the bulk composition as a starting point. Scheil's equation can be used to represent solute enrichment in the solid as solidification proceeds [27], treating the solidifying slab as consisting of three regions, (i) solid, (ii) liquid and (iii) the solid + liquid mushy zone comprising dendritic solid and interdendritic liquid. Positive micro-segregation (solute enrichment) occurs in the interdendritic liquid due to solute rejection from solidifying dendrites [27]. Lee et al. [42] used cellular automata finite difference (CAFD) method to predict the partition ratio of alloying elements in a 0.1 wt % C steel containing 0.04 wt % Nb. The composition of Nb in the interdendritic regions was found to be 5.2 times as high as that in the dendritic regions. With about same amount of Nb (0.045 wt %) Chakrabarti et al. [43] predicted the partition ratio to be 7 for Nb using thermodynamic modelling (Thermo-Calc). This discrepancy could be due to the fact the thermodynamic modelling uses the first solid and last liquid composition to predict the partition ratio where as the diffusion model used by Lee et al. allows change in composition as solidification proceeds.

2.2.2.3 Measurement of microsegregation

A convenient method of measuring micro-segregation in columnar structures is by use of the electron probe; Figure 2.9 shows the results of a typical series of measurements for carbon and manganese segregation across dendritic arms with SDAS ~ 200 - 300 μm in low-alloy steel reported by Krauss [33]. The measured partition ratio of C is 0.75 (here it is the ratio of the composition of solid to that of the liquid, therefore <1) where as the predicted value is 0.13. The greater measured value could be due to the inaccuracies associated with the electron probe in quantifying light

elements such as C. The interdendritic segregation of microalloying elements, such as niobium, has been measured by producing maps (using laser ablation inductively coupled plasma mass spectrometer, LA-ICP-MS) at the quarter-thickness position of a continuously cast steel (0.1 C, 0.007 N, 0.042 Nb, 0.045 Al, 0.0018 Ti, 0.05 V, all wt %) [44]. In the composition maps the distribution of Nb in the as-cast condition appeared to be characteristic of the dendritic as-cast microstructure (Figure 2.10). Therefore, it was suggested that the segregated regions coincided with the interdendritic regions and were separated by the SDAS (~ 200-250 μm). From Figure 2.10, the average Nb composition appears to fall within 0.030-0.037 wt % in the ferrite (dendrite centre region) and 0.060-0.067 wt % in the pearlite (interdendritic region), i.e. the Nb level in the interdendritic region is approximately twice that in the dendrite centre region. In some pearlite regions the Nb-content can reach as high as ~ 0.10 - 0.12 wt %. That results in a partition ratio (i.e. the ratio of composition of liquid to that of solid) of 2 or 3, about half of what is predicted (7) using Thermo-Calc [14, 43] and less than the partition ratio predicted using the CAFD method which allows diffusion of elements during solidification [42].

There are several reasons for the discrepancy in values. Experimental results will be an average for the measurement area for the LA-ICP-MS method used whereas the Thermo-Calc data will be the maximum segregation level for the very final liquid to solidify, therefore the experimental results will show values lower than the theoretical maximum due to the averaging effect. Distribution maps of Ti and V reveal that the segregation levels of Ti and V are far less intense compared to Nb segregation which has also been shown using Thermo-Calc although the actual partition ratio predicted by using Thermo-Calc is greater than that is measured. Chakrabarti et al. [43] has used scanning electron microscopy equipped with energy dispersive spectroscopy (SEM-EDS) and wavelength dispersive spectroscopy (WDS) to measure the local composition

at interdendritic and dendrite center regions over a 1 mm^2 area at the quarter-thickness position of the as-cast slabs containing 0.02 - 0.045 wt % Nb. (Table 2.2). The local Nb levels at interdendritic and dendrite center regions for slabs lie within the range obtained by Couch [44] (~0.075 to 0.10 wt pct at interdendritic and ~0.009 to 0.027 wt % at dendrite centre regions) using LA-ICP-MS on the quarter-thickness position of a slab of the same composition steel. Under SEM-EDS and WDS the distribution of Al, Ti, and V were found to be more homogeneous compared to the Nb distribution (Table 2.2, also supported by LA-ICP-MS). The above finding indicates to the strong interdendritic segregation of Nb that resulted in solute-rich interdendritic regions and solute-poor dendrite centre regions. The partition ratio measured using SEM-EDS is less than predicted by using Thermo-Calc. This could be the averaging effect as mentioned earlier or may be due to the fact that the experimental values are from the quarter thickness position, which is expected to be close to where the solidification sequence can change from initial solidification as δ ferrite to mixed δ ferrite and austenite. From Figure 2.4 it can be seen that the partition ratio for niobium is approximately 3 when solidification changes to mixed δ ferrite and austenite and then increases significantly as austenite forms [23].

SEM-EDS and WDS has also been used to study the spatial variation of alloying elements such as Mn, Cr and Ni across the as cast slab of 8617H steel [33]. Figure 2.11 shows the SEM WDS trace for Mn, Cr and Ni. The measured partition ratio is in good agreement with the predicted value and that is associated with the larger quantity of these elements present in the alloy.

Presslinger et al. [45] analysed segregation levels by quantitative imaging of elemental distribution (concentration mapping, CM) on continuously cast slab (210 mm thick) of HSLA steel (0.1-0.15 C, 1.5 Mn, 0.15 Si, <0.02 P, <0.005 S, 0.015 Nb, 0.002 Ti, all wt %) using an electron probe microanalyser (with WDS). Concentration maps

of C, Mn, Si and P, Figure 2.12 (a), show the spatial distribution in composition resulted from the macro-segregation and / or micro-segregation. The intensity of Mn and Si segregation at solute-rich and solute-poor regions from slab-surface to slab-centre are shown in Figure 2.12 (b). The macro-segregation of microalloying elements to the last solidifying liquid is also evident from the presence of the microalloy carbide/carbonitride network at the slab centre, Figure 2.12 (c) [45].

2.3 Solidification sequence in microalloyed steel

In different grades of HSLA steels the carbon-content can vary between 0.04 - 0.2 wt% [13]. Depending on the C-content of the steel, different solidification modes control the evolution of the cast structure, as shown in Figure 2.13. These sequences are for equilibrium cooling, however, in actual steel solidification, the kinetic effects can modify the phases and sequences expected. Pottore et al. [46] studied the development of the as cast microstructure in low and medium carbon steels using interrupted and isothermal solidification experiments. Figure 2.14 shows the microstructural evaluation during solidification and subsequent cooling of a steel containing 0.08 wt % C [46]. The results of the investigation have established that δ ferrite is the primary solidifying phase in low (0.04 - 0.1 wt% C) carbon steels.

Hence during continuous casting of thick slab the initial metal to solidify at the interface with the water cooled Cu mould will be Nb depleted δ ferrite. This region will be associated with the surface and subsurface regions of the rolled plate. Solidification at the subsurface region will generally be completed as δ ferrite, due to increased cooling rate resulting in non-equilibrium solidification. As a result microsegregation of elements (e.g. Nb) to interdendritic or cellular boundary areas will coincide with the δ/δ grain boundaries. If full transformation from δ ferrite to austenite occurs prior to precipitation of Ti and Nb rich phases then the centre of the austenite

grains will correspond to the solute enriched region whilst austenite/austenite grain boundaries will be solute depleted. As cooling proceeds the higher solute content in the austenite grain centres will result in a greater driving force for precipitation and so formation at higher temperatures leading to greater time for growth and a higher volume fraction due to the greater amount of solute. The number density of the particles will depend on the nucleation rate and so on the precise relationship between the cooling rate and the continuous cooling transformation (CCT) curve for the prior austenite structure. Hence, it is expected that there will be a greater Nb(C,N) precipitate size and number density in pearlite, and the ferrite grains close to the pearlite regions for low carbon steels with limited pearlite content, since the γ/γ grain boundaries will tend to transform to α-ferrite and the centre of the austenite grains will form pearlite. The separation between the high precipitate number density regions is therefore expected to be similar to the separation between δ/δ grain boundaries, i.e. the secondary dendrite arm or cellular spacing. Chakrabarti [14] found an inhomogeneous distribution of Nb-rich microalloy precipitates in the as-cast slabs containing Nb ranging 0.02 - 0.045 wt %, with precipitate-rich regions separated by a distance similar to the SDAS, Figure 2.15, providing a link to the segregation behaviour during solidification. Couch [44] found arrays of Nb rich particles decorating prior-δ or γ grain boundaries.

Davis and Strangwood studied the solidification sequence of four structural steels containing varying Nb content [34] using Thermo-Calc. The composition of the steels they studied is given in Table 2.3 [34]. The solidification sequence for the four slab samples was predicted using Thermo-Calc and are shown in Figure 2.16, along with the critical temperatures. It can be seen from Figure 2.16 that the pipeline and structural steels both solidify fully as δ-ferrite before transforming to austenite, whereas the ship building and Slab 1 steels show initial solidification as δ-ferrite then a temperature range where mixed liquid, δ-ferrite and austenite coexist before final solidification as

fully austenite. The temperature range for solidification as δ-ferrite is quite large for the pipeline steel, whereas for the structural steel there is a very small temperature range (2.8 ^{o}C) before δ-ferrite transforms to austenite, indicating that if equilibrium conditions are not attained, or there is segregation changing the local compositions and hence solidification temperatures, then some mixed δ-ferrite and austenite solidification might occur [34].

2.4 Precipitation in continuous cast microalloyed steel

Several investigations have been carried out to study the precipitates in continuously cast HSLA steel slabs by using optical microscopy, scanning electron microscopy or transmission electron microscopy (using thin-foil or extraction-replica technique) fitted with X-ray analysis (EDS) facility. Some of the microalloying precpipitates such as Nb(C,N), TiN etc that form during solidification are shown in Figure 2.17 [47-52]. Nb-rich carbonitrides (Nb(C,N) or (Nb,Ti)(C,N) or (Nb,Ti,V)(C,N)) can be found in polyhedral, globular and plate-shape (10 – 300 nm) and are expected to form at ~ 1000 °C in austenite [28, 44, 47]. The number density of TiN and (Nb,Ti,V)(C,N) precipitates were found to be higher at the mid-thickness positions of the as-cast slab (TiN: 12-18×10^4/mm^2 and (Nb,Ti,V)(C,N): 16-25×10^6/mm^2) compared to the sub-surface position (TiN: 6-10×10^4/mm^2 and (Nb,Ti,V)(C,N): 8-14×10^6/mm^2) and that could be due to the enrichment of Nb and Ti in the last solidifying liquid [28].

At a particular location, as well as a random distribution, Nb-rich complex (Nb,Ti,V)(C,N) carbonitrides were also found in arrays (following prior δ or γ grain boundaries) or in clusters [44]. With high Ti content (0.03 wt %) along with sufficient N (0.012 wt %), cuboidal TiN particles can form in the liquid steel at high temperatures (> 1350 ºC), where they can grow to a large size (up to 3 μm). Such precipitates can

even be visible under optical microscopy [47] and are distributed randomly. With a drop in Ti (0.001-0.009 wt %) and N (0.006-0.008 wt %) content cuboidal TiN particles become smaller in size (70-800 nm) [28]. Zhang has also reported a higher number density of TiN particles at interdendritic regions compared to dendritic regions and also higher number density at the midthickness position due to the effect of solidification sweeping the particles into the slab centre [28].

As aluminium does not show a strong tendency for segregation between the liquid and solidifying steel Al additions will result in a more uniform distribution of pinning particles [44]. AlN particles are faceted (rod, needle or hexagonal shape) and of size range 100-400 nm [44]. Apart from random distribution AlN can also be found in arrays (similar to Nb(C,N)) along prior-δ or γ grain boundaries. The evidence of Al-Nb complex carbonitride precipitates, with Nb-rich caps epitaxially grown on large (> 100 nm) prismatic AlN precipitates (acting as the core) was reported by Leap and Brown [53]. An increase in the Ti content in the steel can reduce the formation of AlN precipitates [54, 55]. The temperature of formation for AlN will depend on the composition of the alloy.

From the study of precipitates and using Thermo-Calc or Chem-sage software it has been predicted that TiN nucleates first (~ 1200-1400 °C), followed by AlN (~ 1050-1200 °C), Nb(C,N) (~ 900-1100 °C) and V(C,N) precipitates (700-900 °C) during solidification [14, 43, 44].

2.5. Formation of bimodality during casting

Grain growth can occur during the slow cooling process involved with the continuous casting process. Due to the inhomogeneous precipitate population (higher number density in the interdendritic regions compared to dendritic regions as discussed in the previous section) there will be a variation in local grain boundary pinning force.

The higher temperature of formation and greater number density of precipitates in the interdendritic region will result in a greater degree of grain boundary pinning than in the dendritic areas. As a result it is possible to develop a bimodal grain size in the slab [23]. Davis and Strangwood has reported the presence of bimodal ferrite grain size distribution at the subsurface position of a 0.045 wt % Nb steel [22], Figure 2.18 (a). From the previous discussion on segregation behaviour during solidification it would be expected that bimodal grain size distributions can occur at both the sub-surface and mid-thickness positions (and regions in-between), as is observed in Figure 2.18 (a). Although Davis and Strangwood found that the grain size distributions do not show particularly strong bimodality (the 'coarse' and 'fine' distributions are overlapping without a very distinct 'coarse' peak) with a larger average grain size seen for the mid-thickness location of the same slab, Figure 2.18 (b), due to the slower cooling rate and hence greater time for grain growth [22].

It is thus seen that a bimodal grain size can start to form during the continuous casting stage of processing. The microsegregation behaviour of Nb and Ti is difficult to avoid during thick slab processing due to the relatively slow cooling, which gives near equilibrium conditions, and allows the strong segregation tendency of these elements to be developed. That also leads to the development of the inhomogeneous precipitate population in the as-cast condition and that will affect the grain growth behaviour during reheating which is the next stage of processing.

2.6. Summary

The above discussion has indicated that during solidification Nb has the strongest segregation tendency of all the microalloying elements, leading to an inhomogeneous precipitate population in the dendritic and interdendritic regions following solidification. After casting the next processing stage is reheating. The dissolution rate

of precipitates during reheating depends on the solute supersaturation (amount of the solutes above the equilibrium composition). The level of solute supersaturation and hence, the stability of the precipitates, depends on the solubility in the matrix phase (liquid, austenite or ferrite). The local composition of Nb is different in the dendritic and interdendritic regions after solidification and that would alter the precipitate stability and should have an influence on grain structure formation during reheating. This will be discussed in the next section.

2.7. Grain structure development during reheating

The reheating process is designed to ensure complete (or near complete) dissolution of micoalloying precipitates formed during casting in austenite [1, 17] for subsequent precipitation during, or immediately following, rolling to achieve the desired strength levels via grain size control and dispersion strengthening. The reheat temperature and time dictates the dissolution of the precipitates and formation of grain structure. The amount of alloying elements in solution and the grain size distribution after reheating govern recrystallisation and precipitation during deformation, which is discussed later, and that finally dictates the grain size distribution in the final product. Therefore reaustenitisation has a direct influence on final development of grain structure.

Due to micro-segregation during solidification there is a spatial variation in the Nb content in the HSLA steel slab that will affect the local precipitate stability characteristics [57]. Therefore the effect of reheating practice (temperature and time) on the potential development of a bimodal grain size will depend on the spatially varying dissolution of pinning precipitates.

2.7.1 Re-austenitisation during reheating

During reheating of a HSLA steel slab to the reheat temperature, nucleation of austenite grains occurs preferentially at the ferrite-cementite interface as well as ferrite-

ferrite grain boundaries. The austenite grains may grow driven by the minimisation of surface energy until they impinge on each other, upon which grain growth may continue [30]. However, if there is a sufficiently fine dispersion of precipitates present the austenite grain growth may be inhibited such that the austenite grain size distribution is characteristic of the precipitate distribution [1]. As the temperature increases V and Nb go into solution, resulting in a loss or reduction in the size of Nb/V rich precipitates; this in turn results in a loss of grain boundary pinning, hence enabling grain growth to occur. However the solution temperature of TiN is in excess of 1250 °C in a steel containing 0.008-0.012 wt % Ti [28], hence if there is sufficient TiN present of a suitable size (100-250 nm), then growth may still be inhibited [28]. Due to micro-segregation during solidification there is a spatial variation in the Nb and Ti content in the HSLA steel slab that will affect the local precipitate solubility characteristics [14, 43, 44]. Therefore the effect of reheating practice (temperature and time) on the potential development of a bimodal grain size will depend on the spatially varying dissolution of pinning precipitates.

2. 7.2. Precipitate dissolution during reheating

On reheating, the size of the precipitates generally decreases and eventually disappears due to dissolution. Dissolution can be described by the following equation:

$$T_{DISS} = \frac{B}{A - \ln(K_S)} \qquad (2.6)$$

where, A and B are constants, K_S is the solubility product and T_{DISS} is the equilibrium dissolution temperature [1].

The application of equation 2.6 is limited as solubility products should only be applied to: (i) equilibrium conditions, that rarely exist in practice; (ii) binary or ternary systems, hence there will be lot of variability in commercial steels as the other elements

present can alter the solubility product through their effect on the interaction coefficient [58]; and (iii) fixed particle geometry, the solubility product will be altered by the Gibbs-Thompson or capillary effect that considers the role of particle curvature on solubility (the solubility of a particle varies inversely with its curvature [30]). Solubility products can also be determined experimentally by different techniques [1, 12], which can account for the non-equilibrium condition, but every technique has its own limitations and errors. This leads to wide range of solubility product values being reported in the literature and limits their use in a predictive manner [59].

The use of simple solubility products or thermodynamic models was common when computing power was limited but has been superseded for more than 20 years by thermodynamic programs based on sub-regular models for ternary and higher interactions. Thermo-Calc, MT-DATA and ChemSage are some of the computer programmes used to predict the compositional changes and precipitation. Thermo-Calc software can handle single equilibria, property diagrams or phase diagrams with up to twenty elements in steel with a large number (~ 200) of possible phases [60]. A large number of thermodynamic models have been implemented for use with different databases. To study the precipitation and compositional changes along with phase transformations during casting / reheating, 'property diagrams' are very useful. Using Thermo-Calc for a particular steel composition property diagrams can provide mole fraction, driving force, or composition of different phases / precipitates / inclusions at every temperature step (temperature is the single variable) during casting / reheating [60].

The equilibrium dissolution temperature (T_{DISS}) indicates a particular temperature at which precipitates dissolve completely. However, during reheat gradual dissolution of complex precipitates is seen. For example, Hong et al. [61] have observed the gradual

dissolution of Nb-rich (Nb,Ti)(C,N) precipitates over 1100-1300 ºC in 0.06 wt% C, 0.056 wt% Nb steel when the steel was reheated at a rate of 20 ºC/s. Thermodynamic software can predict this gradual dissolution and can also show the change in concentration of complex carbonitrides (e.g. more TiN in (Nb,Ti)(C,N)) as the temperature increases during reheating [62, 63]. However, the thermodynamic models cannot predict the exact temperature for the complete precipitate dissolution. For example, Davis and Strangwood [22] and Palmiere et al. [59] have observed that (Nb,Ti)(C,N) precipitates remain after reheating to temperatures 40-90 ºC above the complete dissolution temperatures, and holding for one hour, that are predicted by using thermodynamic models for steels with 0.05-0.1 wt % C, 0.023-0.057 wt % Nb. Precipitates retained at such a high temperature could be due to (i) increase in size, larger size particles take longer time to dissolve and (ii) increase in solubility of Nb-precipitates formed at the interdendritic regions, where the local composition of Nb was higher than the average. The increase in solubility product leads to an increase in dissolution temperature. Therefore segregation of microalloying elements needs to be considered for the prediction of the dissolution temperatures.

2.7.3. Precipitate coarsening during reheating

During reheating the undissolved precipitates have a tendency to coarsen at the expense of the smaller ones in order to reduce the interfacial energy [1, 30]; this is a diffusion-controlled process [64, 65].

Particle coarsening not only depends on the diffusivity coefficient but on the total diffusion flux. Diffusion flux for any particular solute (say microalloying element M) is the product of the diffusion coefficient and the matrix concentration, D.[M], and thus the concentration of solute (in solution) is also important in determining coarsening [1]. For more stable precipitates (say TiN) or if the solute / interstitial ratio ([M]/[X]) in the

matrix is close to stoichiometric, there is less [M] free in solution (most of the M will be combined with X as precipitate) and that will decrease the coarsening rate. Partial dissolution of the precipitates can also increase the rate of coarsening by increasing the solute level in the matrix [1, 66]. In microalloyed steel it has been shown that the higher the temperature before the precipitates completely dissolve, the coarser the Nb(C,N) particles become, although the volume fraction of those precipitates present in the matrix was reduced [1, 67-70].

As a result in the presence of micro-segregation the rate of coarsening is expected to be higher in the solute-rich region, depending upon the initial segregation level and the stability of the precipitates in the solute-rich and the solute-depleted regions. Therefore, micro-segregation has an effect on precipitate coarsening and dissolution of precipitates resulting in variation in precipitate pinning in the solute-rich and solute-depleted region. As precipitates pin the austenite grain boundaries such variation can influence the grain growth on reheating.

2. 7. 4. Diffusion in microalloyed steels

The rate of coarsening of complex precipitates is considered to be controlled by the slowest diffusing species, hence it is also the slowest diffusing species that controls the rate of growth and dissolution in the ripening process. The diffusion constant $(D_0)_{diff}$ and activation energies (Q_{diff}) for the microalloying elements and important interstitials (C and N) in the austenite and ferrite phase are listed in Table 2.4 [71]. Diffusion of Nb and Ti within precipitates is much slower (~ 10^4 times less) than within the matrix [72, 73]. The variations of diffusion coefficients (D_{diff} in m^2/s) calculated from the given $(D_0)_{diff}$ and Q_{diff} values, $\left[D_{diff} = (D_o)_{diff} \exp\left(-\frac{Q_{diff}}{RT} \right) \right]$ with temperature (T) are given in Table 2.5 and are shown in Figure 2.19, R is the universal gas constant,8.314 $Jmol^{-1}K^{-1}$.

The presence of vacancies can change the diffusion mechanism by making the diffusion faster [74]. That may lead to increased diffusion flux and increased rate of particle coarsening.

2. 7.5. Grain growth during reheating

Grain growth occurs by the growth of larger grains at the expense of smaller grains such that the material volume remains constant. The driving force for growth is the minimisation of grain boundary energy and can be considered in terms of grain boundary curvature and grain angle. The grain boundary energy is reduced by the flattening of curved interfaces and the change in grain boundary and edge angles towards their equilibrium values [1]. Hence grains with convex curvature and less than equilibrium edge and corner angles tend to shrink, whereas concave and large angled grains tend to grow.

Modelling of grain growth in microalloyed steels is complex due to the nature and distribution of the precipitates that may inhibit grain growth. Inhibition of grain growth by the precipitates may be simplistically described by the Zener equation, which relates the maximum grain radius to the mean precipitate radius and volume fraction of the precipitates [75]. Microalloying elements produce fine precipitates in steel and those precipitates inhibit austenite grain growth (when undissolved) during reheating by grain boundary pinning, which results in a finer grain size. When the precipitates have dissolved then solute drag, by the microalloying elements, also reduces the rate of grain growth, but less effectively than precipitates.

There are three stages of austenite grain growth: restricted normal grain growth in the presence of pinning particles retaining the initial unimodal grain size distribution, coarsening / partial dissolution of precipitates making the pinning unstable and then large grains, which have a size advantage, grow abnormally producing a bimodal

distribution, and upon long holding times or an increase in reheat temperature precipitates dissolve completely and more grains grow rapidly (until they impinge upon each other), bringing back the unimodal distribution.

The intersection of an isolated grain of radius, R, by a spherical second-phase particle of radius, r, is shown in Figure 2.20. The retardation of grain growth model proposed by Zener [75] is based on the balance between the driving force for grain growth and the pinning force exerted by the second phase particles.

$$D = \xi . \frac{d}{f} \tag{2.7}$$

where, grain diameter D=2R, particle diameter, d=2r, f is the volume fraction of particles and in Zener model $\xi = 4/3$. Abnormal grain coarsening occurs when newly formed austenite grains are kept fine by the presence of a distribution of second phase particles such as Nb(C,N) [59].

Gladman [76] showed that there exists a critical condition where the energy release rate per unit displacement of grain boundary during grain coarsening is equal to the rate of energy release due to the absence of particle pinning. The maximum particle size that would effectively counteract the driving force for austenite grain coarsening is:

$$r^* = \frac{6R_0 f}{\pi}\left(\frac{3}{2} - \frac{2}{Z}\right)^{-1} \tag{2.8}$$

R_o is the initial matrix grain size, f is the volume fraction of particles, and Z is used to account for the heterogeneity of the matrix grain size.

Rearranging equation 2.8 gives:

$$R_0 = \frac{\pi}{6}\left(\frac{3}{2} - \frac{2}{Z}\right)\frac{r^*}{f} \tag{2.9}$$

Considering $D = \xi.\frac{d}{f}$ (equation 2.7), therefore, $\xi = \frac{\pi}{6}\left(\frac{3}{2} - \frac{2}{Z}\right)$ in Gladman's model. For the growth of austenite grains in the presence of AlN and NbC particles in steel, Gladman showed that Z ~ 1.41 - 2 and hence, ξ = 0.05 - 0.26.

According to Gladman [76] some particles can become ineffective in pinning the grain boundaries (particle size, r > r*) during reheating due to coarsening (increase in r) or even dissolution (decrease in f, and hence, decrease in r*). In such a situation, the growth of the large grains in the microstructure can offer the higher release in energy (due to higher Z value), and that can exceed the energy increase in unpinning. Therefore, the large grains become unpinned and grow in size. Small grains cannot grow as those are still pinned. This will create the situation of abnormal grain growth. Hence, precipitate coarsening or partial dissolution of precipitates leads to a situation where abnormal grain growth can occur. Upon complete dissolution of precipitates abnormal grain growth will stop and normal grain growth will resume (as in the absence of particles) for the larger grains, Z > 4/3, consuming smaller grains, till the large grains impinge upon each other.

In the presence of a non random particle distribution i.e. array of particles at the grain boundary unpinning of the grain boundaries would be very difficult as the most of the particles are in contact with the grain boundaries, as studied by many researchers [78, 79]. The limiting condition of grain growth from such studies can be summarised in the following form:

$$D = \xi.\frac{d}{f^{0.5}} \qquad (2.10)$$

Dogan et al. [80] considered the non-random distribution of pinning particles to explain the retention of fine grains upon long holding at high temperature. This

indicates an important limitation of all the grain growth models, discussed earlier, that the models do not consider the effect of segregation on grain growth.

Davis and Strangwood [22], Couch [44] and Chakrabarti [14] indicated that the interdendritic segregation can give rise to an inhomogeneous precipitate distribution and different precipitate solubility in different regions. Therefore, the local composition influences the grain structure rather than the overall composition and that may lead to a wide variation in grain size in the different regions. A typical example of a duplex or bimodal grain size distribution is shown in Figure 2.21. Chakrabarti [14, 43] quantified the inhomogeneous precipitate distribution and related it to the formation of bimodal grain structures in as-cast slab containing Nb(C,N) as the major pinning particles during reheating. Figure 2.22 (a) shows the bimodal prior austenite grains which has been formed after reheating at 1150 °C for 1 hour in a 0.045 wt % Nb steel [14, 43]. The fine Nb(C,N) particles associated with the fine grained regions are shown in Figure 2.22 (b-e). The distance between two fine grained regions was found to be similar to the secondary dendritic arm spacings. That established the link between micro-segregation of Nb and the development of the bimodal grain size distribution during reheating.

It was also shown that Thermo-Calc software can be used to predict the temperature range that could result in the generation of a bimodal grain size distribution, but that required the composition of Nb in the solute-rich and the solute-depleted regions [14, 43]. Thermo-Calc predicted precipitate stability in the solute-rich and solute-depleted regions for 0.045 wt % Nb steel is presented in Figure 2.23. However, the quantification of segregated material after reheating and prediction of grain size distribution in the solute-rich and the solute-depleted regions has not been carried out.

This is required to predict recrystallisation kinetics in the presence of segregation as will be discussed in a later section.

Various researchers have studied the reheating response of C-Mn steels, microalloyed steels and Al containing steels in the range 900 to 1300 °C. Cuddy and Raley [81] observed discontinuous austenite grain growth in Nb-microalloyed steels compared to continuous grain growth in C-Mn steel, and that produced a duplex grain structure comprising of abnormally coarse and fine austenite grains. Palmiere et al. [59] also measured the austenite grain size distribution upon reheating and found three regimes of behaviour in Nb-microalloyed steels, with an increase in temperature from 950 to 1300 °C: (a) unimodal distribution of initial grains exhibiting suppressed normal grain coarsening; (b) bimodal distribution of retained grains and abnormally coarsened grains; and (c) unimodal distribution of abnormally coarsened grains exhibiting accelerated normal grain coarsening. Couch and Chakrabarti [14, 43, 44] have also reported such bimodal austenite grain structures upon reheating Nb-microalloyed steels (0.1 wt % C, 0.04 wt % Nb) to 1100 - 1150 °C for 60 minutes. Cuddy and Raley [81] and Palmiere et al. [59] tried to measure a grain-coarsening temperature, T_{GC} (the temperature at which abnormal or discontinuous grain growth starts) from the point of discontinuity in the average grain diameter vs reheat temperature plot. It was found that T_{GC} increases with an increase in the complete dissolution temperature, T_{DISS}, of the microalloy precipitates but was always lower than T_{DISS} based on an atom probe microscopic study of Nb(C,N) precipitate dissolution. Also T_{GC} has been found to vary with the type and concentration of microalloying element in the steel. According to Cuddy and Raley [81] steels containing insoluble TiN coarsen at higher temperatures (~ 1200 - 1250 °C) than steels containing more soluble V(C,N) (980-1050 °C). T_{GC} for Nb-microalloyed steels increased with the increase in Nb-level (from ~ 1000 °C for

0.01 wt % Nb to ~ 1200 °C for 0.11 wt % Nb for Cuddy and Raley [81]; and from ~ 1000 °C for 0.02 wt % Nb, ~ 1100 °C for 0.049 wt % Nb, ~ 1200 °C for 0.090 wt % Nb for Palmiere et al. [59]).

Apart from microalloy precipitates AlN particles also play a role in controlling the grain growth behaviour of steel during reheating. Dogan et al. [80] have observed suppressed, abnormal and uniform grain growth conditions during reheating of two different Al-containing steels; where the AlN particles were studied using TEM. Abnormal grain growth started at a higher temperature (T_{GC} ~ 1100 °C) for the higher Al- and N-containing steel (therefore, lower AlN solubility), compared to the low Al, N steel (T_{GC} ~ 1000 °C). After abnormal grain growth started, the growing large grains did not consume all the small grains, even after long holding (3 hrs) at 1200 °C, and ~ 1 area percent of small grains remained within the large grains as colonies. It has been explained by Dogan [80] that the distribution of AlN particles might not be perfectly random and the regions of higher AlN particles would be more resistant to grain growth and give rise to the fine grain regions. TEM images of AlN particle distribution after reheating at 1100 °C for 1 hour of 0.027 (L-AlN) and 0.086 (H-AlN) wt % Al are shown in Figure 2.24. The reason why the AlN particles are distributed non randomly is not mentioned in the paper. Cabrara et al. [82] noticed the onset of abnormal grain growth during reheating was only due to the dissolution of AlN particles even in presence of more stable TiN or (Ti,V)(C,N) particles > 400 nm in size in steels containing Ti, V and Al. However the detailed quantification of particles has not been done and the particle size distribution has not been related to the grain size distribution after reheating.

2. 7. 6 Summary

The studies on reheating of microalloyed steels suggest that there are three stages of austenite grain growth: restricted normal grain growth in the presence of pinning particles retaining the initial unimodal grain size distribution, coarsening / partial dissolution of precipitates making the pinning unstable and then large grains, which have a size advantage, grow abnormally producing a bimodal distribution, and upon long holding times or an increase in reheat temperature precipitates dissolve completely and more grains grow rapidly (until they impinge upon each other), bringing back the unimodal distribution. Dogan et al. [80] considered the non-uniform distribution of pinning particles to explain the retention of fine grains upon long holding at high temperature. This indicates an important limitation of all the grain growth models, discussed earlier, that the models do not consider the effect of segregation on grain growth. Davis and Strangwood [22] and Couch [44] indicated that the interdendritic segregation can give rise to an inhomogeneous precipitate distribution and different precipitate solubility in different regions. Therefore, the local composition decides the grain structure rather than the overall composition and that may lead to a wide variation in grain size at different regions. Chakrabarti [14, 43] related the formation of bimodal grain size distribution during reheating to the inhomogeneous precipitate distribution of Nb(C,N) due to microsegregation of Nb. It has been indicated in section 2.3 that Al shows limited segregation tendency during solidification. Therefore AlN particles should be uniformly distributed through out the matrix. However presence of other segregating elements such as Nb may alter the distribution of AlN as Nb has a stronger affinity toward N than Al. That may reduce the available nitrogen in the solute-rich regions. This has not been studied before.

Tables and Figures

Table 2.1. The equilibrium partition ratio ('k_p') of various alloying elements in steel [33, 35, 36].

Element	Equilibrium partition ratio, 'k_p'
S	0.02
O	0.02
P	0.13
C	0.13
Nb	0.23
N	0.28
Ti	0.61
Si	0.66
Ni	0.80
Mn	0.84
V	0.90
Al	0.92

Table 2.2. Segregation levels of Nb, Ti, V, and Al in interdendritic and dendrite center regions of three steel slab containing three different levels of Nb, 0.045 wt % in Slabs 1 0.027 wt % in Slab 2 and 0.02 wt % in Slab 3 [43].

Slab Location	Nb (Wt Pct)	Ti (Wt Pct)	V (Wt Pct)	Al (Wt Pct)
Slab 1, interdendritic	0.075	0.0024	0.056	0.048
Slab 1, dendrite center	0.027	0.0018	0.047	0.041
Slab 2, interdendritic	0.050	0.001	0.055	0.031
Slab 2, dendrite center	0.020	0.001	0.047	0.026
Slab 3, interdendritic	0.040	0.010	—	0.039
Slab 3, dendrite center	0.016	0.008	—	0.032

Table 2.3. Chemical compositions of as cast slabs, wt% [34].

Steel	C	Si	Mn	P	S	Al	V	Nb	Cr	Other
Pipeline	0·03	0·25	1·70	0·008	0·005	0·052	0·082	0·063	…	…
Structural	0·06	0·30	1·52	0·01	0·003	0·0358	…	0·052	0·021	…
Ship building	0·14	0·38	1·35	0·015	0·007	0·039	0·003	0·002	0·027	0·01 Ni, 0·01 Cu, 0·004 Ti, 0·001 Mo
Slab 1 (Ref. 7)	0·10	0·31	1·42	0·017	0·005	0·046	0·052	0·045	…	0·52 Ni, 0·002 Ti, 0·008 N

Table 2.4. The diffusion constant $(D_0)_{diff}$ and activation energies (Q_{diff}) for the microalloying elements (also for Al) and important interstitials (C and N) in austenite and ferrite phase [71].

Element	D_0 (m^2s^{-1}) in ferrite	Q (kJ per mol^{-1}) in ferrite	D_0 (m^2s^{-1}) in austenite	Q (kJ per mol^{-1}) in austenite
C	0.62×10^{-6}	80.4	0.10×10^{-4}	135.7
N	0.50×10^{-4}	77.0	0.91×10^{-4}	168.6
Ti	3.15×10^{-4}	248.0	0.15×10^{-4}	251.2
V	0.61×10^{-4}	267.1	0.25×10^{-4}	264.2
Nb	1.30×10^{-4}	240.0	5.30×10^{-4}	344.6
Al	0.30×10^{-2}	234.5	-	-

Table 2.5. Diffusivity $(D)_{diff}$ for the microalloying elements and important interstitials (C and N) within austenite phase at various temperature (T (C): Temperature in ºC and T(K): Temperature in K) [72, 74].

T (ºC)	T (K)	Diffusivity (m^2s^{-1})				
		Nb	Ti	V	C	N
900	1173	2.39004E-17	9.7622E-17	4.2902E-17	9.0563E-12	2.82407E-12
1000	1273	3.83613E-16	7.38418E-16	3.6034E-16	2.70184E-11	1.09819E-11
1050	1323	1.3131E-15	1.81077E-15	9.2561E-16	4.38636E-11	2.00513E-11
1100	1373	4.10944E-15	4.1596E-15	2.2198E-15	6.87417E-11	3.50399E-11
1150	1423	1.18699E-14	9.01276E-15	5.006E-15	1.04382E-10	5.88775E-11
1200	1473	3.19034E-14	1.85296E-14	1.0683E-14	1.54069E-10	9.55067E-11
1250	1523	8.03587E-14	3.63348E-14	2.1692E-14	2.21667E-10	1.5008E-10
1300	1573	1.90864E-13	6.82632E-14	4.2105E-14	3.11634E-10	2.29158E-10
1350	1623	4.29801E-13	1.23361E-13	7.8455E-14	4.29015E-10	3.40896E-10
1400	1673	9.22015E-13	2.15182E-13	1.4085E-13	5.79432E-10	4.9522E-10

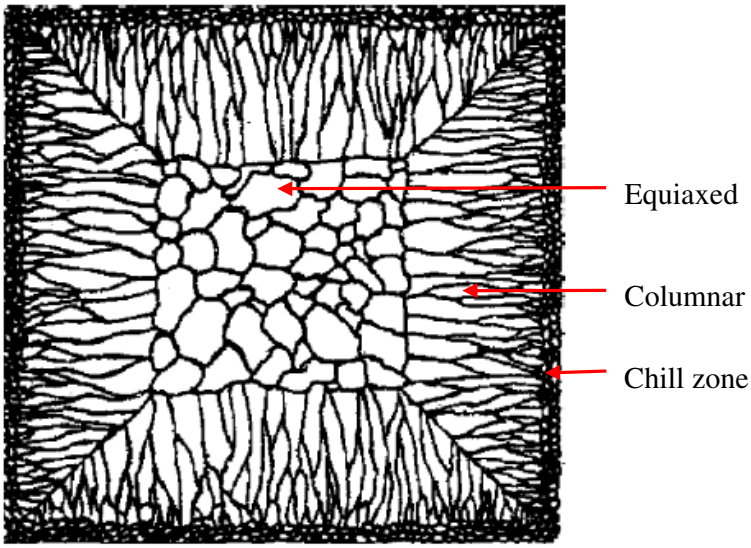

Figure 2.1. Sketch of a cast structure showing chill, columnar and equiaxed crystal zones [31].

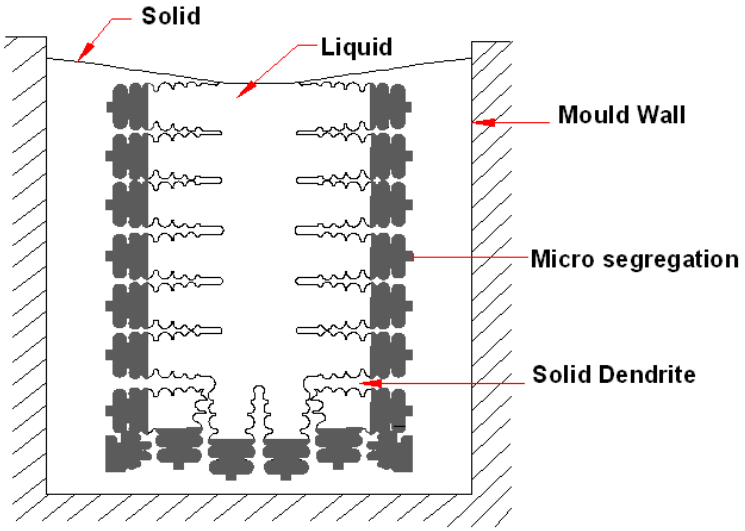

Figure 2.2. Schematic of dendritic solidification during casting [32]. The dark shading in the liquid adjacent to the dendrites represents microsegregation, i.e. higher concentration of solute atoms in the liquid at interdendritic regions due to the rejection of solute by the newly formed solid, which is lean in solute.

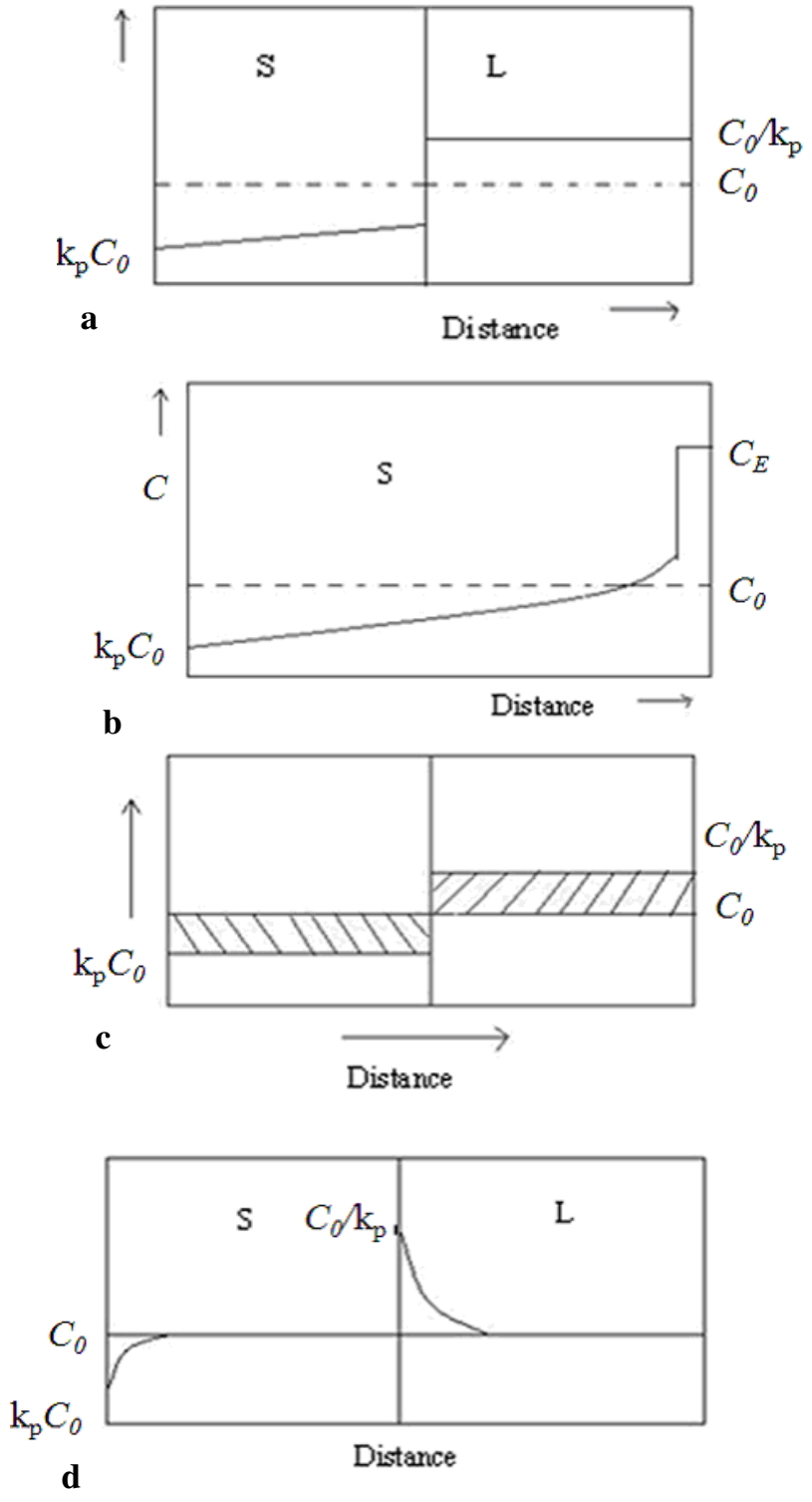

Figure 2.3. Planar front solidification of alloy C_0 (a) composition profile assuming complete equilibrium, (b) composition profile assuming no diffusion in solid but complete mixing in the liquid, (c) composition profile assuming when liquid has reached the eutectic composition i.e. C_E, (d) steady state solidification assuming no diffusion in the solid but diffusional mixing in the liquid.

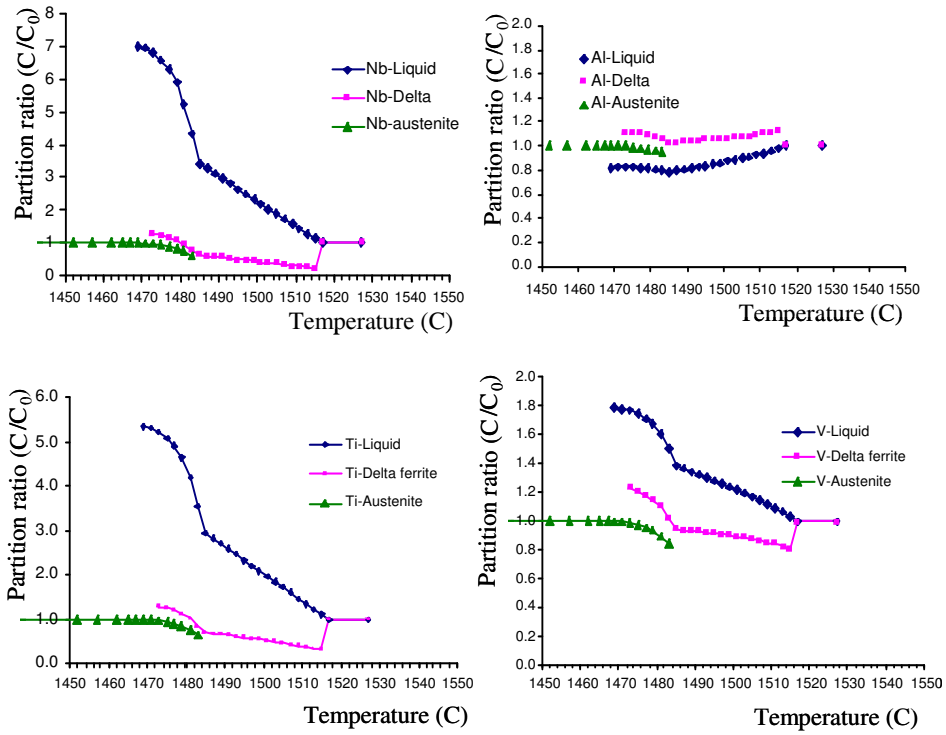

Figure 2.4. Microalloying element partitioning ratios predicted using Thermo-Calc [14].

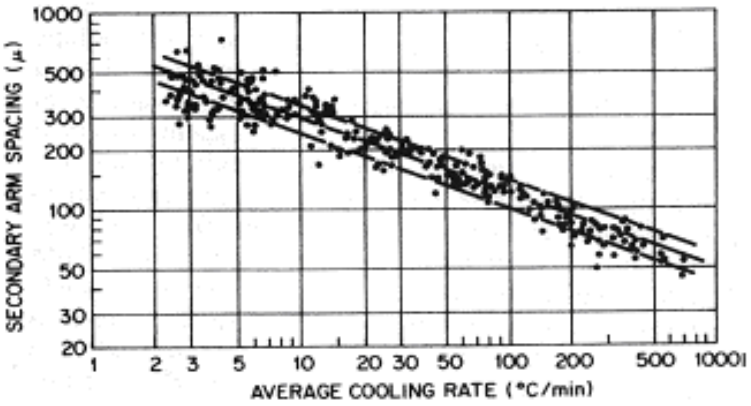

Figure 2.5. Secondary dendritic arm spacing as a function of cooling rate (for commercial steels containing 0.1-0.9 wt. percent carbon) [32].

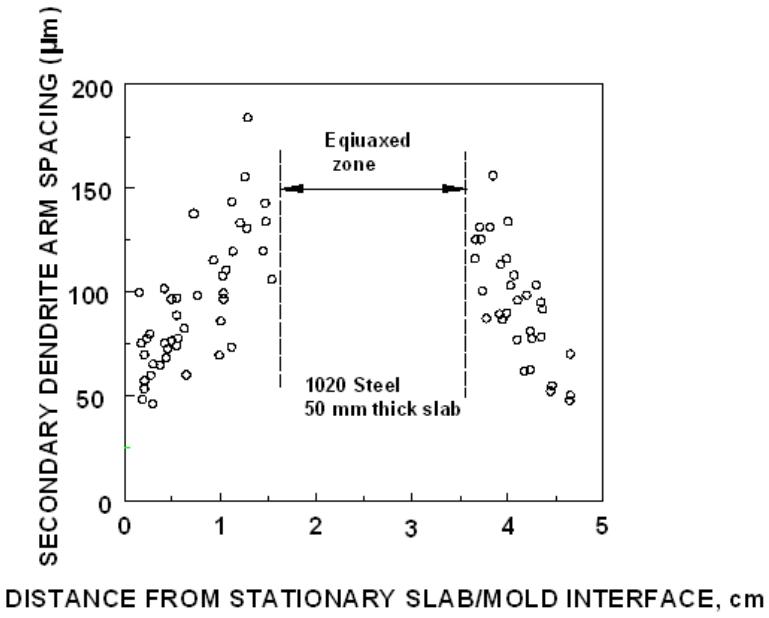

Figure 2.6. Secondary dendritic arm spacing as a function of distance across an as-cast 1020 steel slab [32, 33].

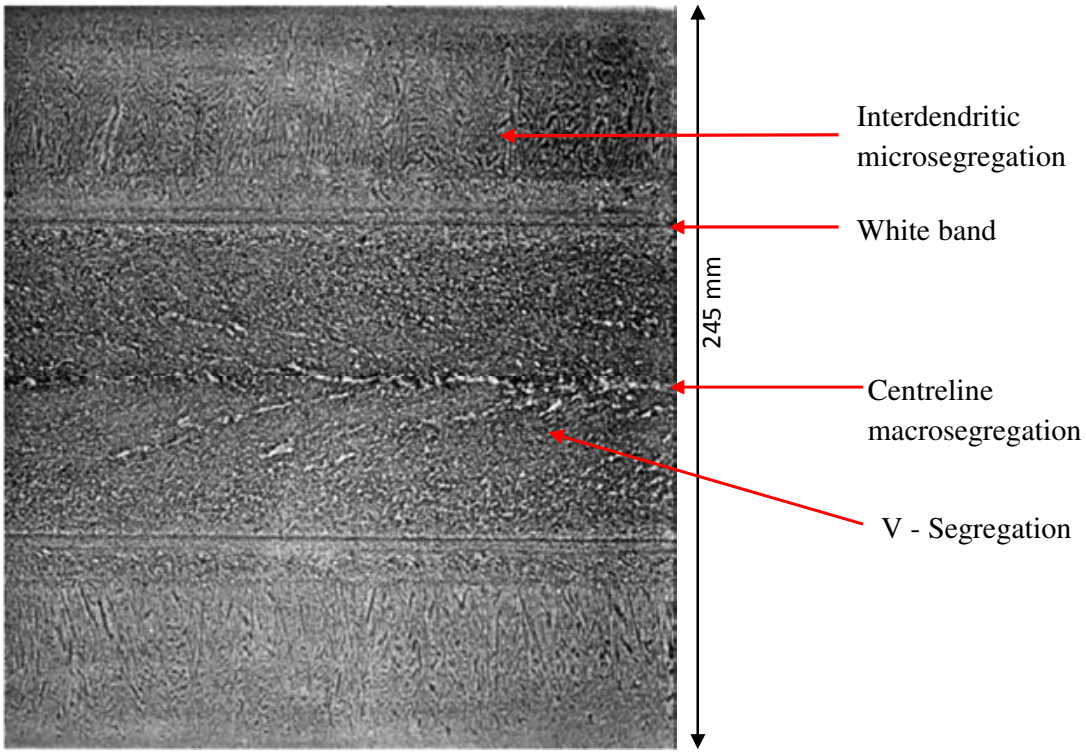

Figure 2.7. Longitudinal section of a carbon steel continuous cast slab (245 mm thick), showing interdendritic microsegregation in the columnar zone close to the upper and lower surfaces, centreline macrosegregation and V-segregation around the central region. Also shown are the white bands at quarter-thickness position from top [15, 40].

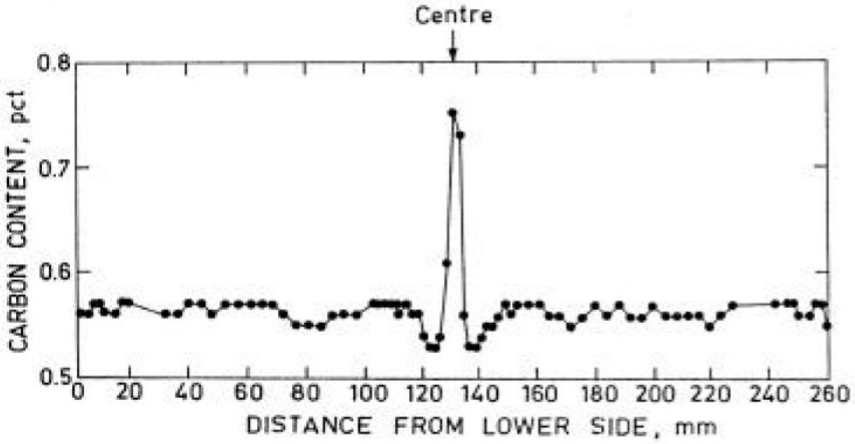

Figure 2.8. Typical concentration profile of carbon (wt %) along the thickness of continuously cast slab [41].

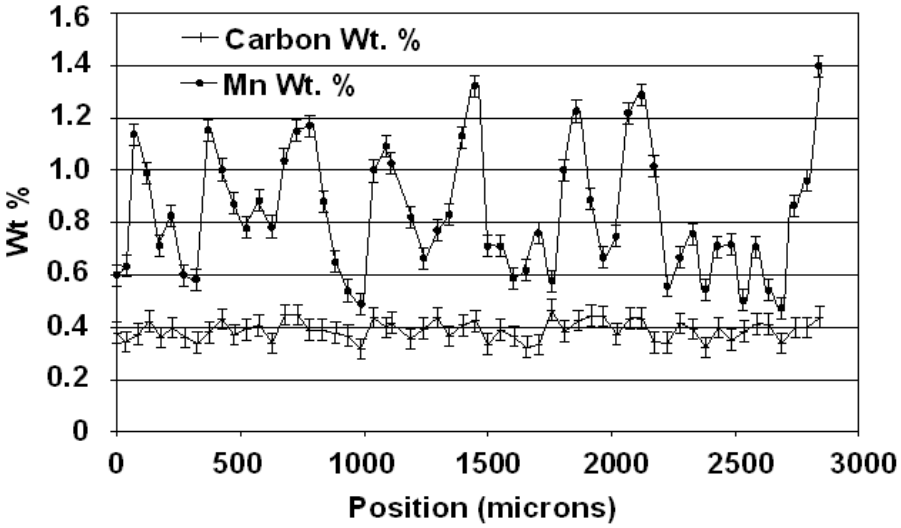

Figure 2.9. Variation of C and Mn content, electron microprobe analysis across 4140 steel slab [33].

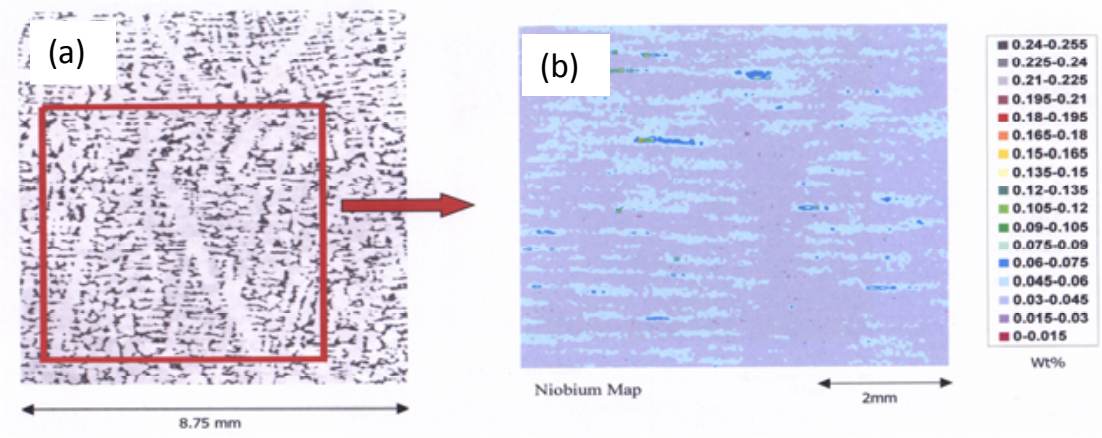

Figure 2.10. Laser ablation study on the quarter-thickness sample of cast stab (0.1 C, 0.04 Nb in wt % steel) (a) Macro etched area on which laser ablation study was carried out and (b) composition map showing weight-percent distribution of Nb in the same area [44].

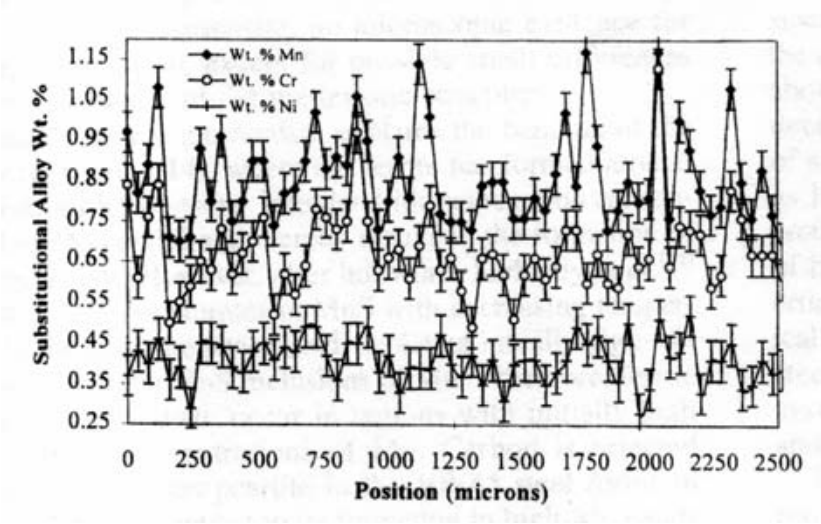

Figure 2.11. Variation of Mn, Cr and Ni across the as cast slab of 8617H steel [33].

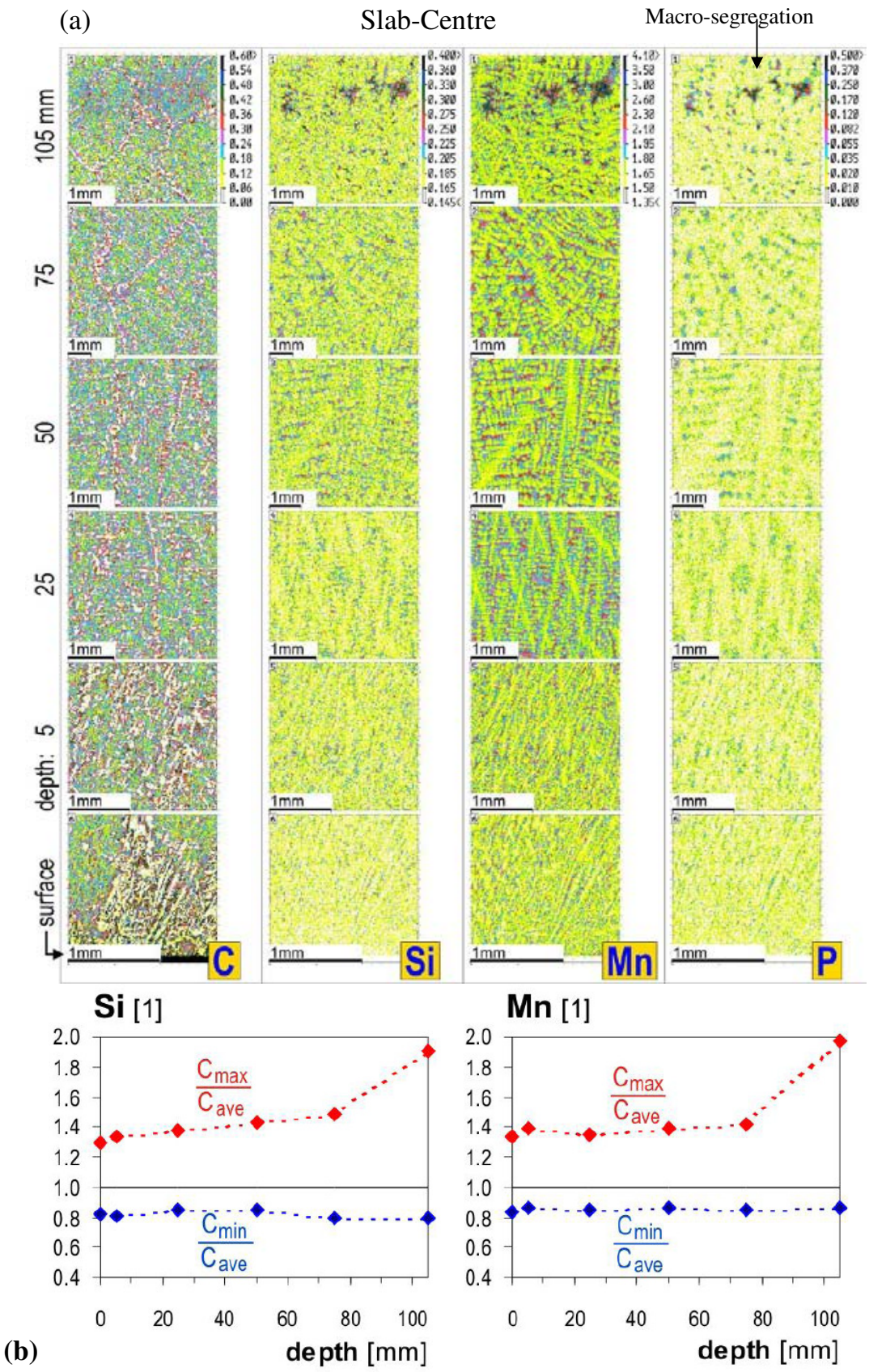
(a)
Slab-Centre
Macro-segregation
105 mm
75
50
25
depth: 5
surface
1mm
C
Si
Mn
P
(b)
Si [1]
Mn [1]
Cmax / Cave
Cmin / Cave
2.0
1.8
1.6
1.4
1.2
1.0
0.8
0.6
0.4
0
20
40
60
80
100
depth [mm]

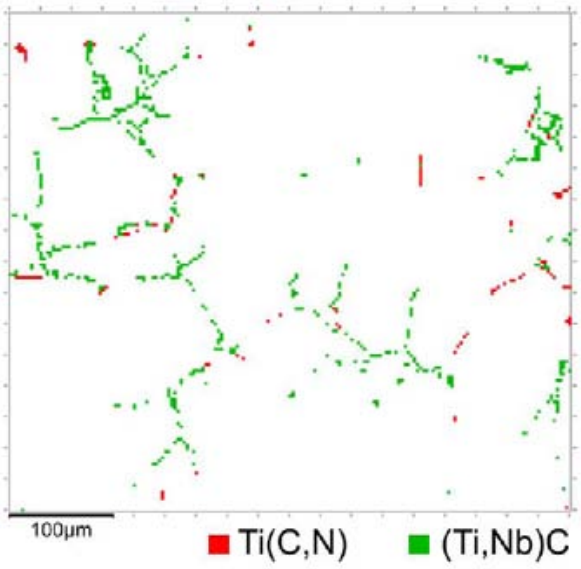

(c)

Figure 2.12. (a) Concentration mapping (CM) results for C, Si, Mn and P from continuously cast HSLA steel slab (210 mm thick) with a ferrite + pearlite structure. Colour level coding: wt % by mass (scale captions in each element column is given at the top right); the darker the colour of a region in Fig. 2.7 (a), the higher the concentration of an element in that region and the local concentration increases with the following sequence in colour coding: white < yellow < light green < light blue < red < dark green < dark blue < black. **(b)** Segregation intensities (represented by the ratios maximum / average concentration and minimum / average concentration) of Si and Mn with depth below slab surface (from surface to centre). **(c)** Phase map derived from concentration mapping (CM) results showing the network of microalloy carbonitrides at the slab centre [45].

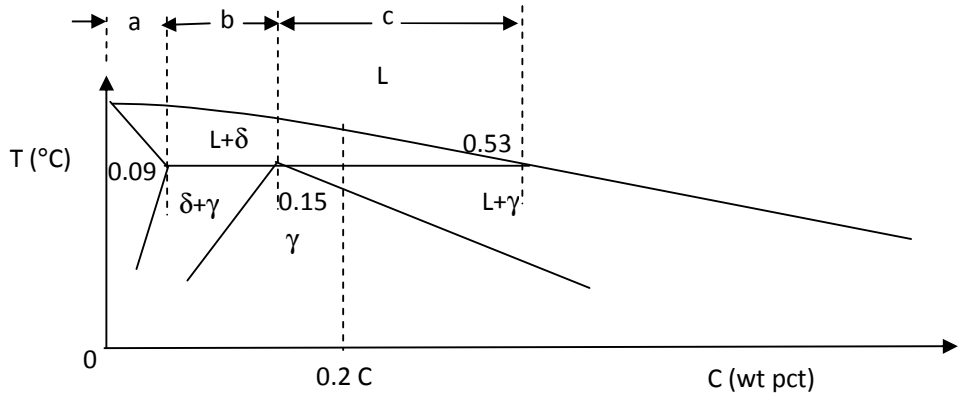

Figure 2.13. Schematic representation of Fe-C phase diagram and different solidification modes possible in HSLA steels: **(a)** first mode (0.0-approx 0.09 wt % C): the dendrites begin to nucleate and grow as delta ferrite phase (δ) until the end of solidification; **(b)** second mode (0.09-0.15 wt % C): dendrites nucleate and grow as primary δ-ferrite only until the peritectic temperature. At the peritectic temperature secondary austenite (γ) forms around the periphery of δ-phase following the (peritectic) reaction, L+δ → γ; **(c)** third mode 0.15-0.24 wt % C: the primary dendrites nucleate and grow as δ-phase, L → δ, until the peritectic temperature. Then the austenite layer solidifies around δ-ferrite and gradually the primary δ transforms to secondary γ. Finally the remaining liquid (L+γ) solidifies to γ.

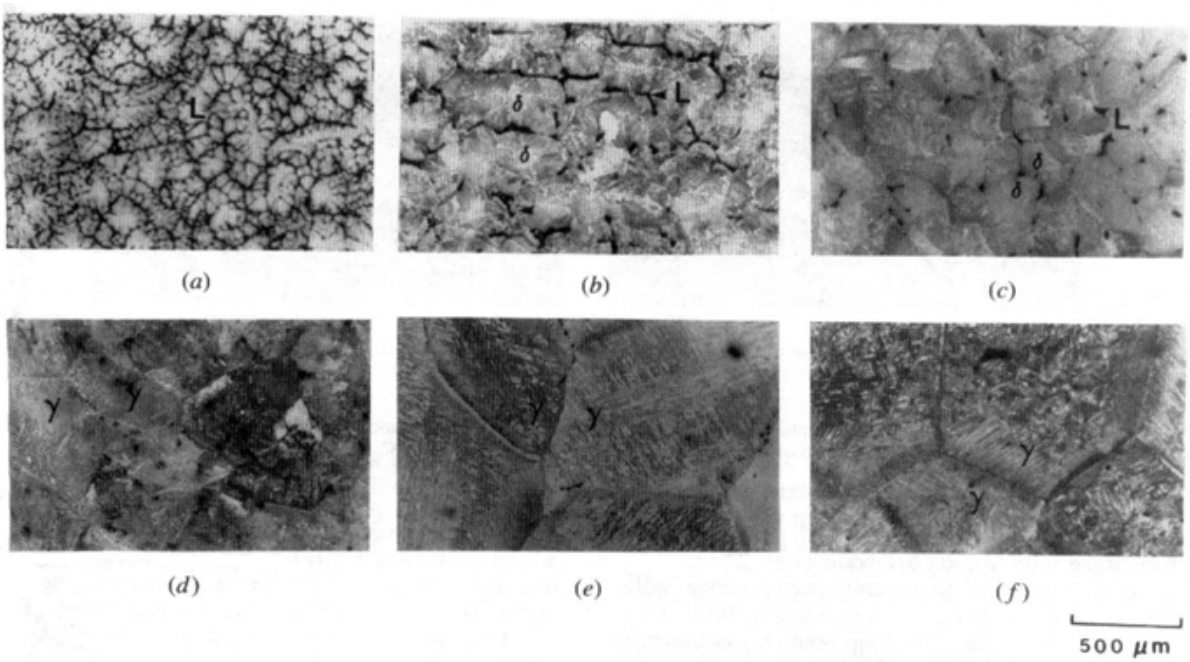

Figure 2.14. TEM micrographs illustrating the evaluation of the microstructure during the solidification and subsequent cooling of a steel containing 0.16 wt % C. The temperature at the time of quench were (a) 1520 °C (b) 1500 °C (c) 1480 °C (d) 1460 °C (e) 1430 °C and (f) 1380 °C [46].

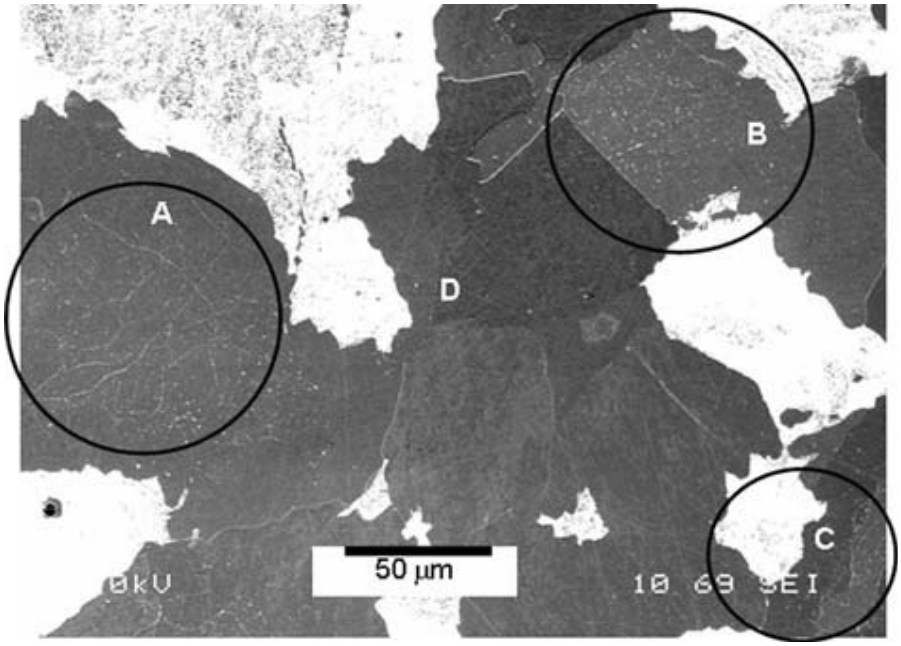

Figure 2.15. Inhomogeneous distribution of precipitates of Nb(C,N) on as cast 0.045 wt % Nb steel [14, 43].

Pipeline steel:	L	→	L + δ	→	δ	→	δ + γ	→	γ
Temperature, °C		1523.2		1492.8		1480		1425.4	
Structural steel:	L	→	L + δ	→	δ	→	δ + γ	→	γ
Temperature, °C		1520.7		1480.7		1477.9		1446.4	
Ship building steel:	L	→	L + δ	→	L + δ+ γ	→	L + γ	→	γ
Temperature, °C		1513.3		1482.8		1478.7		1463.5	
Slab 1 steel:	L	→	L + δ	→	L + δ+ γ	→	L + γ	→	γ
Temperature, °C		1516		1485		1472		1469	

Figure 2.16. Solidification sequence for four steels, with critical temperatures: liquid (L), delta ferrite (δ) and austenite (γ) [34].

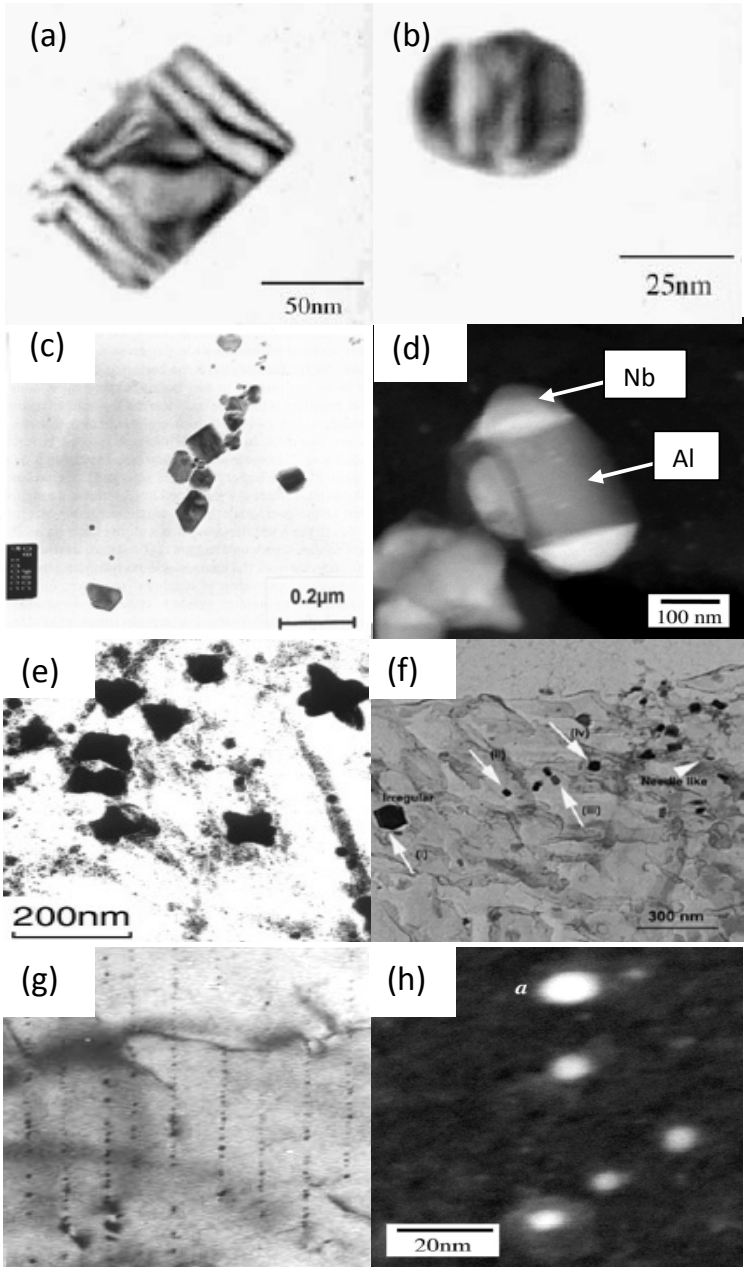

Figure 2.17. Precipitates commonly observed in microalloyed steels: (a) Cuboidal shaped TiN (b) round shaped mixed (Ti,Nb)(C,N) (both from [22]), (c) faceted AlN particles [48], (d) formation of NbC caps on AlN particles [49], (e) cruciform precipitates of complex (Ti,Nb)(C,N) [50], (f) V-rich complex (Ti,Nb,V)(C,N) precipitates of different shapes such as (i) irregular, (ii) and (iii) cuboidal and (iv) spherical [51], (g) interphase precipitates of Nb(C,N) and V(C,N) arranged in parallel arrays formed during austenite to ferrite transformation [52] and (h) near-spherical NbC particles [49].

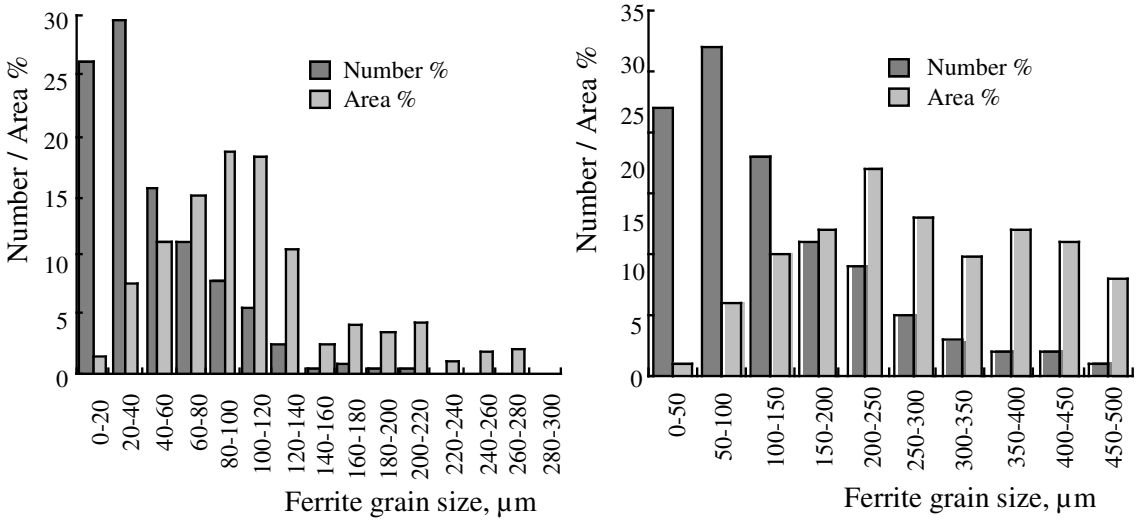

(a) (b)

Figure 2.18. Grain size distribution histograms for a HSLA continuously cast slab with 0.045 wt% Nb at a) 10 mm from the slab surface and b) slab centre [22].

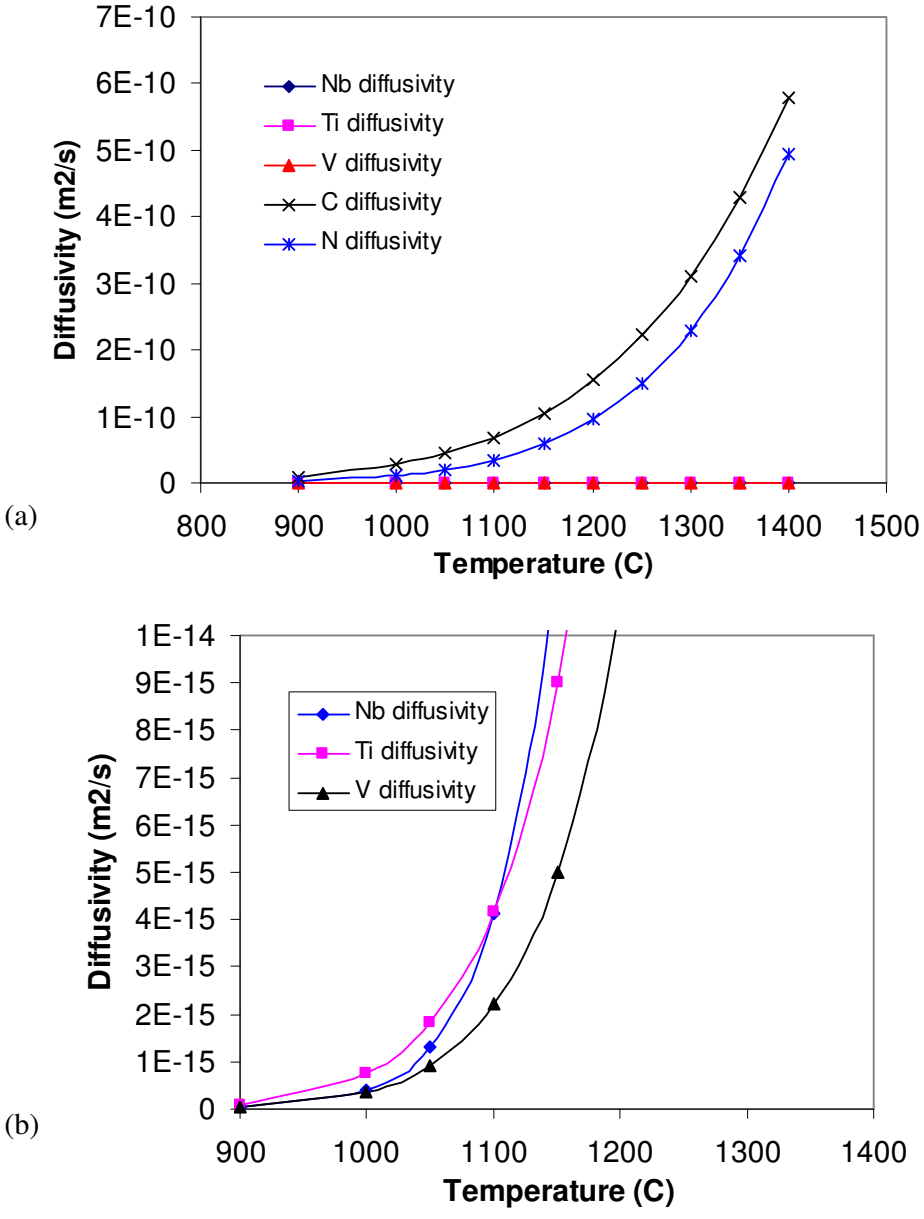

Figure 2.19. Variation in diffusivity of microalloy and interstitial elements in microalloyed steel, (a) showing C and N diffuse much faster than Nb, Ti, or V, (b) showing the variation of diffusivity of Nb, Ti and V with temperature.

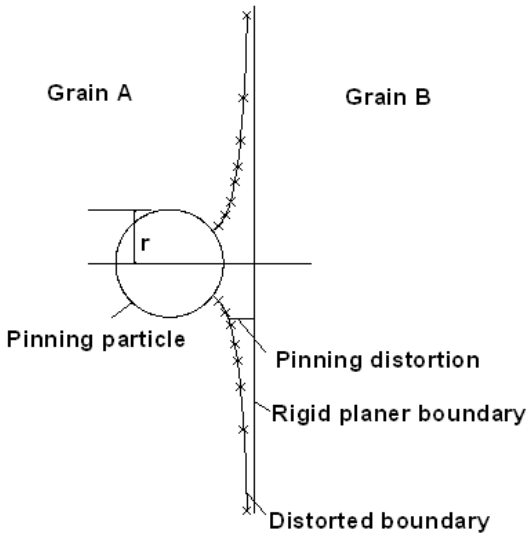

Figure 2.20. Pinning of grain boundaries (between two grains, A and B) by a spherical second phase particle (particle radius, r) [1].

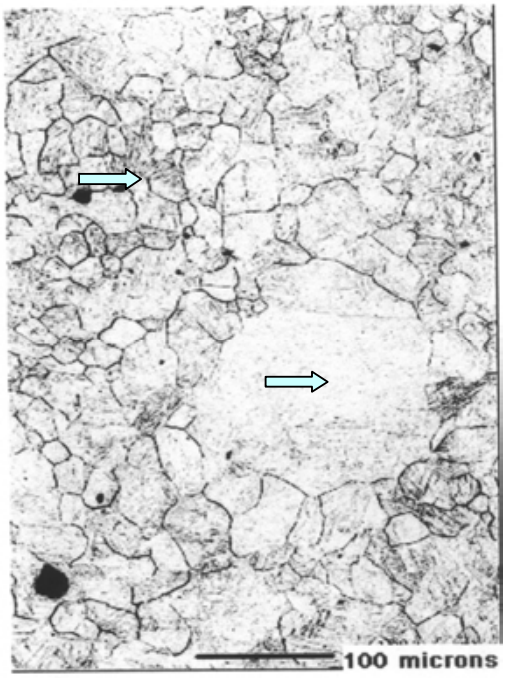

Figure 2.21. Duplex or bimodal austenite grain structure with abnormally large grains present along with fine austenite grains after 1100 °C reheating (for 1 hr.) of 0.1 C - 0.04 w % Nb microalloyed steel [44]. Arrows indicate both large and small grains.

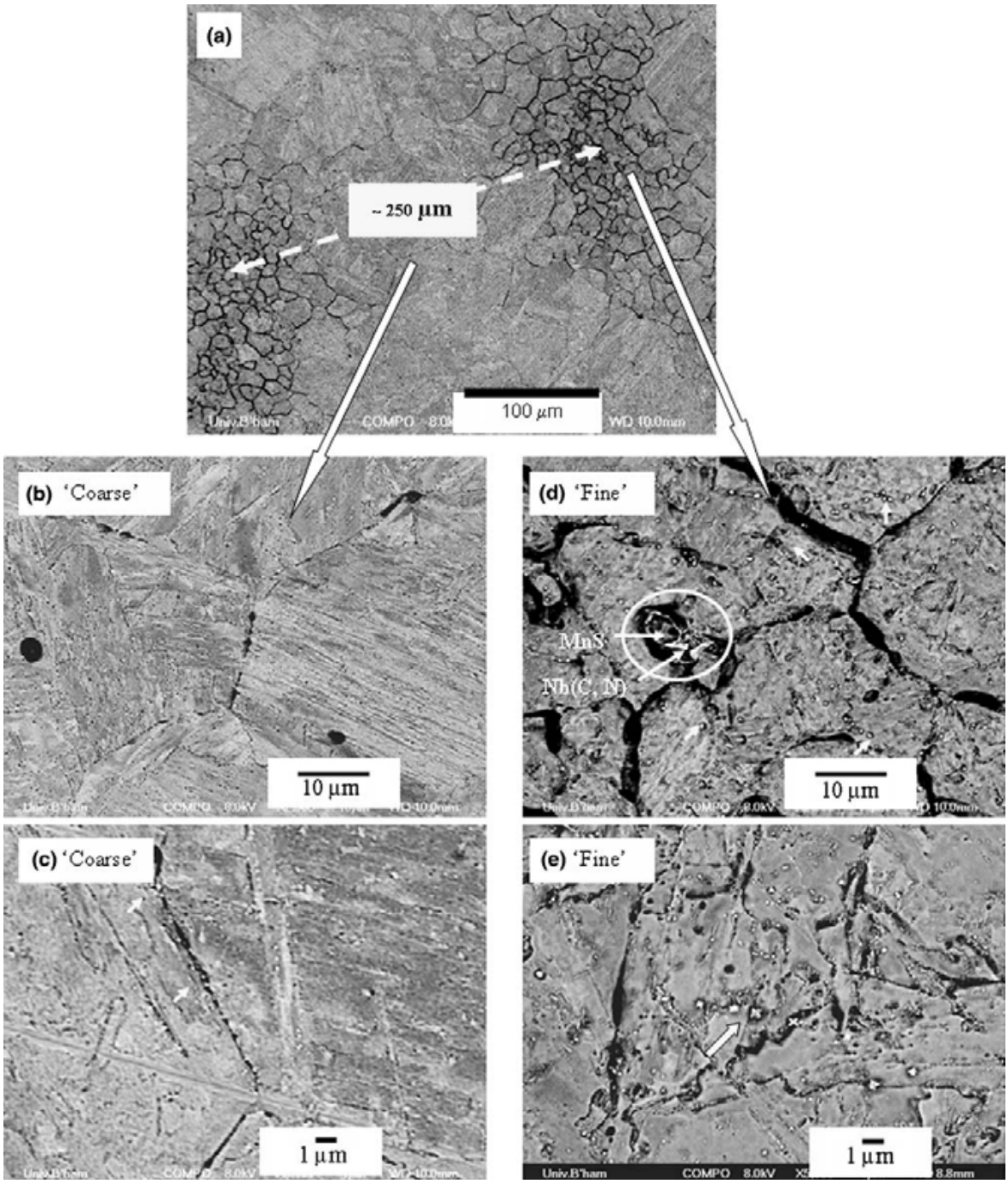

Figure 2.22. (a) BSE images of the bimodal austenite grain structure in slab 1–1150 sample, showing the bimodal grain structure, where the fine grain regions are separated by a distance ~250 µm, same as secondary dendrite arm spacings. Closer view on (b) and (c) coarse grain region and (d) and (e) fine grain region showing the higher density of precipitates (some precipitates from both regions are arrowed) [43].

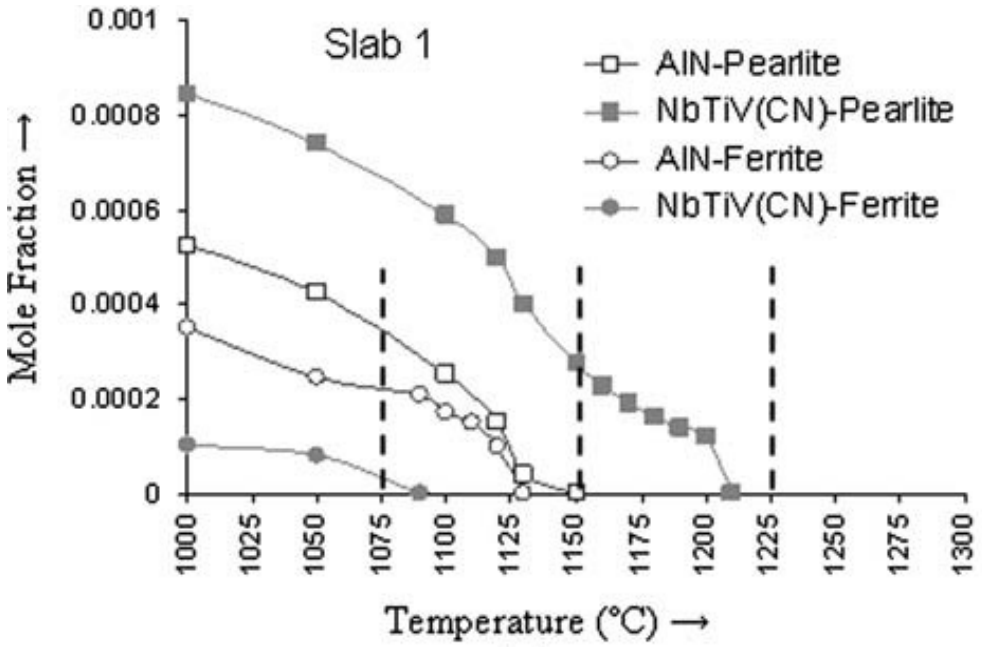

Figure 2.23. Thermo-Calc software prediction of precipitate stability at interdendritic (pearlite) and dendrite-center (ferrite) regions of as-cast slab containing 0.045 wt % Nb [14, 43]. (Nb,Ti,V)(C,N) would undergo dissolution in the dendritic regions at 1150 °C but in the interdendritic regions the particles will be stable above 1200 °C. The stability of AlN is almost the same in the dendritic and the interdendritic regions. That leads to the formation of bimodal grain size distribution upon reheating to 1150 °C due to differential precipitate pinning in the dendritic and in the interdendritic regions [43].

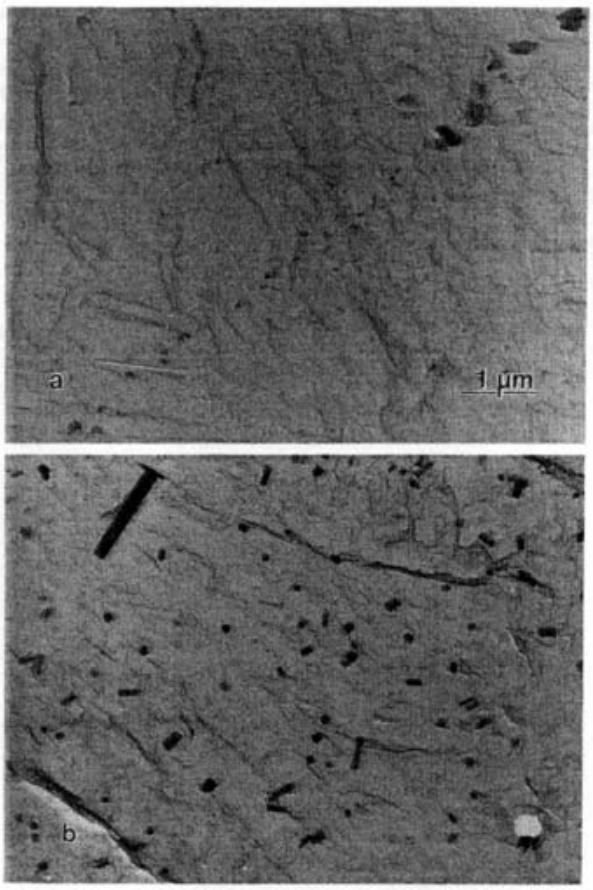

Figure 2.24. TEM images of carbon extraction replicas showing the AlN precipitate distribution in (a) 0.027 wt % Al (L-AlN) (b) 0.086 (H-AlN) wt % Al steels, both the microstructures are at the same magnification [80].

CHAPTER - 3

Review of grain structure formation during hot deformation of microalloyed steel

3.1. Introduction

The evolution of the final ferrite grain structure and any precipitate population are influenced by the rolling schedule. Typically this could be hot rolling (HR) or thermomechanical controlled rolling (TMCR), through the interaction between recrystallisation and precipitation effects [1, 10, 12, 13, 17, 18, 20, 21, 83-86]. It has been shown that the final grain size in the steel is controlled by the metallurgical condition and transformation temperature of the parent austenite [5, 6, 12, 57, 87, 88]. The metallurgical condition of austenite refers to its grain size, composition and crystalline defects while the transformation temperature is controlled by the metallurgical condition as well as the cooling rate [1, 5, 6, 12, 57, 88].

A typical TMCR schedule is characterised by reheating (or soaking) the steel at ~ 1150-1250 ℃ to ensure complete or near complete dissolution of microalloying elements in austenite, followed by rolling deformations through multiple stages with different hold periods in between the deformation stages [1, 12]. Theoretically, the recrystallisation temperature range is defined by the upper temperature limit (the recrystallisation limit temperature, RLT) and the lower temperature limit (the recrystallisation stop temperature, RST or no recrystallisation temperature, T_{NR}). The RLT and RST have been defined as $T_{95\%R}$ and $T_{5\%R}$ [88] respectively (Figure 3.1.a). Here, $T_{95\%R}$ and $T_{5\%R}$ represent the temperatures where 95% and 5% of the deformed structure recrystallise within the interpass delay time (~10-20 s for commercial rolling).

The deformation stages for TMCR are as follows (Figure 3.1.b) [17]:

Stage - I: Deformation in recrystallisation region above RLT (or $T_{95\%R}$)

The coarse austenite grains after reheating are refined in size by repeated deformation (several roughing passes) and complete recrystallisation. The presence of fine TiN particles inhibits grain growth during interpass delay times and maintains a fine recrystallised grain structure [17]. The microstructure after deformation in the complete recrystallisation region is shown in Figure 3.1.c [21]. After stage-I rolling a delay time is given during which the temperature drops below the RST.

Stage - II: Deformation in non-recrystallisation region below RST (or T_{NR} or $T_{5\%R}$)

Successive deformation passes below the RST (~950-1050 °C in Nb steels [1, 17]) generates a heavily deformed austenite grain structure, with elongated and pancake-shaped austenite grains containing a high density of near-planar crystalline defects (such as, grain / sub-grain boundaries, deformation bands, and incoherent twin boundaries), which act as nucleation sites for ferrite grains producing a fine ferrite structure (high rate of ferrite nucleation) after suitable cooling below A_3 (austenite to ferrite transformation temperature). The prior austenite grain structure after deformation in the non recrystallisation region is shown in Figure 3.1.d [89].

Stage - III: Deformation within the intercritical (austenite + ferrite) region

Intercritical rolling is applied only in cases where high strength is required. After stage-II rolling a delay time is given so that the temperature of the steel drops below A_3. In stage-III, deformation bands or twins continue to form within untransformed austenite grains, which enhance ferrite nucleation resulting in a finer ferrite grain size. Also the recovery of deformed ferrite grains produces fine sub-grains within deformed ferrite grains. Smaller sub-grain sizes result in higher strength steels [1]. Lowering the finish rolling temperature within the intercritical region increases the strength of the steel but decreases the ductility and impact toughness due to a higher retained strain within the

microstructure [1, 90]. During intercritical rolling V(C,N) (or even Nb(C,N)) can precipitate with a fine scale either as random precipitates at the ferrite-austenite boundary as inter-phase precipitates or row precipitates on dislocation. Such precipitates are fine in size (usually < 10 nm) and offer precipitation strengthening [1, 12, 52, 91-96].

Hence, with an increase in the RST, a large amount of deformation can be imposed in the non-recrystallisation region resulting in increased defect density e.g. grain boundaries, deformation bands and twin boundaries in the material, [5, 6, 97]. This in turn increases the nucleation site density for pro-eutectoid ferrite and decreases the final ferrite grain size. The addition of microalloying elements, such as niobium, titanium and vanadium, is known to increase the RST with Nb having the strongest effect per atomic percent addition [5, 6, 12]. Therefore, to design an appropriate rolling schedule, it is necessary to understand recrystallisation and the influence of variables such as strain, temperature, strain rate and initial grain size, along with the role of microalloying elements, on recrystallisation kinetics.

Research on hot working of C-Mn, low alloy and high strength low alloy (HSLA) steels has resulted in quantitative relationships being developed to describe the microstructural changes [98]. The equations, empirically developed for a range of strains and compositions, describe the hot working process through relationships for recrystallisation and precipitation with time, temperature, strain and strain rate [98].

In the following section special emphasis has been given to the fundamental mechanisms involved in the recrystallisation and precipitation phenomena, which control the formation of the final grain structure under TMCR conditions. These include the nucleation and growth of recrystallised grains; the driving force for recrystallisation; and the drag forces, e.g. solute drag and precipitate pinning effects, which retard recrystallisation. The influences of variables such as initial grain size, strain, solute

content and precipitation on the kinetics of recrystallisation and hence the prediction of final grain size are discussed.

3.2. Recrystallisation

The development of microstructure during hot working depends on recrystallisation. During deformation, energy is stored in the material in the form of various crystalline defects, e.g. dislocations and boundaries. This stored energy is released via recovery, recrystallisation and grain growth. The usual definition of recrystallisation is the formation and the migration of high angle boundaries driven by the stored energy of deformation [99, 100].

Recrystallisation can be of two types; static and dynamic. Static recrystallisation takes place on holding a deformed structure at temperature for a period of time. The critical strain that is required to initiate static recrystallisation in C-Mn steel is 7 % over the temperature range 900-1000 ºC [1, 98]. A subgrain structure tends to develop with an increase of dislocation density from larger amounts of deformation. Since recovery during deformation is relatively slow, the subgrain boundaries are ill formed, and sufficient stored energy remains to nucleate recrystallisation during deformation. This is dynamic recrystallisation. The critical strain that is required to initiate dynamic recrystallisation is of the order of 50-60 % over the temperature range 900-1000 ºC [101, 102]. Hot rolling and TMCR of steel involves strains only up to 40 % [1, 98] so that it is unlikely that dynamic recrystallisation occurs [98]. Therefore it is only static recrystallisation through which softening can take place.

3.2.1 Nucleation of recrystallisation

Three models are generally used to describe the nucleation of recrystallised grains. These are classical nucleation, subgrain growth and strain-induced boundary migration

(SIBM). The classical nucleation model proposed by Burke and Turnbull [103] states that a critical nucleus will be stable if the necessary interfacial energy is balanced by the difference in strain energy per unit volume between the cold worked state and the fully recrystallised condition. The nuclei that form are expected to be close in orientation to that of the matrix as this involves creation of low angle boundaries of low interfacial energy reducing critical nucleus size.

In the subgrain model developed by Cahn [104] a small region of high dislocation density (high strain gradients and high local misorientation) evolves into a small strain-free cell by a process of dislocation climb and rearrangement. Once formed the sub-grain grows by sweeping up further dislocations. The growing sub-grain thus becomes more misoriented with respect to its neighbours and gradually loses its sub-grain character becoming a conventional grain.

SIBM was first reported in aluminium by Beck and Sperry [105]. In this model a sub-grain of low dislocation density will bulge into a sub-grain of high dislocation density. This model relies on the presence of a non-uniform dislocation distribution on a sufficiently large scale. This effectively means that the presence of a particularly large sub-grain adjacent to the grain boundary will cause that boundary to bulge across the entire width of the sub-grain. It is generally observed that the nuclei for recrystallisation form in regions of large strain gradient; favourable sites for recrystallisation nuclei are grain boundaries, phase interfaces, twin boundaries, deformation bands and the surface of the material [107]. Local lattice misorientations are thus a necessary and sufficient condition for nucleation of recrystallisation; the larger the magnitude of the strain gradient, the greater the number of nuclei capable of being formed.

Of the three models above, the most widely used one for rolling deformation is SIBM [99, 100, 107]. SIBM was originally developed for low amounts of strain, but has been

extended through the work of Bailey and Hirsch [108], with the driving force for recrystallisation taken as the difference in volume strain energy (i.e. dislocation density) between adjacent austenite sub-grains [107]. The model proposes that austenite grains of low dislocation density will bulge into grains of high dislocation density [104].

3.2.2 Driving force for recrystallisation

The driving force for static recrystallisation can be taken to be the difference in dislocation density between the deformed or recovered matrix and the recrystallised matrix. This can be estimated using the approach of Keh and Weissman [109] who related the increase in flow stress caused by work hardening to the increase in dislocation density as:

$$\Delta\sigma = \sigma_o + \alpha\mu b(\Delta\rho)^{1/2} \quad (3.1)$$

where, $\Delta\sigma$ is the increase in flow stress caused by work hardening, σ_o is the initial yield strength, α is a constant, μ is the shear modulus, b is the Burgers vector, and $\Delta\rho$ is the difference in dislocation density. The driving force (per unit area) for recrystallisation, F_{RXN}, is given by

$$F_{RXN} = \mu b^2 \Delta\rho/2 \quad (3.2)$$

Using Equations 3.1 and 3.2 the driving force for recrystallisation was estimated, after deformation to 0.3 strain, to range from 22 MPa (at 1100 ºC) to 30 MPa (at 900 ºC) for Nb-bearing microalloyed steels [12, 88].

With increasing deformation temperature the difference in dislocation density decreases due to a number of factors, including increasing number of operating slip systems and more extensive dynamic softening [110, 111], resulting in a decreased driving force for recrystallisation. This decrease in driving force is offset by the enhanced recrystallisation kinetics resulting in an increased recrystallisation rate at higher temperature.

3.2.3 Growth of new grains following recrystallisation

The nucleation process during recrystallisation requires that the potential nucleus is capable of growing into the deformed matrix. For the sub-grain to become a successful new grain there should be an energy advantage in order for it to grow rather than shrink and vanish. The boundary mobility, the driving force and therefore the speed of migration in a whole range of materials depends upon deformation and annealing parameters, and the crystallographic orientations of the deformed matrix [112]. Grain boundary migration is favoured for grains with greater boundary misorientations [99]. During multipass hot deformation sequences, which end in the full recrystallisation regime, a fine grain size is favoured by a pre-existing pinning force that is small enough to allow for static recrystallisation to occur but large enough to suppress grain growth.

The growth of a recrystallised grain as a function of temperature (T) can be written [98, 113-116] as follows:

$$D^n = D_{rex}{}^n + A't \exp(-Q_{gg}/RT) \qquad (3.3)$$

where, A' and Q_{gg} are constants, t is time, D_{rex} is the recrystallised grain size, D is the final grain size and n=10.

Figure 3.2.a was plotted using the experimental results of Foster and Korchynsky and Stuart [116, 117] for a C-Mn steel after deformation with 30 % strain and at three different temperatures (1050, 950 and 871 °C) and three different starting grain sizes of 280, 200 μm (Table 3.1) [98, 116] and 110 μm [98, 117]. In equation 3.3 the value of the exponent, n, is chosen as 10 since it gives a better fit as shown in Figure 3.2.a. From Figure 3.2.b it can be seen that there is some scatter in the result of C-Mn steels which is

not related to differences in C and Mn contents. It can also be seen that Nb causes a marked retardation to grain growth at temperatures below 1200 °C.

The above analysis indicates that when recrystallisation occurs between two rolling passes the grain size on entering the second pass depends almost entirely on the deformation temperature if

$$D_{rex}^{10} << A' \exp(-Q_{gg}/RT) \qquad (3.4)$$

But equation 3.3 predicts very high D_{rex} values compared to those observed experimentally in Nb bearing steel containing 0.03 to 0.045 wt % Nb [98]. To overcome this difficulty a grain growth equation with a much lower exponent time dependence of A' would be required: no such equation is however reported.

3.2.4. Equations to determine the size of the recrystallised grain

Since recrystallisation is a nucleation-dominated phenomenon the recrystallised grain sizes depend on the strain and prior grain size [98]. The recrystallised grain size (D_{rex}) in C-Mn and Nb-treated steels has been found to be related to the initial grain size (D_o) and the applied strain (ε) by the following equations [2, 98]:

$$D_{rex} = D' D_o^{0.67} \varepsilon^{-1} \qquad \text{(C-Mn steel)} \qquad (3.5)$$

$$D_{rex} = D' D_o^{0.67} \varepsilon^{-0.67} \qquad \text{(Nb-bearing steel)} \qquad (3.6)$$

The majority of the results in the literature are consistent with the form of the equations shown above, but the value of D' varies. Different values of D' have been reported in the literature both for C-Mn steels and Nb-bearing steels (Table 3.2).

In these equations there is a larger effect of initial grain size than of strain. A lower value of D' and higher value of strain exponent would lead to a smaller predicted recrystallised grain size than measured.

Toughness depends on the grain size distribution, rather than the average grain size. In the literature there is no mention of any equations that predict the grain size distribution. Uranga et al. [118] successfully modelled the grain size distribution after deformation using thin slab direct rolled (TSDR) steels containing 0.035 wt % Nb (~ 4 % discrepancy between predicted and measured recrystallisation fractions). In their study they have used the 3:1 ratio of coarsest to mode grain size. The processing of TSDR steels involves fewer rolling stages with larger strains, whilst greater supersaturation of [Nb] would be expected than in the thicker continuously cast and reheated steel considered in the present study.

3.2.5 Effect of solute atoms on grain boundary mobility

Solute drag is explained as a dynamic segregation effect. Solutes segregate to (or in a few cases are rejected from) the grain boundaries and due to the migration of the grain boundary an asymmetric segregation profile develops. This profile leads to a net force on the grain boundary, opposing the migration, and slowing it down. Experimental results suggest that the main effect of solute atoms is on the growth process rather than recrystallisation nucleation [1, 5, 6, 12, 86, 98-100]. When solute atoms are located on and attached to a grain boundary, the migration rate of the boundary resulting from a given driving force is influenced by the solute atoms. Most of the work related to solute drag was conducted for recrystallisation experiments where the driving force is quite high. The theory for solute drag was developed in two classic papers by Cahn [119] and Hillert and Sundman [120]. Cahn assumes an ideal very diluted binary mixture in his model, whereas Hillert and Sundman consider the more general case of non-diluted non-ideal binary mixtures. The solute drag force in the theory of Cahn is linearly proportional to the solute concentration, while Hillert and Sundman find a more complex concentration dependence, using a regular solution model. The theory of Cahn is applied

in most of the present models. According to Cahn's theory [119], the rate of grain coarsening G can be given as

$$G^2 = (2 \gamma V_M . n / t) / (\lambda + \alpha C^{/}) \quad (3.7)$$

where, γ is the specific grain boundary energy per unit volume, V_M is the molar volume of austenite, n is the isothermal grain coarsening law exponent (n=10 in equation 3.3), t is the coarsening time, λ is the reciprocal of boundary mobility of pure austenite, α is the reciprocal of boundary mobility at unit solute concentration, and $C^{/}$ is the bulk solute concentration. G continues to increase with $C^{/}$ but with a decreasing rate.

Microalloying elements, such as Ti, V and especially Nb, increase the RST by solute drag. Nb can also pin the moving boundaries through the formation of fine Nb(C,N) precipitates during deformation [1, 5, 6, 12, 17, 23, 86, 88, 91-96]. The experiments of Luton et al. [121, 122] on a decarburised and denitrided steel containing 0.09 wt % Nb have shown that Nb in solution retards both static recovery and recrystallisation by about one order of magnitude in time compared to equivalent C-Mn steel after deformation with 0.15 strain at temperatures above 1050 °C. In a similar way, the work of White and Owen [122] on 0.09 wt % V-doped steel conducted above the solubility temperatures of VN and VC has demonstrated that V in solution retards the recrystallisation of austenite by 10 % with respect to a reference C steel. This can be related to the atomic size and electronic structure differences between Nb and V as solutes and Fe as solvent [123]. The marked effectiveness of Nb compared to V in terms of solute drag is attributed primarily the appreciably greater atomic size difference between solute and solvent. At an equal atom fraction in solution, Nb at a size difference of 15 % has a stronger effect than V with a size difference of 6 % [124].

Medina and Quispe [125] and Somani et al. [126-128] studied the influence of individual alloying elements as solute on recrystallisation kinetics. Quispe [125] measured recrystallisation kinetics for 26 different steels with a large and systematic variation in the composition and they tabulated the recrystallisation parameters (the time at which the volume fraction recrystallised is 0.5 and the Avrami exponent) for all compositions and sets of process parameters. These data were used to derive (empirical) equations for the recrystallisation parameters. The second study is from Somani et al., who measured the recrystallisation kinetics of more than forty steel grades [126-128], to develop an empirical model for characteristic recrystallisation times. Details of experimental results and the chemical compositions were, however, not published. The dependence of the recrystallisation kinetics on the chemical composition is usually modelled with an effective activation energy in an Arrhenius function. The effective activation energies, proposed by both research groups differ quantitatively both in the estimated effective activation energy for pure iron and in the coefficients of the alloying elements. For pure iron Medina and Quispe found an effective activation energy of 149 kJ/mol, while Somani et al. found 109 kJ/mol. The contributions of the alloying elements differ even qualitatively in both models. In the sequence of increasing contribution (per weight percent) Somani et al. proposed the sequence Cu<Mn<Mo<Si<V<Ti<Nb, i.e. niobium has the largest influence per weight percentage on the effective activation energy. Medina and Quispe found a sequence of C<Mn<Si<V<Nb<Mo. The largest difference exists for molybdenum, which is probably a consequence of the low number of molybdenum containing steels in the data set of Somani.

Another empirical approach to model the effect of solutes on the kinetics of recrystallisation was proposed by Andrade, Akben and Jonas with the solute retardation parameter (SRP) [129, 130]. The SRP_a of a specific element y is defined in equation (3.8), where t_{REF} and t_y are the recrystallisation starting times (chosen as the time of 10 or

15 percent volume fraction recrystallised) of a reference steel (a C Mn steel) and of a second steel, with the same composition as the reference steel, but with an extra addition of the element y (measured in atomic fraction):

$$SRP_a = \log\left(\frac{t_y}{t_{REF}}\right) * \frac{0.1}{at\%\ y}. \qquad (3.8)$$

The SRP_a is a practical parameter in comparing the influence of different alloying elements on the recrystallisation rate. Figure 3.3 shows the estimated SRP_a of a number of alloying elements, plotted versus the estimated size misfit parameter (a measure of the relative change of the lattice parameter with an increase of the concentration of the alloying element). For modelling the applicability of SRP_a is limited: the SRP_a is only applicable to compositions that do not differ too much from the reference steel. Moreover, the SRP_a depends on the strain rate and recalculation of SRP_a to other strain rates leads to inconsistencies between different data sets.

A comparison of the solute retarding effects of the three-microalloying elements Nb, Ti, and V is shown in Figure 3.4 [12, 131]. The steel used in that work contained 0.002 wt % C and the deformation experiments were carried out at 1050 °C, above the solubility temperatures of Nb and V precipitates, and the deformation strain was 15 %. Formation of TiN can be ignored as there was no nitrogen present in the steel. Therefore the retarding effects are solely due to solute drag. It is obvious that V has the weakest retarding effect, with Ti intermediate and Nb the strongest. Abad et al. [132] has shown that recrystallisation kinetics is controlled by Nb at low pass strain (i.e. strain < 20 %) and at temperatures higher than 1050 ^{o}C i.e. above the solubility temperatures of Nb on a steel containing 0.045 wt % Nb.

Therefore from the above discussion it can be seen that solute drag is more effective in Nb, V microalloyed steels at temperature above 1050 °C (i.e. above the solubility temperatures of Nb and V precipitates) and at low deformation strain (i.e. strain <20 %).

3.2.6 Interaction between recrystallisation and precipitation

Zener [75] was the first to point out that a dispersed second phase will retard grain boundary migration under a fixed driving force. The retarding force per unit area of the boundary (p_r) is given by:

$$p_r = -3f.\sigma_B / 2r \qquad (3.9)$$

where, f is the volume fraction of particles, σ_B is the specific boundary surface energy and r is the radius of the particles.

The equation is based upon the assumptions that the boundary is inflexible; that the interaction between the grain boundary and particles is independent on the nature of the particle; and that the particles are distributed uniformly throughout the matrix. It follows from equation 3.9 that, for a given volume fraction, smaller stable particles hinder grain boundary migration more than larger ones.

Recrystallisation of supersaturated solid solutions has been reviewed by Hornbogen and Koster [133]. Except when recrystallisation is complete before precipitation is initiated, precipitation and recrystallisation exert a mutual influence upon each other. Thus while the lattice defects themselves promote the nucleation of precipitates, the precipitated particles hinder the formation and migration of recrystallisation fronts. When reheated austenite is deformed at a low temperature where the austenite is supersaturated with respect to the precipitating elements, a temperature will be reached where strain-induced precipitates will form in the deformed or recovered austenite and thereby prevent the nucleation of recrystallisation that would otherwise occur during the interpass time in the absence of precipitation [1, 5, 6, 12, 17, 21, 86, 88, 91-96, 134]. To

retard recrystallisation, the pinning forces developed by strain-induced precipitates must be larger than the driving force available to cause recrystallisation [12, 88, 89, 99, 100, 134]. The precipitate pinning force is found from the following relationship

$$F_{PIN} = 4r\sigma N_s \quad (3.10)$$

where, r is the particle radius, σ is the interfacial energy of the austenite grain boundary, and N_s is number of particles per unit area.

Three models have been proposed for N_s in calculating the pinning forces exerted by arrays of microalloy precipitates [5, 6, 88, 89, 134-136]. These are the rigid boundary, the flexible boundary and the sub-grain boundary models. The rigid boundary model defines N_s through the assumption that the motion of a rigid boundary is capable of interacting only with those particles lying within a distance of +/- r of the boundary plane [136]. In contrast the flexible boundary model defines N_s by assuming that a flexible boundary is capable of interacting with every particle of radius r within a single plane of a three dimensional array until fully pinned [52, 88]. The sub-grain boundary model is the most recent and considers the effect of a precipitate distribution, which could exist on austenite sub-grain boundaries prior to the start of recrystallisation [12, 88, 89, 136-138]. The sub-grain boundary model predicts the pinning force per unit area to be:

$$F^s_{PIN} = 3\sigma f_v l/2\pi r^2 \quad (3.11)$$

where, σ is the austenite grain boundary energy, f_v is the volume fraction of particles, l is the sub-grain size and r is the particle radius.

An example of precipitates causing this pinning effect in Nb-bearing steel is shown in Figure 3.5 [88, 138]. It is apparent from Figure 3.5 that the particles are not randomly distributed but appear to be concentrated on sub-grain boundaries in deformed and recovered austenite. Therefore, an average value of N_s would be inappropriate as the

particle distribution is localised. It has been found that true localised pinning forces at the site of preferential precipitation are far higher than that expected from a uniform distribution of particles [88]. The pinning forces at the grain boundaries were well in excess of the driving force and could be responsible for the observed suppression of recrystallisation. The results are summarised in Figure 3.6.

The reason why Nb is most effective compared to other microalloying elements, such as Ti and V, can be explained with the help of Figure 3.7 where the temperature dependence of the driving force for precipitation i.e. supersaturation, is plotted versus temperature for various microalloying precipitating systems. It is found that only NbC can have high supersaturations over a large portion of the typical hot rolling temperature range [12, 139].

Therefore, from sections 3.2.5 and 3.2.6 it can be seen that Nb, Ti and V retard recrystallisation by causing solute drag and forming precipitates during deformation. An attempt has been made by Abad et al. [132] to distinguish the role of microalloying elements as solute and as pinning particles as a function of strain on a steel containing 0.045 wt % Nb. It was shown that solute drag is most effective in retarding recrystallisation at a lower strain range (i.e. strain < 20 %) and at temperatures higher than 1050 ^{o}C i.e. above the solubility temperatures of Nb. Precipitate pinning is effective at a higher strain range (i.e. strain > 20 %) and at lower temperatures (i.e. temperature < 1050 ^{o}C).

3.2.7 Effect of size and distribution of precipitates (specially Nb(C,N)) in controlling recrystallisation during rolling

The precipitation of Nb(C,N) during deformation in austenite and ferrite is heterogeneous in nature, i.e. it always occurs in conjunction with crystalline defects such as grain boundaries, twin boundaries, stacking faults, sub-grain boundaries, or

dislocations and this is associated with the large mismatch between the particles and the matrix, usually of the order of 25 % lattice strain when formed in austenite [1, 12, 140]. The crystallography of precipitation in steel has been reviewed by Jack and Jack [12, 141] and Davenport and Honeycombe [12, 142]. There is an orientation relationship between particles and matrix. The NaCl crystal structure of the particles occurs parallel to the fcc lattice of the parent austenite [12, 143, 144], i.e.,

$$[100]_{MCN} \| [100]_{\gamma}$$

$$[010]_{MCN} \| [010]_{\gamma}$$

Davenport and co-workers have provided direct evidence that this same relationship holds for the strain induced precipitation of Nb(C,N) in a microalloyed steel [12, 142]. When Nb(C,N) precipitates in ferrite or martensite it does so with the Baker – Nutting orientation relationship [12, 145].

$$[100]_{NbC} \| [100]_{\alpha}$$

$$[011]_{NbC} \| [010]_{\alpha}$$

When austenite transforms to ferrite or martensite, it does so with the Kurdjumov-Sachs orientation relationship [12, 146]

$$(111)_{\gamma} \| (110)_{\alpha}$$

$$[110]_{\gamma} \| [111]_{\alpha}$$

The consequence of this relationship is that when the matrix transform from austenite to bainite or martensite, the orientation of the original austenite and the precipitates that formed in that austenite would be related to the transformation product by the Kurdjumov-Sachs orientation relationship.

The localised distributions of Nb(C,N) particles appear to be characteristics of Nb(C,N) precipitation in a deformed matrix. The distribution of carbonitride particles was studied using TEM of carbon replicas [12, 21, 86, 91-96, 134-138] (Figure 3.8). The mean size of the particles formed during hold periods of up to 1000 s at 900 ^{o}C was found to be 4 - 10 nm in a steel containing 0.042 wt% Nb [10, 12, 23, 91-96] after deformation to 30 % strain. Yamamoto et al. [131] reported the presence of relatively large particles (~ 25 nm) at grain boundaries and finer particles with a mean size of 10 nm along the sub-grain boundaries within the grain; i.e. a bimodal particle distribution for a steel containing 0.097 wt% Nb at 900 ^{o}C after deformation with a true strain of 69 % and 10 s holding time after deformation. However the finer particles were seen to undergo coarsening very rapidly, leading to a normal distribution. The estimated pinning forces due to the particles, by using the average size, for the rigid, flexible and sub-grain boundary models are summarised in Table 3.3 [21, 88, 89, 134, 136]. However these are likely to be conservative estimates as the minimum detectable size of the particles is approximately 2 nm [10, 12, 21, 23, 88, 89, 91-96, 134]. Particles smaller than 2 nm are considered as clusters and should exert substantial pinning forces [10, 12, 21, 23, 88, 89, 91-96, 134, 138]. The pinning force increases at the beginning of precipitation, shows a peak in the intermediate stage, and finally decreases due to coarsening of the particles [10, 12, 21, 23, 88, 89, 91-96, 134, 138].

3.3. Static recrystallisation rate

After deformation, softening by static recovery and recrystallisation takes place with time at rates which depend on the material and deformation conditions such as strain, strain rate, initial grain size, the holding temperatures, solute drag and precipitate pinning. The fraction recrystallised as a function of time follows an Avrami equation of the form:

$$X_v = 1\text{-}\exp\text{-}C(t/t_F)^k \quad (3.12)$$

where X_v is the fraction recrystallised in time t; t_F is the time for some specified fraction of recrystallisation, F; k = 2; and C = -ln (1-F) [98].

3.3.1 Effect of initial grain size on static recrystallisation

Nucleation of recrystallised grains is frequently, though not exclusively, associated with the prior grain boundaries. Thus a refinement of prior grain size will increase the nucleation rate and accelerate recrystallisation. Li et al. [147] studied the effect of initial grain size (seven values from 12 to 83 μm) on the recrystallisation kinetics. The direct relationship between the time for 50% recrystallisation, $t_{0.5}$, and initial grain size (D_o) obtained by plotting log ($t_{0.5}$) vs log (D_o) (Figure 3.9.a) is expressed as:

$$t_{0.5} \propto D_o^{\,q} \quad (3.13)$$

The value of q in this study was 1.7, whereas Sellars reported q as being equal to 2 [Sellars 1980]. The initial grain sizes that were used by Sellars were very large (60 to 450 μm). However Li et al. [147] studied only one composition containing 0.055 wt% Nb which is higher than those studied by Sellars [98]. Therefore the smaller value of q may be attributed to the difference in composition and smaller starting grain sizes.

The influence of initial grain size on static recrystallisation kinetics was also studied by Fernandez et al. [148] on four steels microalloyed with Nb, Ti and Nb–Ti (0.035 wt % Nb and 0.067 wt % Ti). The influence of the grain size on the recrystallisation time has been studied for a wide range of grain sizes (20–1000 μm). For constant strain it was shown that q=2 predicts time for 50 % recrystallisation well for a grain size < 160 μm where as for coarse grains i.e. grain size > 160 μm q=1 gives the best fit (Figure 3.9.b). The grain size range studied by Fernandez et al. is larger than that studied by Sellars and

Li et al. and Fernandez et al. used steels that contains very large amount of Ti. That might lead to smaller value of q.

3.3.2 Effect of strain on static recrystallisation

The dependence of the characteristic time $t_{0.5}$ on strain fits a relationship:

$$t_{0.5} \propto \varepsilon^{-p} \qquad (3.14)$$

A mean value of $p = 4$ is reported by Sellars [98] from observations on ferritic steels. Medina and Mancilla [149] studied the influence of strain (0.35 strain) on steels with varying microalloying elements and the grain size ranges between 182 – 430 μm and found that the value of p ranges between 1.34 and 2.3. It is not clear whether this variation arises from the difference in temperature, composition or both. Karjalainen et al. reported $p = 3.3$ for a Nb-microalloyed steel with a grain size of 60 μm [125, 150]. For Ti, Ti-Ni-Nb and Ti-Ni-V microalloyed steel with grain sizes in the range 40- 56 μm, for the strain range 0.25 to 0.35 exponent values between 2.5 and 3 were reported by Airaksinen et al. [125, 151]. All these results suggest that there is a strong dependence of the exponent on the initial grain size.

Fernandez et al. studied the influence of initial grain size on the strain exponent (Figure 3.10) [148] in HSLA steels containing Nb and Ti. p tends to decrease as the grain size increases resulting in a dependence of $p=5.6D_o^{-0.15}$. With an initial grain size of 806 μm the strain exponent is found to be 2, but for starting grain size of 60 μm it becomes 3. Only 4 initial grain sizes were studied by Sellars and the grain sizes ranges between 60 – 100 μm. That might lead to higher strain exponent value (4). Fernandez et al. studied recrystallisation kinetics on steel that contains very large amount of Ti (0.067 wt %). That might be the cause of different behaviour.

3.3.3 Effect of temperature and microalloying elements such as Nb, V and Ti on static recrystallisation

The empirically fitted relationship that is commonly used to quantify the effect of temperature and Nb content is given by [98]:

$$t_{0.5} \propto \exp[((275000/T)-185).[Nb]] \quad (3.15)$$

where, T is the deformation temperature.

There is considerable scatter in the absolute values of recrystallisation rate, which does not vary systematically with composition, although a trend is revealed that the time for 50 % recrystallisation shifts to longer times with an increase in Nb content [98, 125, 148]. This has been associated with pre-precipitation effects and the solute drag effect of Nb as discussed in sections 3.2.5 and 3.2.6.

However, since the kinetics of precipitation at any temperature depend both on composition and prior deformation history [1, 5, 6, 21, 88, 89, 98], it is unlikely that any simple relationship would satisfactorily describe the influence of variables on recrystallisation after deformation at temperatures below the solubility limit of NbC as precipitation of Nb(C,N) would lead to decrease in available Nb in solution and that would have an effect on recrystallisation kinetics.

There are few observations on V and Ti treated steels compared with those of Nb steels. Irvine et al. [57] found little or no effect of additions of 0.15 wt % V or 0.03 wt% Ti on recrystallisation kinetics although they retarded grain growth after recrystallisation. Cordea and Hook [153] observed some retardation of recrystallisation in a 0.059 wt% V steel at temperatures below 925 ^{o}C, but the effect was less than with 0.011 wt% Nb. Ouchi et al [12, 154] also found little retardation of the start of recrystallisation in a

0.019 wt% Ti steel although there was some evidence for decreased recrystallisation rates. Fernandez et al. modified equation 3.15 by replacing [Nb] by [Nb + 0.374 Ti] in steel containing both Nb and Ti [148]. It is therefore clear that V and Ti are much less effective than Nb in retarding recrystallisation but few quantitative relationships have been put forward at present.

3.4. Modelling recrystallisation and precipitation kinetics

The interaction between recrystallisation and precipitation has been explained with the aid of recrystallisation, precipitation, time and temperature (RPTT) diagrams where both recrystallisation and precipitation kinetics curves are superimposed [134, 136]. A schematic RPTT diagram is shown in Figure 3.11 [134]. The key features of the diagram are as follows:

- T_{sol} refers to the solution temperature above which Nb-rich precipitates are completely dissolved in the austenite matrix, $T^{/}$ is the temperature below which recrystallisation and precipitation compete and T_R is the temperature below which precipitation occurs prior to recrystallisation.
- R_s and R_f refer to the start and finish of recrystallisation in HSLA steels.
- $R_s^{'}$ and $R_f^{'}$ refer to the start and finish of recrystallisation in plain carbon steels.
- $P_s^{'}$ and $P_s^{''}$ refer to the predicted precipitation start times in deformed and undeformed austenite respectively. P_s is the experimentally determined precipitation start time.
- It is observed that recrystallisation is completed before the start of precipitation if deformation is carried out at temperatures between T_{sol} and $T^{/}$ after austenitisation above T_{sol}. In this case the start of recrystallisation is controlled by the type and amount of solute elements present. Since precipitation occurs in the completely recrystallised region (i.e. fine austenite grain size), the start of

precipitation (P_s) is accelerated, shifting towards the left, away from the P_s'' curve which corresponds to the start of precipitation in the undeformed, coarse austenite.

- In the temperature range between T' and T_R, precipitation takes place after partial recrystallisation. Hence an acceleration of the precipitation kinetics will be observed in this temperature region because of the presence of some deformation substructure in the partially recrystallised austenite.
- In the temperature range below T_R (stage III), recrystallisation is preceded by precipitation. When precipitation takes place prior to recrystallisation, the resulting pinning force is high enough locally to retard the initiation and progress of recrystallisation. This follows from the result shown in Table 3.3.

3.4.1 Modelling recrystallisation and precipitation interaction during single hit deformation

The model most frequently used to predict the recrystallisation start and finish time and precipitation start time was proposed by Dutta-Sellars [98, 155-157].

Dutta and Sellars [98, 155-157] suggested the following empirically fitted equations to predict the static-recrystallisation start time, R_s, (i.e. 5 % recrystallisation) and strain-induced Nb(C,N) precipitation start time, P_s (i.e. 5 % precipitation) after deformation and isothermal holding of Nb-microalloyed steels at different temperatures.

$$t_{0.05p} = A[Nb]^{-1}\varepsilon^{-1}Z^{-0.5}\times\exp\left(\frac{270{,}000}{RT}\right)\times\exp\left\langle\frac{B}{T^3(\ln K_S)^2}\right\rangle \qquad (3.16)$$

$$R_s = 6.75\times10^{-20}D_0^2\varepsilon^{-4}\times\exp\left(\frac{300{,}000}{RT}\right)\times\exp\left(\left(\frac{2.75\times10^5}{T}-185\right)[Nb]\right) \qquad (3.17)$$

where, [Nb] is the amount of Nb in solution in austenite; ε is the applied strain; T (in Kelvin) is the isothermal holding temperature where precipitation or recrystallisation is taking place; *A* and *B* are the two constants; K_s is the supersaturation ratio following the solubility product equation (3.18) given by Irvine et al. [57]; D_0 (in microns) is the average austenite grain size after reheating; and Z is the Zener-Hollomon parameter, which is related to strain rate, $\dot{\varepsilon}$, and deformation temperature (T_{def}) by equation (3.19).

$$K_s = [Nb][C+12N/14]_{soln}/10^{2.26-6770/T} \quad (3.18)$$

$$Z = \dot{\varepsilon}\exp\left(\frac{Q_{def}}{RT_{def}}\right) \quad (3.19)$$

where, Q_{def} is the activation energy for deformation. From the recrystallisation start time (i.e. 5 % recrystallisation), R_s, the recrystallisation finish time (i.e. 85 % recrystallisation), R_f, can be predicted from equation 3.12 [98].

It has been shown that the Avrami exponent, k, can vary [125, 149, 158-161], with k being dependent on the temperature of deformation and the composition.

$$K = B'\exp(-Q_{def}/RT) \quad (3.20)$$

where B' is a constant and Q_{def} is the activation energy. For Nb-bearing steel the values of B' and Q_{def} are 38.02 and 438 kJ/mol respectively. In the study by Medina and Mancilla the values of k varied between 0.62 and 1.5 [125, 158].

The predictions according to the Dutta and Sellars model were found to agree with experimental results [98, 114, 115, 155] (for overall range in composition, wt %: 0.06-0.17 C, 0.005-0.015 N, 0.03-0.084 Nb; ε: 10-50 %; initial austenite grain size (D_0): 100-450 μm, T_{def}: 900-1100 °C; T: 800-1100 °C) when using a wide range of values of *A* (~ 3×10^{-6} to 2.5×10^{-5}) and *B* (~ 1×10^{10} to 6×10^{10} K^3). Dutta and Sellars [155] attributed this

variation to the different methods used for the detection of Nb(C,N) precipitation. The values of *A* reported by the different studies are summarised in Table 3.4.

Other models for the precipitation-recrystallisation interaction in Nb-treated steels can be found in the literature and are summarised in Table 3.5.

Medina and Mancilla [125, 158] have studied the influence of the individual alloying elements on the activation energy. The equation proposed by them can be written as:

$$Q_{def}\,(\text{J/mol}) = 124714+28385.68[\text{Mn}]+64716.68[\text{Si}]+72775.4[\text{Mo}]+76830.32[\text{Ti}]^{0.123}+ 121100.37[\text{Nb}]^{0.1} \quad (3.21)$$

Recently, the Dutta and Sellars model has been extended to predict the variation of Nb(C,N) precipitate radius and volume fraction with isothermal holding time, by considering growth and coarsening (controlled by bulk and pipe diffusion of Nb) of heterogeneously nucleated (on the nodes of dislocation sub-structures) strain-induced precipitates. This model assumes uniform dislocation density through out the matrix, which was used to calculate the nucleation rate and effective diffusivity during precipitation. In reality the dislocation density does not decrease uniformly as the stored energy after deformation would be different depending on the grain size and orientation of the grains. That would influence the recrystallisation kinetics leading to a non uniform distribution of dislocation density in the matrix. Zeng and Wang [162] have shown that precipitation kinetics in a matrix with a gradient in dislocation density can be very different from that in a matrix with uniform dislocation density even if the average dislocation density is the same in both cases.

Another interesting phenomenon that needs some consideration is the effect of recrystallisation on the precipitation kinetics. If recrystallisation precedes precipitation, the material will behave as an undeformed material and precipitation kinetics will be

slow. However, when recrystallisation and precipitation occur concurrently, there will be a continuous decrease in the average dislocation density with time, hence, a deceleration in strain induced precipitation kinetics. Akamatsu et al. [163] have attempted to model the effect of concurrent recrystallisation on precipitation. They have estimated the actual dislocation density (ρ_a) as a function of recrystallised area fraction (X) according to

$$\rho_a = (1 - X)\,\rho + X\,\rho_o \qquad (3.22)$$

where, ρ and ρ_a are the dislocation density in unrecrystallised austenite and in completely recrystallised austenite respectively.

Hence, the role of the dislocation density is critical in determining the degree of acceleration in the precipitation kinetics. An accurate estimation of the dislocation density is essential in order to have an accurate prediction of the precipitation kinetics.

Nagarajan et al. [164] developed a new model for strain induced precipitation of Nb(C,N) from the existing model proposed by Dutta et al. [157] for single hit deformation. The key feature of this model is that microband geometry is employed. In the original model proposed by Dutta et al. bulk Nb content is used and in this model local solute concentration is used at the microband. The evaluation of the precipitate radius, number density and volume fraction are compared with the experimental results obtained from thin foil transmission electron micrographs on Fe-30 wt % Ni alloys (that are austenitic at room temperature and are similar to HSLA steel in deformation behaviour [165, 166]) subjected to deformation by plane strain compression to a strain of 1 at 850 °C with 50 s hold period after deformation. The model predicts an average precipitate diameter of 4.8 nm and the experimentally determined average precipitate diameter was 13 nm. Therefore the experimental result differs from the predicted result by a factor of approximately 3. The authors attributed this discrepancy to the fact that particles less than 4 nm are below the resolution limit of the microscope and the

coarsening rate of the precipitates are under predicted by using bulk diffusion phenomena.

Other models for the precipitation-recrystallisation interaction in Nb-treated steels can be found in the literature that consider factors such as; the effect of non-equilibrium vacancy concentration on precipitation and recrystallisation [83]; precipitation-recrystallisation interaction under continuous cooling [167, 168]; dependence of activation energy for recrystallisation (Q_{rex}) on the steel composition and temperature [125, 158-161, 169]; driving forces for precipitation and recrystallisation [155, 157]; and stronger effect of solute drag in retarding recrystallisation at higher temperature (above 1050 °C) compared to precipitate pinning [169] not covered by the above described models.

Despite an extensive study into modelling recrystallisation and precipitation kinetics there is still inconsistency in relating the constants in the equations with composition and process parameters. This may be due to the constants being dependent on more than one process parameter, which makes them difficult to quantify in a systematic way. Additionally, the models were validated mostly for approximately 0.04 wt% Nb steels with 30 % strain and results from other studies in the literature, rather than from a systematic set of experiments. Only a very few results exist for a high strain range or larger amounts of Nb where the model agrees qualitatively.

3.4.2 Modelling recrystallisation and precipitation interaction during multipass deformation

Equations (3.12 and 3.15-3.17) describe the influence of deformation variables and initial grain size on the microstructural changes after a single deformation pass. However most commercial rolling operations involve a series of deformations given in separate

passes that are separated by intervals of time. During these processes the temperature changes continuously, which might influence recrystallisation kinetics. Whittaker calculated the temperature compensated time for recrystallisation [170].

$$W = \Sigma t_i \exp\text{-}Q_{rex}/RT_i \quad (3.23)$$

where, t_i is the finite difference in time at which the temperature was T_i.

A typical calculation of austenite grain sizes at various stages in the sequence of passes used for plate rolling is illustrated in Figure 3.12, together with the temperature profile [132]. Constant strains of 15 % per pass were used in the calculations, which were carried out for plates with various thicknesses. The Nb content of the steel was 0.035 wt %. From the figure it can be seen that progressive refinement of the austenite grains is predicted with 15 % reduction per pass rolling schedule and lowering the soaking temperature promotes a finer grained austenite by reducing the initial austenite grain size and also the deformation temperatures throughout the rolling schedule.

Abad et al. [132] modelled the evolution of the austenite microstructure after each deformation pass after quantifying the progress of recrystallisation using an Avrami equation

$$X = 1 - \exp\left[-0.693 \exp\left(\frac{t}{t_{0.5X}}\right)^k\right] \quad (3.24)$$

$$t_{0.5} = 9.92\times10^{-11} D_0 \varepsilon^{-5.6 D_0^{-0.15}} \dot{\varepsilon}^{-0.53} \times \exp\left(\frac{180{,}000}{RT}\right) \times \exp\left(\left(\frac{2.75\times10^5}{T} - 185\right)\left[[Nb] + 0.374[Ti]\right]\right) \quad (3.25)$$

where, k = 1, t is the time (s) and $t_{0.5X}$ is time for 50 % recrystallisation. $t_{0.5X}$ is calculated

The recrystallised fraction at the end of the deformation can be calculated using the following equation

$$X_{j+1}(\Delta t) = X_{j+1}(\Delta t + t) - X_{j+1}(t) \quad (3.26)$$

where, t is the time at temperature T_{j+1} and Δt is the increment of time ~ 0.01 s at that temperature. The recrystallised grain size after the j-th pass is related to the previous grain size (D_{i-1}) by an expression of the type

$$D_i = k d_{j-1}^{m} \varepsilon_j^{-p} \quad (3.27)$$

where, K, m and p are material dependent constants [168]. The predicted and measured microstructural changes are shown in Figure 3.13. The recrystallised fraction was measured from flow softening after each pass. At temperatures below complete recrystallisation the predicted value is higher than the measured value. The author has attributed the discrepancy at lower strain (ε<20 %) to be due to the solute drag effect and with higher strain (i.e. ε > 20 %) to be due to precipitation as mentioned in sections 3.2.5 and 3.2.6.

The pinning force exerted by the fine particles suppresses the progress of recrystallisation, thus retaining the deformed austenite structure at higher temperature and allowing higher deformation temperatures which leads to smaller rolling loads. Equation 3.16 was used to model precipitation kinetics in multipass deformation conditions after taking into account the hold period in each pass. This method under predicts the precipitation time and this was attributed to the fact that the amount of Nb in solution cannot be detected accurately after each pass [132].

An attempt was made to extend the precipitation pinning force model based on the microband geometry to multipass deformation conditions in an Fe-30 wt % Ni alloy [171]. The theory predicts the change in Nb concentration along with the change in microband geometry due to deformation. Detailed study of the precipitates and

prediction of volume fraction and number density of particles after each pass is required [172].

Sun et al. [168] incorporated the retarding effect of Nb(C,N) precipitates during multipass deformation in continuous cooling conditions for steels containing 0.05, 0.07 and 0.09 wt% Nb. The specimens were deformed in 3 stages with 30 % strain starting from a temperature of 1250 ^{o}C. The cooling rate between the passes was varied from 0.15 - 15 ^{o}C/s. They found that when the interpass time is short and the cooling rate is rapid, the rate of recrystallisation is solute controlled; at intermediate values of interpass time and cooling rate precipitation is rate controlling; and finally when the interpass time is relatively long and cooling rate is relatively slow, particle coarsening weakens the effect of precipitates. Systematic study considering the effect of strain, initial grain size and change in Nb content after each deformation pass is still lacking in this area.

3.5. Summary

The present review explores the mechanisms involved in the recrystallisation and grain growth phenomena of deformed structures. Various models describing the recrystallisation phenomenon, under static recrystallisation conditions, have been discussed. The effect of different variables, (steel chemistry, initial grain size, deformation temperature and strain) on the recrystallisation and precipitation behaviour and their mutual interaction under hot working and thermomechanical controlled rolling conditions of C-Mn and low carbon microalloyed steels vis-à-vis the recrystallisation kinetics and the models to describe the final grain size have been explored in detail. The potential effect of different microalloying elements in retarding recrystallisation kinetics has been looked into in terms of relative size differences. It has been shown that there is quantitative consistency between different observations as to the form of dependence of the kinetics of recrystallisation and the grain size on the processing variables and on the

original microstructure. This has enabled quantitative relationships to be proposed which give a satisfactory description of the structural changes. The constants in the various equations show considerable variation in the literature, which cannot at present be correlated with reported differences in composition. Thus, while there is a reasonable quantitative understanding of the physical metallurgy of hot working, there is still need for further systematic study, particularly on the effects of variables on grain size after recrystallisation, influence of recrystallisation and varying dislocation density on the precipitation kinetics during deformation.

Tables and Figures

Table 3.1. Grain growth following recrystallisation in C-Mn steel. The data have been calculated for the rate constants given in Figure 3.2a. The time within the brackets represent the holding time at deformation temperature. D (rex) refers to the recrystallised grain size after deformation at 1050 and 950 °C [98].

Temperature (°C)	Grain size (μm)			
	D (rex)	D (1 s)	D (5 s)	D (10 s)
1050	50.7	55.5	62.7	66.8
	25	52.7	61.9	66.4
950	50.7	51.1	52.4	53.8
	25	39.4	46.3	49.6

Table 3.2. Values of D' used in the equation 3.5 and 3.6.

Composition (wt %)	D'	Reference
C –0.17, Mn-0.53, Si-0.11	0.35	98
C –0.17, Mn- 1.36 Si-0.36	0.83	102
C –0.15, Mn- 0.66 Si-0.23	0.5	116
C –0.15, Mn- 0.66, Nb-0.04, Al-0.017, N-0.017, Ti <0.005	0.66	102
C –0.16, Mn- 1.41, Nb-0.041, Al-0.02, N-0.0054	1.1	154
C –0.17, Mn- 1.25, Nb-0.015, Al-0.005, N-0.0057, Ti-0.025	1.86	98, 173
C and Nb -0.04	0.9	98

Table 3.3. Estimated pinning force [134]. N_p is the number density of the particles.

Time (s)	Size nm	N_pX10^{14} (m^{-2})	Precipitate pinning force (MN/m^2)		
			Rigid boundary model	Flexible boundary model	Subgrain boundary model
10	4.1	1.02	0.96	4.41	0.67
100	6.5	2.76	3.66	16.32	2.86
1000	9.8	1.52	2.74	6.64	2.38

Table 3.4. Constant *A* used in equation 3.16 reported by various studies [155].

Condition of austenite	Precipitation detection method	*A*	Reference
Reheated and deformed	Microhardness	$1.5*10^{-5}$	102
Reheated and deformed	Microhardness	$1*10^{-5}$	154
Reheated and deformed	Extraction replica	$1*10^{-5}$	136
Recrystallised	Electrolytic extraction and filtration	$2.5*10^{-5}$	174
Recrystallised	Electrolytic extraction and centrifuging	$3*10^{-5}$	175

Table 3.5. Models for static recrystallisation kinetics in single hit deformation.

Model	Steel	Technique	Reference
$t_{0.5} = (-5.24 + 550[Nb]) \times 10^{-18} D_0^2 \varepsilon^{(-4+77[Nb])} \times \exp\left(\frac{330{,}000}{RT}\right)$	0.013-0.032 Nb	S	169
T > 990°C; $t_{0.25} = 1.5 \times 10^{-18} D_0^2 (\varepsilon - 0.025)^{-2.8} \times \exp(30[Nb]) \times \exp\left(\frac{300{,}000}{RT}\right)$ T < 990°C; $t_{0.25} = 1 \times 10^{-42} D_0^2 (\varepsilon - 0.025)^{-2.8} \times \exp(30[Nb]) \times \exp\left(\frac{885{,}000}{RT}\right)$	0-0.043 Nb	Ro	176
T > T_c; $t_{0.5} = 3.94 \times 10^{-13} D_0 \varepsilon^{-1.96} \dot{\varepsilon}^{-0.44} \times \exp\left(\frac{260{,}000}{RT}\right)$ T < T_c; $t_{0.5} = 9.82 \times 10^{-63} D_0^{1.9} \varepsilon^{-4.1} \times \exp\left(\frac{1500{,}000}{RT}\right)$ T_c= 1053.5-178.3 ln(1+ε)	0.042 Nb	S	160
$t_{0.5} = A \times 10^{-20} D_0^2 \varepsilon^{-1.96} \dot{\varepsilon}^{-4} \times \exp\left(\frac{350{,}000}{RT}\right)$; value of A not mentioned	0.025 Nb	Ro	177
$t_{0.5} = 1.27 \times 10^{-18} \varepsilon^{-3.81} \dot{\varepsilon}^{-0.36} \times \exp\left(\frac{404{,}000}{RT}\right)$	0.055 Nb	S	178

$t_{0.05} = 6.75\times10^{-20} D_0^2 \varepsilon^{-4} \times \exp\left(\frac{300{,}000}{RT}\right) \times \exp\left(\left(\frac{2.75\times10^5}{T} - 185\right)[Nb]\right)$ $\times \exp\left(\left(\left(\frac{1.53\times10^7}{T}\right) - \left(\frac{2.06\times10^5}{r}\right)\right)\left[\frac{NbC}{r}\right]\right)$ r is the mean distance between NbC particles (not mentioned)	not given	Based on 98	179
$t_{0.5} = 9.92\times10^{-11} D_0 \varepsilon^{-5.6 D_0^{-0.15}} \dot{\varepsilon}^{-0.53} \times \exp\left(\frac{180{,}000}{RT}\right) \times$ $\exp\left(\left(\frac{2.75\times10^5}{T} - 185\right)[[Nb] + 0.374[Ti]]\right)$	0.035 Nb	S	148
$t_{0.5} = f_R(Mn, C, Mo, Nb) D_0^{0.878} \varepsilon^p \dot{\varepsilon}^{-0.28} \times \exp\left(\frac{Q_{rex}}{RT}\right)$ $Q_{rex}/R=39660 - 6025[C]^{0.4}+755[C]^{0.65}+ 2.848x10^3[Mn]^2+4423[Mo]^{0.2}+ (446.46+5.57x10^{-5}(T_c-T)^4)[Nb]^{0.68}$; $p=D_o^{-0.115}(-3.89+f_p(Nb))$ $f_r(Mn, C, Mo, Nb)$, $f_p(Nb)$ and T_c not mentioned	not given		180

Ro = recrystallisation (i.e. using metallography)

S = softening (i.e. using mechanical testing

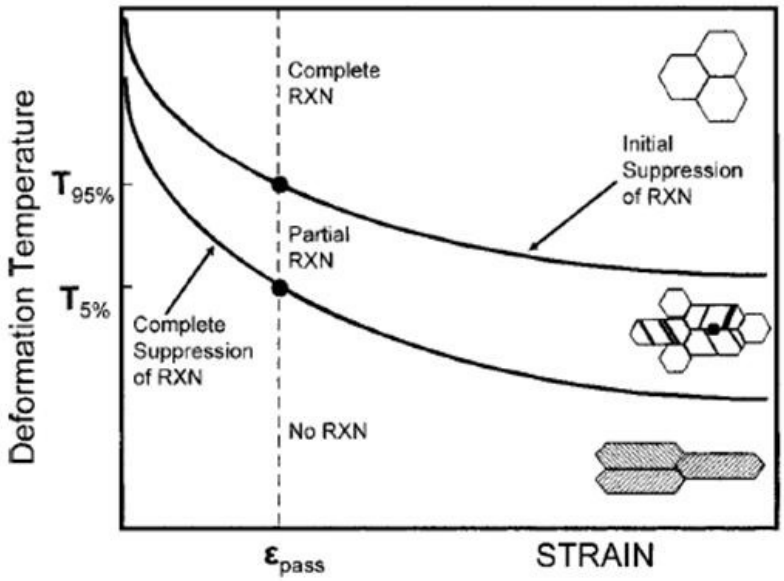

Figure 3.1 a. Schematic illustration of the austenite grain structure resulting from various deformation conditions (deformation temperature and strain) [88]. Dashed line represents the effect of various deformation temperatures at a constant level of strain (ε_{pass}). $T_{95\%}$ and $T_{5\%}$ are the temperatures for 95 % and 5 % recrystallisation respectively.

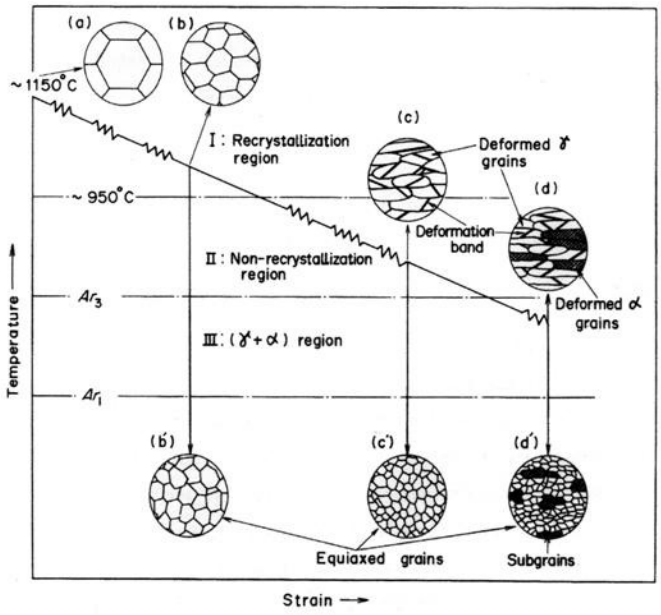

Figure 3.1 b. Schematic diagram showing the typical thermomechanical controlled rolling (TMCR) schedule and the associated microstructural changes [17] of steels.

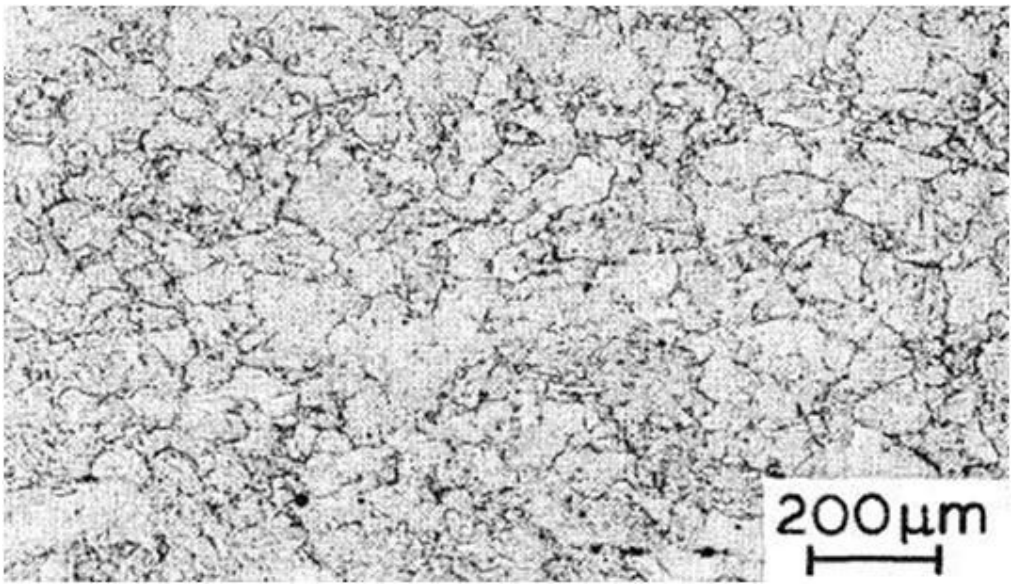

Figure 3.1 c. The microstructure of a 0.045 wt % Nb bearing steel after deformation in the complete recrystallisation region consisting of fine recrystallised austenite grains [21].

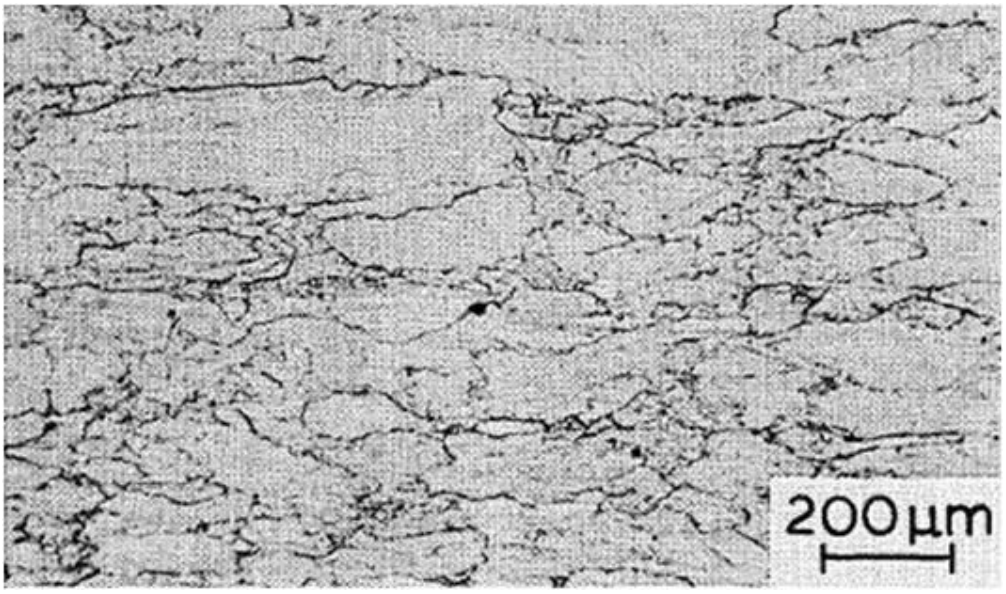

Figure 3.1 d. The microstructure of a 0.03 wt % Nb steel after deformation in the no recrystallisation region consisting of pancake shaped deformed austenite grains [89] revealed using saturated aqueous picric acid etchant.

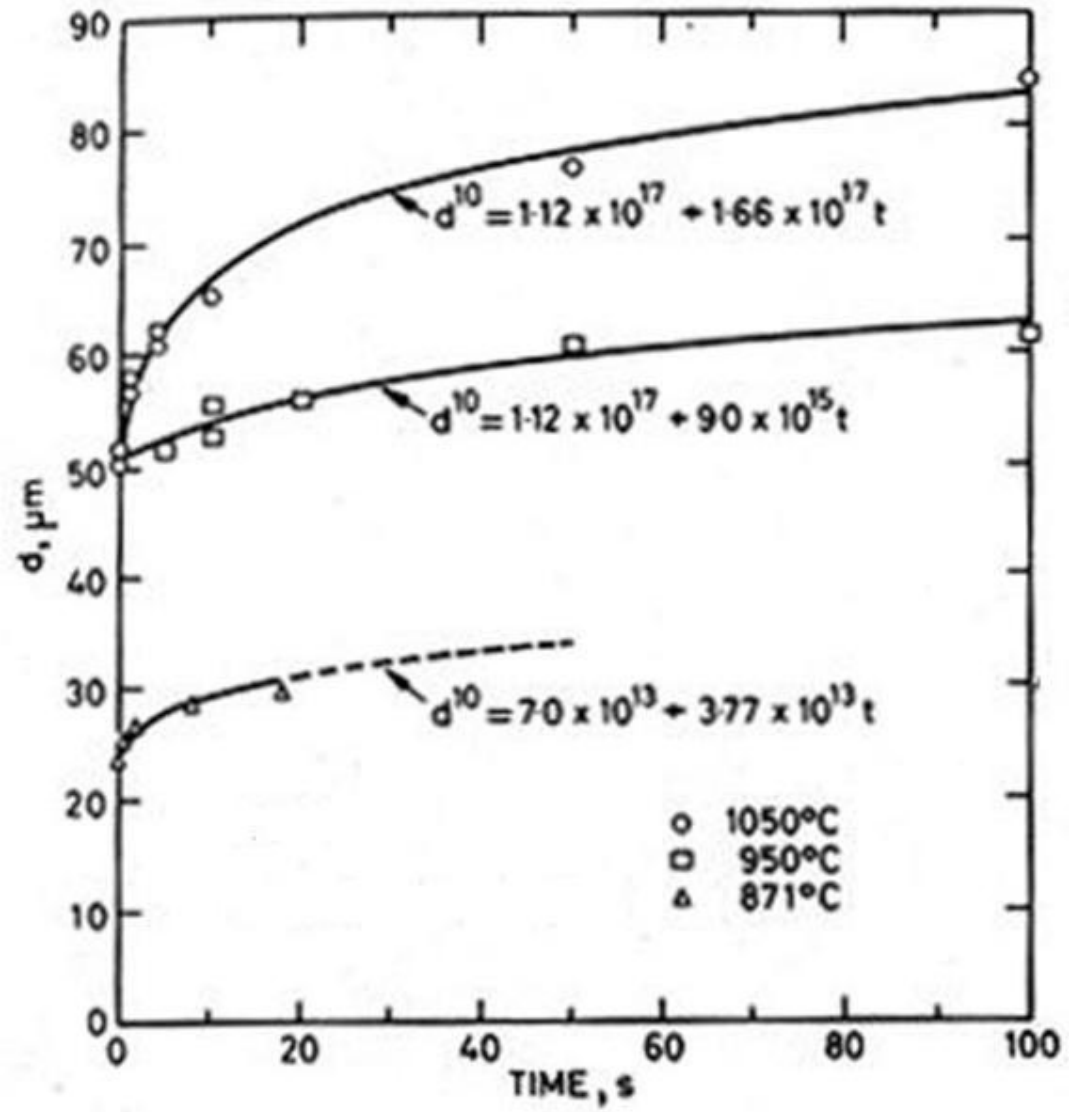

Figure 3.2 a. Recrystallised grain growth as a function of time in C-Mn steel plotted using the experimental results of Foster and Korchynsky and Stuart [98, 116, 117] for a C-Mn steel after deformation with 30 % strain at three different temperatures (1050, 950 and 871 °C) with three different starting grain sizes of 280, 200 μm (Table 3.1) [116] and 110 μm [117]. The exponent 10 was chosen as this gives the best fit to the experimental results. d refers to the grain size.

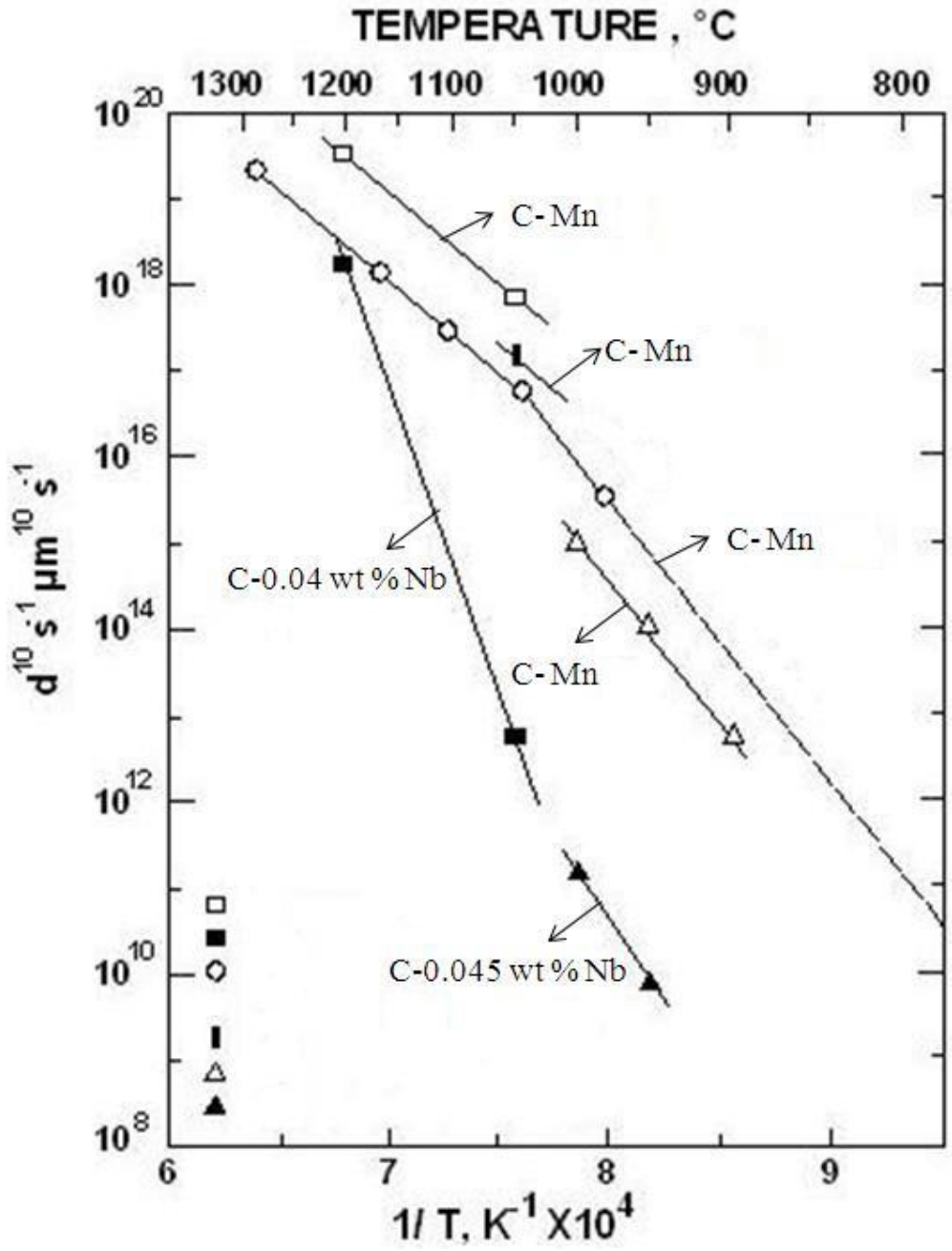

Figure 3.2 b. Temperature dependence of grain growth for C-Mn and Nb treated steel [98] showing that there is some scatter in the result of C-Mn steels and that Nb causes marked retardation to grain growth at temperatures below 1200 °C [98]. The results were plotted using equation 3 and n=10.

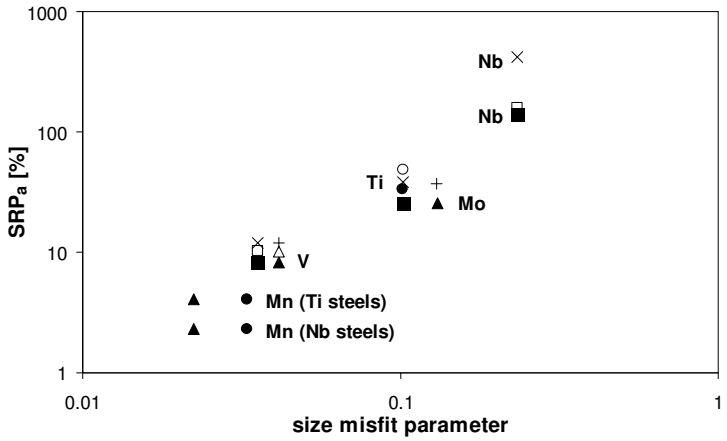

Figure 3.3. The solute retardation parameter (SRP_a) as a function of the size misfit parameter, based on data from [130]. Solid markers represent data from dynamic recrystallisation experiments, open markers from static recrystallisation both from [130], crosses represent static recrystallisation data from Yamamoto [131].

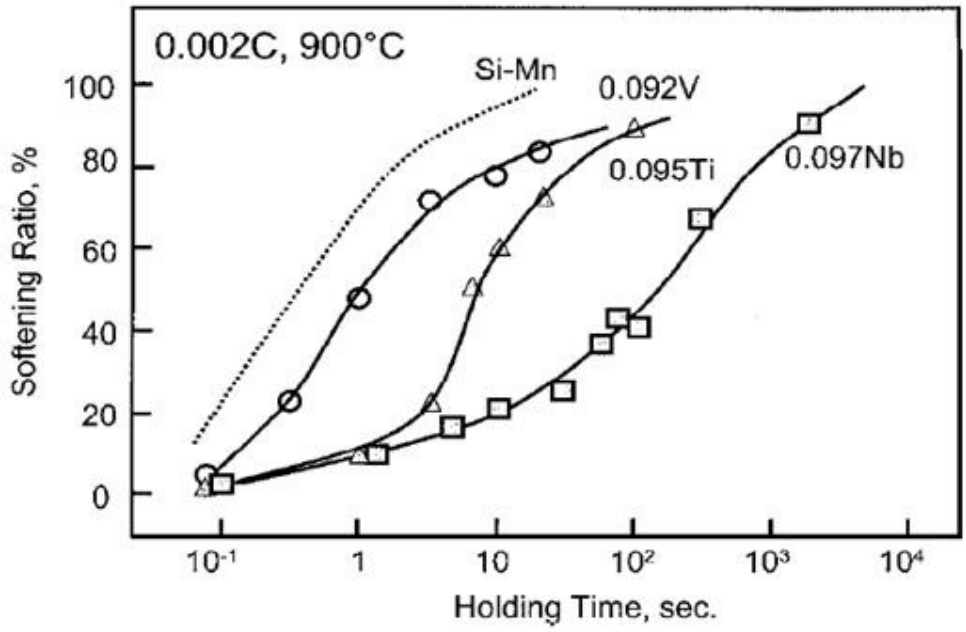

Figure 3.4. Comparison of the effects of Nb, V and Ti as a solute on softening behaviour in 0.002 wt % C Steels after deformation at 1050 °C [131] showing Nb has the strongest effect on retarding recrystallisation (here softening ratio).

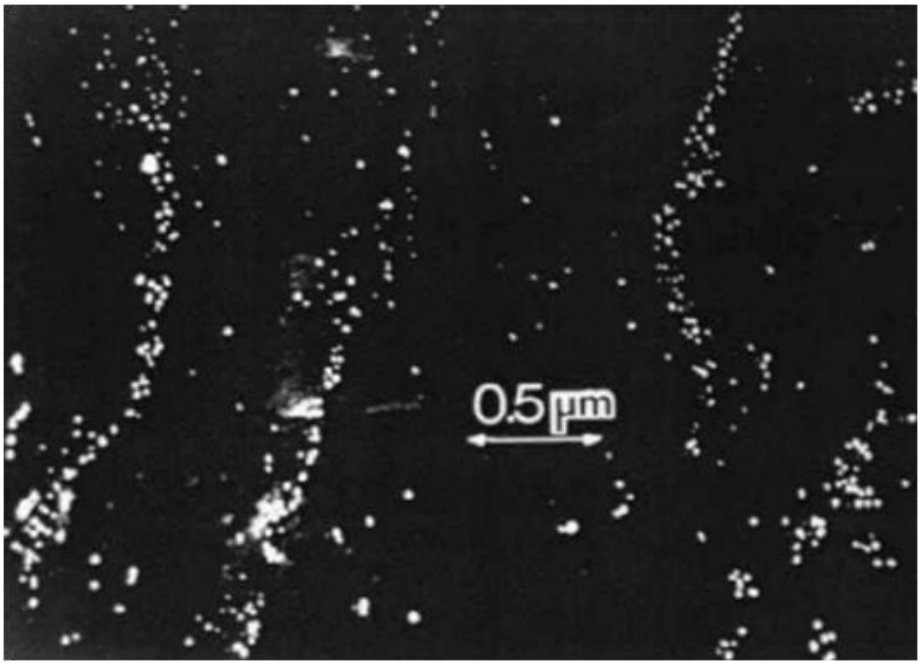

Figure 3.5. Dark field TEM micrograph showing heterogeneous distribution of strain-induced Nb(C,N) precipitates in 0.09 C-0.07 Nb (all wt %) steel after 25 % rolling and 100 s holding at 950 °C [138].

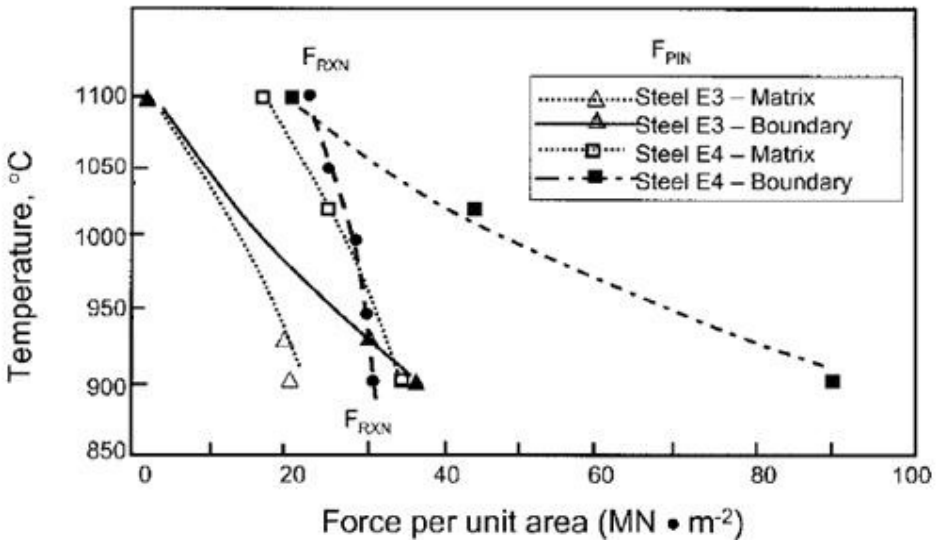

Figure 3.6. Driving force for recrystallisation and pinning forces exerted by the strain induced Nb(C,N) on the grain boundary and the matrix after deformation with 30 % strain in 0.03 (E3) and 0.09 wt % (E4) Nb bearing steel [88]. Recrystallisation is retarded when the pinning force exceeds the driving force for recrystallisation.

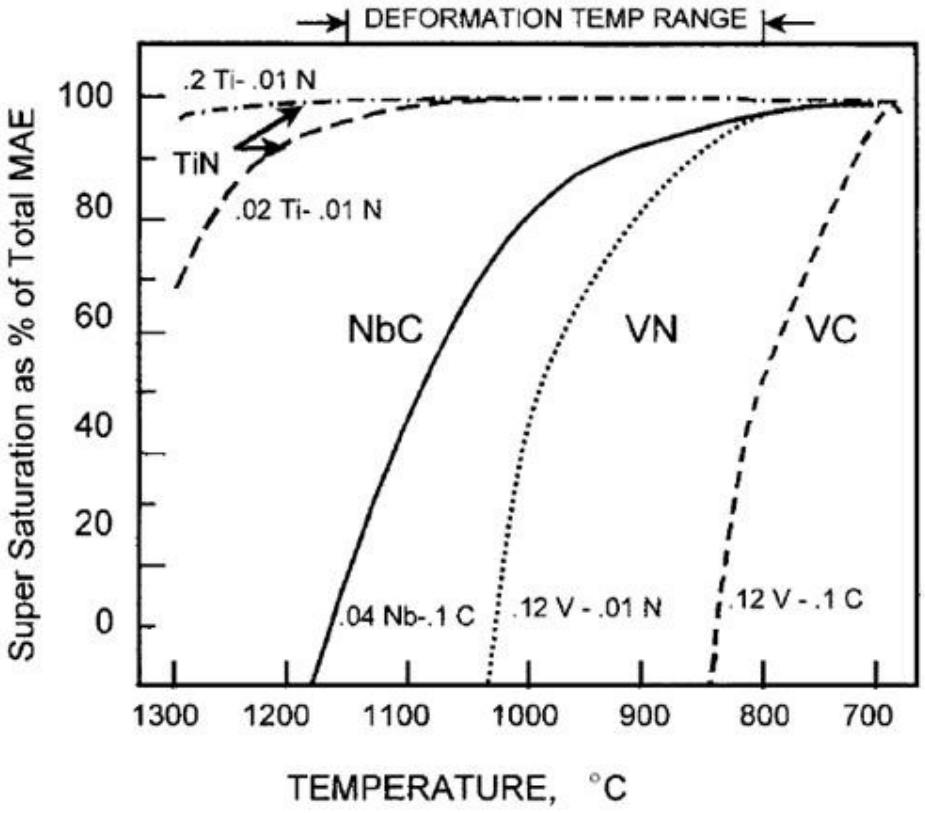

Figure 3.7. Precipitation potential of various microalloying elements showing only NbC has the highest supersaturation in austenite in the hot deformation temperature range i.e. 1000-1200 ^{o}C [12, 139]. MAE refers to microalloying elements.

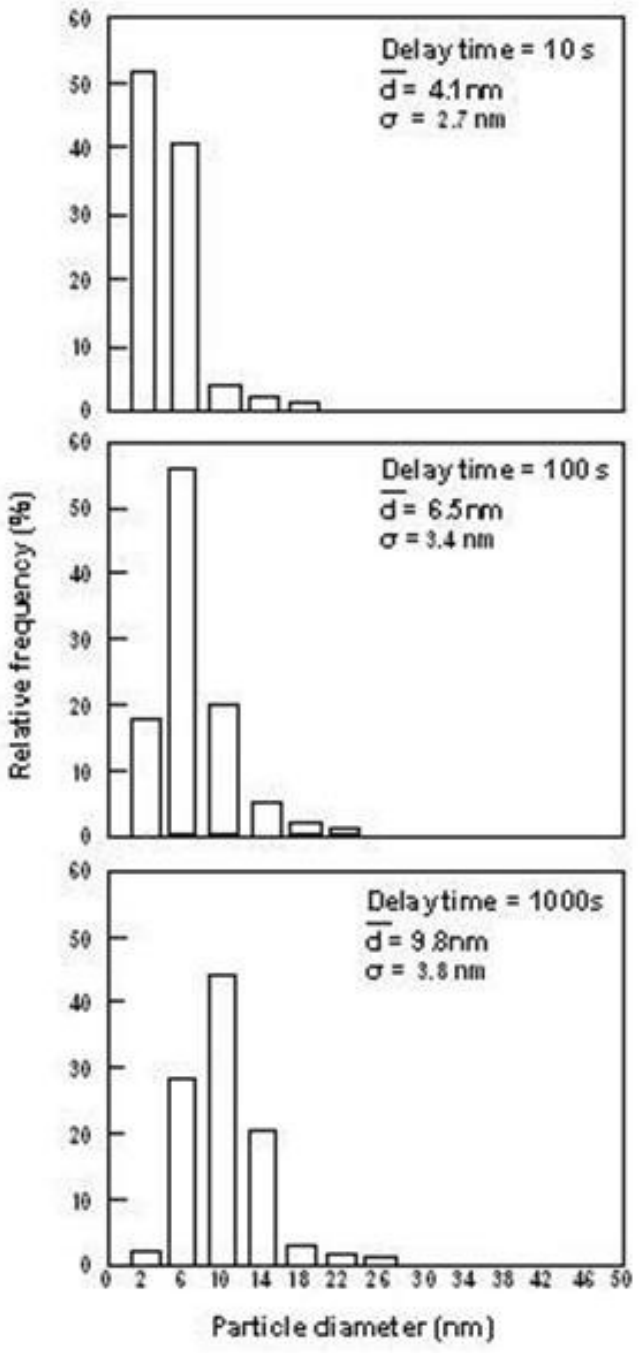

Figure 3.8. Nb(C,N) precipitate size distribution in a 0.042 wt % Nb bearing steel after deformation at 900 ^{o}C with 30 % strain and for holding at three different times 10 s, 100 s and 1000 s [134].

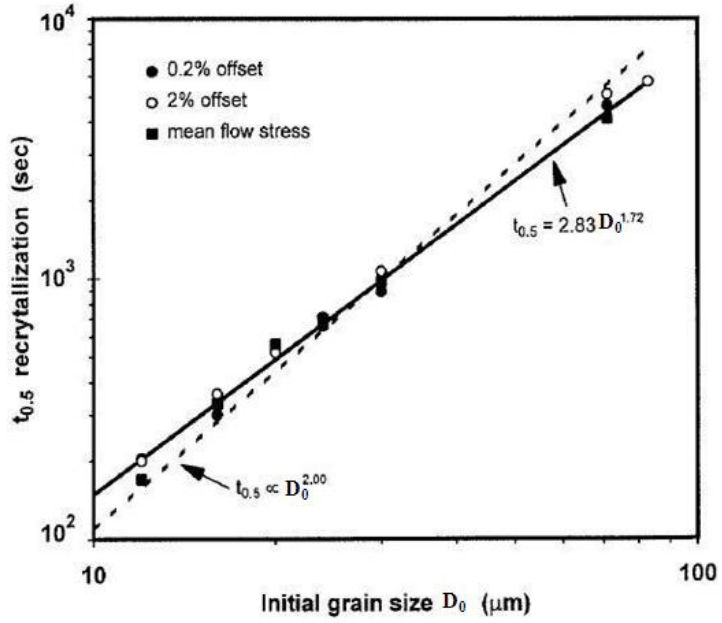

Figure 3.9 a. Curves of $t_{0.5}$ vs D_o obtained from three methods after plotting log ($t_{0.5}$) vs log (D_o) [147]. $t_{0.5}$ refers to the time for 50 % recrystallisation and D_o is the starting grain size ranging from 12 to 83 μm. Smaller starting grain size leads to higher exponent value.

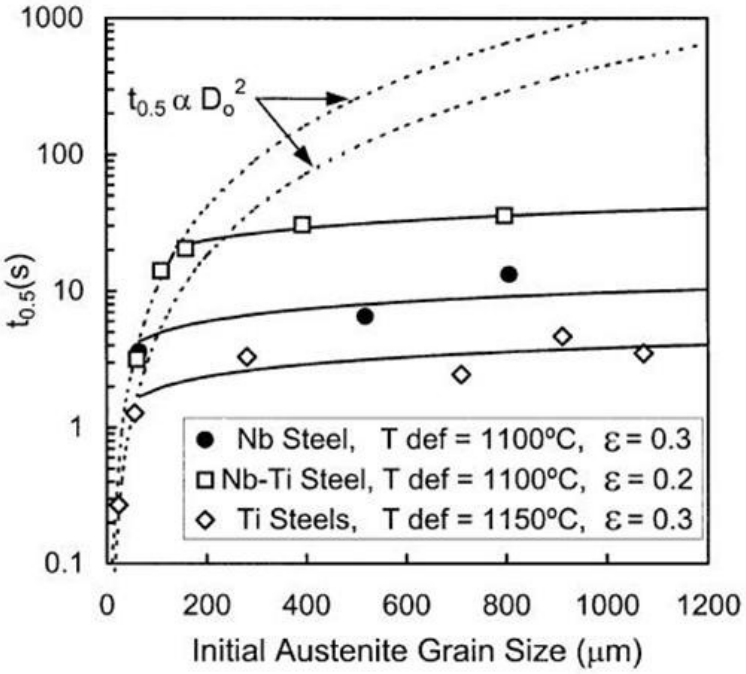

Figure 3.9 b. Effect of initial grain size on time for 50 % recrystallisation in microalloyed steel containing Nb, Nb-Ti and Ti. T def refers to the deformation temperature and ε refers to the strain [148].

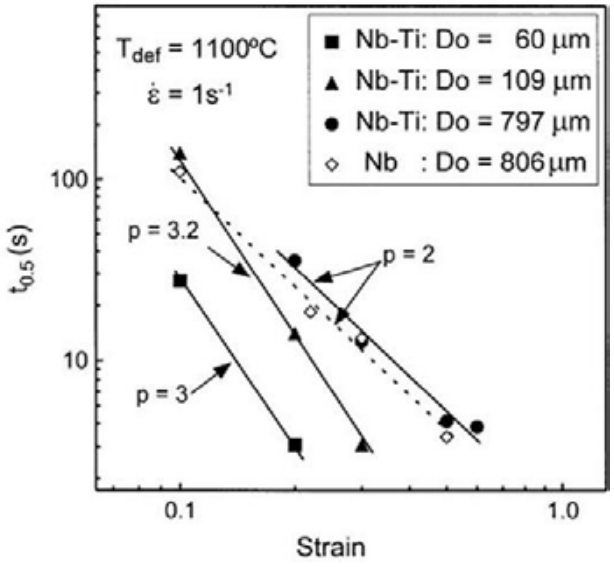

Figure 3.10. Influence of initial grain size on strain exponent in HSLA steels containing Nb and Ti. p tends to decrease as the grain size increases resulting in a dependence of $p=5.6D_o^{-0.15}$. With an initial grain size of 806 μm the strain exponent is found to be 2, but for starting grain size of 60 μm it becomes 3 [148].

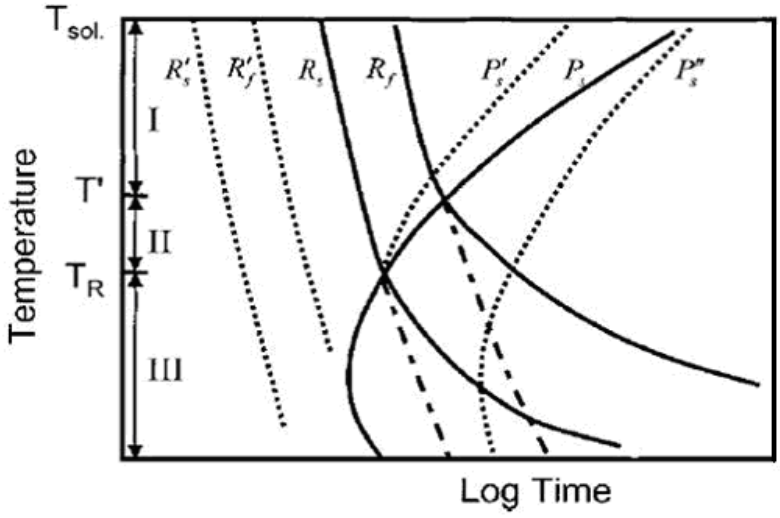

Figure 3.11. Schematic recrystallisation-precipitation diagram [134]. T_{sol} refers to the solution temperature above which Nb-rich precipitates are completely dissolved in the austenite matrix, T' is the temperature below which recrystallisation and precipitation compete and T_R is the temperature below which precipitation occurs prior to recrystallisation. R_s and R_f refer to the start and finish of recrystallisation in HSLA steels. R_s' and R_f' refer to the start and finish of recrystallisation in plain carbon steels. P_s' and P_s'' refer to the predicted precipitation start times in deformed and undeformed austenite respectively. P_s is the experimentally determined precipitation start time.

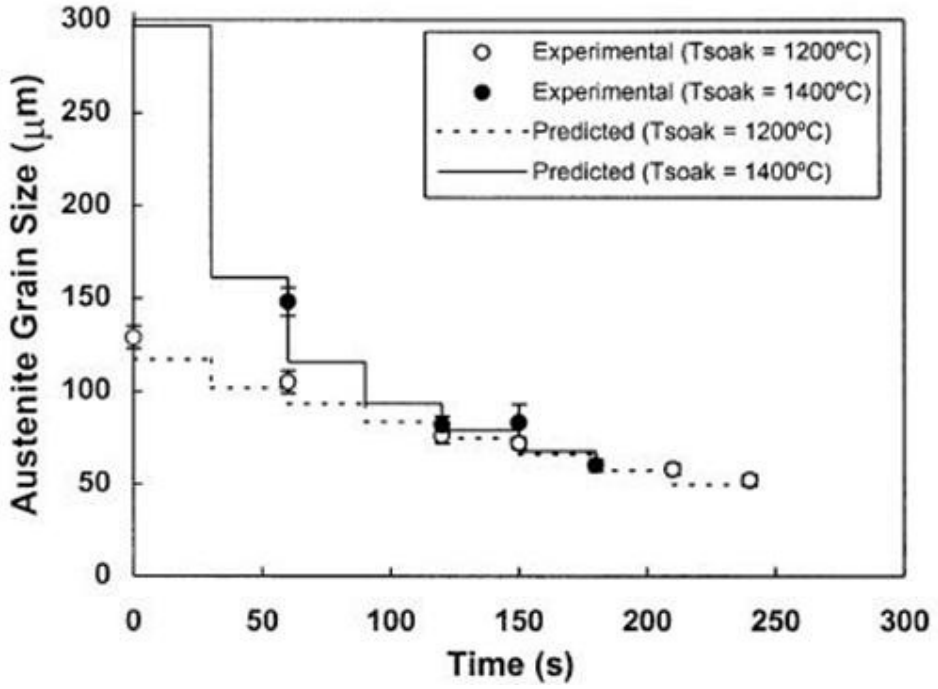

Figure 3.12. Comparison between predicted and experimental data for the evolution of the austenite grain size during multipass deformation (ε=20 %, $\dot{\varepsilon}$=1 s^{-1}, t_{ip}=30 s) after different reheating conditions (*T*soak=1200 and 1400°C) [132].

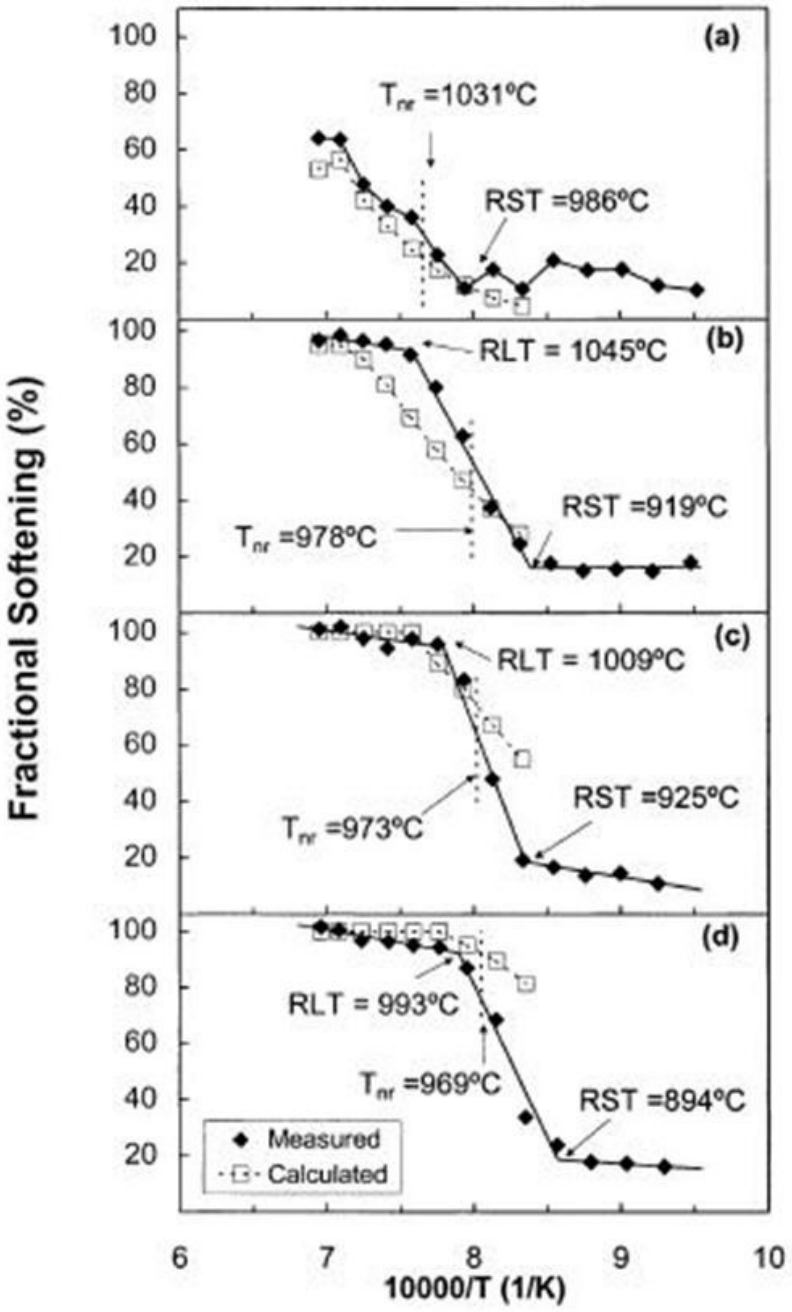

Figure 3.13. Comparison between the measured fractional softening and the values predicted by the recrystallisation model plotted against the mean interpass temperature for soak at 1200 °C and pass-strains of: a) ε=10 %, b) ε=20 %, c) ε=30 %, d) ε=40 % [132].

3.6 Objectives of the present study

The aim of the work is to investigate the development of the grain size distribution during processing (casting, reheating and deformation) in Nb containing microalloyed steels, taking into account segregation. To achieve this the following objectives were defined:

1. To quantify the amount of segregated material present in the as-cast slab of 0.045 wt % Nb steel. To include predicting and experimentally verifying the levels of segregation of microalloying elements, mainly Nb, in Nb bearing microalloyed steel. To use the amount of segregated material present in the as-cast condition to determine the grain size distribution of solute rich and solute-depleted regions after reheating.

2. To examine the limits of validity of the Dutta-Sellars model on quantifying the amount of recrystallisation at 0.3 strain for a range of starting grain sizes using the literature and experimentally generated data in Nb containing steels. To predict the grain size distribution after deformation in homogenised condition (with respect to Nb). To extend the approach to take into account Nb segregation and starting bimodal grain size distribution.

3. To study the effect of Nb content on recrystallisation kinetics in a homogenised 0.094 wt % Nb steel using literature data and experimentally generated data and to quantify the effect of strain induced precipitates on recrystallisation kinetics.

4. To study the effect of strain on recrystallisation kinetics in homogenised 0.045 and 0.094 wt % Nb steels using literature data and experimentally generated data and to quantify the effect of strain induced precipitates on recrystallisation kinetics as a function of strain.

5. To determine if there is an alternative microalloying element that can be used for grain boundary pinning during reheating compared to Nb, which is known to segregate and can result in bimodal grain size development.

CHAPTER – 4

Materials and Experimental Techniques

4.1 Material

An as-continuously cast (290 mm thick and 1800 mm wide) low-carbon microalloyed steel slab and two ingot casts of 130 mm thickness and 340 mm width with high Nb and high Al content were provided by Tata Steel, UK. The cast chemical compositions are given in Table 4.1.

4.2 Heat treatment of as-cast slabs

Two different heat treatments were given to the as-cast samples: a) homogenising treatment and b) re-heating treatment.

4.2.1 Homogenising treatment

Specimens of size 10 x 15 x 20 mm (machined from the ¼ thickness position of Slab 1 and High Nb in the as-cast condition) were homogenised at 1225 ºC for 4 days under vacuum and slowly cooled at a rate of 3 ºC/min. Homogenisation was carried out to remove microsegregation of Nb.

4.2.2 Re-heating treatment

Following homogenisation, specimens of Slab 1 and High Nb were sealed inside silica tubing under a partial Ar atmosphere and re-heated to 1225 ^{o}C, soaked for 1 hour and then quenched (tube intact) into water to represent a commercial re-heating temperature and time; quenching was used to preserve the Nb in solution prior to deformation trials.

Re-heat treatments on the as-cast samples were designed to investigate the stability of precipitates such as Nb(C,N) and AlN and the grain size distribution development in the

presence of segregation. Specimens of size 10 x 15 x 20 mm were machined from the ¼ thickness position of the as-cast slab. These were encapsulated inside silica tube under a partial Ar atmosphere and re-heated, at a rate of 3 ^{o}C/min, held for the required time then quenched into water with the silica tube intact. Re-heat temperatures and holding time on different as-cast samples were selected based on Thermo-Calc predicted precipitate stability temperatures:

- Slab 1 samples were re-heated to either 1225 ^{o}C or 1150 ^{o}C and soaked for 1 hour.
- High Al samples were reheated 1150 ^{o}C, soaked for 1 hour and 1125 ^{o}C for 1, 2 and 8 hours.

4.3 Deformation simulations on homogenised and re-heated specimens

The homogenised, re-heated and quenched specimens were subjected to single hit plane strain compressive deformation in a Gleeble 3500 (Dynamic Systems, Inc, Poestenkill NY, USA) thermo-mechanical simulator using Quicksim software. Within the Gleeble 3500, the specimens were rapidly re-heated (10 ^{o}C/s) to their original re-heat temperatures (e.g. 1225 ^{o}C), soaked for 5 minutes and then cooled to a range of deformation temperatures (T_d) selected following calculations based on the Dutta-Sellars model [98, 155], at a rate of 100 ^{o}C/s. 1 hour reheating in the furnace was carried out before reheating the samples within the Gleeble simulator as holding for an hour in the Gleeble simulator has been found to result in aborted thermal cycles due to thermocouple failure. Using tungsten carbide plane strain anvils, shown in Figure 4.1, the specimens were compressed at a high strain rate, $\dot{\varepsilon}$ = 10/s, to a range of strains (ε) from 0.15 to 0.45, held there for a range of times (t_h), between 4 - 10 s and then cooled by water sprays. The heating rate, cooling rate, strain, strain rate and holding period used in the present

investigation are typical of passes in multi-pass commercial plate rolling [88, 134]. Although a high strain rate was used, the temperature profile noted in the Gleeble during deformation and holding was constant (within experimental scatter of ± 2 ^{o}C). This suggests that the high deformation temperatures used and thermal conductivity at these temperatures give little effect of adiabatic heating. The water quenching avoided the formation of ferrite and gave fully bainitic / martensitic structures from which the prior austenite grain size and shape could be determined. Graphite and tantalum foils were used to separate the anvils from the sample. The thermo-mechanical schedules are summarised in Figure 4.2 (a) and (b) and Table 4.2.

4.4 Microstructural Characterisation

4.4.1. Sample preparation

Longitudinal sections were cut from the sub-surface, ¼ thickness and ½ thickness positions of the as-cast slabs (to allow observation of the plane normal to the casting direction) along with longitudinal sections of homogenised, re-heated and deformed samples. The equivalent plane was observed in specimens after reheating and deformation. In the deformed samples this involved sectioning mid-length and examining the deformed area, Figure 4.1, that had previously been shown to have uniform deformation [14]. The specimens were mounted in Bakelite and then metallographically polished to a 0.05 μm SiO_2 finish. Metallographically polished specimens were etched with 2 % nital solution (2 ml conc. HNO_3 in 98 ml ethanol). Etching the polished surface in a saturated aqueous picric acid solution at 60 ºC revealed the prior austenite grain structures of re-heated and deformed samples. To reveal solidification structures, the polished samples of High Nb were etched with diluted picric acid solution (1 gm picric acid in 200 ml ethanol + 1 ml HCl+ 0.5 gm $CuCl_2$+ 1 ml Teepol).

4.4.2 Image analysis

The as-cast, heat treated and deformed specimens were examined in a Leica DMRX microscope equipped with KS300 image capture and analysis software. Quantitative determination of austenite and ferrite grain size in terms of equivalent circle diameter (ECD), fraction of second phases (pearlite, bainite, degenerate pearlite), secondary dendritic arm spacing (SDAS), coarse particle and inclusion distributions was carried out using the image analysis software. The as-polished specimens of Slab 1, High Nb and High Al were examined using KS300 image analysis system to quantify the coarse, i.e., optically resolvable, TiN and MnS particle size and number density distributions. Five through thickness traces at equidistant intervals along the specimen length were examined totalling an area of approximately 10 mm^2. The coarse TiN particle size was measured in terms of side length, side width and particle area. The secondary dendritic arm spacing were determined by measuring the centre to centre distance of the second phases after taking 60 continuous fields of view and merging them into a montage. About 2000 grains were measured in terms of individual grain area and ECD (obtained directly from KS300 software) on the as-cast, re-heated and deformed samples to construct grain size distributions.

Deformed and unrecrystallised grains will be elongated and so ECD is not strictly valid. However, the use of plane strain compression means that grain area is constant after recrystallisation and so ECD can be used to compare unrecrystallised and recrystallised grains. Standard stereological correction factors apply to unimodal (normal) distributions of equiaxed grains, but, in this study, a mixture of equiaxed (recrystallised, aspect ratio 0.8-1) and elongated (unrecrystallised, aspect ratio 0.2-0.3) grains will be present and so these factors have not been applied.

4.4.3 Scanning Electron Microscopy (SEM)

The compositions of the coarse particles (TiN and MnS) were determined using a JEOL 7000 scanning electron microscope (SEM) operating at 20 kV and equipped with an Oxford INCA energy dispersive X-ray spectroscopy (EDS) system. Precipitates in the as-cast slabs were characterised using the JEOL7000 SEM fitted with a field emission gun (FEG) to resolve fine particles (< 50 nm). The number density and area fraction of precipitates resolvable in the SEM (> 20 nm) were measured over 50 continuous fields of view (each field of view covers ~ 12 μm^2 area). The particle composition was determined using the Oxford INCA EDS system for an SEM operating voltage of 10-20 kV and 10 mm working distance. A dead time of 20 % at an acquisition rate > 2 kcps (160 s acquisition time) was used for EDS analysis. For elemental analysis of precipitates the EDS spectrum collected from the precipitate was compared against the EDS spectrum from the matrix. From the EDS spectra the characteristic peaks were identified both manually using the 'confirm elements' option and automatically using the 'Auto ID' option [181]. The elemental concentrations were directly obtained from the 'quantify spectra' option available in the INCA software. Generally K_α lines were used for identification. Some times L_α peaks were also used for identifying elements such as Nb. XPP correction method was used to calculate the matrix correction term [181].

EDS area analyses were carried out in a JEOL 7000 SEM to determine the spatial variation of Nb, Al, Ti and V in as-cast slab at an accelerating voltage 10 kV (the lower voltage was used in order to decrease the interaction volume) over ~ 8000 μm^2 area using spot area of 100 μm^2. A pure Co foil was used to standardise the counts while carrying out EDS analysis in as-cast slab. Measurements were repeated in the same area to check its repeatability. The K (and L for Nb) characteristic X ray lines were used for quantitative analysis.

4.4.4 Transmission Electron Microscopy (TEM)

4.4.4.1 Preparation of thin foil samples

Slices, approximately 0.75 - 1 mm thick, were sectioned from the heat treated or deformed samples using an Accutom 5, and then discs of 3 mm diameter were either punched from slices ground to 120 - 130 μm thickness or trepanned by electro-discharge machining and then thinned by hand grinding on 400 - 1200 grade SiC papers to a thickness of approximately 100 μm. The discs were electro-polished using a twin jet electro polisher (Struers Tenupol 3) containing a polishing solution of 10 % (by volume) perchloric acid and 90 % acetic acid at room temperature. The optimum polishing conditions were a closed circuit potential of 30 - 35 V; a current of 150 - 200 mA; and a flow rate varying between 6.8 and 7.5.

4.4.4.2 TEM examination

The foils were examined in a Tecnai F20 equipped with Oxford INCA EDS systems respectively. At least two foils for each sample were examined to identify the precipitates. The precipitates were identified by selected area diffraction pattern (SADP) analysis. The $<001>_{\alpha}$ (Figure 4.3) zone axis as discussed in section 3.2.7 in the literature review was used to identify the precipitates as there is an orientation relationship between the forming particles and the austenite matrix [12, 140, 141], and then with the martensitic structure after quenching due to the austenite-martensite relationship [12, 146]. The compositions of the precipitates were determined by EDS. Precipitate sizes were determined using the KS 300 software after analysing the TEM images. Volume fractions of the precipitates were quantified after determining the foil thickness using a convergent beam diffraction technique [182] over 50 continuous fields of view (each field of view covers ~ 0.01 μm^2 area). The foil thickness was measured to be in the

range 85 - 125 nm. The number of particles collected to measure the volume fraction ranged between 60 - 400 in each condition.

4.5 X-ray diffraction (XRD)

Slices of approximately 5 mm thickness from Slab 1 in the homogenised and re-heated condition were examined in a Philips PW4000 X-ray diffractometer with the X'pert system. Bcc phase peaks (110), (200), (211), (220), (310) and (321) (Figure 4.4) occurring at 2θ values of 44.5°, 65.1°, 82.4°, 99°, 116.5° and 137.1° for the incident X-radiation wave length, λ, of 0.15406 nm (Cu Kα) were examined using a slow scan rate (0.02 step size and 1 s counting time) for 2θ value between 10° and 140°.

The lattice parameter, a, for the bcc phase was determined from the 2θ values of the indexed peaks and the individual a values plotted against $\cos^2\theta / \lambda$. Accurate lattice parameters were determined by extrapolation back to the value of a at $\cos\theta = 0$, Figure 4.5. Accurate estimation of lattice parameter is required to index SADP.

4.6 Thermodynamic prediction using Thermo-Calc

Thermo-Calc software (version Q) from the Royal Institute of Technology, Stockholm, Sweden was used in DOS mode for the theoretical prediction of solidification sequence, phase fractions (including precipitates) and compositions under equilibrium condition. All the alloying elements shown in Table 4.1 were considered as input (along with temperature and pressure) for the predictions. Predictions were made over the temperature range 1600 ºC to 500 ºC. In the present study Thermo-Calc software was also used to predict various metallurgical phenomena, such as, solidification sequence during casting, partitioning of elements within solid and liquid phases during solidification, precipitation sequence and stability of precipitates. Predicted compositions of first-formed δ ferrite, last solidifying liquid and experimentally determined compositions from segregated and non-segregated regions

were input into Thermo-Calc software to understand the role of segregation on the stability of microalloy precipitates.

Tables and Figures

Table 4.1: Chemical compositions (wt %) of the as-cast materials.

Element	Slab1	High Nb	High Al
C	0.1	0.041	0.1
Si	0.31	0.16	0.29
Mn	1.42	1.29	1.42
P	0.017	0.011	0.018
S	0.005	0.0013	0.004
Cr	-	0.26	0.01
Mo	-	0.005	0.005
Ni	0.32	0.16	0.32
Cu	-	0.25	-
Al	0.046	-	0.057
N	0.008	0.008	0.008
Nb	0.045	0.094	0.019
Ti	0.002	0.011	0.001
V	0.052	0.001	0.052

Table 4.2. Summary of the deformation simulation parameters used.

Material	Re-heat Temperature (^{o}C)	Deformation Temperature (^{o}C)	Strain	Time (Sec)
Slab1 (homogenised)	1225	1125	0.15, 0.225	10
		1075	0.15, 0.3, 0.45	10, 4
		1050, 1025	0.15, 0.225, 0.3, 0.375, 0.45	10
		1050, 1025, 1010, 990	0.15, 0.3, 0.45	4, 6, 8, 10
		1010	0.3	10
		990	0.3, 0.375, 0.45	6, 8,10
		975	0.3, 0.45	10
High Nb (homogenised)	1225	1125, 1090	0.15, 0.225, 0.3, 0.375, 0.45	10
		1125, 1090, 1075	0.15, 0.3, 0.45	4, 6, 8, 10
		1075, 1050	0.3, 0.45	10
Slab1	1225	1025, 975, 925, 880	0.3	10
	1150	990, 950, 910, 870	0.3	10

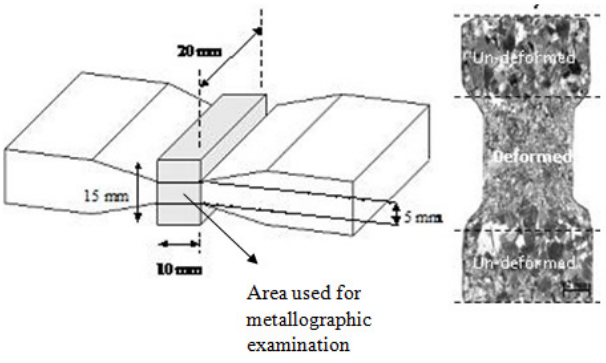

Figure 4.1. Schematic diagram of plane strain compression set-up in Gleeble 3500 showing the area used for metallographic examination in the deformed sample and macro-view of post-tested sample showing deformed and undeformed regions.

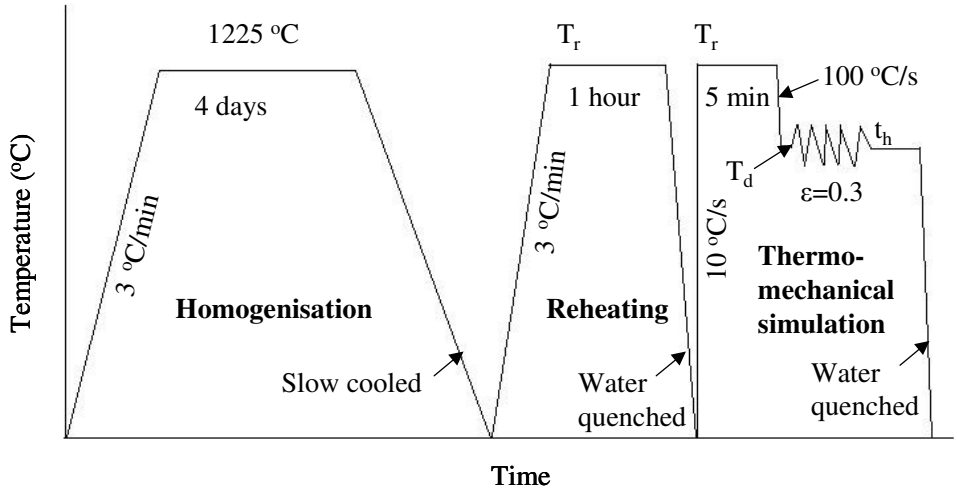

a

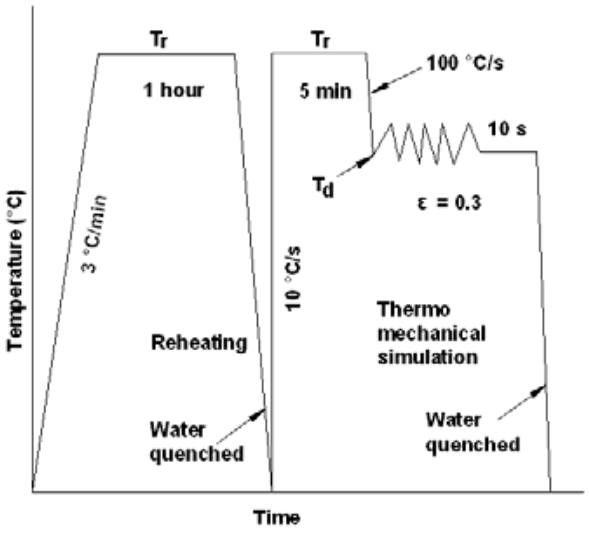

b

Figure 4.2. Schematic diagram showing the heat treatment and deformation schedules carried out on (a) homogenised and reheated samples (b) reheated samples in this study. T_r and T_d in the diagram refers to the re-heat and deformation temperatures and t_h refers to the holding time in s after deformation.

Figure 4.3. Selected area diffraction pattern of $<001>_{\alpha}$.

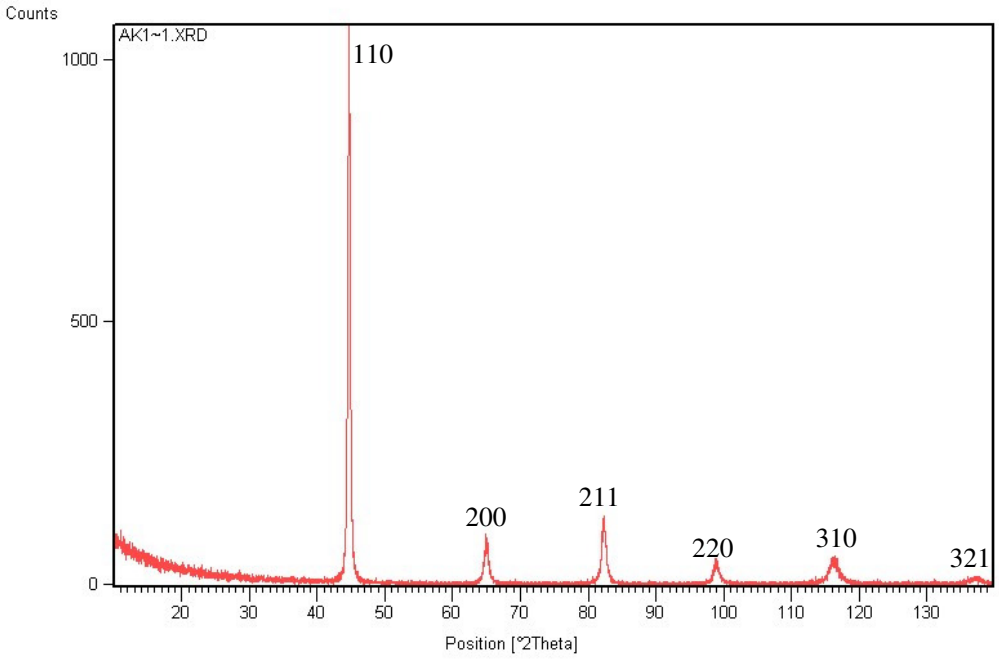

Figure 4.4. XRD result showing the peaks corresponding to the bcc phase.

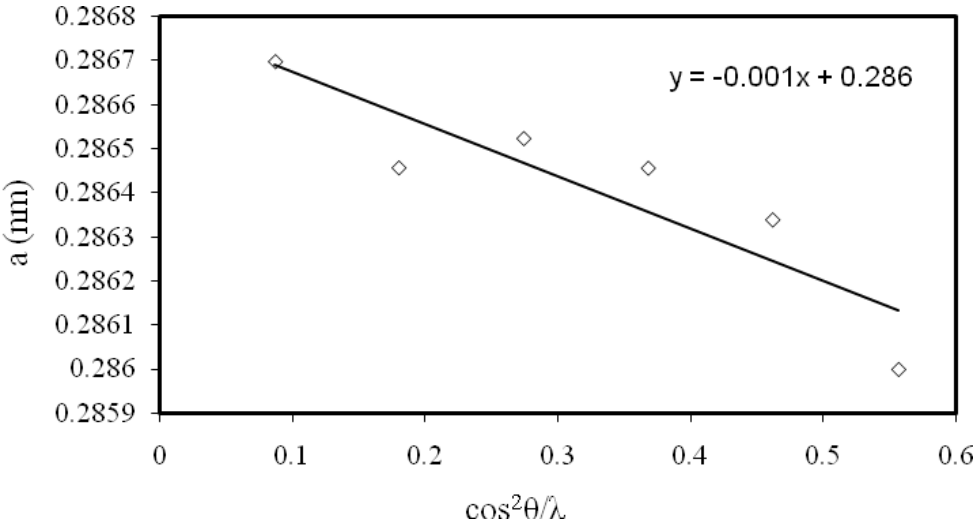

Figure 4.5. Graph showing the extrapolation to determine the accurate lattice parameter, a, for Slab 1 from the lattice parameters values determined from the 2θ values for the peaks shown in Figure 4.3.

CHAPTER – 5

Microstructures of as-cast, reheated and homogenised slab: Prediction and quantification of microsegregation

Microsegregation of microalloying elements, such as, Nb will lead to local variations in the response of the slab to reheating and rolling influencing the scatter in final plate mechanical properties [7, 14, 19, 22, 23, 43]. Accurate prediction of the solidification sequence or, in other words, quantification of the solute-rich and solute-depleted fractions is essential to determine the subsequent microstructural development. For a number of continuously cast slabs, it has been shown that the centre-line composition arising from macrosegregation can be predicted by equilibrium thermodynamics (although not for slabs from all types of caster) [34]. In all cases studied, however, 80 % of the slab thickness solidified as the bulk composition and equilibrium thermodynamics applied to the liquid and solid compositions in that region [34]. Hence, for those areas, microsegregation can be predicted using the bulk composition as a starting point.

This chapter describes the applicability of equilibrium thermodynamics to predict the amount of microsegregation and relate that to the proportion of second phase present in the interdendritic regions in Slab 1 (0.045 wt % Nb steel) in the as-cast condition and then the microstructures and grain size distribution that develops after reheating and homogenisation of the slab.

5.1 Solidification sequence predicted by Thermo-Calc: Prediction and quantification of microsegregation in Slab 1

The solidification sequence was predicted, based on the bulk composition, using Thermo-Calc software, Figure 5.1 with the variations in equilibrium C and Nb content

between the three phases i.e. liquid, δ ferrite and austenite as a function of temperature given in Figure 5.2. The composition of first solid δ last liquid and austenite (γ) predicted by using Thermo-Calc is listed in Table 5.1. Equilibrium solidification is predicted to start at 1516 ^{o}C as δ ferrite. The first solidified δ would be depleted in solute. The remaining liquid in the interdendritic regions would be gradually enriched in solute. δ ferrite will continue to form dendritically until the start of the peritectic reaction at around 1485 °C. Dendritic growth would proceed as shown schematically in Figure 2.3 (d) [27, 30] until the remaining liquid had saturated in solute. This should correspond to the δ / liquid phase balance at 1485 °C, but that is based on Nb redistribution by solid-state diffusion through the dendritic δ-ferrite, Figure 5.2. That diffusion process is very slow leading to little variation in Nb content through the dendrites, whereas stirring in the liquid allows more complete solute redistribution [27, 30]. The dendrites will continue forming until mass balance is achieved between the solute-enriched liquid and the solute-depleted dendrites. The solute-enriched liquid will approach its maximum solute level - that of the last liquid, whilst the dendrites are close to the composition of the first δ to form.

The peritectic transformation in Slab 1 is not predicted to go to completion, but would leave some liquid (4.2 %) to solidify directly as γ, Table 5.2. The volume fraction of liquid (L), δ and γ as a function of solidification temperatures were predicted using Thermo-Calc predicted mass fraction of the phases present at each temperatures. There is predicted (Table 5.2) to be a large volume fraction of dendritic δ formed prior to the peritectic reaction. Using the composition of δ and last liquid (predicted from Thermo-Calc, Table 5.1) gives a solute-rich volume fraction between 0.24 (based on C levels) and 0.25 (based on Nb levels).

5.2 As-cast microstructure

The as-cast microstructure at the slab quarter thickness position consists of ferrite (α) in a dendritic morphology and interdendritic pearlite; the area fraction of pearlite is 0.19 ± 0.06, Figure 5.3. The mean pearlite colony spacing, which corresponds to the secondary dendrite arm spacing, was ~ 200 - 250 μm.

The α present in the dendritic regions is expected to be solute depleted [22, 23, 34] as, during the start of solidification, the first dendrites to form are solute depleted δ (*k* values for most solute elements > 0, Table 5.1). The remaining liquid in the interdendritic region would be solute enriched. On further cooling, i.e. at temperature below 1486 °C austenite (γ) would start nucleating at the δ / liquid interfaces, i.e. in the interdendritic regions when liquid and δ will undergo a peritectic reaction and where the higher solute content for elements such as C favours γ formation. Once nucleated the γ grains will grow in the direction parallel to the direction of maximum thermal gradient [27, 30].

Upon further cooling γ would transform to proeutectoid ferrite (α) with nucleation occurring at γ / γ grain boundaries in regions of low C content. The transformation starts at 950 °C. As a result, α would form initially in the solute-depleted regions from solidification, i.e. the dendrite centres. Growth of α would be expected to slow and then cease as the solute-enriched regions were encountered. C rejection from the growing α would contribute to the effects of solute enrichment slowing α formation until the edges of the solute-rich regions transform to pearlite. The centres of the solute-rich regions will not be as enriched in C rejected from the growing α as the edges and would still contain potential α nucleation sites, such as MnS inclusions. The number density of the MnS at the quarter thickness position is 40-70 / mm^2.

Thus, at a lower temperature than that at which the solute-depleted dendritic regions transformed, pro-eutectoid ferrite idiomorphs can form in the interdendritic (solute-enriched) regions, Figure 5.3. Second phase (pearlite) colonies would form at the dendrite – interdendritic interface (highest C level due to rejection from dendritic α and grow until impingement with each other and the α idiomorphs [1]. The pearlite colonies may, therefore, contain some α idiomorphs between them. In order to quantify the solute-rich fraction accurately, the area fraction of pearlite and the area fraction of the interdendritic α idiomorphs were considered. This combined area fraction of second phases present at the quarter thickness position was 0.26 ± 0.06. This agrees well with the Thermo-Calc predicted solute-rich volume fraction using the composition of δ and last liquid. The amount of segregated material quantified here will be used to model grain size distribution during deformation of the same steel slab in presence of segregation will be discussed in Chapter 8.

5.3 Variation of solute along the slab thickness

EDS area analyses for Nb, Al and Ti were carried out across regions containing both dendritic and interdendritic material. One example is shown in Figure 5.4, indicating that the analyses include dendritic α, second phase (pearlite) and interdendritic α idiomorphs, Figure 5.4 (a). The corresponding elemental variation across the dendritic arm spacings, Figure 5.4 (b), indicates a steep rise in both the Nb and Ti contents on crossing from dendritic α to the second phase. Within the dendrite arms the profiles for Ti and Nb are very level, albeit at low values. There is more apparent scatter through the interdendritic region, although the higher solute contents would make this more obvious. Importantly, however, there was no decrease in Nb and Ti level (beyond the average scatter) seen when an α idiomorph was sampled compared with the surrounding second phase. The similarity

in the composition of the α idiomorphs and the pearlite colony indicates that the idiomorphs are formed in the interdendritic regions and that the assumption to take into account the α present in the interdendritic region when quantifying the fraction of solute-rich material is valid. The local Nb content in the dendritic and interdendritic centre regions lie within the range obtained by Couch [44] using LA-ICP-MS and Chakrabarti [14, 43] using SEM EDS for the same Nb containing steel (i.e. 0.045 wt % Nb).

The average Nb content in the solute-depleted region (dendritic α) is 0.0095 wt % compared with a predicted value of 0.0096 wt %, Table 5.1. However, the value of Nb in the interdendritic regions was only 0.095 wt % and not the predicted 0.15 wt %, which resulted in the partition ratio of only 10.02 (15.7 predicted). Chakrabarti [14] and Couch [44] have also found measured partition ratio of Nb is less than the predicted partition ration using Thermo-Calc, discussed in section 2.2.2.3 in Chapter 2.

There are several reasons for the discrepancy in values. Experimental results will be an average for the measurement area used whereas the Thermo-Calc data will be the maximum segregation level for the very final liquid to solidify, therefore the experimental results will show values lower than the theoretical maximum due to the averaging effect. The profile for Al indicates that back diffusion is also likely to play a role in this slab. The absolute values of Al content recorded were too low compared with the predicted values using Thermo-Calc (0.041 and 0.028) although the partition ratio recorded of 0.69 was in reasonable agreement with that predicted (0.7). As before, the low levels of Ti and V present mean that the SEM-EDS results are likely to be prone to errors in their absolute values, but the experimentally determined partition ratios of 7.48 (Ti) and 1.48 (V) are similar, but smaller than, those predicted from equilibrium thermodynamics (9.56 and 1.72) for δ / liquid.

5.4 Reheated microstructure

After continuous casting the next stage is reheating. The reheating process is designed to take microalloying elements, particularly V and Nb, back into solution for subsequent re-precipitation during or immediately following rolling. Chakrabarti [14] reported Thermo-Calc predicted stability temperatures of (Nb,Ti,V)(C,N) in the solute-rich and solute-depleted regions (Figure 2.23, Section 2.7.5) in a steel with same composition as Slab 1. The reheat temperatures were selected based on the Thermo-Calc predicted stability temperatures of (Nb,Ti,V)(C,N) in the solute-rich and solute-depleted regions (Figure 2.23, Section 2.7.5, [14]). Commercial reheating usually carried out in the temperature range 1100-1200 ^{o}C [1, 12, 13, 17, 23]. In the present study the as-cast Slab 1 was reheated to 1225 and 1150 ^{o}C. Reheating at 1225 ^{o}C would lead to complete dissolution of (Nb,Ti,V)(C,N) in both solute-rich and solute-depleted regions leading to growth in both the regions. Therefore, a coarse unimodal grain structure is expected. Thermo-Calc predicts, for 0.045 wt % Nb steel the dissolution of (Nb,Ti,V)(C,N) in the solute-depleted regions at 1090 ^{o}C. Reheating to 1150 ^{o}C would lead to grain growth in the solute-depleted regions but in the solute-rich regions grains should be pinned by the undissolved (Nb,Ti,V)(C,N) particles. This would lead to formation of bimodal grain structure.

A coarse unimodal austenite grain structure with a mode grain size of ~ 160 - 180 μm is developed after reheating at 1225 ^{o}C (Figure 5.5 a and b). Reheating at 1150 ^{o}C gives rise to significant bimodality in the austenite grain structure with an average size of ~ 220 μm in the coarser region and ~ 41 μm in the finer area (Figure 5.6 a and b). The bimodal grain size distribution is due to dissolution of (Nb,Ti,V)(C,N) precipitates in the solute-depleted regions resulting in grain growth in these regions, whereas the grains in the

solute-rich regions are still pinned by (Nb,Ti,V)(C,N) particles, where the distance between two fine grained regions is 250 µm; this has been reported previously [14].

The mode grain size after reheating and available Nb content in solution are required to model recrystallisation and precipitation kinetics using Dutta-Sellars equations [98, 155, 156] to select the deformation temperatures, will be discussed in Chapter 8.

5.5 Homogenised microstructures

To determine how well the Dutta-Sellars equations [98, 155, 156] predict recrystallisation and precipitation in the Nb-bearing steel used in this study the as-cast material was homogenised to generate a uniform Nb solute distribution and unimodal grain structure. The spacing between interdendritic regions in the as-cast slab has been measured as ~ 200-250 µm at the quarter thickness position so that Nb atoms would need to diffuse over a distance of 100-125 µm to reach the dendrite centres thereby approaching a uniform composition. The time predicted, using equation (5.1), Figure 5.7, for Nb atoms to diffuse 100 µm is around 2 - 3 days at 1225 °C.

$$x=(Dt)^{1/2} \quad (5.1)$$

where, x is the diffusion distance, D is the diffusivity of Nb in austenite and t is the time [71, 73].

Samples of the as-cast slab were homogenised at 1225 °C for 4 days leading to a coarse mode grain size of 280 µm and a unimodal grain size distribution, Figure 5.8, albeit skewed to larger grain sizes. Nb levels determined by EDS for homogenised and as-cast samples are shown in Figure 5.9. It can be seen from comparing Figure 5.9 with Figure 5.4 that, while in the as-cast sample, there is a periodic variation in the Nb level, with up to 10 times as much Nb in the interdendritic area, compared with the dendritic areas (Figure

5.4b), there is no systematic variation in the Nb level in homogenised sample (Figure 5.4b). The mode grain size after homogenisation has been used to model Dutta-Sellars equations [98, 155, 156] to select deformation temperatures and will be discussed in Chapter 6.

5.6 Conclusions and Further Work

Composition line profiles (SEM-EDS) through secondary dendrite arms and the intervening interdendritic regions were flat through the two regions for Nb, Ti and V undergoing steep changes between them. For these elements the degree of back diffusion was limited, but was more apparent for Al. α idiomorphs formed in the interdendritic regions with the higher levels of Nb, Ti and V associated with those solute-rich regions.

The slabs in this study solidified to a large extent as dendritic δ and experimental determination of the composition and extent of solute-rich regions is consistent with isolation of the interdendritic liquid by dendritic δ and isolation of the liquid and dendritic δ by the start of the peritectic reaction. Under these conditions, mass balance under equilibrium thermodynamics could be used to predict the fraction of solute-rich material (second phase and α idiomorphs) along with reasonable estimates of the partition ratio and hence the composition of the solute-rich and solute-depleted regions. This provides a rapid assessment of the likely response of the slabs to reheating and hot rolling processes.

The verification of the simple equilibrium-based model used in this study is for a steel composition and casting parameter. However, the analysis should apply to low carbon steels and so cover most HSLA grades. Future work is needed to investigate the composition ranges and caster type for which this simple analysis may not be valid and for which more complex (e.g. phase field) modelling is needed.

Reheating the same as cast slab to 1225 and 1150 °C for an hour generates unimodal and bimodal prior austenite grain size distribution.

Homogenisation of the as-cast slab takes 4 days at 1225 °C leading to the formation of a coarse unimodal grain distribution with a mode grain size of 280 μm.

Tables and Figures

Table 5.1. Thermo-Calc predicted first solid and last liquid compositions (mass %) and maximum ratios for Slab 1.

Element	First Solid (δ)	Last Liquid	First austenite (γ)	Max. Ratio (δ)	Max. Ratio (γ)
C	0.016	0.36	0.11	22	3.35
Mn	1.01	1.99	1.44	1.96	1.38
Al	0.052	0.036	0.042	0.7	0.851
N	0.0024	0.019	0.01	8.01	1.79
Nb	0.0096	0.15	0.024	15.7	6.29
Ni	0.25	0.38	0.34	1.51	1.11
P	0.0051	0.043	0.0093	8.38	4.62
S	0.00013	0.031	0.0039	231	79.2
Si	0.2	0.45	0.28	2.22	1.59
Ti	0.0006	0.0057	0.0011	9.56	4.90
V	0.041	0.071	0.041	1.72	1.72

Table 5.2. Volume fraction of phases as a function temperature during solidification.

Temperature (^{o}C)	Phase	Volume fraction
1516	L	0.9376
	δ	0.0624
1486	L	0.1387
	δ	0.8613
1485	L	0.125
	δ	0.826
	γ	0.049
1472	L	0.042
	γ	0.958
1469	γ	1.000

Slab 1	L	→	L+δ	→	L+δ + γ	→	L+ γ	→	γ
Temperature (°C)			1516		1485		1472		1469

Figure 5.1. Predicted equilibrium solidification sequence of Slab1.

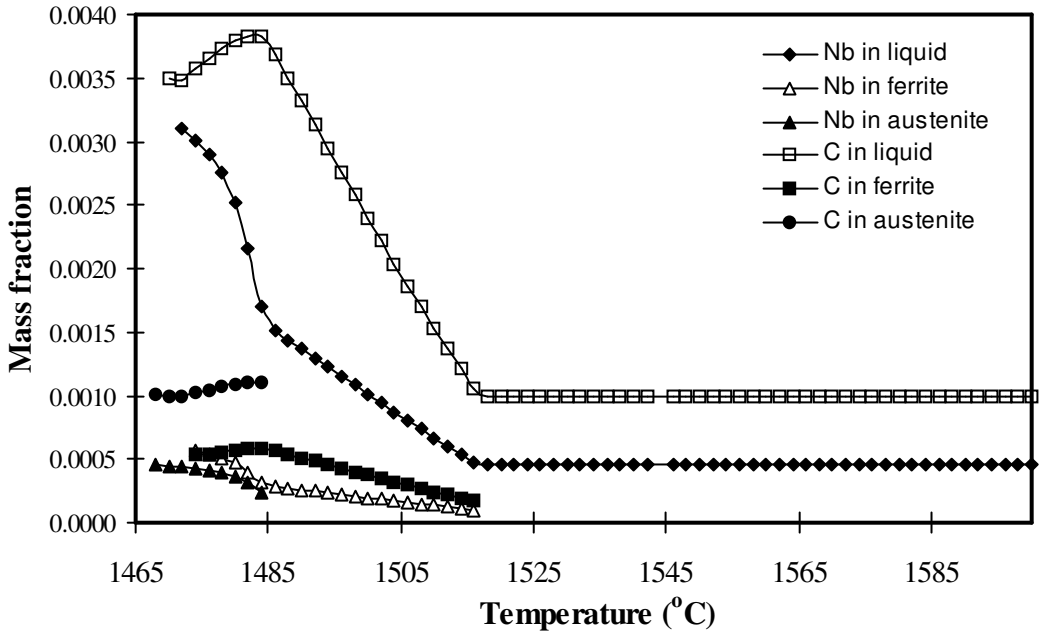

Figure 5.2. Predicted variation of C and Nb in liquid, δ and γ in Slab 1 as a function of temperature.

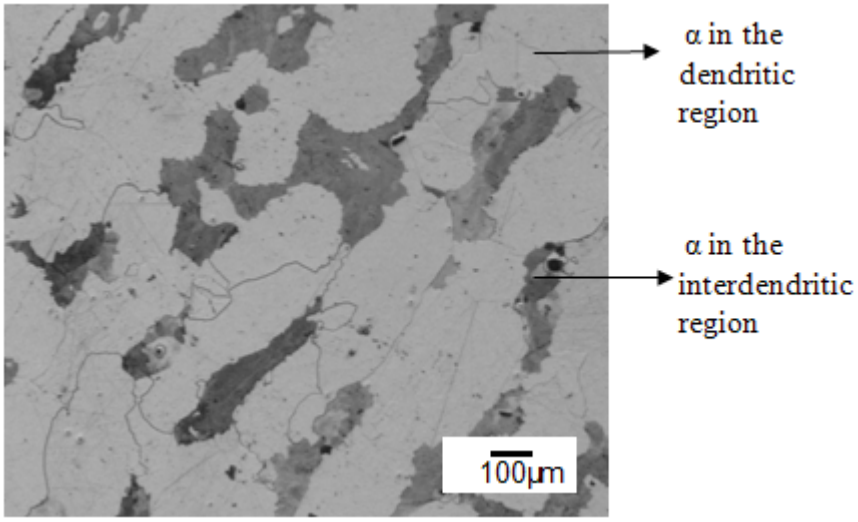

Figure 5.3. Optical microstructure of Slab 1 at quarter thickness position showing ferrite in the dendritic regions (solute-depleted) and pearlite in the interdendritic (solute-rich) regions.

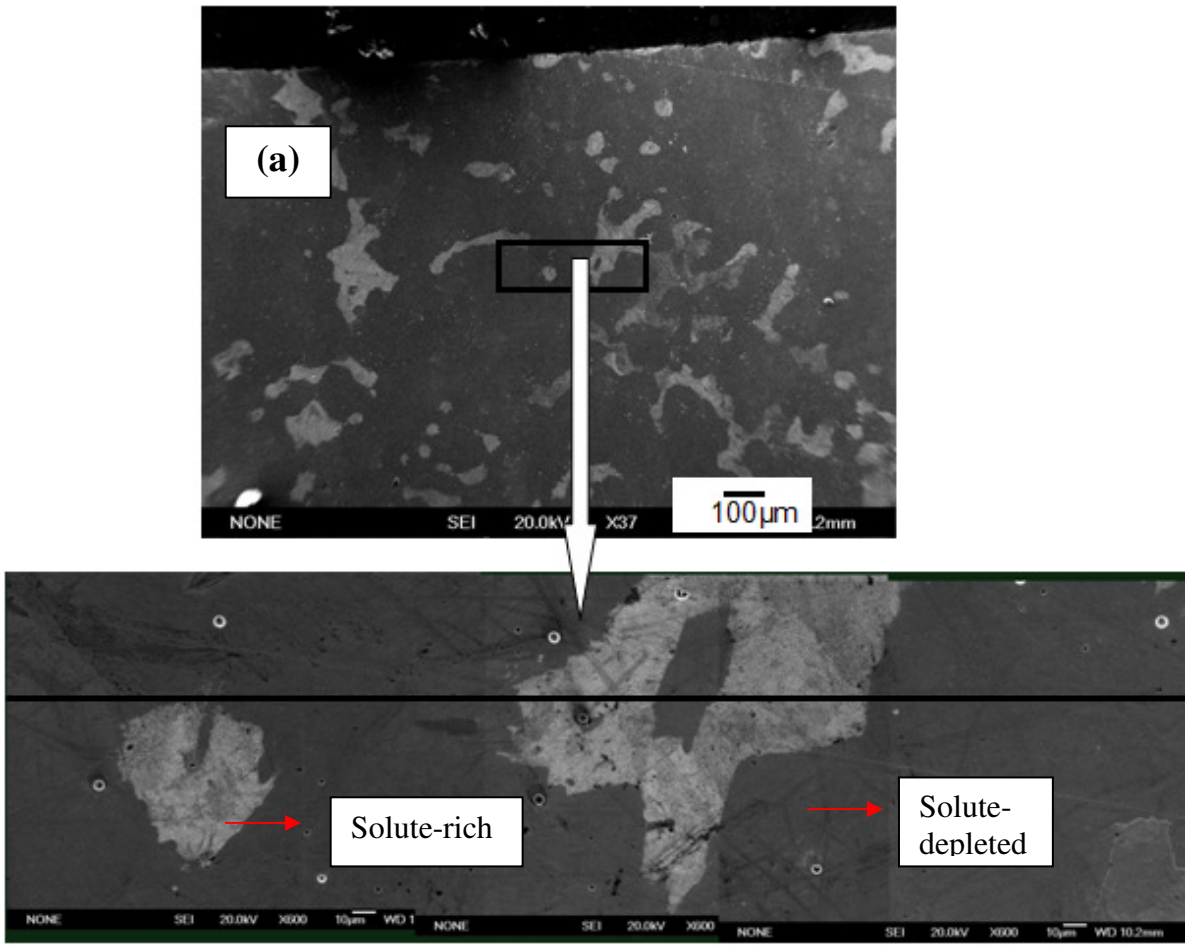

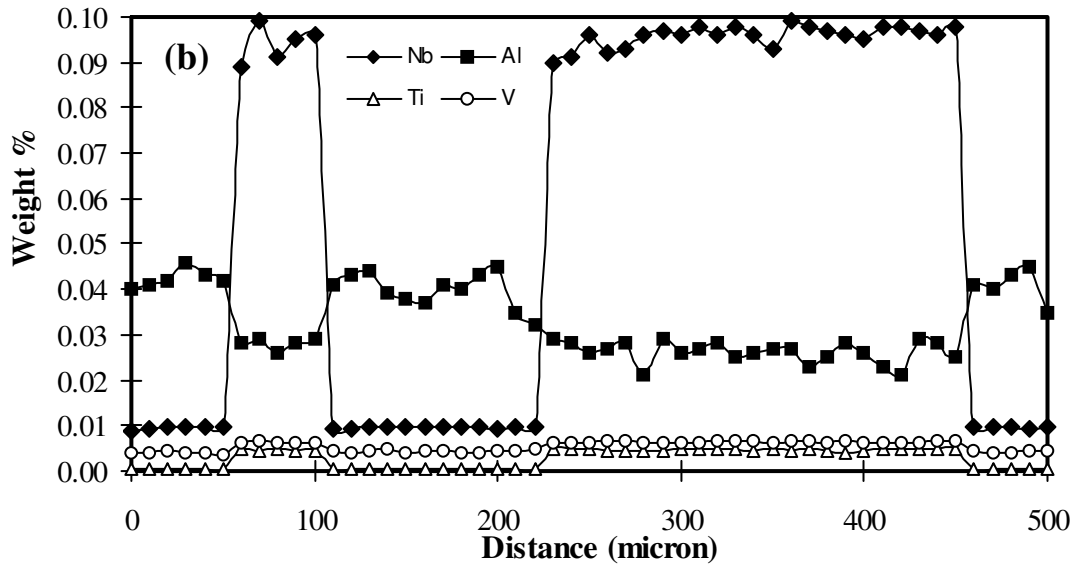

Figure 5.4. (a) SEM images for Slab 1 showing the line along which the EDS traces were taken and (b) EDS traces showing the weight % variation of Nb, Al, Ti and V across the secondary dendrites.

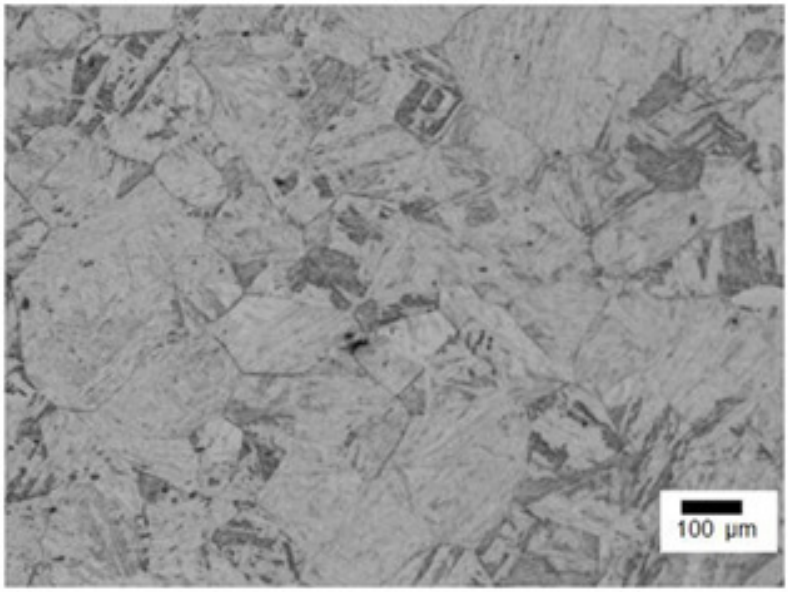

(a)

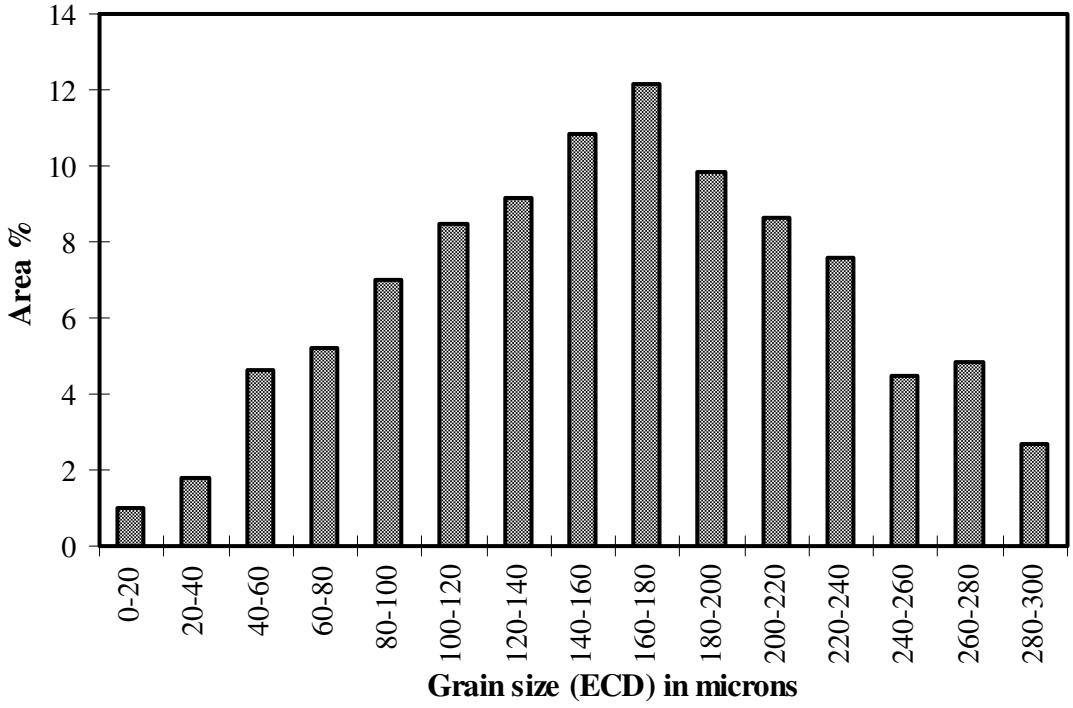

(b)

Figure 5.5. (a) Microstructure (as-quenched) and (b) prior austenite grain size distribution for the segregated Slab 1 sample reheated for 1 hour at 1225 °C.

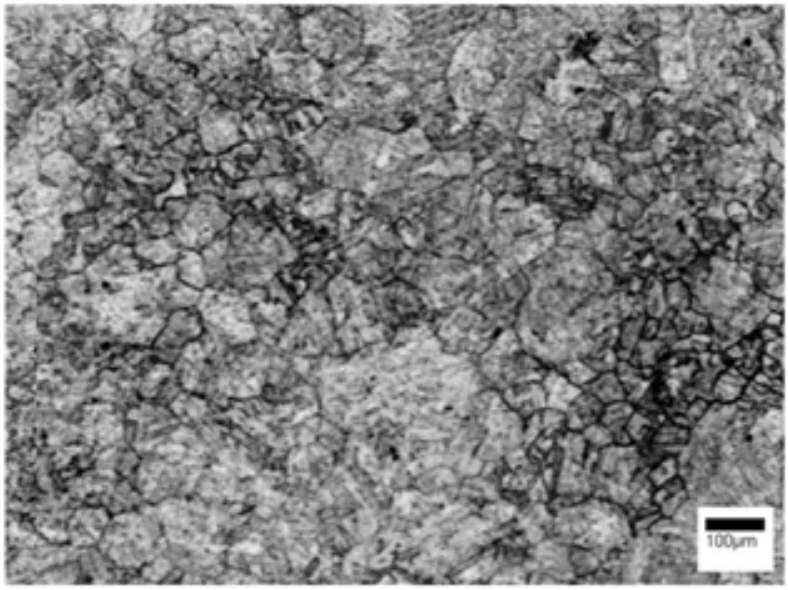

(a)

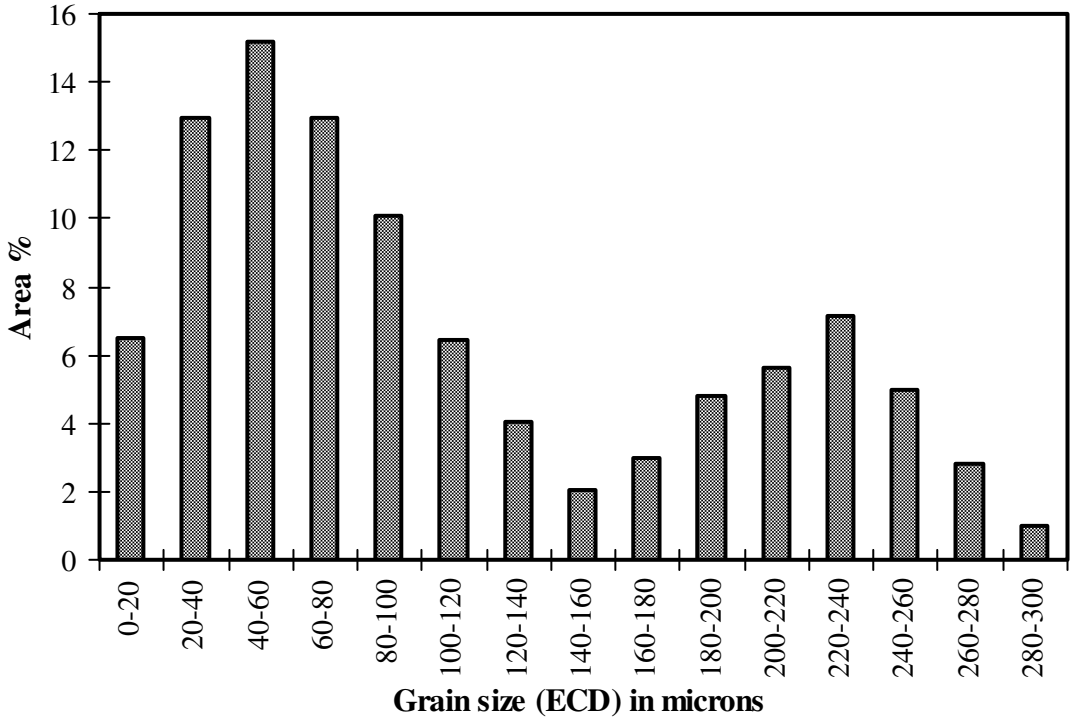

(b)

Figure 5.6. (a) Microstructure (as-quenched) and (b) prior austenite grain size distribution for the segregated Slab 1 sample reheated for 1 hour at 1150 °C.

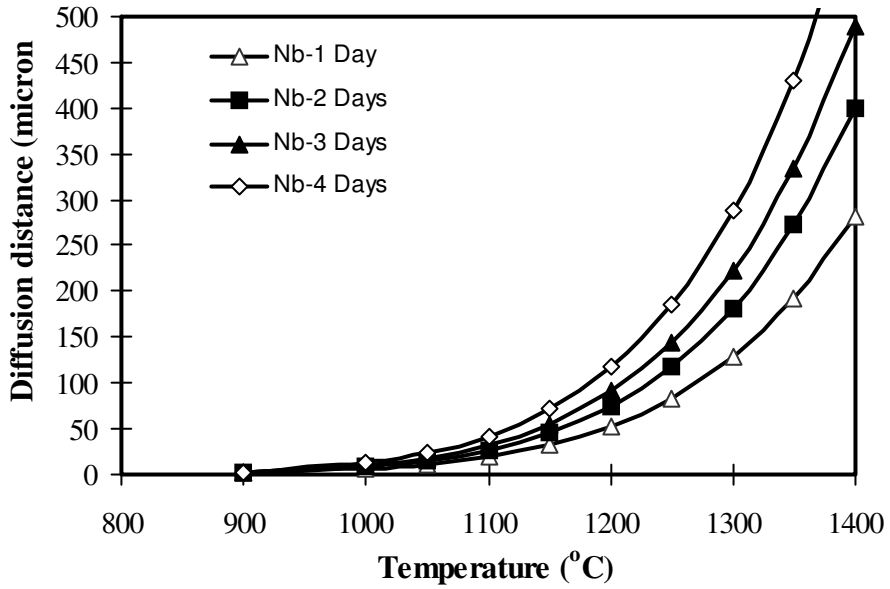

Figure 5.7. Predicted diffusion distances of Nb at various reheating temperatures for 1 to 4 days time.

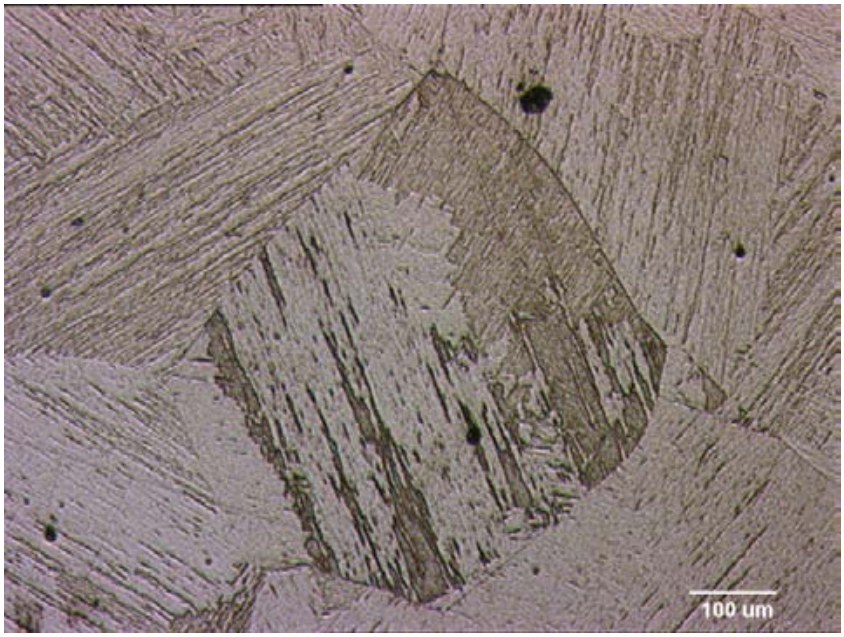

(a)

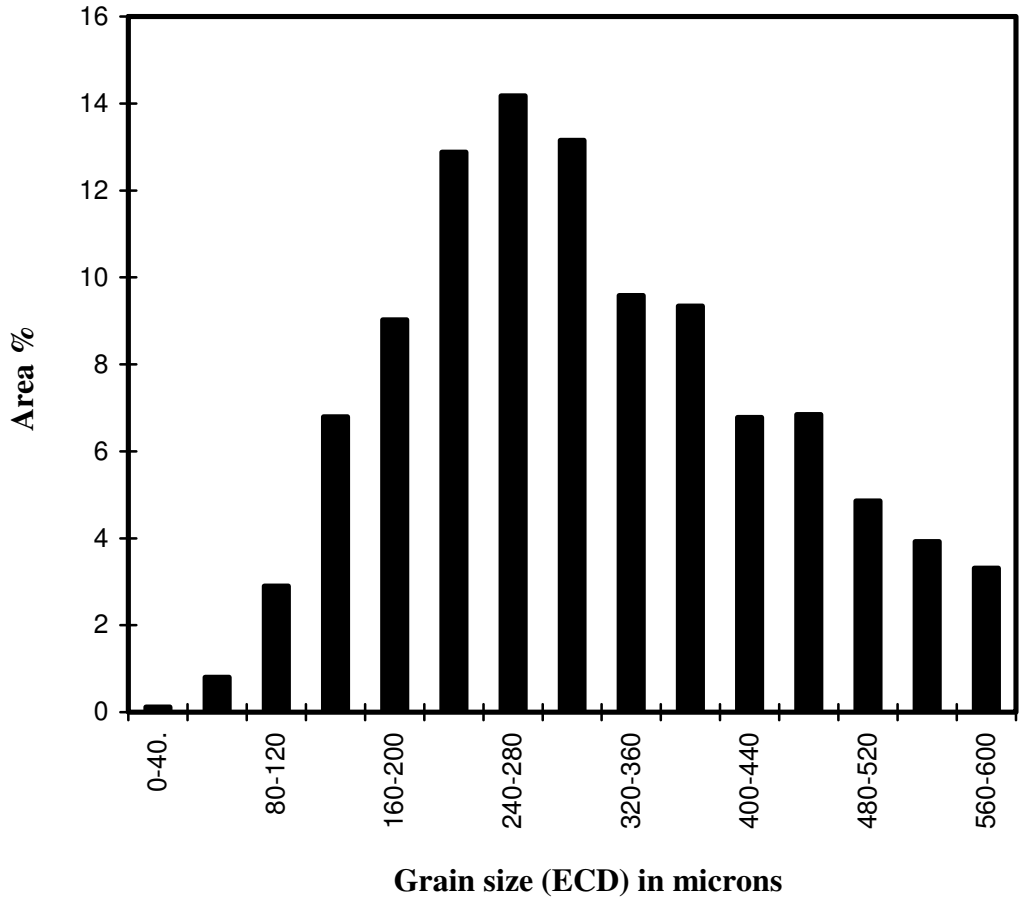

(b)

Figure 5.8. (a) Microstructure (as-quenched) and (b) prior austenite grain size distribution for the homogenised and reheated Slab 1 (1225 °C) sample.

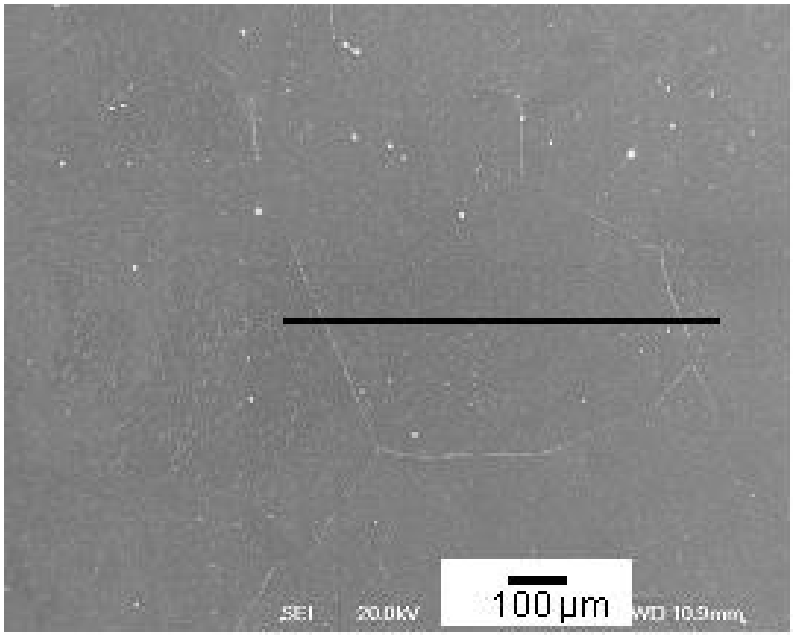

(a)

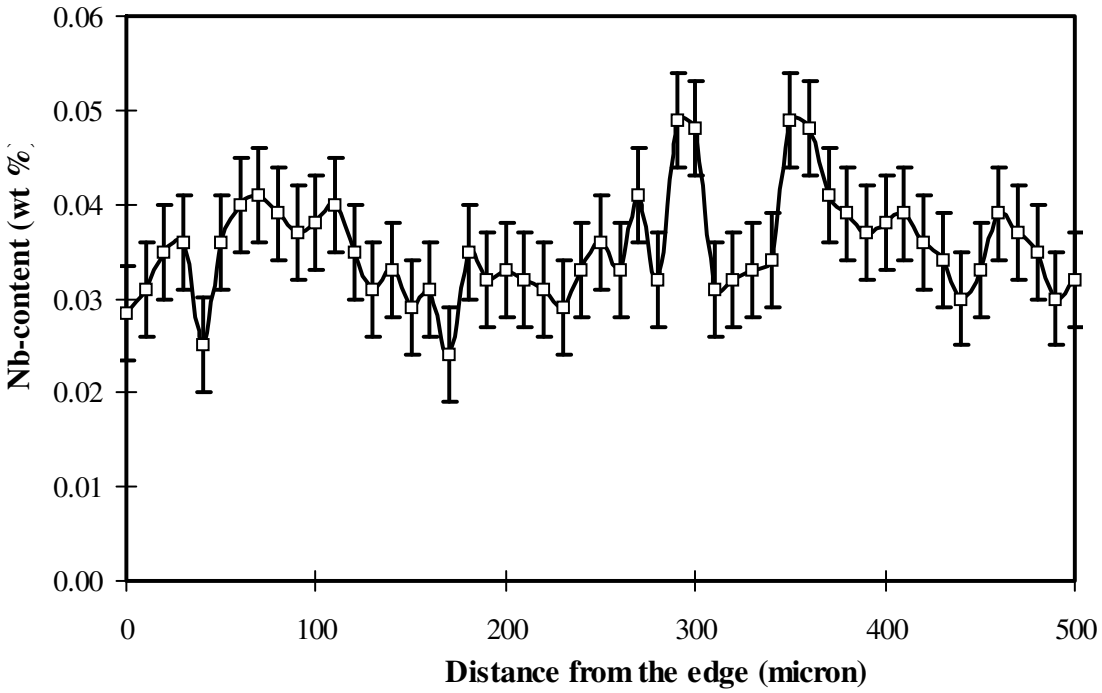

(b)

Figure 5.9. SEM image of (a) homogenised Slab 1 sample. The black line in the image represents the place from where the EDS traces were taken. (b) Nb distribution in homogenised sample plotted as a function of distance.

CHAPTER – 6

Limits of validity of Dutta-Sellars equations: Prediction of grain size distribution after deformation

As indicated in the literature review that grain structure development during hot deformation of microalloyed steel depends on recrystallisation, precipitation and the interaction of recrystallisation and precipitation [1, 5, 6, 12, 17]. The model most frequently referred to for strain-induced precipitation, austenite recrystallisation and recrystallisation-precipitation interaction in Nb-microalloyed steels is that proposed by Dutta and Sellars [98, 155].

The input parameters used in the Dutta-Sellars equations are average grain size, available Nb in solution and strain; the values of the constants and the exponents were then generated by fitting to experimental results from various research group [98].

The expressions D_0^2, $\varepsilon^{-4}\exp\left(\frac{300{,}000}{RT}\right)$, $\exp\left(\left(\frac{2.75x10^5}{T}-185\right)[Nb]\right)$, and k in Dutta-Sellars equations (Equations 3.12 and 3.17) represent the available area for nucleation of the recrystallised grains, the stored energy for recrystallisation, the solute drag exerted by the available Nb in solution and the Avrami exponent respectively.

Figure 6.1 shows the predicted amount (%) of recrystallised grains compared to the measured amount at 0.3 strain (the Dutta-Sellars equations were mostly validated at 0.3 strain) using the data given in the Dutta-Sellars papers [98, 155]. The recrystallised percentage was predicted using the Dutta and Sellars equations and assuming a linear variation between 5 and 85 % recrystallisation. From Figure 6.1 it can be seen that predicted and measured amounts of recrystallisation are in good agreement.

Figure 6.2 presents a summary of the amount of predicted recrystallised grains compared to the measured amount using the data available in the literature encompassing a wide range of grain sizes (20-806 μm) and compositions, all at 0.3 strain. It can be seen from Figure 6.2 that the predicted amount is consistently more than the measured value. The red data points are for the steels containing about 0.03 - 0.046 wt % Nb, which is in the range of validity of the Dutta-Sellars equations, however the grain sizes range from 20-806 μm is greater than that used by Dutta-Sellars. The details of the compositions, the test method and the method of quantifying the amount of recrystallisation are listed in Table 6.1. Therefore, it can be seen that with wider grain size range there is a discrepancy between the predicted and the measured amount of recrystallisation even when the Nb content is within the range used for the original equations. The discrepancy is greater with high/low Nb (compared to the range used in the original Dutta-Sellars equation), high N (green, orange and black data points in Figure 6.2). Therefore, at 0.3 strain good agreement, using the Dutta-Sellars equations, is seen only for steels that contain Nb about 0.03 - 0.046 wt % Nb and grain sizes ranging from 100 to 450 μm, i.e. for the original conditions the equation was developed for.

Sellars developed his model fitting to the experimental data of other workers; i.e. his model was not derived from a systematic series of tests on a single grade using a standardised experimental technique. In addition, the initial grain sizes in his study were fine, from 100 to 450 μm, and only three or four initial grain sizes were studied at each deformation temperature. Whilst Kwon and DeArdo [134] and Palmiere et al. [88] have identified the presence of strain-induced Nb(C,N) precipitates (green and orange data points) which might slow down the recrystallisation process and that could be the cause of predicted amount of recrystallised being greater than the measured for those two results, in

the other papers no effect of strain-induced precipitation was mentioned and the discrepancy is also seen for low Nb steels under deformation conditions that would not favour strain-induced precipitation.

The Dutta-Sellars equations has been modified by other researchers, through a range of proposed values for the constants and the exponents (Table 3.5), to account for different grain sizes, compositions, deformation conditions etc that have been examined experimentally as indicated in the section 3.4.1. The form of the equations remains the same in each case, with only the constants and the exponents being modified. The different exponents used in the Dutta-Sellars equations in the literature can lead to significant differences in predictions. Therefore the objectives of the present chapter are as follows.

- To examine the limits of validity of the original Dutta-Sellars equations and recently modified equations proposed in the literature.
- To investigate the influence of starting grain size taking into account greater grain size variability using both literature data and new experimental results.
- To predict grain size distribution after deformation using Dutta-Sellars equations.

It has been shown in Figure 6.2 that the Dutta-Sellars equations over predict the amount of recrystallisation for wider grain size range. It has been reported that the square dependence of grain size on the recrystallisation kinetics is not accurate when the grain size is greater than 100 μm [148]. The influence of initial grain size (20-806 μm) on static recrystallisation kinetics was also studied by Fernandez et al. [148] using four steels microalloyed with Nb, Ti and Nb-Ti (in the range 0.034-0.035 wt% for Nb and 0.005-0.067 wt % for Ti). For constant strain it was shown that a grain size exponent (q)=2 predicts the time for 50 % recrystallisation well for a grain size < 160 μm where as for coarse grains i.e. grain size > 160 μm, q =1 gives the best fit. Medina et al. [125] studied

the hot deformation kinetics of twenty six different steel containing Nb (0.007-0.093 wt %), V (0.043-0.12 wt %) and Ti (0.021-0.055 wt %) with the grain size ranging from 83 to 430 μm and found that q=1 gives the best fit of recrystallisation kinetics. However, these modifications to the Dutta-Sellars equations do not explain all the discrepancies in Figure 6.2, as shown in Figure 6.3 where the data is re-plotted using the equations and constants (given in Table 6.2) proposed by Fernandez et al. and Medina et al. [125, 148].

The scatter is considerably larger when the Fernandez et al. equation is used (Figure 6.3 (a)) to predict the percentage recrystallised compared to that when the original Dutta-Sellars equation is used (The red square and diamond data are from Fernandez et al.'s work and those fits well [148]). The scatter is reduced on using the equation proposed by Medina et al. (Figure 6.3 (b)), however there are still some outlying data points. Fernandez et al. developed their equations for 0.035 wt % Nb steel deformed at temperatures above 1100 ^{o}C whereas Medina et al. developed their equation for 26 different steels across a greater range of deformation temperatures (975-1200 ^{o}C). This may be the reason for the reduced scatter for the Medina et al.'s equation.

From Figure 6.3(a) it can be seen that the discrepancy is greatest for the 0.02 wt % Nb steel, with significant error also being seen for the steels with high (> 0.04 wt %) Nb content. In addition the predicted amount of recrystallisation is not always greater than the measured value, as was seen in Figure 6.2 using the original Dutta-Sellars equations. Whereas Medina et al.'s equations predicts the amount of recrystallisation more accurately for the higher Nb steel, but there is significant discrepancy for the low Nb steel (0.02 wt % Nb) (Figure 6.3 (b)). The discrepancy is also reasonably high for 0.043 wt % Nb steel; the reason for this is not obvious from the original reference [147]. Figure 6.3(a) and (b) also indicates that neither the equations proposed by Fernandez et al. nor by Medina et al. can

be applied to all the experimental results in all deformation conditions. This implies that changing the grain size exponent alone will not improve the overall accuracy of the equations.

6.1 Deformation simulation at 0.3 strain

6.1.1 Modelling recrystallisation precipitation kinetics for the homogenised Slab 1

A recrystallisation-precipitation time temperature (RPTT) diagram was constructed using Dutta-Sellar's equations (Equations 3.12, 3.16 and 3.17) for the homogenised Slab 1 using a mode grain size of 280 μm (Figure 5.8, Chapter 5) and bulk Nb composition (i.e. 0.045 wt % Nb based on Thermo-Calc prediction of full solubility at 1225 °C) in equations 3.16 and 3.17 for an applied strain of 0.3 with holding up to 10 s (Figure 6.4) to select the deformation temperatures.

The predicted recrystallisation-precipitation conditions for the homogenised sample are summarised in Table 6.3. Full recrystallisation temperature refers to the temperature greater than R_f (85 % recrystallisation after 10 s) and no recrystallisation temperature refers to temperature lower than R_s (5 % recrystallisation after 10 s).

From Table 6.3 it can be seen that full recrystallisation is predicted to take place at temperatures above 1040 °C and that there should be no recrystallisation at temperatures below 975 °C. The partial recrystallisation region in the absence of precipitation is 975 – 1040 °C, whereas in the presence of precipitation it is predicted to be 1010 – 1040 °C assuming that recrystallisation ceases once 5 % precipitation has occurred. Figure 6.4 was used to select deformation temperatures of 1075, 1050, 1025, 1010, 990 and 975 °C for the experiments. Figure 6.4 indicates that, for deformation at 1075 °C, a 10 s hold places the

specimen well beyond the recrystallisation finish (85 %) line at this temperature so that close to 100 % recrystallisation should be completed prior to precipitation giving a fine, unimodal grain structure. Deformation at 1050 °C and holding for 10 s should result in 95 % recrystallisation completed. Lowering the deformation temperature to 1025 °C will give partial recrystallisation within the 10 s hold and should lead to the generation of a mixed grain structure. At 1010 and 990 °C there would be two competing factors controlling the deformation process: recrystallisation and precipitation. Precipitation should restrict the moving grain boundaries and therefore slow or stop recrystallisation. At 975 °C precipitation precedes recrystallisation, which is only predicted to start after the 10 s hold, therefore a fully unrecrystallised microstructure should be retained.

6.1.2 Result of deformation simulation at 0.3 strain

Figure 6.5 and Table 6.4 shows the predicted vs measured percentage of recrystallised from the present study using the original Dutta-Sellars equations, the mode grain size of 280 μm and assuming a linear variation between the 5 and 85 % recrystallisation lines and extrapolating to give 0 to 100 %. From Figure 6.5 it can be seen that there is a discrepancy between predicted and measured percent of recrystallised and this discrepancy is consistent with the trend shown using the literature data for a similar Nb content steel (the red data points in Figure 6.2).

The equations proposed by Fernandez et al. and Medina et al. [125, 148] have been used to predict the amount of recrystallisation and these results are compared with the experimental results in Figure 6.6. From Figure 6.6 it can be seen that neither of the equations predict the amount of recrystallisation accurately. The predicted values using the Fernandez et al. equation are greater than the measured values up to a deformation temperature 1050 ^{o}C. The amount of over prediction decreases with an increase in

deformation temperature and then gradually changes to an under prediction for deformation at 1075 ^{o}C. On the other hand Medina et al.'s equations under predicts the amount of recrystallisation above a deformation temperature of 990 ^{o}C. Comparing the predictions using the three sets of equations it can be seen that the discrepancy between predicted and measured values is lowest when the original Dutta-Sellars equations are used (root mean square error (RMS) 10 %) than the equations proposed by Medina et al. (21.5 %) and Fernandez et al. (18 %).

One of the reasons for this discrepancy could be due to deformation induced precipitation of Nb(C,N) slowing down recrystallisation as the effect of precipitation has been ignored while predicting recrystallisation.

In microalloyed steel precipitation and recrystallisation interact in four distinct ways [12, 185, 199].

1. Strain-induced precipitation occurs primarily on dislocations in the deformed matrix. A decrease in the dislocation density through recrystallisation reduces the potential number of precipitate-nucleation sites and the onset of precipitation can be retarded as a result.
2. A fine dispersion of precipitate particles may greatly restrict the rearrangement of dislocations. As a result, precipitation may delay the onset of recrystallisation by limiting the dislocation processes needed for the nucleation of recrystallisation [185, 199].
3. Precipitate particles also exert a pinning (*Zener*) force on moving grain boundaries. This force could slow down or even halt the growth stage of recrystallisation [88,155, 185, 199].

4. When present in solution, the microalloying elements can reduce the mobility of grain boundaries. The progress of precipitation, which reduces the matrix solute content, will therefore result in a gradual increase in boundary mobility [119].

In the absence of precipitation, the recrystallised fraction evolves in a monotonic manner as described by the Johnson–Mehl–Avrami–Kolmogorov (JMAK) theory [99, 100, 112]. When simultaneous precipitation takes place, the kinetics of recrystallisation can be modified in two ways:

1. The particle pinning of dislocations hinders the recrystallisation nucleation event and thus delays the onset of recrystallisation without changing the sigmoidal appearance of the recrystallised fraction versus time curve [99, 100, 104, 112].
2. The exertion of a particle pinning (Zener) pressure on the migrating grain boundary reduces the recrystallisation growth rate. Recrystallisation comes to a complete stop when the instantaneous Zener pressure exceeds the driving force for recrystallisation [12, 88, 99, 100, 104, 112, 134, 185].

In summary, the recrystallised fraction versus time curve in microalloyed steels is expected to show only one of two shapes [12, 99, 100, 112, 134]: (a) the standard sigmoidal shape described by the JMAK theory and going to a recrystallised fraction of 1 and (b) an incomplete recrystallisation curve with a permanent plateau.

TEM investigation has been carried out at 0.3 strain to see whether precipitation is having an effect in slowing down recrystallisation and will be discussed in the next section. Quantification of deformation induced Nb(C,N) precipitates will also help to quantify the available Nb in solution that would provide solute-drag.

6.1.3 Quantification of precipitates that form during / after deformation

In order to quantify the retarding effect of the strain-induced precipitates it is necessary to identify the precipitates that form during deformation. Therefore, it is required to investigate the precipitate development in each stage of processing i.e. homogenisation, reheating and deformation (i.e. the sample slowly cooled to the deformed temperature from 1225 ^{o}C and then deformed at 0.3 strain and held at that temperature for 10 s and then water quenched). Then comparing the precipitate distribution and the volume fraction of the deformed sample to that of the sample which has been given the same treatment (i.e. the sample slowly cooled to the deformation temperature from 1225 ^{o}C and held at that temperature for 10 s and then water quenched) without deformation it would be possible to identify the precipitates that form during deformation. SEM and TEM were used to characterise the precipitates that form after each stage of processing.

SEM investigation of homogenised slow cooled sample revealed the presence of coarse cuboidal TiN particles of size (side length of square particles) > 400 nm and Nb(C,N) (diameter) with size ranging from 100-400 nm. The area fraction of the particles is 0.0003. Following homogenisation the samples were reheated at a rate of 3 ^{o}C/min to 1225 ^{o}C held at that temperature for an hour and then quenched in water. This reheating was carried out to dissolve Nb(C,N) that precipitated during homogenisation and quenching was carried out to preserve Nb in solution. SEM investigation of quenched sample found out the presence of undissolved TiN and coarse Nb(C,N) particles, although very small area fraction. The size distribution of the particles presents after homogenisation and after reheating at 1225 ^{o}C for 1 hour followed by water quench (i.e. the second thermal cycle in Figure 4.2 a, Chapter 4) is shown in the Figure 6.7.

After reheating in the furnace the samples were rapidly reheated within the Gleeble thermomechanical simulator to 1225 ^{o}C and then cooled down to the deformation temperature as discussed in the experimental section. TEM investigations were carried out on the deformed samples. TEM investigation was also carried out on the sample after quenching following the reheat furnace treatment and the 5 minutes hold followed by cooling down to deformation temperature in the Gleeble to determine if any precipitates were present in the samples prior to deformation as these particles being coarser in size will not influence recrystallisation kinetics [12, 99, 100, 112] and will be discarded for subsequent quantification of strain-induced precipitation. A small volume fraction of Nb(C,N) (e.g. 0.000002 at 1050 ^{o}C) with the size (diameter) ranging from 20-150 nm was revealed on the sample that is reheated in Gleeble and cooled down to the deformation temperature and then quenched without deformation.

The distribution of carbonitride particles was studied using the TEM examination of thin foil specimen. Nb(C,N) particles were identified using dark field imaging, Figure 6.8 (a) and (b) following the same procedure as described in Chapter 4, section 4.4.4.2. Compositions of the particles were determined using EDS. An example of the precipitate size distribution that form after deformation at 1025 ^{o}C with 0.3 strain and the comparison with that of the precipitates form without deformation at 1025 ^{o}C is shown in Figure 6.8 (c) and (d). Comparing Figure 6.8 (c) and (d) it can be seen that a greater number density of finer Nb(C,N) particles (< 20 nm) are present on the deformed sample as the particles are collected from the same area (~ 0.01 μm^2) in both the conditions. The volume fraction of the deformation-induced Nb(C,N) was quantified considering particles size < 20 nm. The result of TEM investigation is summarised in Table 6.5.

6.1.4 Discussion on influence of deformation-induced Nb(C,N) precipitates on recrystallisation at 0.3 strain

Deformation simulations were carried out 1050 and 1025 ^{o}C with 0.3 strain, for 4, 6, 8 and 10 s to determine whether there is any influence of precipitation on the kinetics of recrystallisation. The variation of measured amount of recrystallisation as a function of hold period after deformation is shown in Figure 6.9. At 1050 °C precipitation is not predicted to start within 10 s hold period. Both at 1050 and 1025 ^{o}C the measured amount of recrystallisation as a function of hold period shows a linear relationship, i.e. approximating to the straight line part of a JMAK plot, suggesting that there may not be any effect of strain-induced precipitates.

Figure 6.10 (a) shows the presence of recrystallised grains in a matrix of coarse deformed grains after deformation at 1050 ^{o}C at a 0.3 strain and holding for 4 s. From the grain size distribution (Figure 6.10 (b)) and the microstructure (Figure 6.10 (a)) it can be seen that the grain size in the range 240 µm to 600 µm has not undergone any recrystallisation after comparing the deformed grain size distribution with the reheated grain size distribution i.e. the grain size distribution before deformation. The grain sizes from 0-100 µm have fully recrystallised whereas the grains in the range 120-240 µm have undergone partial recrystallisation. With an increase in holding time to 6 s there is an increase in recrystallised fraction, Figure 6.10 (c and d). The recrystallisation progresses consuming the finer grained area. Coarser grains are found to be unrecrystallised due to their low stored energy and low nucleation site density [12, 99, 100, 112, 186, 187].

Assuming a random distribution of grains in the starting microstructure then nucleation of recrystallised grains will first take place in the finer grains rather than in the coarse

grains due to there being more available grain boundary area per unit volume, which provides a higher number density of nucleation sites and also due to their having a higher driving force for recrystallisation [12, 99, 100, 112, 186-194]. Once a stable bulge has nucleated then its rate of motion increases leading to the consumption of the higher strain energy grains [12, 99, 100, 112, 134, 186-194]. This would lead to the development of an interconnected recrystallised grain network resembling a coarse grain boundary network shown in Figure 6.10 (a) and (c). The coarser grains taking part in recrystallisation with progress of hold time after deformation suggesting finer grains have greater tendency to recrystallise. The gradual progress of recrystallisation consuming more and more coarse grains also indicates that precipitation may not have any effect on slowing down recrystallisation at this temperature.

TEM investigation on the samples deformed at 1050 ^{o}C for 4, 6, 8 and 10 s hold period revealed that only the sample that has experienced the 10 s hold period after deformation contained any <10 nm Nb rich particles. The measured volume fraction of deformation-induced Nb(C,N) precipitates was 0.00002, which is 11 % of the equilibrium amount of precipitates predicted at that temperature. The variation of recrystallised fraction with time represents the linear part of JMAK plot (Figure 6.9) without showing any influence of 0.00002 volume fraction of precipitates that forms after 10 s suggesting there is no influence of deformation-induced precipitates on recrystallisation under these conditions.

At the lower deformation temperature of 1025 °C greater and faster precipitation occurred (0.000044 volume fraction of < 20 nm diameter Nb(C,N) formed between 6 and 8 s), which appeared to cause some slowing of recrystallisation, Figure 6.11. However, increased holding to 10 s only increased the volume fraction to 0.00005 (average diameter remained at 4 nm) and this apparent saturation of strain-induced precipitation gave an

acceleration of recrystallisation to 42 %. For this driving force (0.3 strain at 1025 °C) the formation of 0.00005 fraction of strain-induced precipitates does not slow overall recrystallisation. A plateau, which is characteristic of recrystallisation precipitation interaction on a recrystallisation time curve, showing that recrystallisation has been stopped by precipitation [134, 185] is absent in Figure 6.9 and 6.11. Together these results suggest that 0.00005 volume fraction of Nb(C,N) precipitates in Slab 1 homogenised (0.045 wt % Nb) is not sufficient to stop recrystallisation at 1025 ^{o}C when deformation carried out at 0.3 strain.

Deformation simulation has been carried out with 4, 6, 8 and 10 s delay after deformation at 0.3 strain at 990 ^{o}C. No recrystallisation was measured up to 8 s, and 10 % recrystallisation was measured after 10 s. TEM investigation has revealed the presence of Nb rich particles after 6 s hold period with a volume fraction of 0.000016, which is 5 % of the equilibrium amount of precipitates at that temperature. After 8 s there is increase in the volume fraction of precipitates, 0.00006 and after 10 s the volume fraction of the Nb rich particles increases to 0.00008, which is 25 % of the equilibrium amount of precipitates at that temperature. There is no change in the average size (~ 3.9 nm) of the particles with time. That indicates that the progress of recrystallisation is not due the coarsening of the particles but does suggest that at 990 ^{o}C there is no effect of strain-induced precipitation in this steel at 0.3 strain.

Kwon and DeArdo found that deformation induced Nb(C,N) particles are effective in halting recrystallisation after 25 s of hold period at 900 ^{o}C with 0.05 wt % Nb steel after deformation with 0.3 strain [134]. This also supports the finding from the present study. At 975 ^{o}C less than 5 % recrystallisation is predicted but experimentally no

recrystallisation is measured. Together with the TEM results at 990, 1025 and 1050 ^{o}C this suggests that precipitation is not having an effect on stopping recrystallisation at 0.3 strain.

6.2 Discussion on the cause of the discrepancy between predicted and measured amount of recrystallisation at 0.3 strain

The TEM investigation on the deformed samples have indicated that deformation-induced precipitates are not slowing down recrystallisation at 0.3 strain. Therefore precipitation is not the cause of predicted amount of recrystallisation being greater than that is measured.

Recrystallisation is a nucleation dominated process and grain boundaries play an important role in the nucleation event, which is why the initial grain size has an influence on the recrystallisation kinetics. The smaller the grain, the greater the grain boundary area per unit volume and hence faster the nucleation of recrystallised grains. D_0^2 in equation 3.17 represents the available area for nucleation of recrystallised grains and that should not change with grain size as this represents an area term.

Changing grain size does change the available area for nucleation and this will influence the recrystallisation kinetics. The equations present in the literature use the mode or average grain size to quantify the amount of recrystallisation. But the recrystallisation kinetics will be different for the different grain sizes present in the matrix. The effect of grain size will be more significant in presence of a skewed grain size distribution as in the present study. Therefore considering only the mode grain size for quantifying recrystallisation fraction may result in significant error.

Another effect of the starting grain size is on the driving force for recrystallisation. At 0.3 strain nucleation at the grain boundaries can be assumed to be by strain induced boundary migration (SIBM) [99, 100, 112]. In this model the driving force for recrystallisation is the difference in volume strain energy (i.e. dislocation density) between adjacent austenite subgrains [107]. The model proposes that austenite grains of low dislocation density will bulge into grains of high dislocation density [119]. A starting grain size range between 0-600 μm would result in a different response to the recrystallisation process as the driving force for recrystallisation, i.e. the dislocation density, will be different in the different grain sizes, assuming that the strain is uniform.

The driving force (per unit area) for recrystallisation [12], F_{RXN}, is given by

$$F_{RXN} = \mu b^2 \Delta\rho/2 \qquad (6.1)$$

where, μ ($4x10^4$ MPa) is the shear modulus [134], b ($2x10^{-10}$ m) is the Burgers vector [134], and Δρ is the difference in dislocation density.

As initially considered by Ashby [188] deformation in polycrystals results in statistically stored and geometrically necessary dislocations. The latter are required to accommodate strain incompatibility at grain boundaries between grains of different orientations (and hence Taylor and Schmid factors) deforming to different strains. Refinement of grain size would be expected to give more complex deformation and so increased density of geometrically necessary dislocations (ρ^G). The transformation of austenite during cooling makes direct observation of dislocation densities impossible and requires indirect determination of stored energy necessary, e.g. through softening, so that measurement of the effect of prior austenite grain size on stored energy is difficult. Most studies on stored energy as a function of grain size have used copper (similar stacking fault energy (SFE) to austenite in HSLAs [189]), or austenitic grades (stainless steels with much

lower SFEs; Fe – 30 wt % Ni; or Ni – 30 wt % Fe, [172]). In deformed copper [187, 190-192], grain sizes ranged between 60 and 760 μm and variations in stored energy across all or part of this size range were between 6 and 30 %. As an example of the size of this effect, at 0.4 strain the stored energy in copper increases by 0.59 MPa for a grain size decrease from 300 to 30 μm [192].

Theoretical assessments of the stored energy as a function of grain size in pure nickel [193] and austenite [194] have used combinations of the densities of statistically stored (ρ^S) and geometrically necessary dislocations (ρ^G) to estimate the stored energy based on Ashby's equations. This yields equations of the form:

$$E_t = \frac{\alpha G b M \varepsilon}{d}\left(\frac{1}{\alpha_S} + C\right) \qquad \text{[194]} \qquad (6.2)$$

and

$$E_t = \alpha G b^2 \left(\rho^S + \rho^G\right);\ \rho^G = \frac{4\gamma}{C_1 d b} \qquad \text{[193]} \qquad (6.3)$$

where, E_t, α, G, b, M, ε, α_S, C, γ and C_1 are total stored energy, a material dependent constant, shear modulus (42.74 GPa, [195]), burgers vector, Taylor factor (3.06 for random crystal distribution on FCC materials, [194]), strain, material-dependent constant, a constant for each material, shear strain and a constant [193, 194].

SFE will affect these precise results through recovery and cell formation and so a direct comparison is not possible, however, Baker showed a variation on stored energy of 10 % for nickel samples deformed to 0.4 strain with grain sizes of 50 and 340 μm. These relationships do, however, show a common inverse relationship on grain size that is not accounted for in the Dutta-Sellars equations. Analysis of grain size studies does indicate a marked difference in stored energy with grain size with the sharp transition occurring

around 80 μm in pure copper [191]. If the copper behaviour is carried through to austenite then this would indicate a likely difference between the parameters determined in the original Dutta-Sellars fit and those appropriate for a wider range of grain sizes.

Further analysis of the Ashby model [193] indicates that the difference in stored energy should be greatest for low strains, whilst alloying elements have been shown to increase the stored energy for a given grain size and strain [196]. The variation of stored energy as a function of grain size using the equation proposed by Kazeminezhad [194] shown in Figure 6.12. Two literature data from 0.042 wt % Nb [134] and 0.09 wt % Nb [88] steels (measured from increase in flow stress after carrying out double hit tests) were superimposed on the Figure 6.12. The experimentally measured stored energy values are an order of magnitude higher than that is calculated, but it does decrease with increase in grain size showing the similar trend. The stored energy increases by 2.33 MPa for a grain size decrease from 600 to 20 μm which is 4 times more than that shown by Williams [192].

In the Dutta-Sellars equations the driving force for recrystallisation is represented by $\varepsilon^{4}\exp\left(\frac{300{,}000}{RT}\right)$ and it is independent of grain size. From Figure 6.12 it can be seen that up to a grain size of 100 μm the decrease in driving force with grain size is rapid, after that the rate decreases. Given that strain energy would be expected to be a function of the square of strain, then the increased exponent value would appear to incorporate some of the grain size variation in the originally fitted data. Fernandez et al. and Medina et al. have identified the dependence of strain exponent (p) on grain size (Table 6.2), although these do not approximate to the inverse grain size relationship of the Ashby-based models. The steel compositions and the grain size ranges they studied, and the accuracy of their modified Dutta-Sellars equations, have already been mentioned: Figures 6.3 (a) and (b)

showed that the Fernandez et al. and Medina et al. approaches do not apply to all the data available in the literature.

To improve the accuracy of the Dutta-Sellars equations it is necessary to take into account the effect of the grain size dependence on nucleation and driving force. To account for the effect of the grain size on nucleation, for a wide grain size range, the individual grain size classes can be considered separately; this is discussed below. It has been mentioned earlier that experimental determination of stored energy during hot deformation of steel is impossible due to phase transformation and it has been shown in the literature and in the Figure 6.12 that the difference in driving force with grain size is not significant and it would reduce further at hot deformation temperature [88]. Therefore the effect of stored energy on grain size was found to be a less significant compared to the grain size effect on nucleation, as discussed below. It should also be noted that both these effects result in small grains having a greater tendency to recrystallise than coarse grains (for the same deformation conditions, i.e., for the same strain level) also shown experimentally in Figure 6.10 (a) to (d).

6.3 Prediction of amount of recrystallisation using the starting grain size distribution

The grain size distribution in the present study ranges between 0 to 600 μm with 58 % of grains (by area) in the size range 280 to 600 μm (Figure 5.8, Chapter 5). Using the mode grain size i.e. 280 μm to predict recrystallisation would not necessarily be expected to predict the amount of recrystallisation accurately when the majority of the grains lie in the coarser size range. Therefore in the present study a simple approach has been used to predict the amount of recrystallisation after deformation, which is summarised in Figure 6.13. The percent recrystallised was predicted by assuming a linear variation between R_s

(5 % recrystallisation) and R_f (85 % recrystallisation) in the recrystallisation, precipitation and time temperature diagram (RPTT), at each deformation temperature. Avrami-type expressions exist for the variation in recrystallised fraction, but these approximate well to a linear variation for the volume fraction range and conditions in this study. Outside the 5 – 85 % range, which should be outside linear range of a Avrami plot, the variation is expected to be non-linear due to initiation / impingement effects. The prediction of recrystallisation was carried out after generating the diagram for individual grain size classes starting from 20 μm to 600 μm present in the starting grain size distribution.

The result of the deformation simulations are summarised in Table 6.4 and Figure 6.14. From Figure 6.14 it can be seen that the deformation state can be predicted more accurately if the complete starting grain size distribution is considered rather than just using the mode grain size. Using this approach also successfully predicts the grain size distribution after deformation and will be discussed in the later section. The percentage recrystallised has also been predicted considering the influence of precipitation (Table 6.4) i.e. assuming 5 % strain induced precipitation of Nb(C,N) would be sufficient to halt recrystallisation [98, 155]. It can be seen that the predicted percentage of recrystallised considering the influence of precipitation is less than the measured amount at all deformation temperatures. This also suggests that precipitation is not retarding or stopping recrystallisation at 0.3 strain for this steel and the deformation temperatures considered. Detailed TEM characterisation, discussed in the earlier section, has shown that precipitation does not slow down the recrystallisation kinetics at 0.3 strain over the temperature range studied for the homogenised Slab 1 (0.045 wt % Nb).

In order to see how this present approach works for the literature data, presented in Figure 6.2, it is necessary to have the starting grain size distribution. In the literature the

starting grain size distributions have not been reported. Only the mode or average grain is given. To generate a grain size distribution the following assumptions were made:

- The reheat grain size distribution, i.e. the grain size distribution before deformation, has a log normal distribution [197].
- The largest grain size present in the distribution is thrice the average grain size [118].
- The log normal distribution was generated after generating a normal distribution.
- In all the cases a total of 1000 grains were considered to generate the distribution.

Figure 6.15 shows the predicted amount of recrystallisation, considering the complete grain size distribution, vs. the measured amount. The discrepancy for the red data points (0.03 to 0.05 wt % Nb, and 60 - 806 μm grain size) has reduced to 3.5 % from 11.5 % (in Figure 6.2). The orange data points (0.09 - 0 .093 wt % Nb) and the green data points (0.05 Nb and 0.024 - 0.025 wt % N) are the least well predicted values with an error of 16 %. The predicted amount of recrystallisation in each case is more than the measured amount.

In the original papers [88, 134] the authors observed the presence of deformation-induced Nb(C,N) precipitates and they calculated that the precipitate pinning force was greater than the driving force for recrystallisation. Precipitate pinning force were measured after quantifying the precipitates present in the replica and driving force for recrystallisation was estimated after measuring increase in flow stress during double hit deformation tests [88, 134]. While predicting the amount of recrystallisation the effect of precipitation has been ignored and this may be the cause of the discrepancy.

The black data points in Figure 6.15 are from a low Nb steel (0.02 wt % Nb). The discrepancy between predicted and measured amount has been reduced to 14 % from 32 %

in Figure 6.2. In the original paper for this low Nb steel there was no mention of any precipitates present after deformation. At present it is not clear the cause for the discrepancy for this steel, although it is the only low Nb (<0.03 wt% Nb) steel reported. Using the composition of the steel the predicted volume fraction of Nb(C,N) using Thermo-Calc at the lowest deformation temperature for this steel is 0.00014. For homogenised Slab 1 (0.045 wt % Nb) studied experimentally, TEM investigation (discussed earlier) has shown that measured volume fraction of strain-induced precipitates is lower than that predicted by Thermo-Calc and there is no effect of strain-induced precipitates in slowing down recrystallisarion kinetics at 0.3 strain. Therefore it is unlikely that this discrepancy is due to deformation-induced precipitates. It may be that at low Nb levels the effect of solute-drag is under represented in the Dutta-Sellars equations.

In summary, this new approach can be seen to be significantly more accurate in its predictions than using the mode grain size, however it is not 100% accurate, the average root mean square (RMS) error using this approach is 10 %, which is less than the discrepancy (RMS error 22 %) present by using original Dutta-Sellars equations (i.e. using mode grain size, Figure 6.2); this may be due to errors in the assumed starting grain size distribution, and / or because the driving force dependence on grain size has not been included in the modifications.

6.4 Predicting the grain size distribution following full recrystallisation

In order to predict toughness it is necessary to know the complete grain size distribution [7, 14, 19, 22, 23], especially in presence of bimodal or mixed grain size distribution. It was shown in the previous section that the amount of recrystallisation can be predicted

accurately for the individual grain size class present in the matrix. This approach can be used to predict the grain size distribution after deformation once the recrystallised grain size is known.

The grain size after recrystallisation was determined using equation 3.6 [98] and with the 3 values of D' (i.e. 0.66, 1.1 and 1.86) quoted for Nb-microalloyed steels. The grain size distributions predicted and experimentally measured are shown in Figure 6.16. Deformation at 1075 °C resulted in refinement of the prior austenite grain size (mode) to ~ 140 µm from 280 µm indicating that recrystallisation has been completed within the 10 s hold. From the grain size distribution it can be seen that the predicted grain size distributions ('class') are narrower than the experimentally determined one either shifted to a finer size range (with $D' = 0.66$ and 1.1) or to a coarser (with $D' = 1.86$) size range. The grain size exponent used in the equation was 0.67. After deformation from the experimentally determined grain size distribution it can be seen that the grain size mode has shifted to 140 µm from 280 µm and the distribution ends at the grain size 300 µm, which presumably comes from the largest grain size class in the distribution (600 µm). After deformation for this alloy using this range of thermomechanical simulation conditions the grain sizes became almost half the starting value. None of the combinations of D' and strain exponent for the form of equation 3.6 will reproduce the distribution measured experimentally from the starting distribution.

A simple approach therefore has been taken in the present study to predict the grain size after deformation assuming that the strain is uniformly distributed throughout all the grains by halving the initial grain size (for these grains that recrystallised) after determining the percent recrystallised in terms of area using equations 3.12 and 3.17 and assuming a linear

progression between 5% (R_s) and 85% (R_f) curves ('class' prediction) discussed in the previous section. This would result in up to 20 % error if no account were taken for classes giving predictions below R_s and above R_f. Without detailed knowledge of the Avrami parameters for recrystallisation in this alloy, the linear variation between 5 and 85 % recrystallisation has been extrapolated to 0 and 100 %. It is recognised that this will give some error. The procedure followed to determine the grain size distribution is summarised by the flow diagram in Figure 6.17.

Figure 6.18 presents the grain size distributions predicted using the halved reheated grain size distribution and determined experimentally showing a much better fit than obtained using equation 3.6, Figure 6.16. The grain size distributions in each condition were divided into 30 ECD classes in order to produce a smooth distribution. Full recrystallisation is measured experimentally whereas the RPTT diagram based on individual grain size class predicts 93 %. There is a greater area percent of finer grains measured experimentally than predicted by the model. This is not due to the linear extrapolation, but can be explained by the lack of stereological correction and the fact that the formation of recrystallised grains is a nucleation-dominated phenomenon and grain boundaries act as nucleation sites [1, 99, 100, 112, 114]. Fine grains provide more grain boundary area per unit volume for nucleation resulting in an increase in area percent of fine grains. The nucleation behaviour represented in the model appears to be underestimating the rate of this process for the larger grains. When the mode value (280 μm) was used full recrystallisation was predicted (using a comparable linear extrapolation). This may indicate that the Dutta-Sellars assumptions need modification for large grain sizes. In Figure 6.18 it was assumed that the entire original grain size distribution has recrystallised by halving the grain size of each class in the undeformed

reheated grain size distribution. This gives a predicted recrystallised grain size distribution that fits the experimentally determined distribution well, but underestimates the proportion of < 80 μm sized grains; this is balanced by an overestimate for 120 - 240 μm size grains. Some of this error may arise from the lack of any stereological corrections. This simple approach was used in the rest of the study [198].

6.5 Predicting the grain size distribution in the no recrystallisation regime

At 975 ^{o}C, after deformation, there is predicted to be no recrystallisation over the entire reheated grain size range and the initial unimodal grain structure should remain unimodal after deformation (grain size mode 280 μm). As there is no recrystallisation the initial grain size distribution would therefore be duplicated in the deformed grain size distribution. However the grain shape changes after deformation keeping the area constant as the deformation was carried out under plane strain condition. The average aspect ratio was measured to be 0.3. Good correlation between the predicted and measured grain size distribution was seen (Figure 6.19).

6.6 Predicting grain size distribution in the partial recrystallisation regime

According to Figure 6.4 (based on the mode grain size) 95 % recrystallisation should be completed after 10 s delay at 1050 °C. The grain size distributions (predicted and measured) show (Figure 6.20) the presence of coarse unrecystallised grains and fine recrystallised grains (~ 72 % by area for measured distribution and 73 % for the predicted distribution based on each grain size class). It was found that complete recrystallisation occurs for grains up to a size range of 200 - 240 μm. Grain size classes from 240 - 280 μm to 400 - 440 μm undergo partial recrystallisation whereas grains in the classes from 440 -

480 µm to 560 - 600 µm do not recrystallise. The recrystallised fraction is lower than that predicted based on the mode grain size (95%) by the RPTT diagram (Figure 6.4) (i.e. based on a mode grain size of 280 µm). This greater fit of percent recrystallised for 'class' prediction at 1050 °C is in contrast with the behaviour at 1075 °C and may indicate greater accuracy of the Dutta-Sellars assumptions for large grain recrystallisation nucleation at lower deformation temperatures. The experimental and predicted grain size distributions show the same underestimation of proportion for finer (< 100 µm) grain size classes with an overestimation for the 120 - 300 µm grain size classes.

Lowering the deformation temperature to 1025 °C results in partial recrystallisation and hence an expected bimodal grain size distribution. It should be noted that at this temperature precipitation is expected to occur before recrystallisation is completed. The predicted grain size distributions were generated assuming no influence of precipitation. Figure 6.21 (a and b) shows the experimentally measured bimodal structure produced with the mode grain size in the fine region of ~120 - 140 µm and in the coarse region of ~ 320 µm. Both the measured and predicted ('class') grain size distributions show 56 - 58 % of grains remain unrecrystallised, however the predicted distribution gives a mode grain size of 140 - 160 µm, i.e. slightly larger than the measured value. Figure 6.4 predicts, using the reheated mode grain size, 25 % recrystallisation after 6 s, when precipitation is predicted to start. If precipitation restricts recrystallisation then less than the 44 % recrystallisation predicted based on the class grain size after 10 s, should occur. The good agreement between the predicted ('class') grain size distribution, made assuming no influence of precipitation, and measured distribution, Figure 6.21 (a and b), suggests that, at this temperature, little influence of precipitation occurs. This has also been confirmed by TEM investigation discussed in the earlier section.

Deformation at 1010 °C was carried out in order to check whether precipitation is sufficient to stop recrystallisation as the P_s line is predicted to intersect the R_s line after 4 s at 1010 °C (Figure 6.4). The predicted recrystallised fraction based on mode grain size is 5 % with precipitation or 27.4 % if precipitation has no effect. The measured and predicted (assuming no influence of precipitation) grain size distributions based on individual grain size classes (Figure 6.22) are bimodal consisting of fine recrystallised grains (19 %) and coarse unrecrystallised grains. The recrystallised fraction is between those predicted by the mode-based predictions (with and without any effect of precipitation) as was the case for deformation at 1025 °C, but shows good agreement with that predicted using the individual grain size class (~ 17 %) whilst the grain size variation is consistent with the higher deformation temperatures. Additionally, this suggests that, at 1010 °C, there is no significant effect of precipitation on recrystallisation in this steel.

At 990 °C precipitation is predicted to precede recrystallisation, Figure 6.4 predicts that, after 10 s, 5 and 9.2 % recrystallisation are expected to occur according to the model based on mode grain size with and without precipitation effects respectively. The grain size distribution (Figure 6.23) contains fine recrystallised grains and coarse deformed grains with approximately 10 % recrystallised grains measured experimentally. 8 % is predicted based on the individual grain size classes present in the undeformed condition. This indicates again that precipitation is not having any effect (confirmed by TEM investigation), but the mode- and class-based predictions are closer in terms of percentage recrystallised. The measured area percent present in the grain size classes 0 - 20 and 20 - 40 μm is higher than that predicted for these two area classes, which is again consistent with the higher deformation temperatures and may reflect a higher nucleation rate in the finer grains.

6.7 Conclusions

The validity of the original and modified Dutta-Sellars equations in quantifying the amount of recrystallisation has been reviewed for a larger range of grain size and composition than used in the original work. A modified approach using the full grain size range has been reported using experimental data from this work, and literature data. The major findings are as follows:

1. The original Dutta-Sellars equations over predicts the amount of recrystallisation for steels with larger grain sizes and a greater range of Nb content than used to develop the original equation.
2. Modified Dutta-Sellars equations proposed by Fernandez et al. and Medina et al. do not predict the amount of recrystallisation well for the full range of data available in the literature.
3. Using the original Dutta-Sellars equations but taking into account the starting grain size range via an individual grain size class approach more accurately predicts deformation behaviour in terms of percent recrystallised for all literature data (assuming a log-normal starting grain size distribution) at 0.3 strain.
4. Grain size distributions following deformation (based on the amount recrystallised) were determined using the Dutta-Sellars equations for the individual grain size class present in the reheated grain size range. The equation in the literature for recrystallised grain size gave poorer agreement to the experimental values than a simplified approach based on halving the grain size values in the original reheated distribution.
5. Good agreement between the measured grain size distributions and predicted grain size distributions was obtained for deformation in the partial and no

recrystallisation regimes. The prediction underestimated the proportion of the fine grain classes.

6. No significant effect of precipitation on recrystallisation was observed for this steel and the deformation strain and temperature ranges studied.

Tables and Figures

Table 6.1. Literature data used to predict percent recrystallised using Dutta-Sellars equations.

Reference	Strain	Temperature (^{o}C)	Composition	Experimental method	Method of detection of recrystallised fraction
88	0.3	1100, 1050, 1000, 950, 900	0.049 Nb 0.008 N	Compression test using MTS machine	% softening
			0.048 Nb 0.024 N		
			0.02 Nb 0.008 N		
			0.09 Nb 0.008 N		
89	0.1, 0.2, 0.3, 0.4	1050, 1000, 950, 900, 850	0.03 Nb 0.005 N	Plane strain compression, Servo hydraulic compression machine	% softening
134	0.3	900, 1000	0.042 Nb 0.008 N	Compression test	metallography
			0.042 Nb 0.025 N		
148	0.1, 0.2, 0.3, 0.5, 0.6	1100	0.034 Nb 0.0053 N	Torsion	% softening
			0.035 Nb 0.0043 N		
125	0.2-0.35	1050, 1000, 975, 950, 900	0.007-0.093 Nb	Torsion	% softening
101	0.25	1150, 1050, 950	0.04 Nb 0.02 N	Torsion	metallography
114	0.46	1025	0.04 Nb	-	-
183	0.3	900, 950, 975, 1000	0.04 Nb	Torsion	metallography
			0.03 Nb		
184	0.3	850, 900, 1000	0.035 Nb	Compression	metallography

Table 6.2. Values of the constants and exponents used in the equations proposed by Sellars [98], Fernandez et al. [148] and Medina et al. [125].

Parameters	Sellars	Medina	Fernandez
A	6.75×10^{-20}	$3.754\times10^{-4}\exp(-7.869\text{x}10^{-5}Q)$	9.92×10^{-11}
Strain exponent (p)	4	$4.3D_0^{-0.169}$	$5.6D_0^{-0.15}$
Strain rate exponent (q)	0	-0.53	-0.53
Grain size exponent (s)	2	1	1
Q (J/mol)	300000	$124714+28385.68[\text{Mn}]+64716.68[\text{Si}]+72775.4[\text{Mo}]+76830.32[\text{Ti}]^{0.123}+121100.37[\text{Nb}]^{0.1}$	180000
k	2	$28.33\exp\left(-\frac{36{,}000}{RT}\right)$	1

Table 6.3. Predicted recrystallisation precipitation behaviour after homogenisation based on mode grain size of 280 µm.

Region	Temperature range (°C) in absence of precipitation	Temperature range (°C) in presence of precipitation
Full recrystallisation within 10 s after strain to 0.3	T > 1050	T > 1050
Partial recrystallisation within 10 s after strain to 0.3	975 < T < 1050	1010 < T < 1050
No recrystallisation within 10 s after strain to 0.3	T < 975	T < 1010

Table 6.4. Summary of deformation results; predictions taking into account precipitation in the mode-based analysis are given in brackets.

Deformation temperatures (°C)	Fraction recrystallised measured (area %)	Fraction recrystallised predicted based on mode grain size (area %)	Fraction recrystallised predicted based on individual grain size class (area %)
1075	100	100	93
1050	72	95	73
1025	42	54 (25)	44
1010	19	27 (5)	17
990	10	9 (<5)	8
975	0	4 (<<5)	0

Table 6.5. Summary of quantification of deformation induced Nb(C,N) precipitate after deformation at 0.3 strain.

Deformation temperature (^{o}C)	Strain and hold period after deformation	Average particle size (nm)	Volume fraction (F_v) (deformed)	Volume fraction (F_v) (without deformation)	Volume fraction (F_v) (predicted using Thermo-Calc)
1050	0.3,10 s	4.2	0.00002	0.000002	0.00016
	0.3, 8 s	Not found	Not found		
	0.3, 6 s	Not found	Not found		
1025	0.3,10 s	4	0.00005	0.0000035	0.00024
	0.3, 8 s	4.2	0.000044		
	0.3, 6 s	Not found	Not found		
	0.3, 4 s	Not found	Not found		
990	0.3,10 s	3.9	0.00008	0.000005	0.0003
	0.3, 8 s	5.5	0.00006		
	0.3, 6 s	4.5	0.000016		
	0.3, 4 s	Not found	Not found		

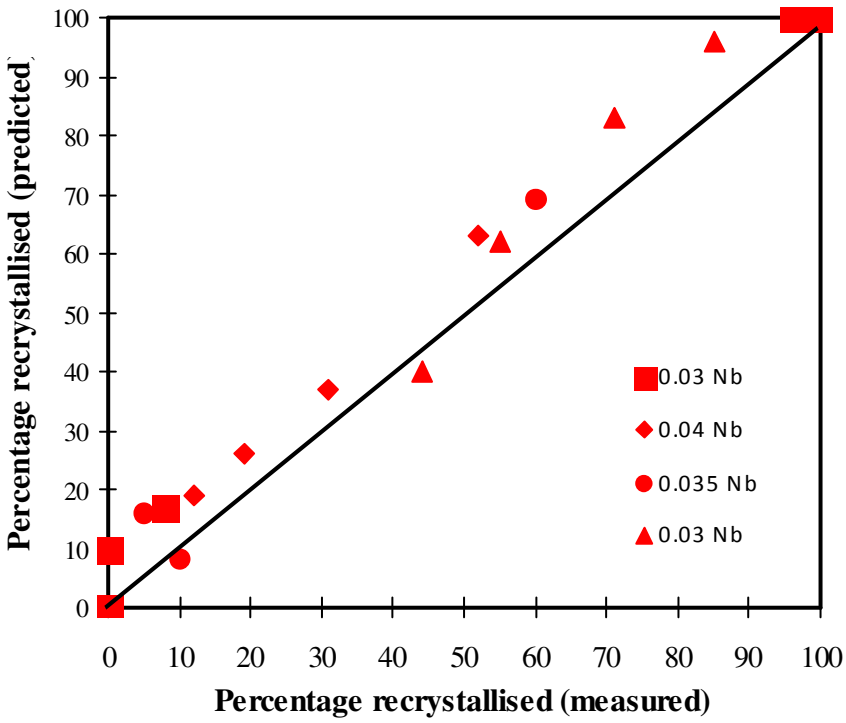

Figure 6.1. The amount (%) of predicted compared to measured recrystallised grains at 0.3 strain using the literature data [98].

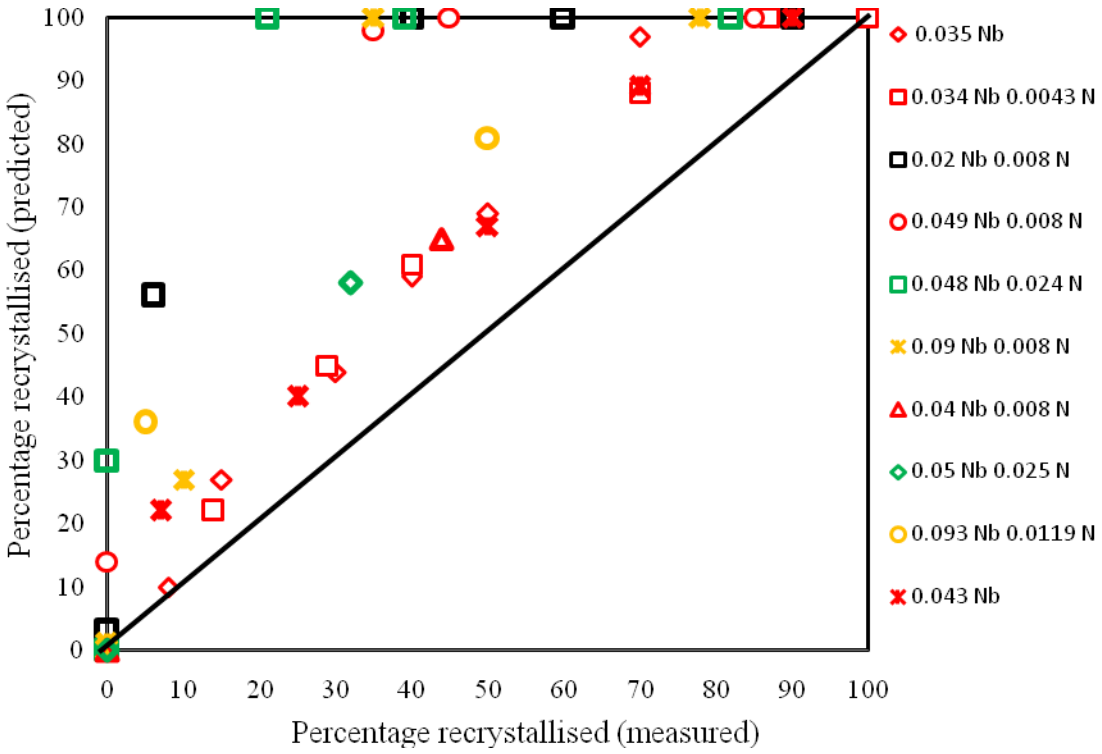

Figure 6.2. The amount (%) of predicted compared to measured recrystallised grains at 0.3 strain using the literature data mentioned in Table 1.

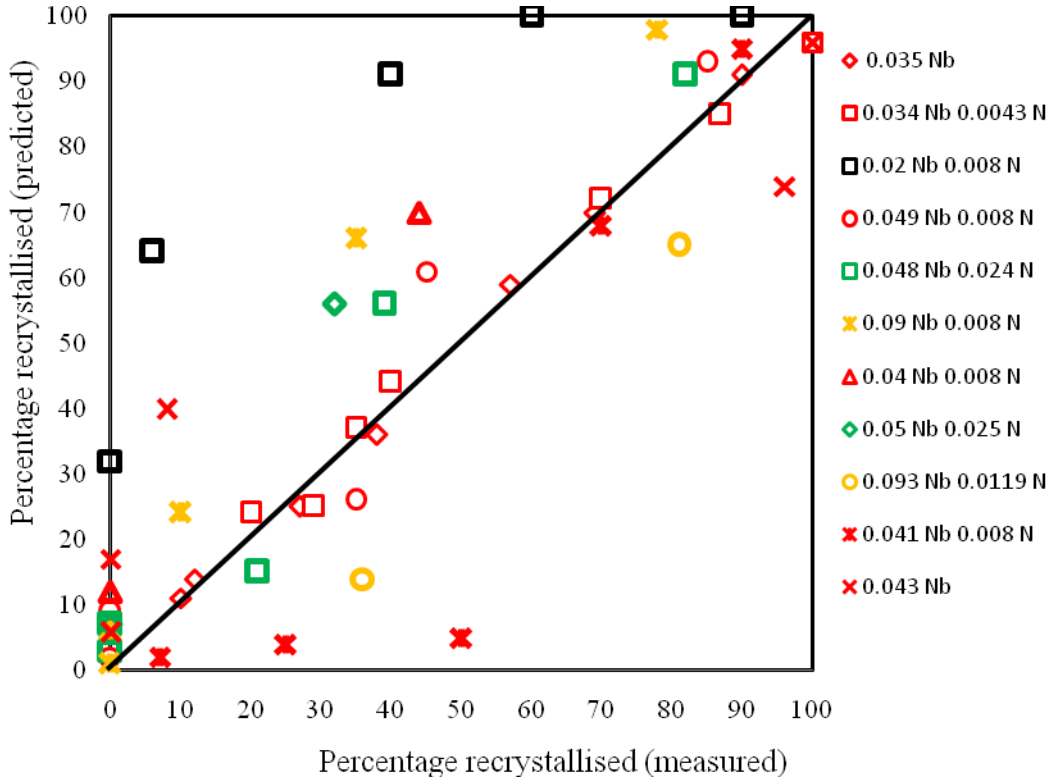

Figure 6.3 a. The amount (%) of predicted compared to measured recrystallised grains at 0.3 strain using the literature data mentioned in Table 2 and using the equation proposed by Fernandez et al. [148].

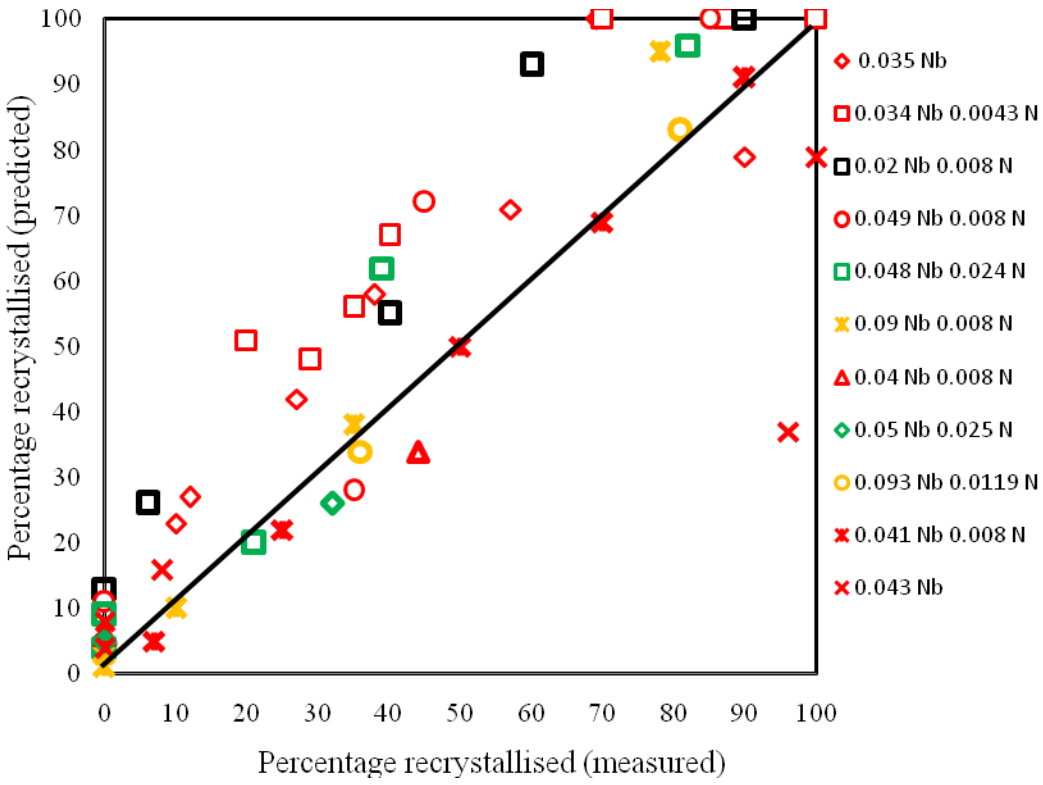

Figure 6.3 b. The amount (%) of predicted compared to measured recrystallised grains at 0.3 strain using the literature data mentioned in Table 2 and using the equation proposed by Medina et al. [125].

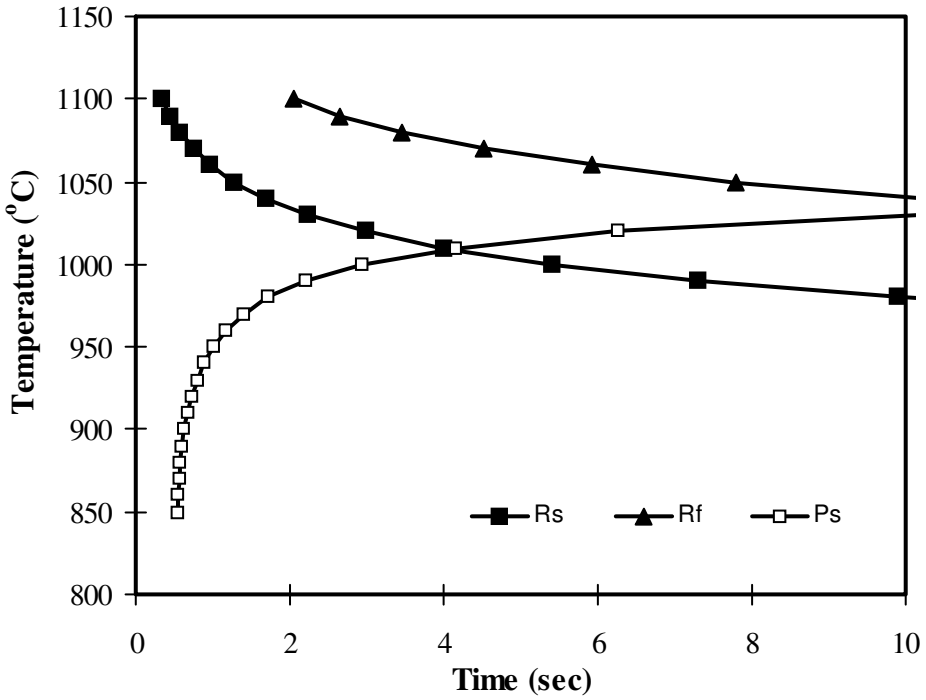

Figure 6.4. Recrystallisation – precipitation diagram based on mode grain size of 280 µm for sample reheated to 1225 °C assuming uniform composition, where R_s and R_f are 5 and 85% of recrystallisation and P_s is 5% deformation-induced precipitation of Nb(C,N).

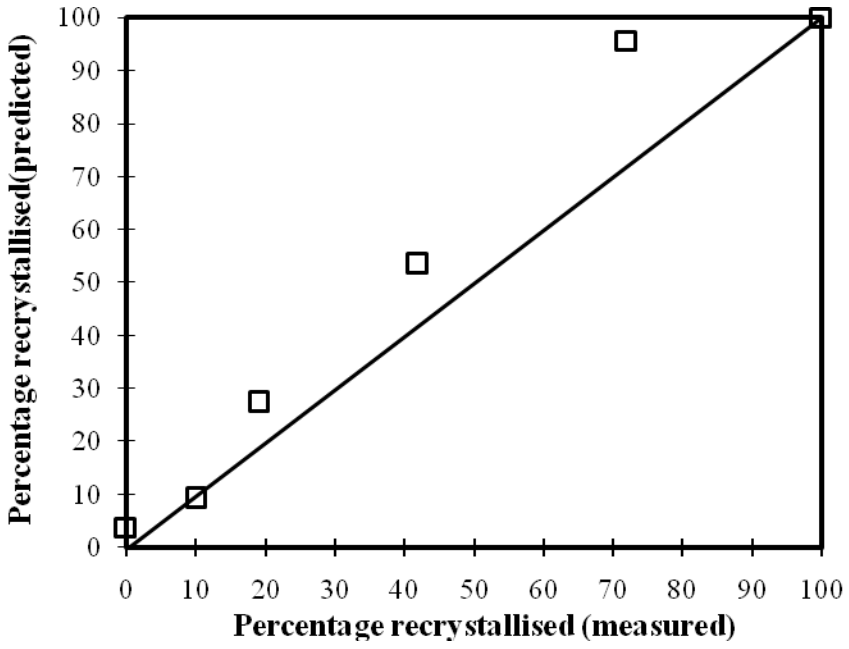

Figure 6.5. Variation of predicted % recrystallised vs the measured amount at 0.3 strain from the present study. The prediction was carried out using the mode grain size of 280 µm and original Dutta-Sellars equation.

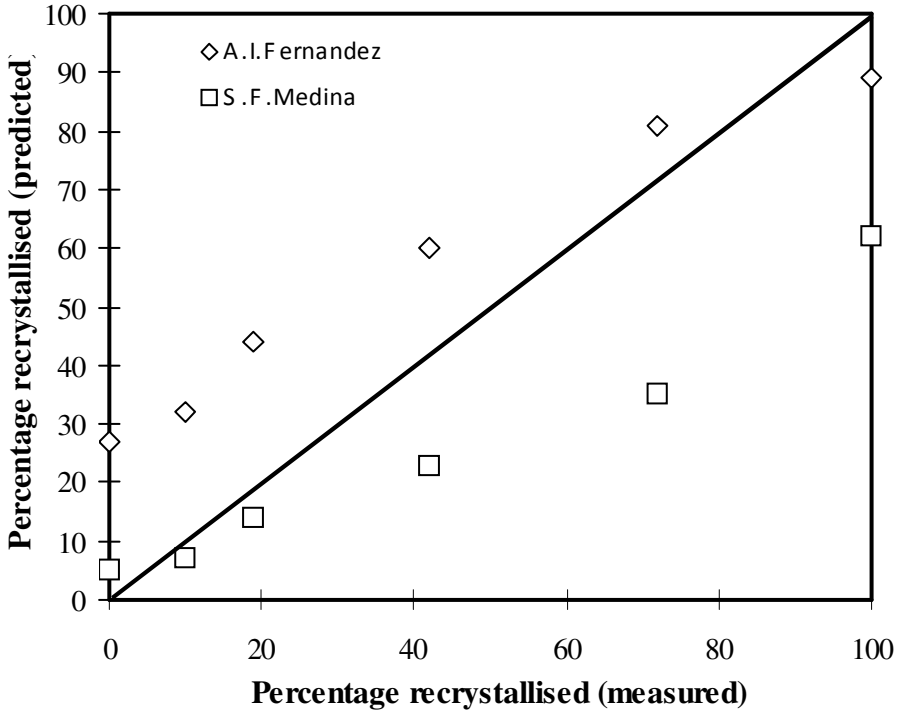

Figure 6.6. Variation of predicted % recrystallised vs the measured amount at 0.3 strain from the present study using the equations proposed by Fernandez et al. and Medina et al. [125, 148].

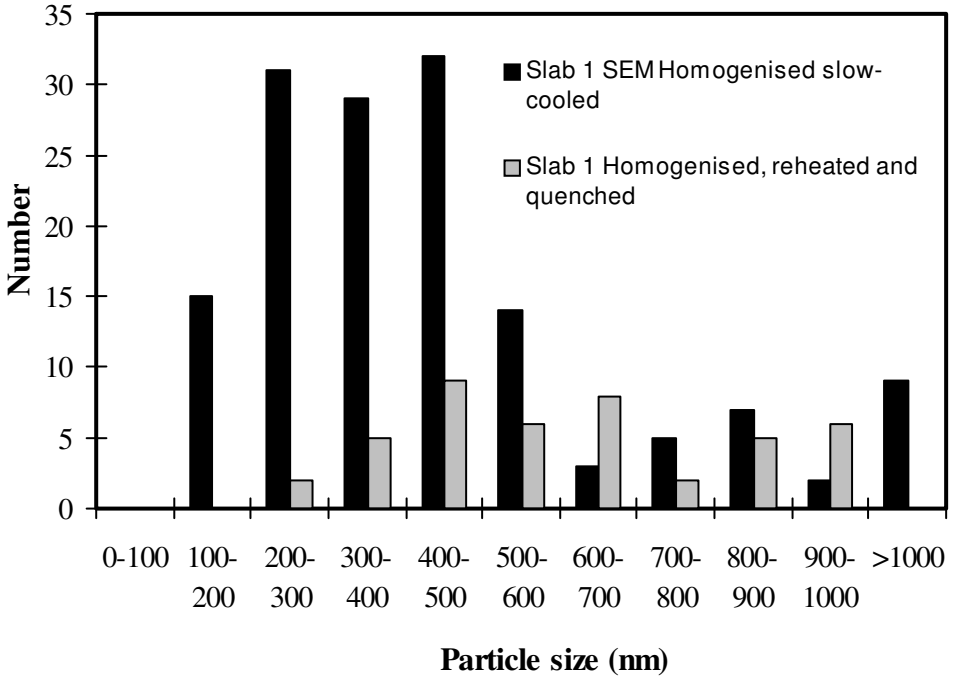

Figure 6.7. Nb(C,N) and TiN particle distribution after homogenisation and after reheating of homogenised sample at 1225 ^{o}C followed by water quench using SEM. Particles were collected from equal number of field of view in both the conditions at 2000 x.

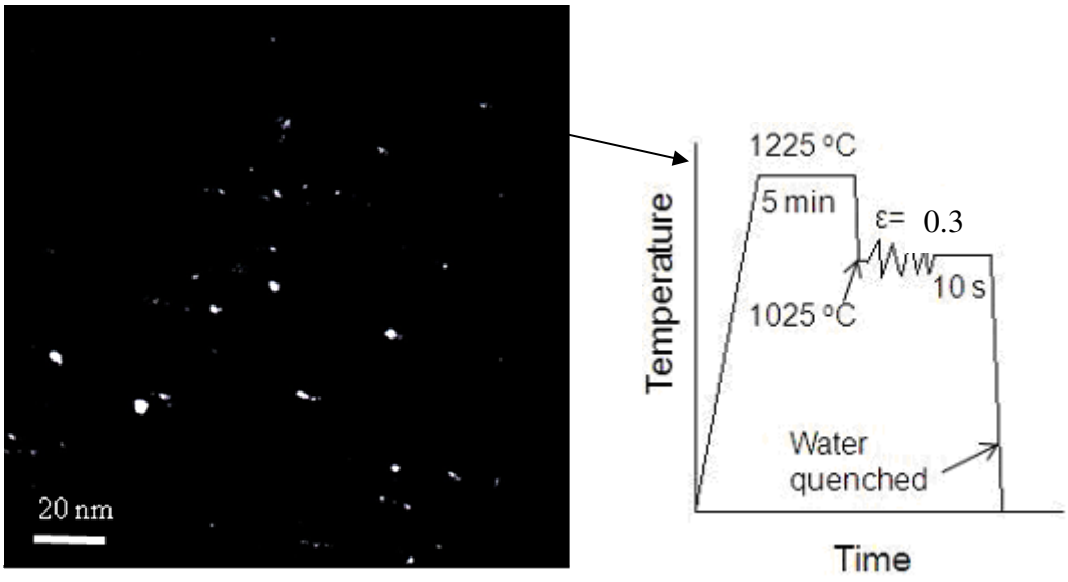
20 nm
1225 °C
5 min
ε= 0.3
10 s
1025 °C
Temperature
Water
quenched
Time

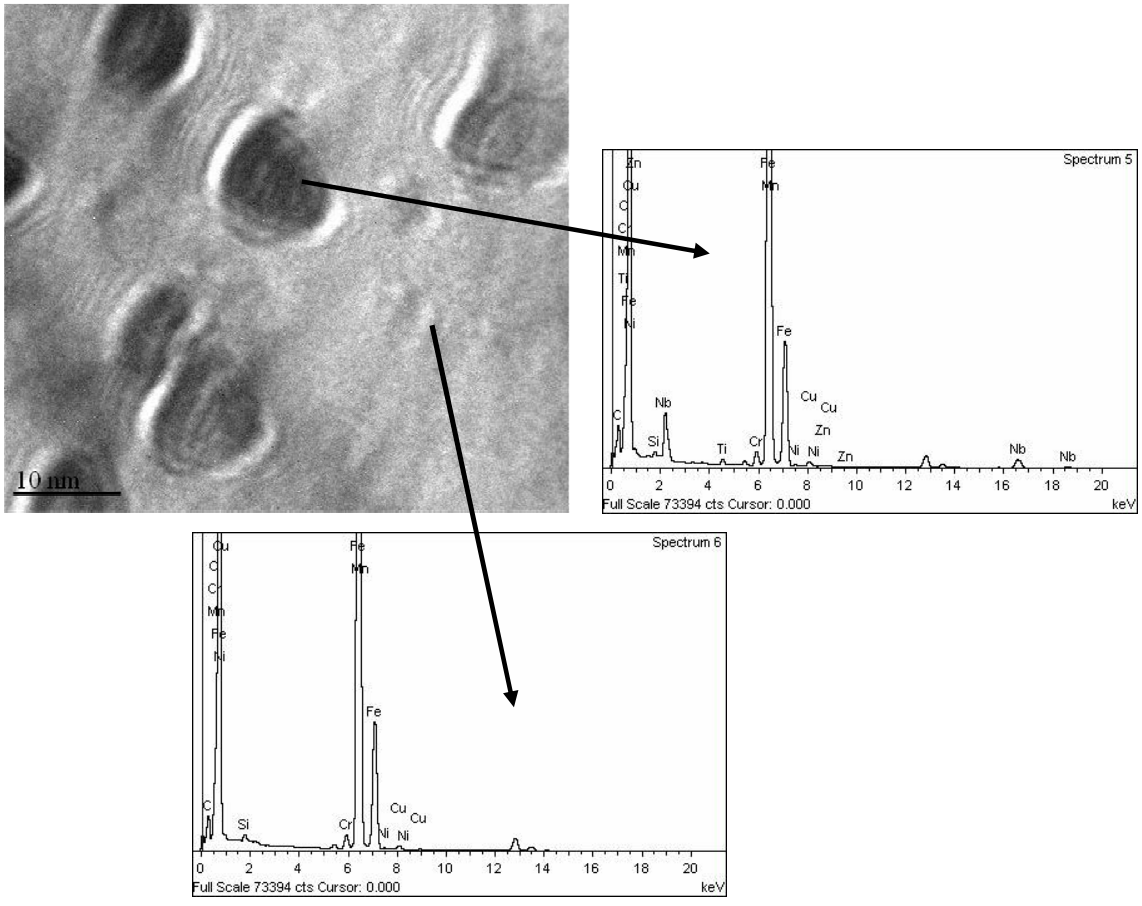
10 nm
Spectrum 5
Full Scale 73394 cts Cursor: 0.000
keV
Spectrum 6
Full Scale 73394 cts Cursor: 0.000
keV

(a)

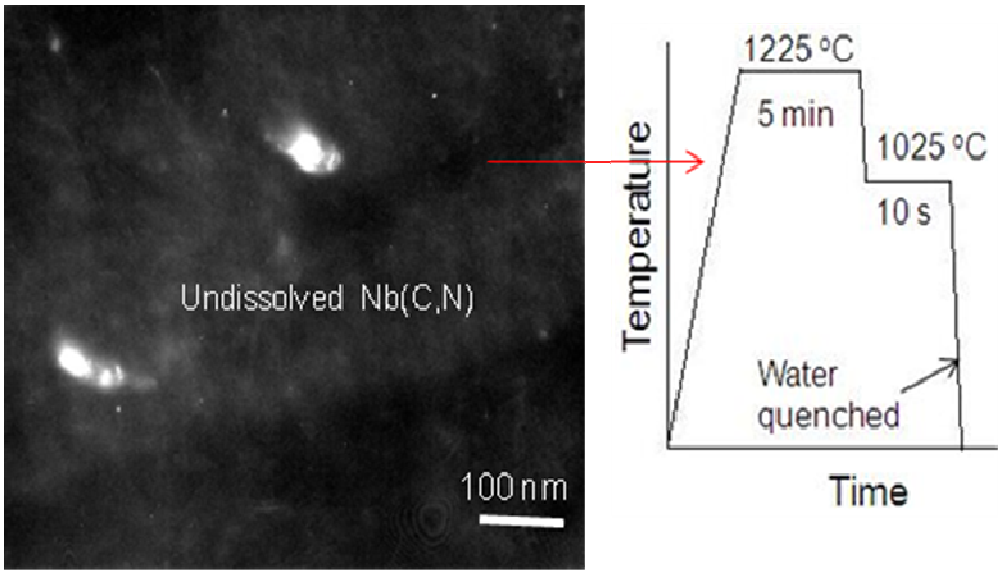
Undissolved Nb(C,N)
100 nm
1225 °C
5 min
1025 °C
10 s
Temperature
Water
quenched
Time

(b)

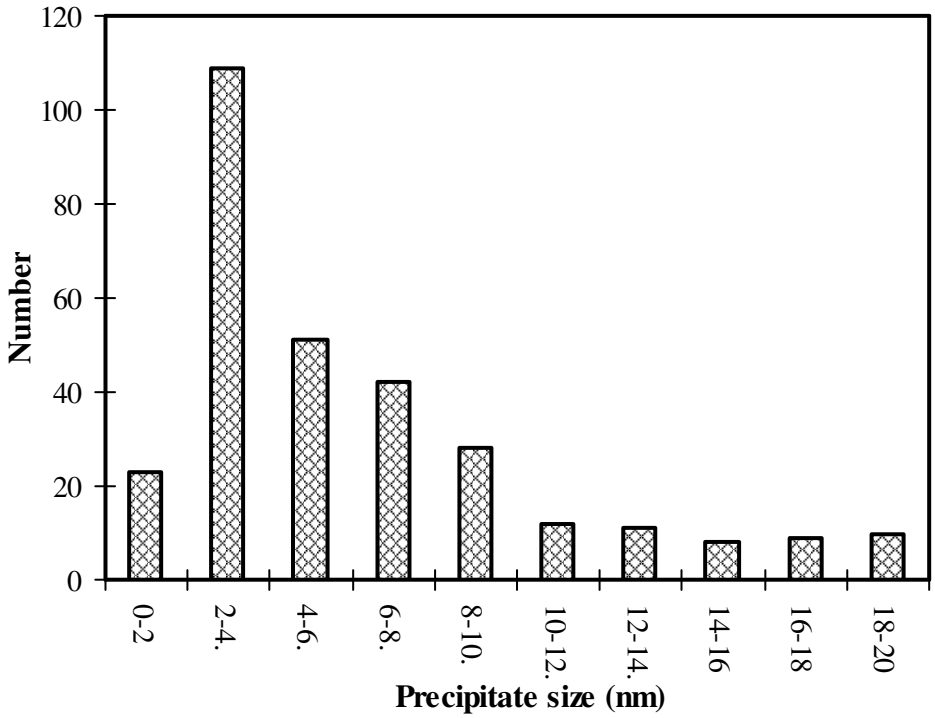
120
100
80
60
40
20
0
Number
0-2
2-4.
4-6.
6-8.
8-10.
10-12.
12-14.
14-16
16-18
18-20
Precipitate size (nm)

(c)

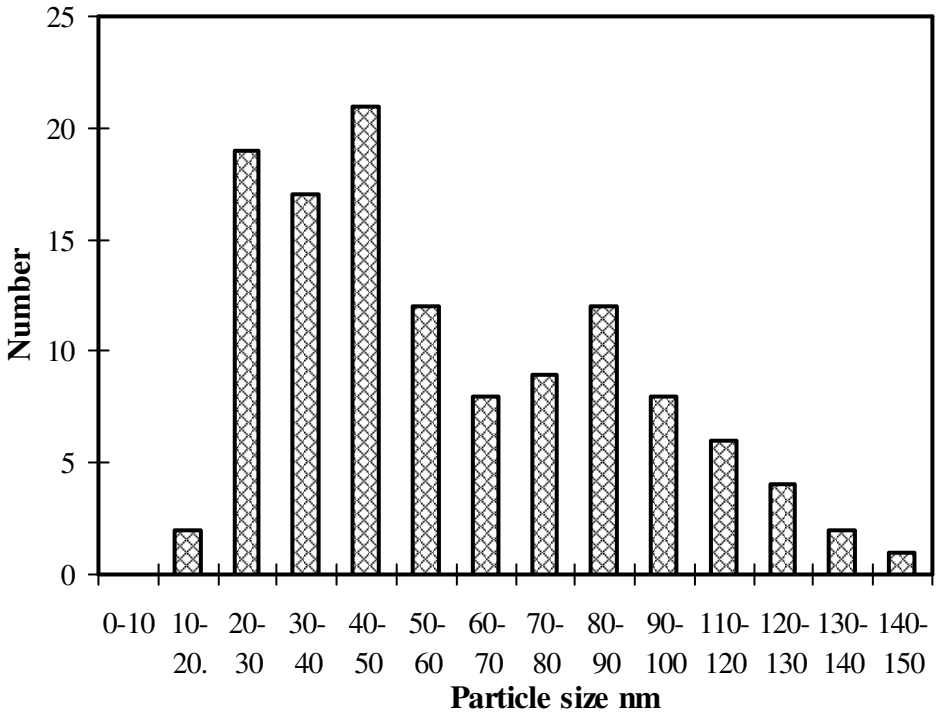

(d)

Figure 6.8. (a) Dark field and bright field TEM images, EDS traces, showing Nb rich precipitates preferably Nb(C,N), and the sample deformation history. Nb(C,N) particles were identified using a <220> pole for the fcc phase. (b) Dark field TEM images and the sample history showing undissolved Nb(C,N) using the same diffraction spot. (c) & (d) are the size distribution of Nb(C,N) from the samples shown in (a) and (b) respectively. Particles were collected from equal number of field of view in both the conditions i.e. from the same area.

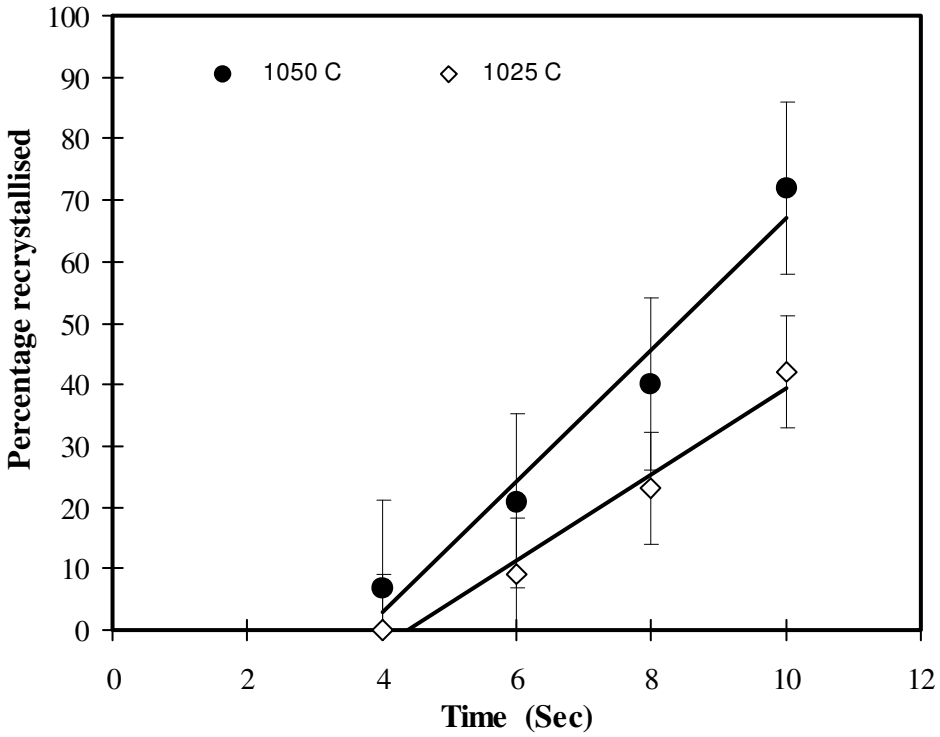

Figure 6.9. Variation of measured amount of recrystallisation with time after deformation at 1050 and 1025 ^{o}C with 0.3 strain.

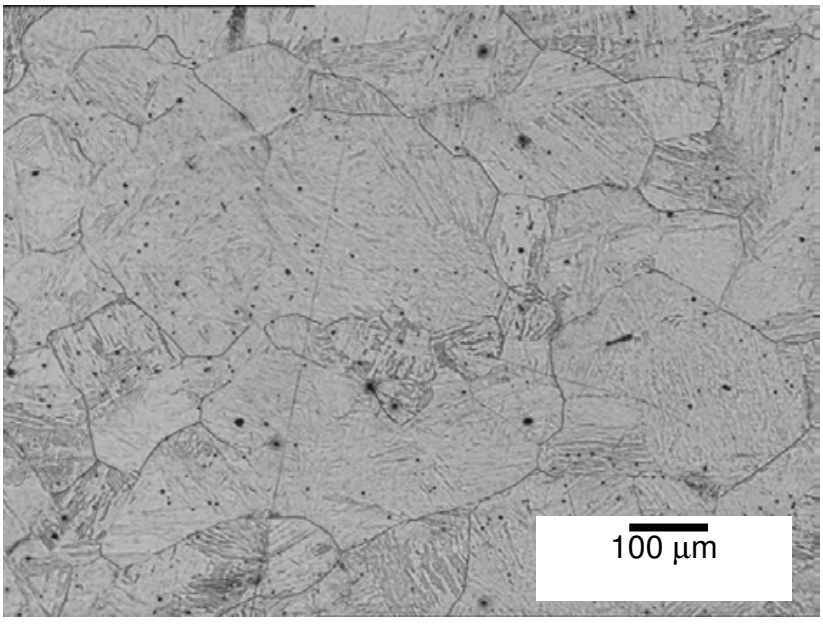

(a)

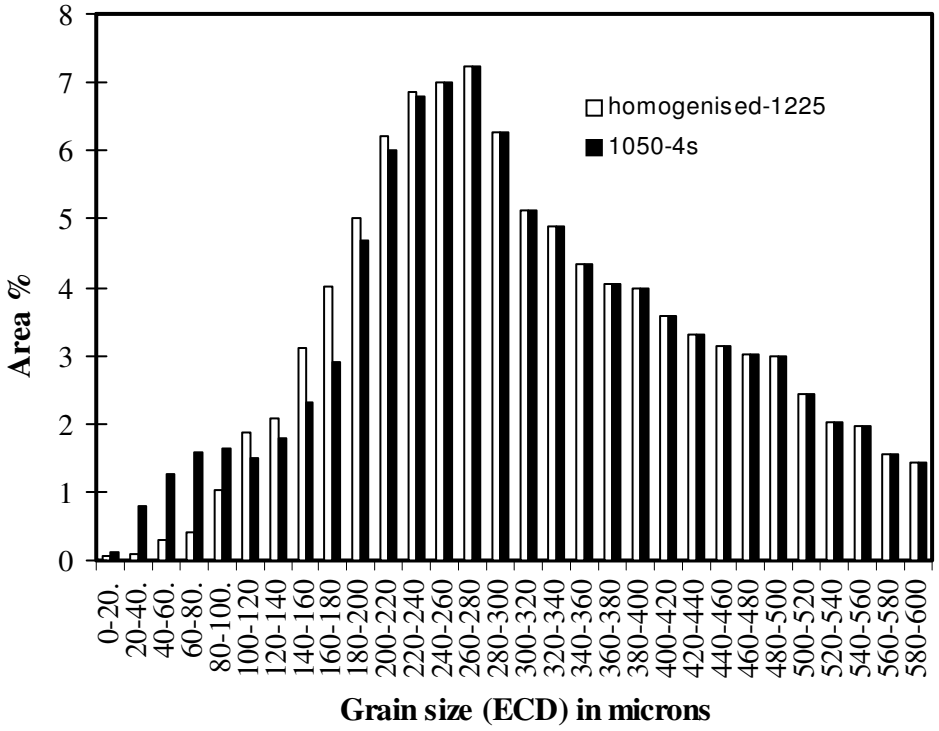
homogenised-1225
1050-4s
Area %
Grain size (ECD) in microns
0-20.
20-40.
40-60.
60-80.
80-100.
100-120
120-140
140-160
160-180
180-200
200-220
220-240
240-260
260-280
280-300
300-320
320-340
340-360
360-380
380-400
400-420
420-440
440-460
460-480
480-500
500-520
520-540
540-560
560-580
580-600

(b)

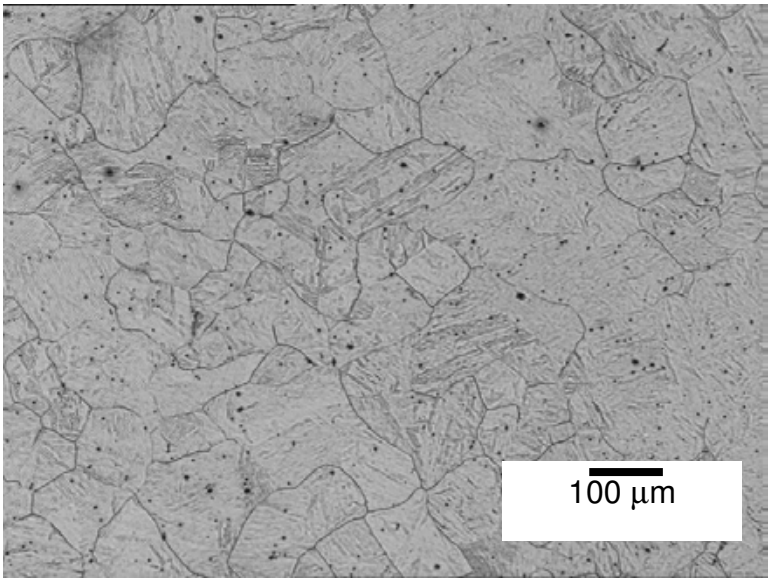
100 µm

(c)

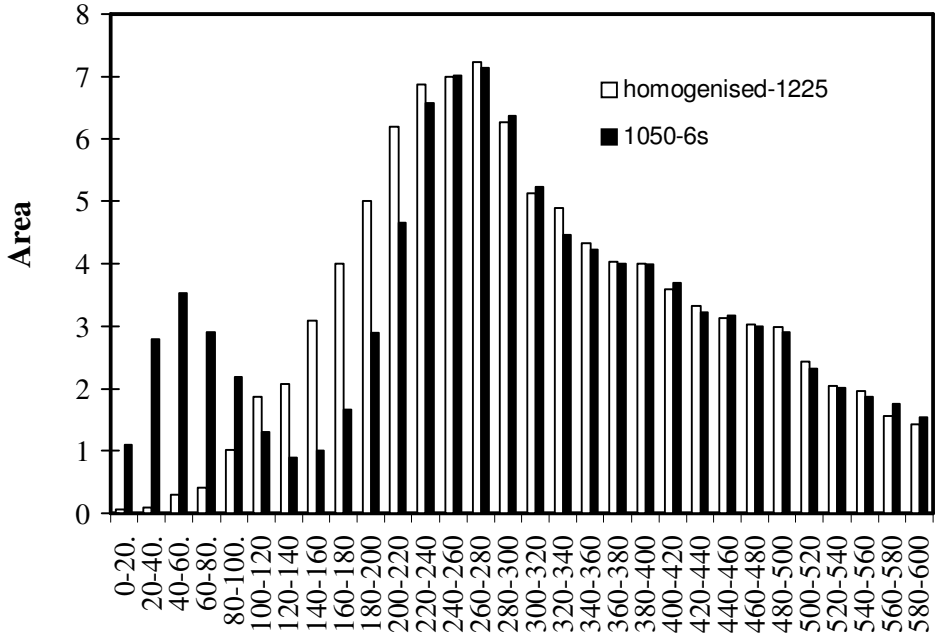

(d)

Figure 6.10. (a) Microstructure and (b) grain size distribution for a sample deformed to a strain of 0.3 at 1050 °C and held at that temperature for 4 s. (c) Microstructure and (d) grain size distribution for a sample deformed to a strain of 0.3 at 1050 °C and held at that temperature for 6 s.

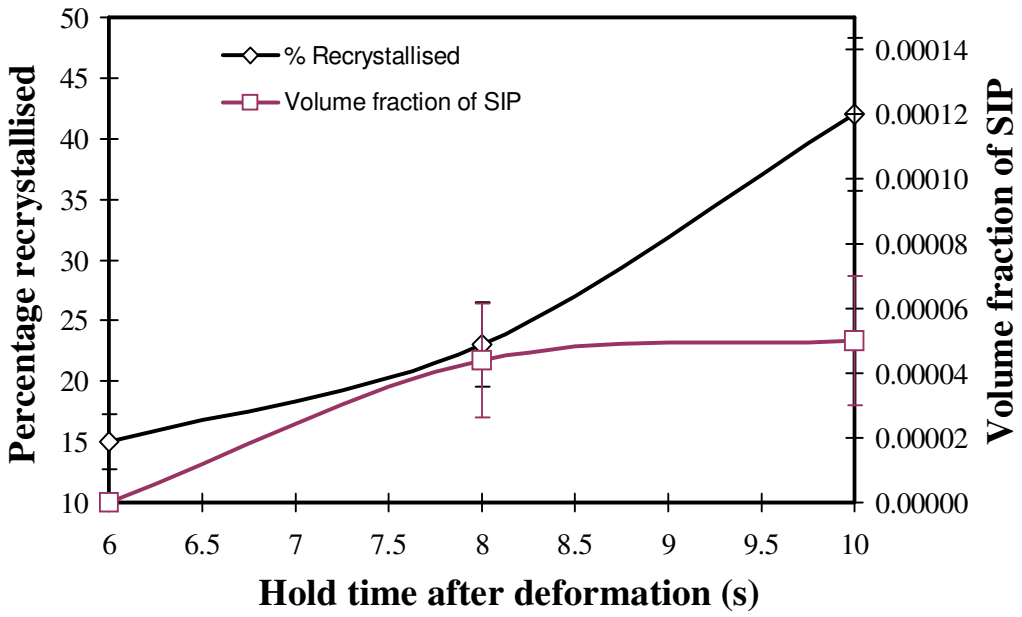

Figure 6.11. The variation of measured % recrystallised and volume fraction of strain induced precipitates (SIP) of Nb(C,N) as a function of hold period after deformation at 1025 °C with 0.3 strain.

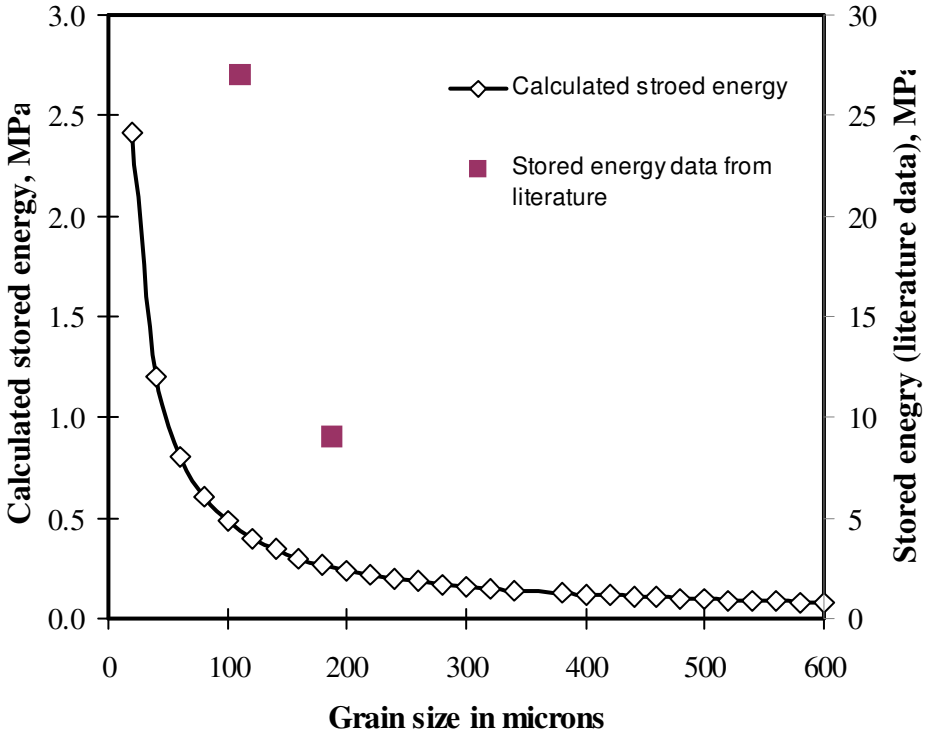

Figure 6.12. Variation of stored energy as a function of grain size using the equation 6.2. Two literature data of measured stored energy from 0.042 wt % Nb [134] and 0.09 wt % Nb [88] steels (measured from increase in flow stress after carrying out double hit tests) were superimposed on the same figure.

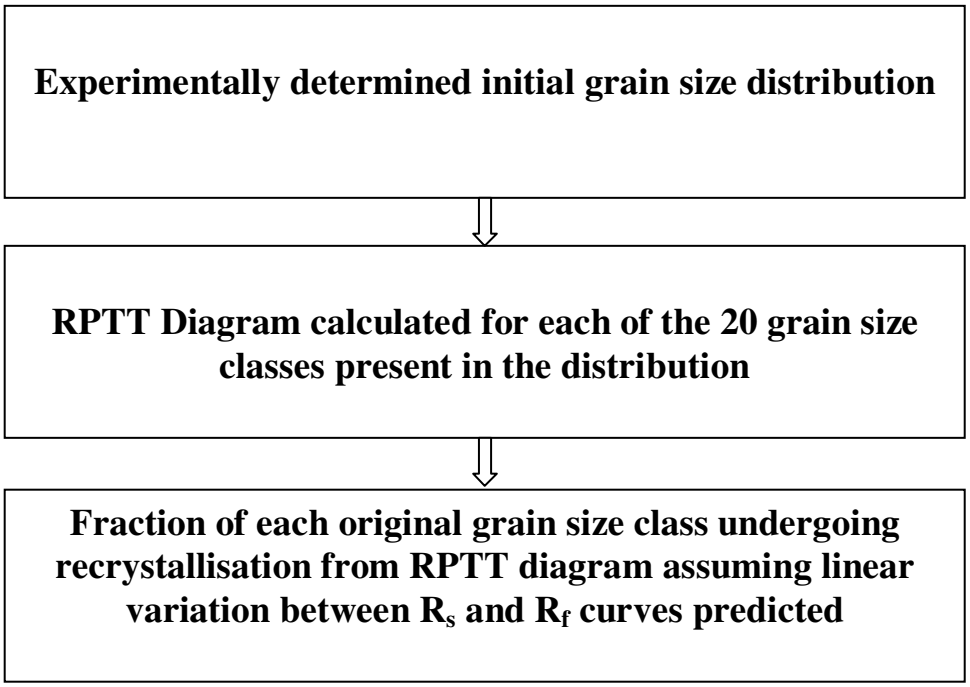

Figure 6.13. Flow diagram showing the modelling approach ('class' prediction) to predict the amount of recrystallisation after deformation.

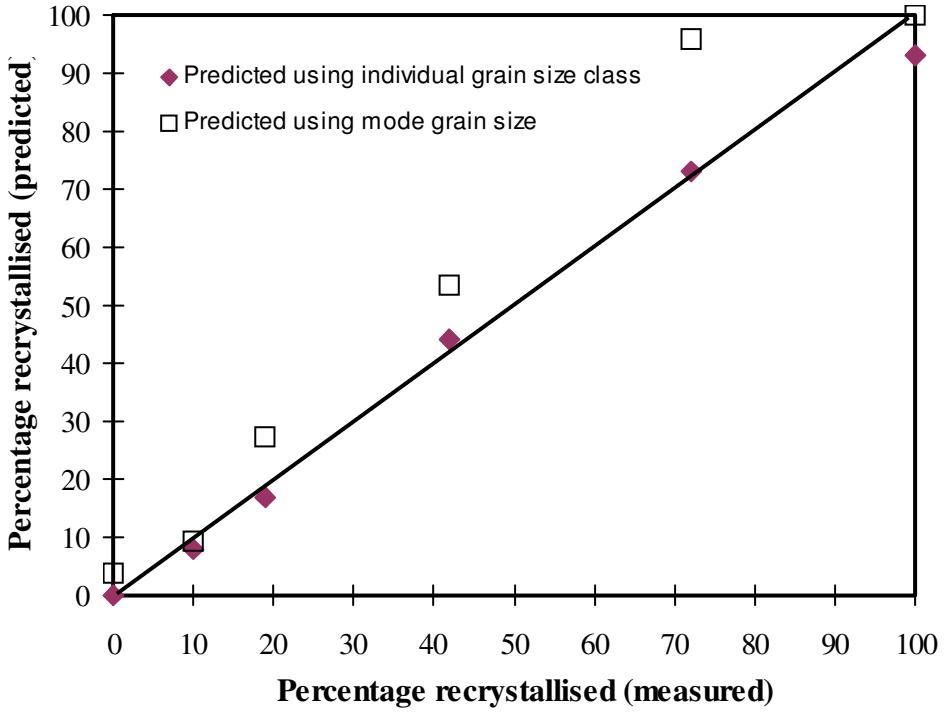

Figure 6.14. Variation of predicted % recrystallised vs the measured amount at 0.3 strain from the present study using the complete starting grain size distribution (individual grain size class) and the mode grain size.

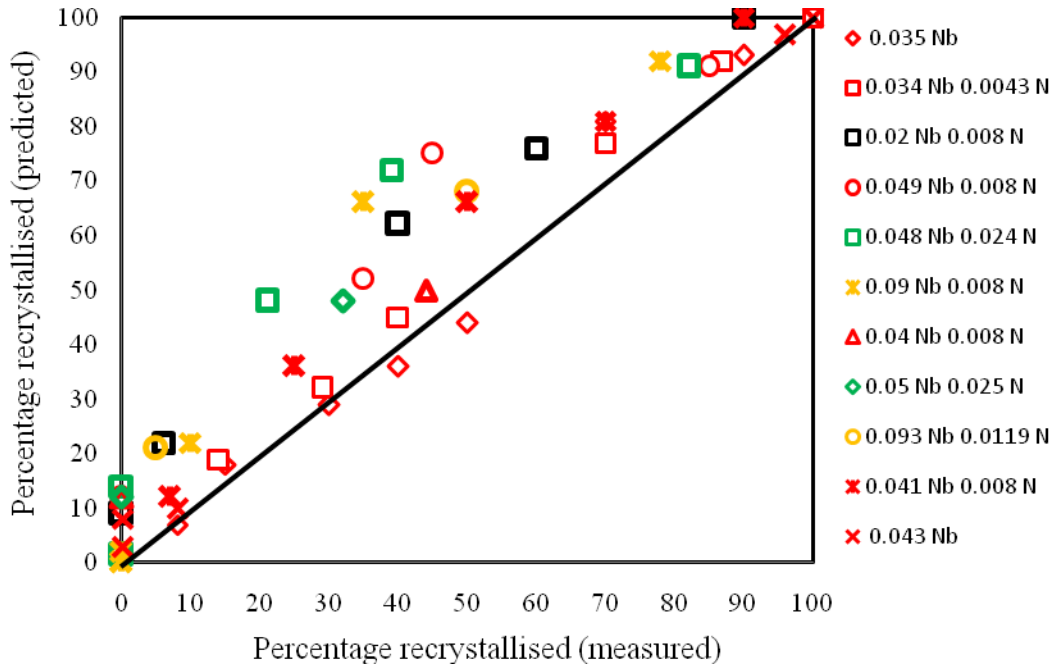

Figure 6.15. The variation of predicted % recrystallised vs the measured amount at 0.3 strain for the literature data using individual grain size class.

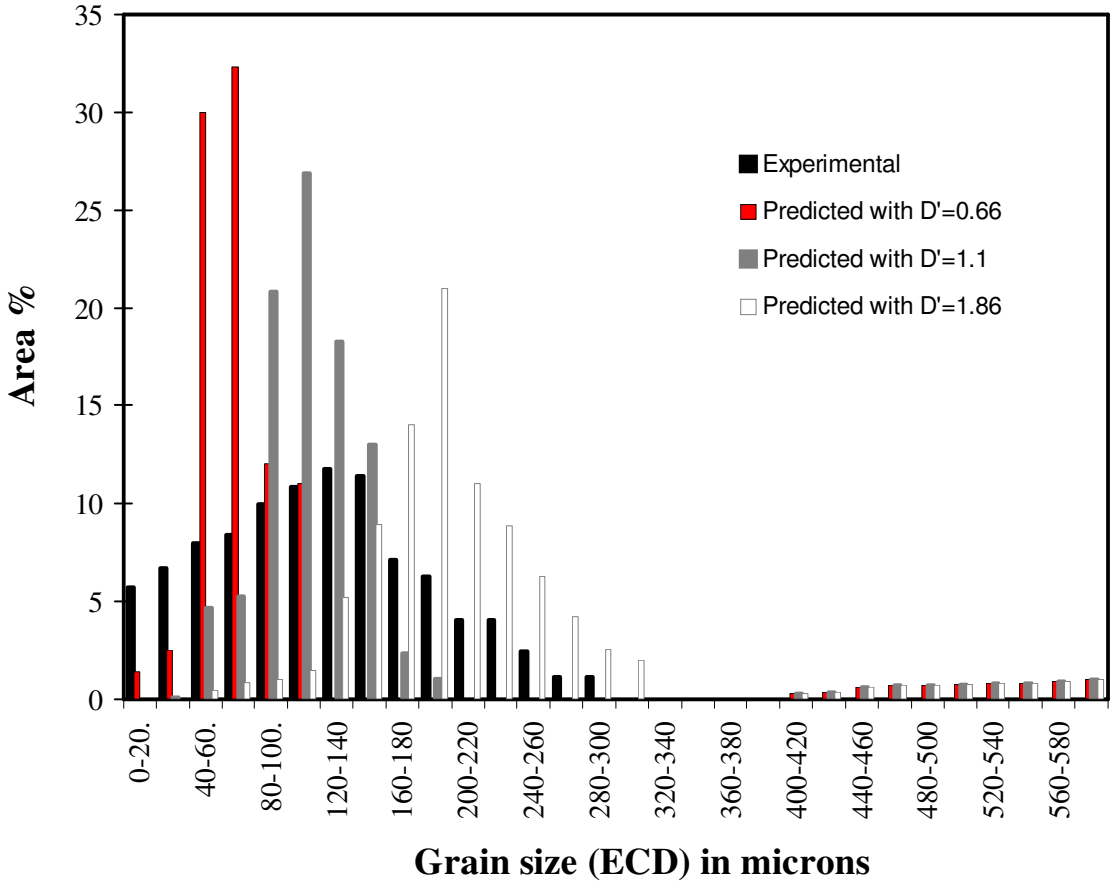

Figure 6.16. Grain size distributions experimentally determined and predicted after deformation at 1075 °C.

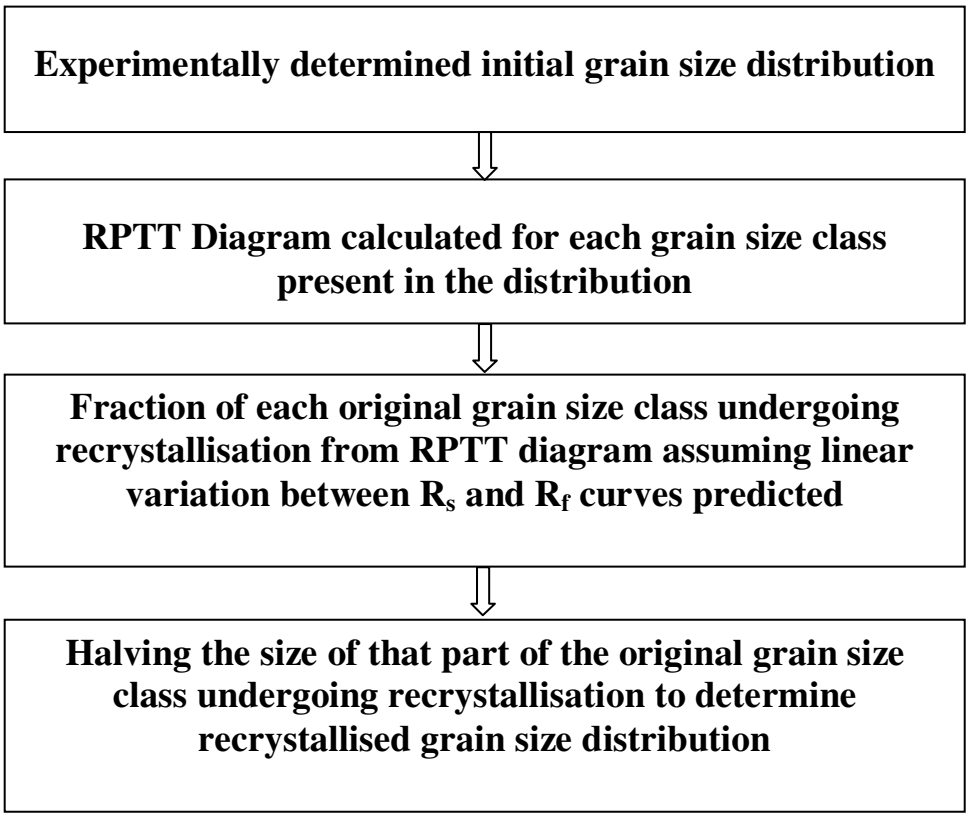

Figure 6.17. Flow diagram showing the modelling approach ('class' prediction) to predict the grain size distribution after deformation.

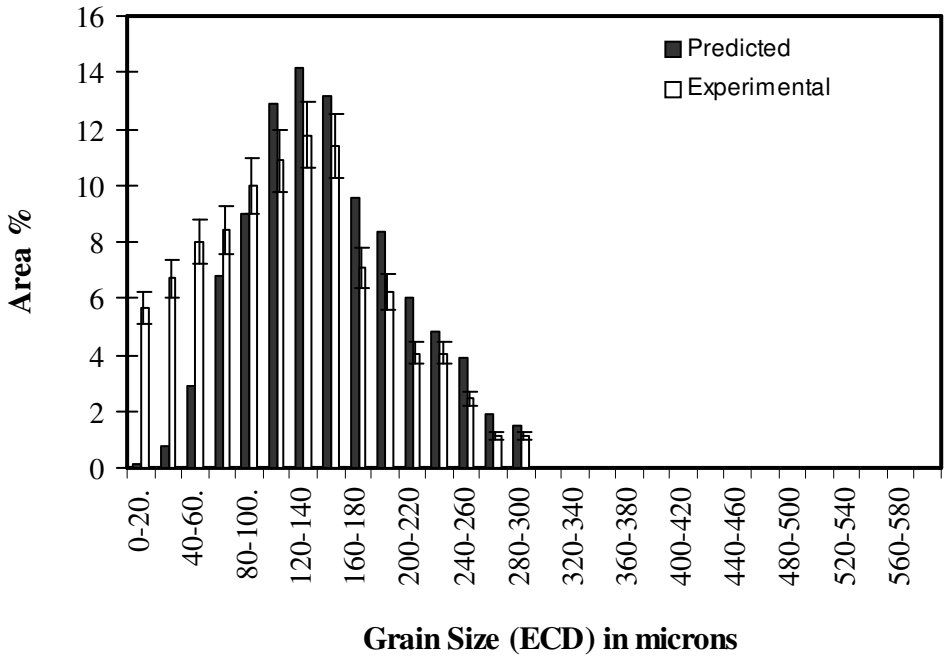

Figure 6.18. Grain size distributions for the sample deformed to a strain of 0.3 at 1075 °C and predicted at that temperature.

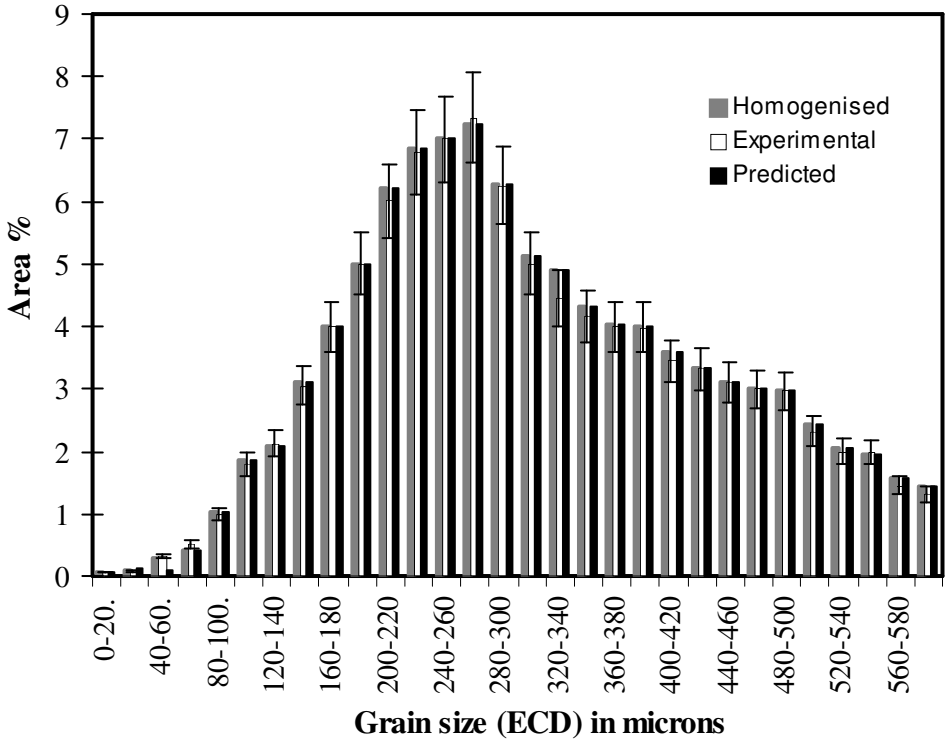

Figure 6.19. Grain size distribution (measured and predicted) for the homogenised sample deformed to a strain of 0.3 at 975 °C.

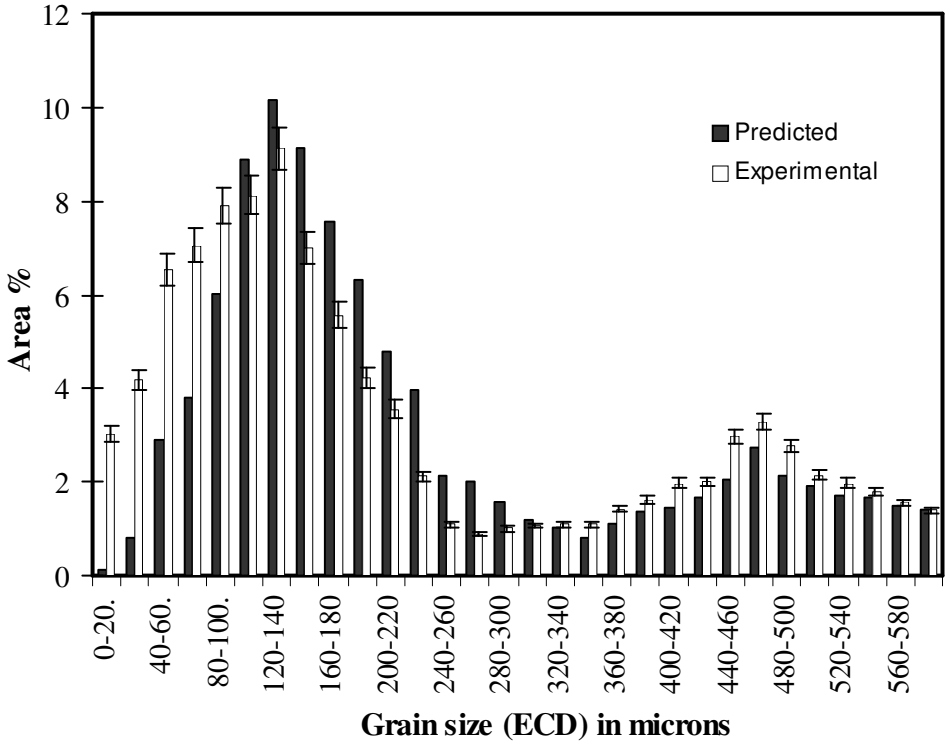

Figure 6.20. Grain size distributions for the homogenised sample deformed to a strain of 0.3 at 1050 °C.

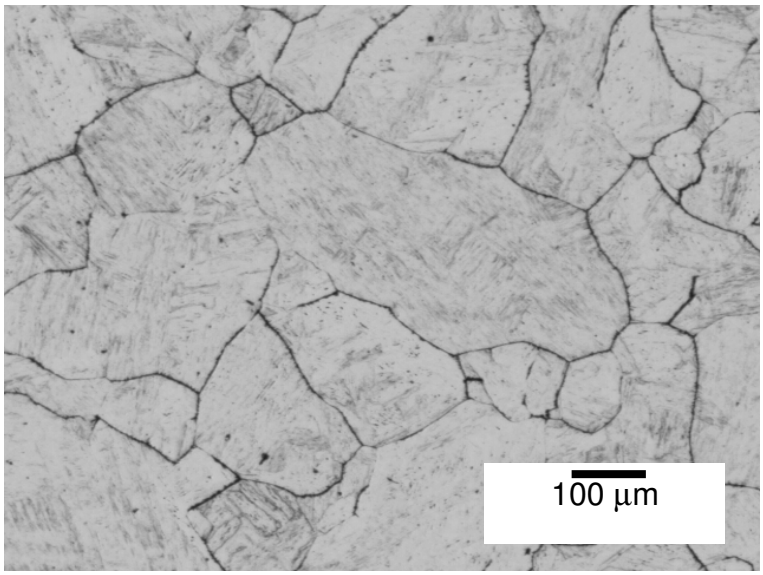

(a)

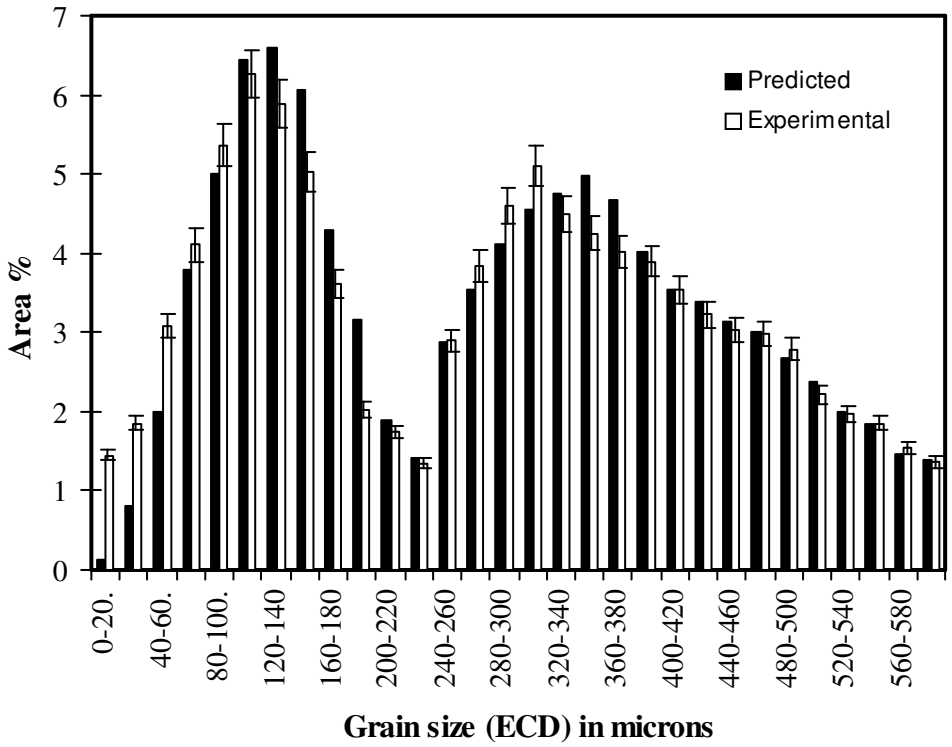

(b)

Figure 6.21. (a) Microstructure and (b) grain size distribution for the sample deformed to a strain of 0.3 at 1025 °C.

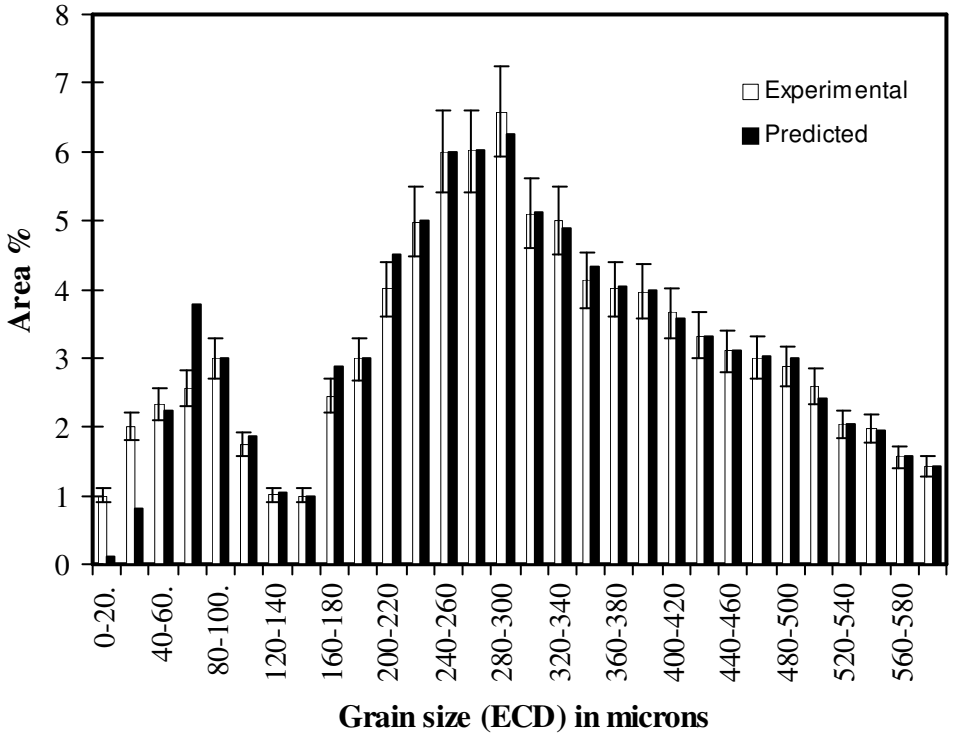

Figure 6.22. Grain size distribution for the sample deformed to a strain of 0.3 at 1010 °C.

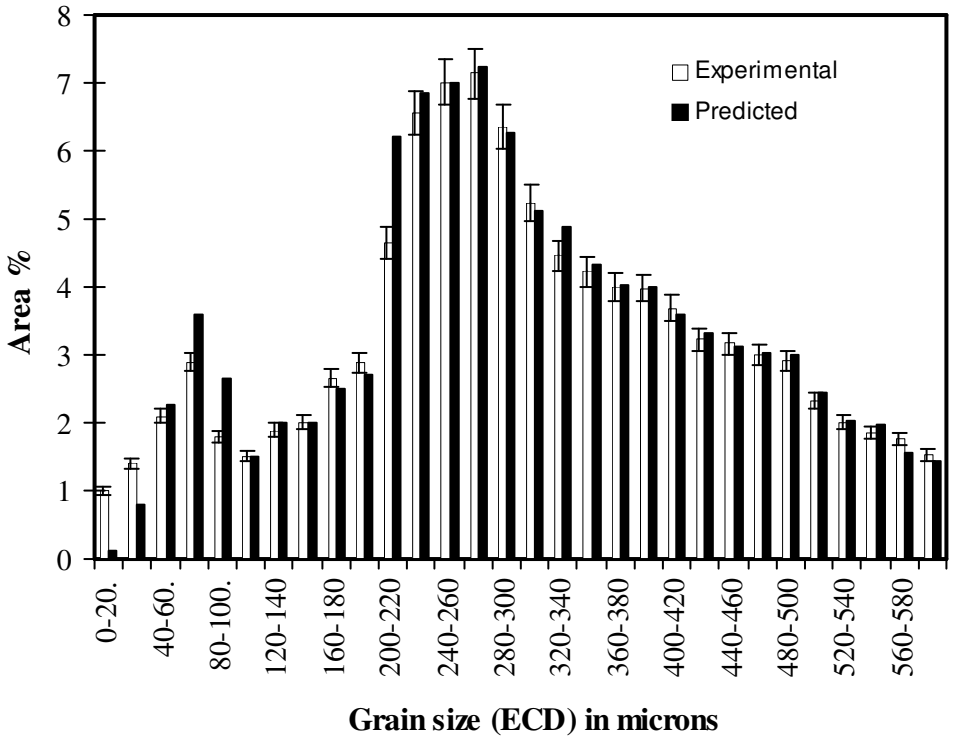

Figure 6.23. Grain size distribution for the sample deformed to a strain of 0.3 at 990 °C after homogenising at 1225 °C.

CHAPTER – 7

Effect of Nb on recrystallisation kinetics

In the previous chapter it was shown that the Dutta-Sellars equations, using an individual grain size class (i.e. considering the starting grain size distribution), predicted the amount of recrystallisation and grain size distribution well for steels with approximately 0.045 wt% Nb, however they did not predict the amount of recrystallisation accurately for the steels with 0.09-0.093 wt % Nb. In order to determine whether the discrepancy is due to deformation-induced precipitation of Nb slowing down recrystallisation a 0.094 wt % Nb steel in the homogenised condition (to avoid any Nb segregation effects) has been investigated, and the results discussed in this chapter.

7.1 As-cast and homogenised microstructure

The as-cast microstructure of the 0.094 wt% Nb slab from the quarter thickness position is shown in Figure 7.1. The secondary dendrite arm spacings was derived from the average of 500 measurements of the centre-to-centre distance between two consecutive secondary dendrite arms, in the direction perpendicular to the arms, within the field of view at 5×. The measured secondary dendrite arm spacing at the quarter thickness position is 150 ± 25 μm. For Nb atoms to diffuse 75 μm, i.e. to reach the dendrite centres and produce a uniform composition, 2-3 days are required at 1225 °C (as discussed in Chapter 5, Figure 5.7).

Samples from the quarter thickness position of the as-cast slab were homogenised at 1225 °C for 4 days leading to a coarse mode grain size of 325 μm and a unimodal grain size distribution, Figure 7.2, albeit skewed to larger grain sizes. Nb levels, determined by

EDS for homogenised and as-cast samples, are shown in Figure 7.3. It can be seen from Figure 7.3 that, in the as-cast sample, there is a periodic variation in the Nb level, with up to 7 times as much Nb in the interdendritic area compared with the dendritic areas. This agrees well with Thermo-Calc predictions for first solid and last liquid compositions, whilst for the homogenised sample there is no systematic variation in the Nb level, indicating that the homogenisation heat treatment was successful.

7.2 Modelling recrystallisation precipitation kinetics for the homogenised steel

A recrystallisation precipitation diagram based on Dutta-Sellars equations [98, 155, 156] was constructed for the homogenised sample using a mode grain size of 325 μm, bulk Nb composition (i.e. 0.094 wt % Nb based on Thermo-Calc prediction of full solubility at 1225 °C) in equations 3.12, 3.16 and 3.17 in Chapter 3 and with an applied strain of 0.3 for holding up to 10 s (Figure 7.4). Although it has been identified in the previous chapter that using the mode grain size the amount of recrystallisation cannot be predicted accurately, Figure 7.4 was used to select the deformation temperatures covering full, partial and no recrystallisation regions.

The predicted recrystallisation-precipitation conditions for the homogenised sample are summarised in Table 7.1. The full recrystallisation temperature refers to the temperature greater than R_f (after 10 s) and no recrystallisation temperature refers to temperature lower than R_s (after 10 s).

From Table 7.1 it can be seen that full recrystallisation is predicted to take place at temperatures above 1090 °C and that there should be no recrystallisation at temperatures

below 1030 °C. Strain-induced precipitation of Nb(C,N) is predicted to start after 2.6 s at 1125 °C and at temperatures below 1090 °C precipitation precedes recrystallisation. The partial recrystallisation region, in the absence of precipitation, is 1030 – 1090 °C, whereas if recrystallisation ceases once 5 % precipitation has occurred there will be no recrystallisation below 1090 °C. Deformation temperatures of 1125, 1090, 1075 and 1050 °C were used for the experiments. Figure 7.4 indicates that, for deformation at 1125 °C, a 10 s hold places the specimen well beyond the recrystallisation finish (85 %) line at this temperature so that close to 100 % recrystallisation should be completed prior to precipitation giving a finer, unimodal grain structure. Deformation at 1090 °C and holding for 10 s should result in 85 % recrystallisation (i.e. definition of R_f) completed, if precipitation has no effect. Lowering the deformation temperature to 1075 and 1050 °C will give partial recrystallisation within the 10 s hold and should lead to the generation of a mixed grain structure, ignoring the influence of precipitation.

7.3 Deformation simulation

Figure 7.5 shows the predicted vs measured percentage of recrystallised from the present study using the original Dutta-Sellars equations, the mode grain size of 325 μm and assuming a linear variation between the 5 and 85 % recrystallisation lines and extrapolating to give 0 to 100 %. From Figure 7.5 it can be seen that there is a discrepancy between predicted and measured percent of recrystallised and this discrepancy is consistent with the trend shown using the literature data for a similar Nb content steel (the orange data points in Figure 6.2 in Chapter 6). The root mean square error (RMS) between predicted and measured amount of recrystallisation is 26.5 %.

It was shown in the previous chapter that using the Dutta-Sellars equations it is possible to predict amount of recrystallisation more accurately by considering the total starting grain size distribution rather than using the mode grain size at 0.3 strain. Figure 7.6 shows the predicted vs measured percentage of recrystallisation from the present study using the Dutta-Sellars equations based on the individual grain size class i.e. considering total starting grain size distribution. From this figure it can be seen that the predicted amount of recrystallisation is more than that measured, as was seen in the case of homogenised Slab 1 (0.045 wt% Nb) steel, although the error was less in that case. The RMS error between the predicted and measured amount of recrystallisation in this steel is 15 %, and was 2 % for homogenised Slab 1 steel discussed in the previous chapter. In the previous chapter it was been pointed out that a 10 % discrepancy between the predicted and measured amount of recrystallisation can occur, based on considering the literature data (Figure 6.15, Chapter 6) even after considering the starting grain size distribution but this is less than the RMS error shown in Figure 7.6 (The dashed line on the figure shows the mean error that can occur even after considering the grain size distribution). It has been shown in Figure 6.15, Chapter 6 that for steels containing 0.09-0.093 wt % Nb the RMS error is 16 %. This is consistent with the error found in the present study. Palmiere et al. [88] quantified the pinning force on recrystallisation due to deformation-induced Nb(C,N) and found that the precipitate pinning force is in excess of driving force of recrystallisation for 0.09 wt % Nb steel. Therefore deformation-induced Nb(C,N) could be a cause of the greater discrepancy between predicted and measured amount of recrystallisation found in this steel.

It has been mentioned in the previous section that precipitation is predicted to precede recrystallisation at temperatures below 1090 ^{o}C. From Figure 7.6 it can be seen that the discrepancy increases with a decrease in deformation temperature (i.e. lower amount of

recrystallisation). This can be explained by the fact that the amount of deformation-induced Nb(C,N) precipitation should increase with a decrease in deformation temperature at constant strain leading to greater discrepancy between predicted and measured amount of recrystallisation at lower deformation temperatures. Although it was pointed out in the previous chapter that deformation-induced precipitates of Nb(C,N) did not have any effect on slowing down recrystallisation at 0.3 strain on homogenised Slab 1 (0.045 wt % Nb steel), the increased amount of Nb in this steel may lead to increased amount of precipitation that could slow down recrystallisation at 0.3 strain. TEM investigation has been carried out to see whether there is any effect of deformation induced Nb(C,N) on slowing down recrystallisation.

7.4 Discussion on influence of deformation-induced Nb(C,N) precipitates on recrystallisation at 0.3 strain

Deformation induced precipitates have been identified following the same procedure as discussed in Chapter 6. TEM investigation was carried out after quenching following the reheat furnace treatment and the 5 minutes hold followed by cooling down to deformation temperature in the Gleeble to determine if any precipitates were present in the samples prior to deformation, as these particles, being coarser in size, will not influence recrystallisation kinetics [12, 99, 100, 112] and should be discarded from subsequent quantification of strain-induced precipitation. The TEM microstructure and the size distributions of the particles present in the sample that has been reheated in Gleeble 3500 to 1225 ^{o}C and the cooled down to 1090 ^{o}C and held at that temperature for 10 s (i.e. representative of pre-existing particles after a deformation simulation hold time) are shown in Figure 7.7. The sample has been held at the deformation temperature for 10 s to see whether any (Ti,Nb)(C,N) precipitates at that temperature without deformation during the

hold period (10 s). A small area fraction (0.000001) of undissolved (Ti,Nb)(C,N) precipitates were identified, with a size (diameter) ranging from 20-140 nm, these were therefore discarded from analysis of any strain induced precipitates subsequently imaged.

Considering Palmiere et al.'s [88] results on 0.09 wt % Nb steel, the maximum discrepancy due to deformation-induced precipitation of Nb(C,N) that exists between the predicted and measured amount of recrystallisation is 31 % (the orange data points in the Figure 6.15 in Chapter 6). The discrepancy in the amount of predicted recrystallisation (96 %) compared to the experimental value (82 %) at 1125 ^{o}C in this work is 14 %, i.e. less than that found in Palmiere et al.'s work. TEM investigation on the sample that has been deformed at 1125 ^{o}C and held at that temperature for 10 s did not reveal the presence of any deformation induced Nb(C,N) particles. This suggests that the discrepancy between predicted and measured amount of recrystallisation at this temperature is not due to deformation-induced precipitation, in this steel. The RMS error that could be present even after considering the grain size distribution is 10 %, as discussed in previous chapter, less than the discrepancy that is present at 1125 ^{o}C. This suggests that the Dutta-Sellars equations taking into account starting grain size distribution are not predicting the amount of recrystallisation accurately for this steel.

In order to determine the possible cause of the discrepancy, the variables that influence R_s need to be considered. The effect of prior austenite grain size on nucleation of recrystallisation and driving force of recrystallisation has been dealt with using the class based prediction. The grain size distribution in this steel after homogenisation ranges between 0-750 μm (Figure 7.2). This is similar to the Slab 1 homogenised grain size distribution, which ranged between 0-600 μm (Figure 5.7 (b), Chapter 5) where the individual grain size class based prediction accurately predicts amount of recrystallisation.

Therefore it is suggested that the grain size distribution does not contribute to the additional error seen for the high Nb steel. As the deformation has been carried out at 0.3 strain, the driving force part i.e. $\varepsilon^{-4}\exp\left(\frac{300{,}000}{RT}\right)$ present in the equation of R_s is the same as used for homogenised Slab 1 at 0.3 strain and can be excluded for causing any additional discrepancy. That leaves the solute drag term i.e. $\exp\left(\left(\frac{2.75x10^5}{T}-185\right)[Nb]\right)$, present in the R_s equation and may indicate that the solute drag of Nb is being underestimated as a function of temperature at this high level of Nb. It has been pointed out in the literature that recrystallisation at higher temperatures is controlled by solute drag of Nb [132]. Therefore the discrepancy between the predicted and measured amount of recrystallisation at 1125 ^{o}C is suggested to be due to the under predicted solute drag using the Dutta-Sellars equations.

The above discussion may also suggest that a discrepancy up to 14 % between measured and predicted amount of recrystallisation may occur for all other deformation conditions due to solute drag in this steel. However if precipitation of Nb(C,N) occurs during deformation then that may reduce the available amount of Nb present in the solution bringing the amount of Nb closer to 0.045 wt % where it has been established that the equation can predict the amount of recrystallisation accurately. The discrepancy due to solute drag of Nb should therefore decrease with a decrease in deformation temperature as a greater amount of Nb(C,N) precipitation during deformation is expected. Therefore the greater discrepancy at lower deformation temperatures i.e. at 1090, 1075 and 1050 ^{o}C cannot be due to solute drag but may be due to deformation-induced precipitation of Nb(C,N).

At 1090 ^{o}C the discrepancy between the predicted and measured amount of recrystallisation is 17 %. Figure 7.8 shows the deformation induced Nb(C,N) particles present in the sample that was deformed at 1090 ^{o}C and held at that temperature for 10 s. The EDS spectrum obtained from the particle shows a Nb peak which is absent in the spectrum from the adjacent matrix. The particle size distribution is shown in Figure 7.9, and the quantification results are summarised in Table 7.2. Deformation-induced particles are very fine in size, average diameter 4 nm (Figure 3.5 Chapter 3) [12, 21]. The size distributions of Nb(C,N) particles present in the deformed sample ranges between 2-20 nm which appears to be characteristic of Nb(C,N) precipitates in a deformed matrix. It should be noted that the number density of Nb(C,N) particles has also increased compared to that present in the reheat simulated sample as the particles were collected from the identical areas in both the conditions i.e. with and without deformation at 1090 ^{o}C and 10 s hold period (Figure 7.7 and Figure 7.9).

At 1090 ^{o}C, with 0.3 strain, precipitation is predicted to start after 0.82 s during the hold period. Deformation simulations were carried out with 6, 8 and 10 s hold period after deformation to determine the progress of recrystallisation with time. In the absence of precipitation, the recrystallised fraction evolves in a monotonic manner as described by the Johnson–Mehl–Avrami–Kolmogorov (JMAK) theory [99, 100, 112]. This should follow the standard sigmoidal shape described by the JMAK theory and going to a recrystallised fraction of 1. However if precipitation has an effect on slowing down recrystallisation then an incomplete recrystallisation curve with a permanent plateau may be obtained [12, 134, 185]. The predicted and measured amounts of recrystallisation as a function of hold period after deformation are shown in Figure 7.10. The discrepancy between the predicted and measured amount of recrystallisation increases with the increase in hold period, which is

opposite to the behaviour shown in Chapter 6, where the predicted amounts of recrystallisation taking into account starting grain size distribution are in good agreement with the measured values at 1050 and 1025 ^{o}C in the homogenised Slab 1 sample. This suggests there might be an influence of deformation-induced Nb(C,N) precipitates slowing down recrystallisation. Although the deformation temperature here is higher than that used in case of homogenised Slab 1 samples, the higher amount of Nb may lead to the formation of larger amount of Nb(C,N) during deformation at higher temperatures. The increased hold period may be expected to lead to an increase in the volume fraction of deformation-induced Nb(C,N) precipitates leading to the increased discrepancy between predicted and measured amount of recrystallisation.

TEM investigation was used to quantify the volume fraction of deformation-induced Nb(C,N) precipitates as a function of hold time after deformation at 1090 ^{o}C. Figure 7.11 shows the variation of the measured amount of recrystallised and the volume fraction of deformation- induced Nb(C,N) precipitates as a function of hold period after deformation. Unlike in Figure 6.11 in Chapter 6 it can be seen that the rate of increase in the recrystallised amount decreases with time whilst the rate of increase in volume fraction of Nb(C,N) increases. The variation of recrystallised fraction with time reaches a plateau after 8 s instead of the sigmoidal shape expected when recrystallisation progresses without any delay. This is associated with deformation-induced Nb(C,N) precipitation [12, 134, 185, 199] as discussed in the previous paragraph. This can be explained by the fact that strain-induced Nb(C,N) precipitates form and pin the defects present in the microstructure, and thereby slow down the recrystallisation kinetics.

Recrystallisation and deformation induced precipitation can be considered as two competing mechanisms. In this case deformation-induced Nb(C,N) precipitation precedes

recrystallisation as predicted, Figure 7.4 and therefore the significant amount of precipitates that form (volume fraction of Nb(C,N) is 0.00008 after 8 seconds, which is 33 % of the equilibrium amount of precipitates predicted at that temperature) can slow down recrystallisation, which appears to be happening after 8 s. The increased volume fraction of precipitates during the hold period increases the Zener drag [75] due to precipitate pinning as the average size of the particles remains approximately the same (Table 7.2) with increased volume fraction and results in a reduced rate of recrystallisation. The dark field TEM image (Figure 7.8 (b)) taken from the sample which had been deformed to a strain of 0.3 at 1090 ^{o}C and held at that temperature for 10 s, shows a fine scale Nb(C,N) particle distribution, which is typical of strain-induced precipitates [12, 21, 23, 88, 134, 164, 165]. Direct evidence of particles nucleating on dislocations has not been seen as the matrix microstructure consists of martensite and bainite which alters the dislocation structure that forms during deformation. In summary, the results suggest that at this temperature the high level of deformation-induced Nb(C,N) precipitates in the 0.094 wt% Nb steel is the cause of the discrepancy between the measured and predicted amount of recrystallisation.

Deformation simulations were also carried out at 1075 and 1050 ^{o}C with 0.3 strain and 10 s hold period after deformation. At 1075 ^{o}C the discrepancy between the predicted and measured amounts of recrystallisation is 18 % (17 % at 1090 ^{o}C) and the measured volume fraction of strain induced precipitates is 0.00012. At 1050 ^{o}C no recrystallisation has been measured and the measured volume fraction of strain-induced particles is 0.00019. Figure 7.12 shows how the discrepancy between predicted and measured amounts of recrystallisation varies with the measured volume fraction of strain-induced precipitates. The graph shows that the discrepancy increases with the increase in volume fraction of

deformation induced precipitates. Therefore a greater volume fraction of deformation-induced precipitates generates greater Zener drag (particle size distribution is approximately the same) leading to a greater amount of discrepancy between the predicted and measured amounts of recrystallisation and recrystallisation can be halted with 0.00019 volume fraction of particles at 1050 ^{o}C. It has been shown in Chapter 6 that 0.00002 volume fraction of deformation-induced Nb(C,N) particles that form after deformation at 1050 ^{o}C with 0.3 strain and 10 s hold period in Slab 1 homogenised steel (0.045 wt % Nb) does not have any influence on slowing down recrystallisation kinetics at that temperature. This suggests that the presence of strain-induced particles is not enough; it needs to be greater than 0.00019 volume fraction of deformation-induced Nb(C,N) to stop recrystallisation at this temperature in homogenised 0.094 wt % Nb steel.

The above discussion has indicated the a minimum of 17 % discrepancy could be introduced due to strain-induced Nb(C,N) particles slowing down the progress of recrystallisation in the 0.094 wt % Nb steel. In the absence of strain-induced precipitation 14 % discrepancy can occur between the predicted and measured amount of recrystallisation, as was shown for the 1125 ^{o}C deformation simulation and this is linked to under predicted solute drag with the higher amount of Nb. In the previous chapter it was shown that a 10 % RMS error could occur between the measured and predicted amount of recrystallisation after considering the starting grain size distribution for prediction. Therefore the greater discrepancy that exists in this steel is due to deformation-induced Nb(C,N) slowing down recrystallisation at temperatures below 1090 ^{o}C and under predicted solute drag at a temperature of 1125 ^{o}C. In order to predict the amount of recrystallisation accurately the temperature dependence of solute drag needs to be considered, which was not in the scope of the present investigation.

7.5 Conclusions

The validity of the original and modified Dutta-Sellars equations in quantifying the amount of recrystallisation has been examined for a 0.094 wt % Nb steel in an homogenised condition. The major findings are as follows:

1. The modified approach of predicting the amount of recrystallisation using the starting grain size distribution over predicts the amount of recrystallisation in a 0.094 wt % Nb steel after deformation at 0.3 strain.

2. TEM quantification of deformation-induced particles of Nb(C,N) has shown that they slow down the recrystallisation kinetics at temperatures below 1090 ^{o}C when a volume fraction greater than 0.00008 forms.

3. The error in prediction is due to the combined effect of enhanced levels of deformation-induced precipitation of Nb(C,N) at temperatures below 1090 ^{o}C and under predicted solute drag at a temperature of 1125 ^{o}C.

Tables and Figures

Table 7.1. Predicted recrystallisation precipitation behaviour after homogenisation based on mode grain size of 325 μm.

Region	Temperature range (°C) in absence of precipitation
Full recrystallisation within 10 s after strain to 0.3	T > 1090
Partial recrystallisation within 10 s after strain to 0.3	1030 < T < 1090
No recrystallisation within 10 s after strain to 0.3	T < 1030

Table 7.2. Summary of the TEM quantification of strain induced Nb(C,N) precipitates after deformation at 0.3 strain.

Deformation temperature (^{o}C)	Hold period after deformation (s)	Average particle size (nm)	Volume fraction, F_v (deformed)	Volume fraction, F_v (without deformation)	Volume fraction, F_v (predicted using Thermo-Calc)
1090	10	4.2	0.000094	0.000001	0.00024
	8	3.9	0.00008		
	6	4.1	0.000076		
1075	10	3.6	0.00012	0.0000029	0.00031
1050	10	3.7	0.00019	0.000005	0.00039

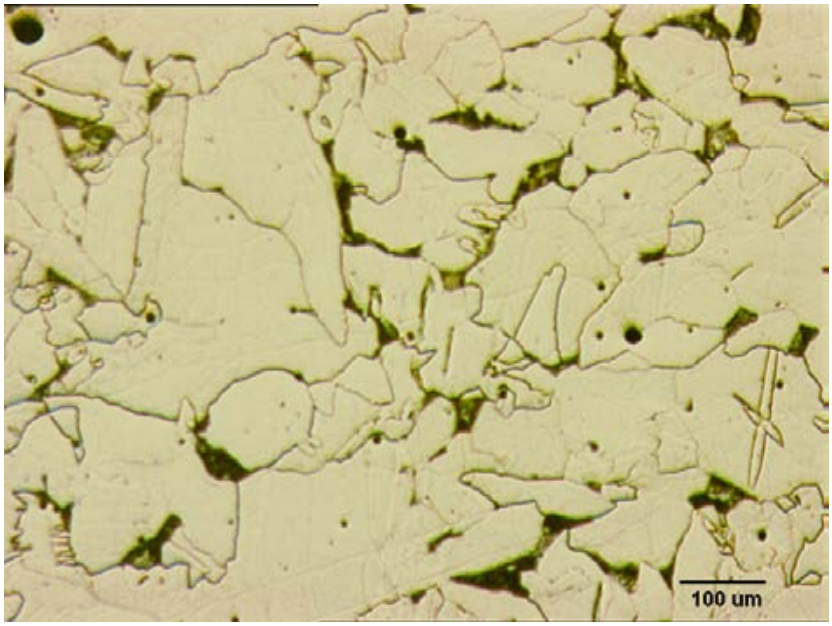

Figure 7.1. The as-cast microstructure of a 0.094 wt % Nb steel at the quarter thickness position.

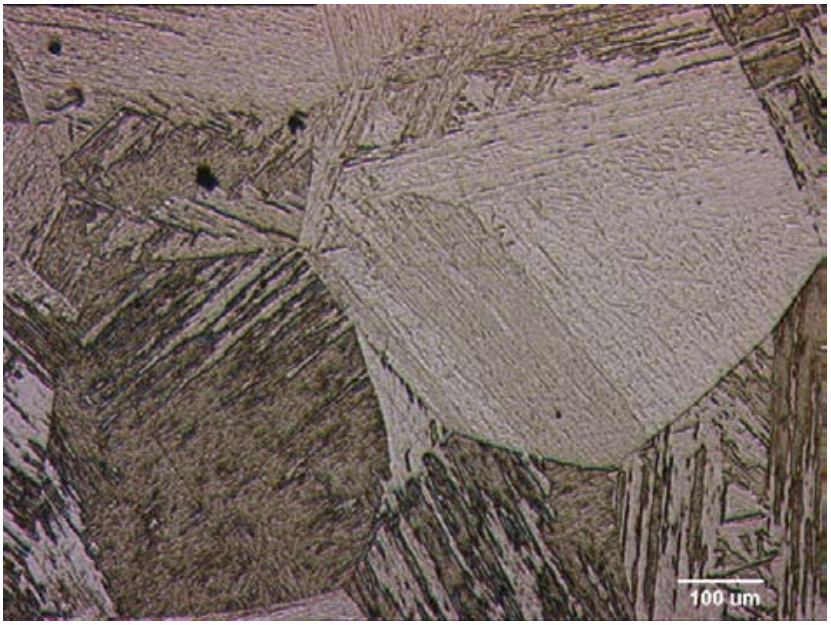

(a)

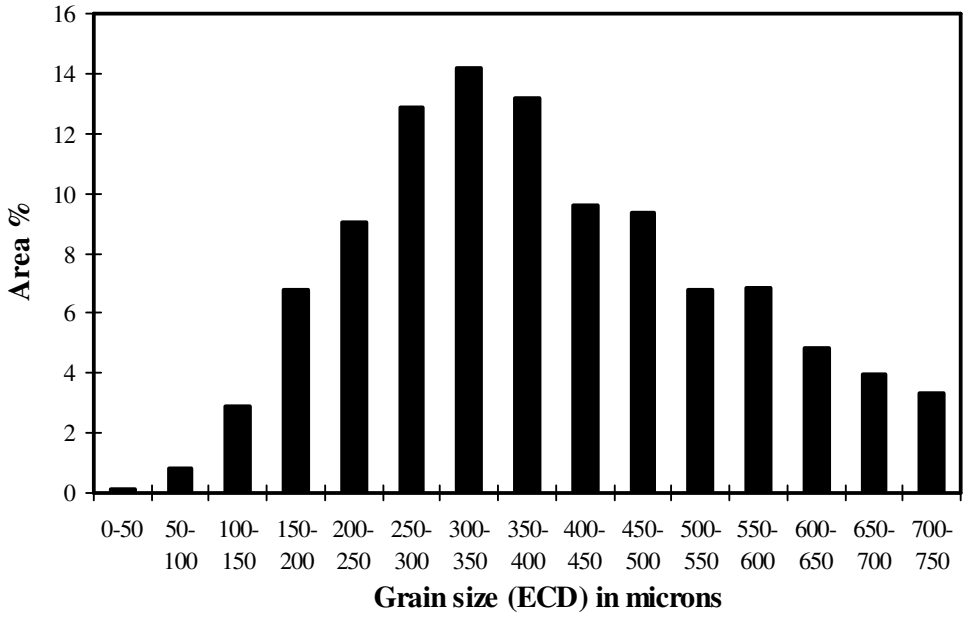

(b)

Figure 7.2. (a) Microstructure (as-quenched) and (b) prior austenite grain size distribution for the homogenised reheated sample.

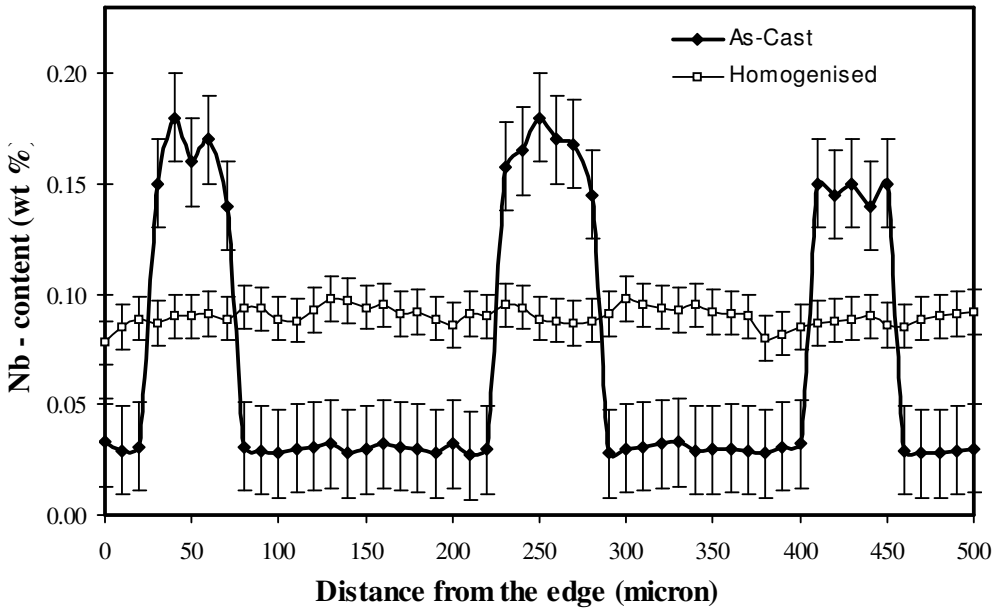

Figure 7.3. Nb distribution in the as cast and homogenised samples plotted as a function of distance from the edge of the sample.

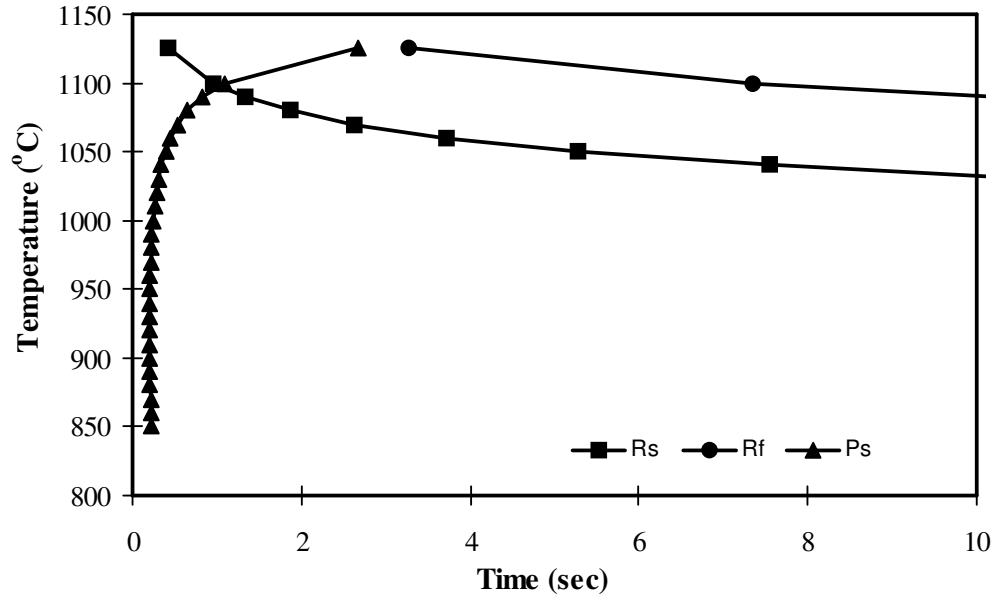

Figure 7.4. Recrystallisation – precipitation diagram based on a mode grain size of 325 µm for a sample reheated to 1225 °C assuming uniform composition, where R_s and R_f are 5 and 85% of recrystallisation and P_s is 5% deformation-induced precipitation.

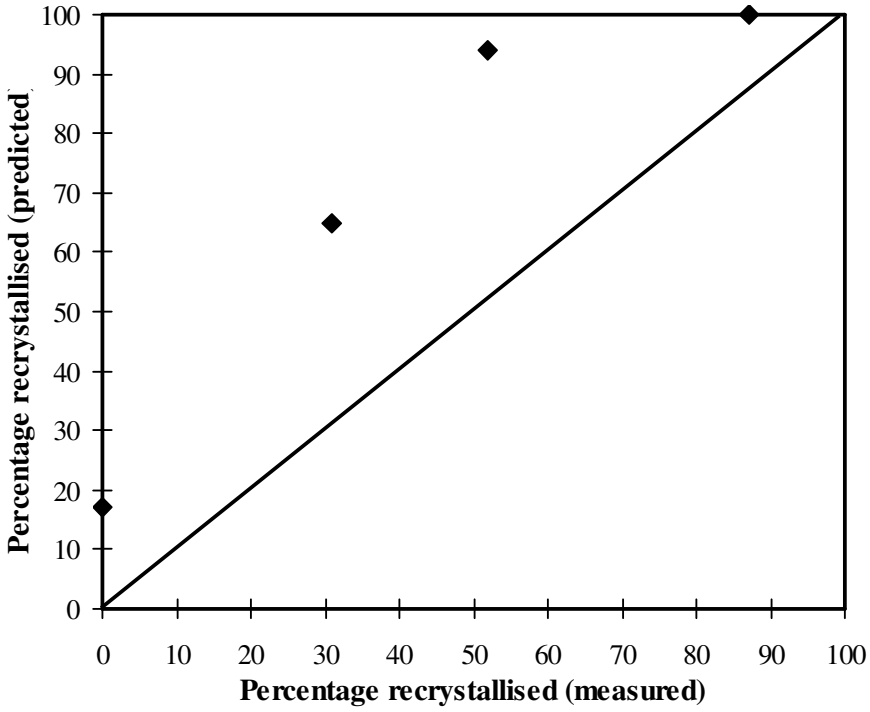

Figure 7.5. The variation of predicted % recrystallised vs the measured amount at 0.3 strain from the present study. The deformation simulations were carried out at temperatures 1125, 1090, 1075 and 1050 ^{o}C. The prediction was carried out using the mode grain size of 325 μm and original Dutta-Sellars equation.

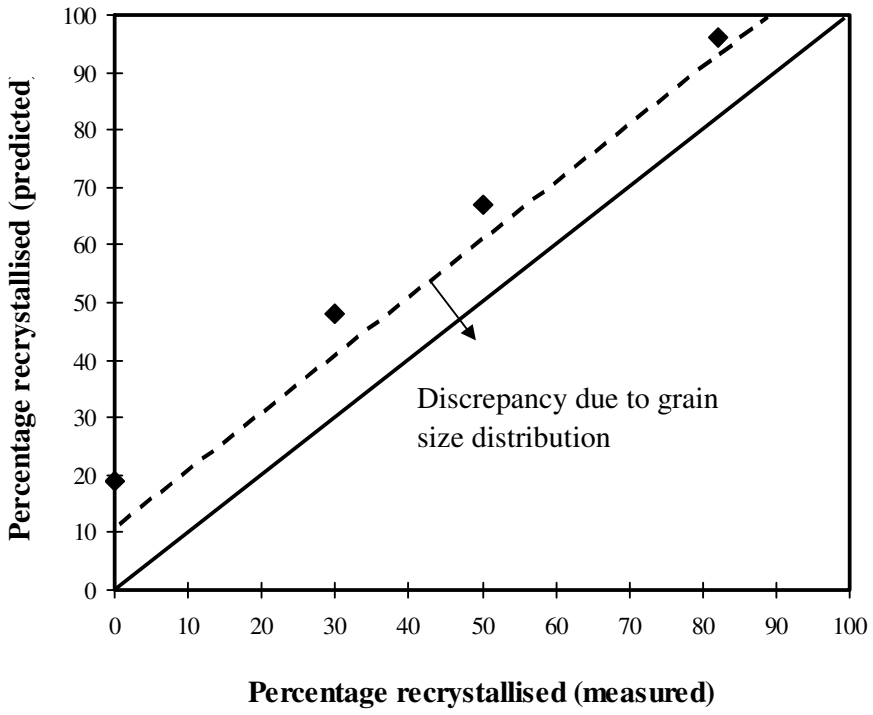

Figure 7.6. The variation of predicted % recrystallised vs the measured amount at 0.3 strain from the present study using the complete starting grain size distribution (individual grain size class).

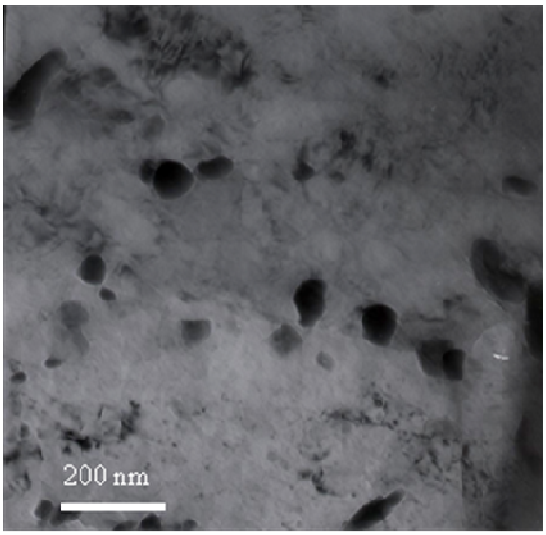

(a)

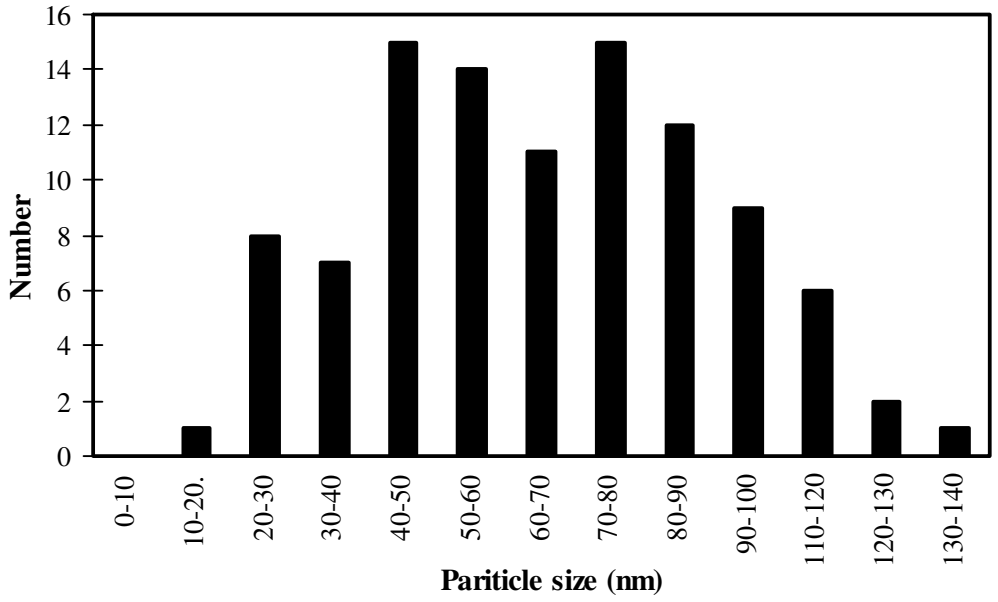

(b)

Figure 7.7. (a) TEM micrograph and (b) Size distribution of Nb(C,N) particles present in the sample that was reheated to 1225 ^{o}C and then cooled down to 1090 ^{o}C, held at that temperature for 10 s and then quenched in water.

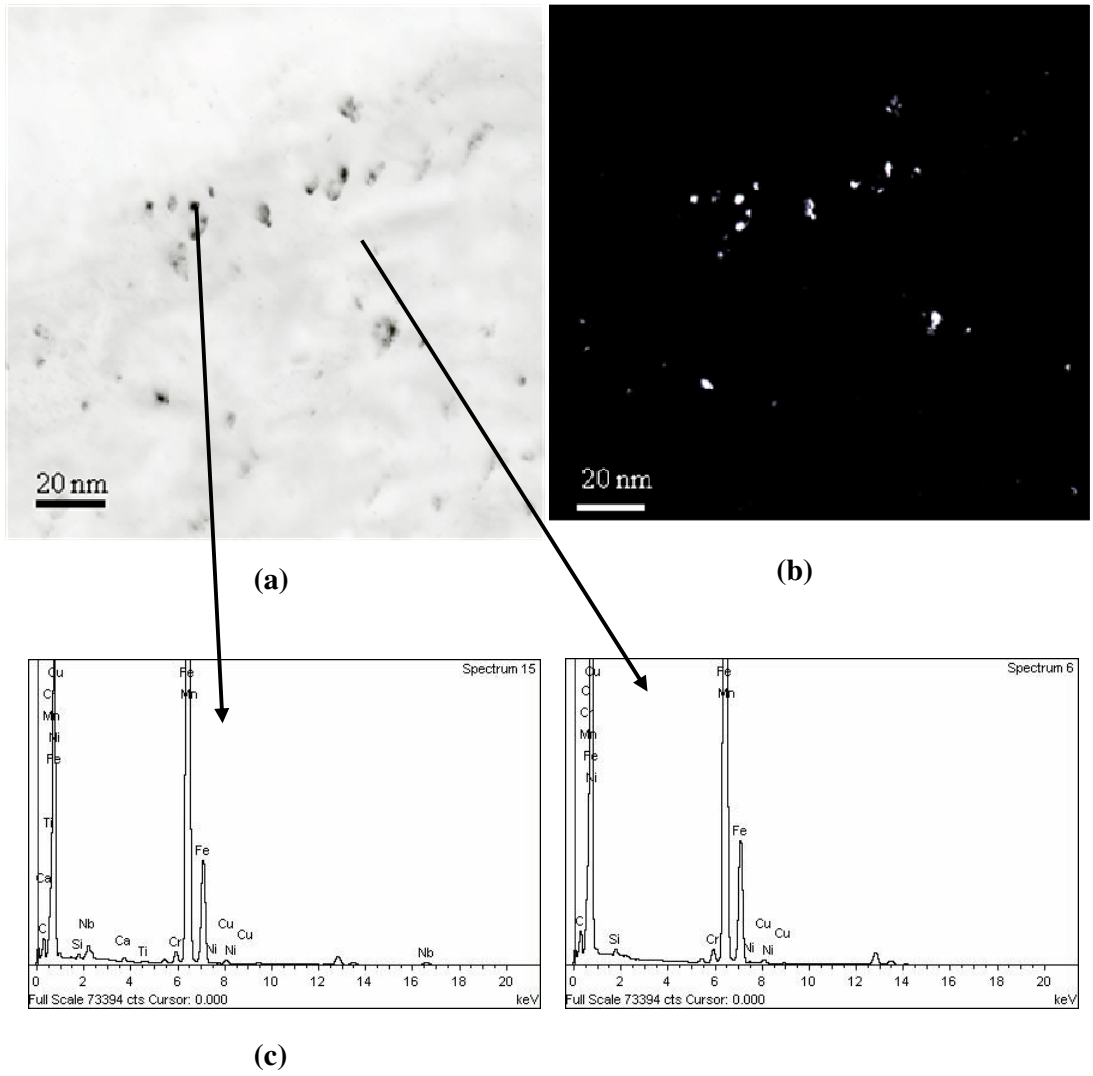

Figure 7.8. (a) Bright field, (b) dark field TEM image (Nb(C,N) particles were identified using the <220> pole for the fcc phase) and (c) EDS trace, showing Nb rich precipitates in a sample that was reheated to 1225 ^{o}C, cooled down to 1090 ^{o}C, deformed to a strain of 0.3, held at that temperature for 10 s and then quenched in water.

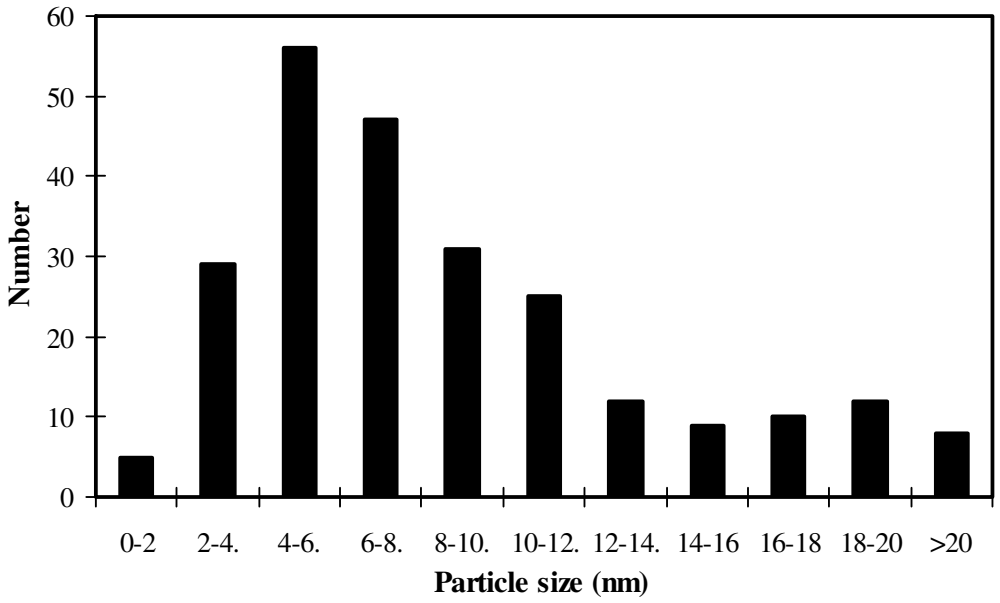

Figure 7.9. Size distribution of Nb(C,N) particles present in the sample that was reheated to 1225 ^{o}C, cooled down to 1090 ^{o}C, deformed to a strain of 0.3, held at that temperature for 10 s and then quenched in water.

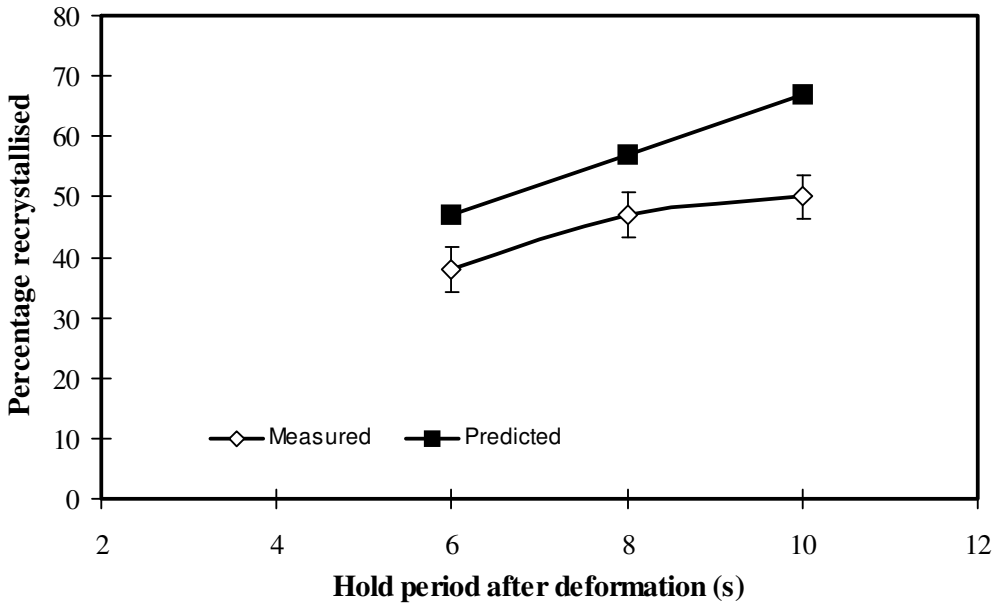

Figure 7.10. Variation of measured and predicted amount of recrystallisation as a function of hold period at 1090 °C.

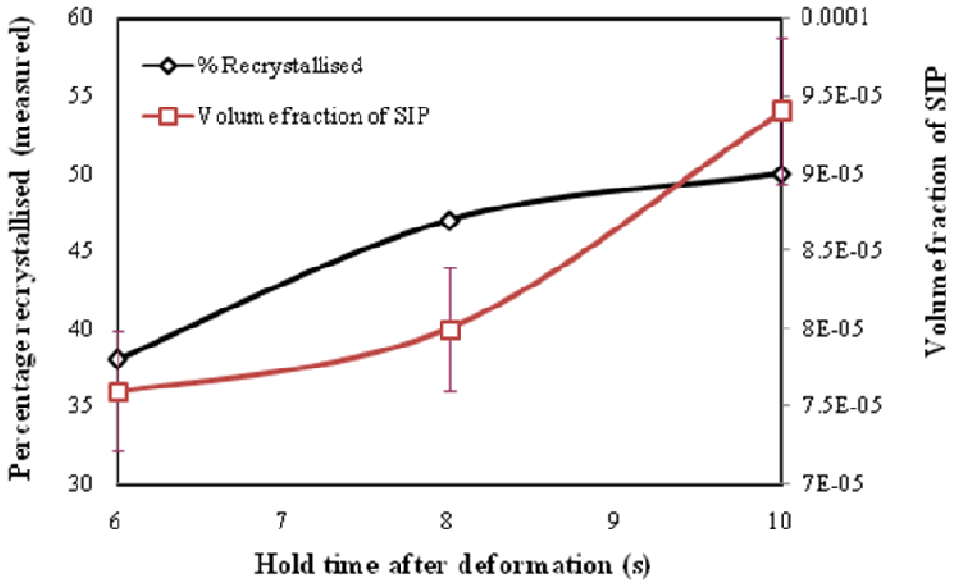

Figure 7.11. Variation of measured % recrystallised and volume fraction of strain induced Nb(C,N) precipitates (SIP) as a function of hold period after deformation at 1090 ℃ with 0.3 strain.

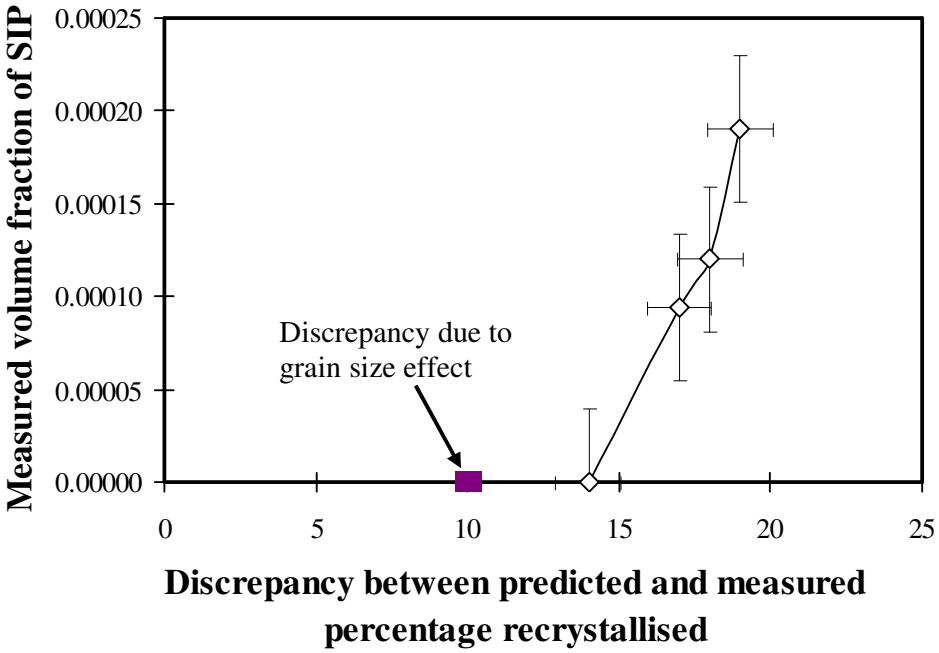

Figure 7.12. Variation of measured volume fraction of strain induced Nb(C,N) precipitates (SIP) with discrepancy between the predicted and measured amounts of recrystallisation at 0.3 strain.

CHAPTER – 8

Grain size distributions after single hit deformation of segregated Slab 1: prediction and experiment

It has been pointed out in the section 2.2.2.2 that Nb segregates strongly to the interdendritic regions along with C and N during solidification [14, 19, 22, 23, 43, 44]. The segregation of Nb and its potent grain boundary pinning action (as Nb(C,N)) mean that there can be a substantial difference in pinning force between the dendritic and interdendritic regions [14, 19, 22, 23, 43, 44]. This difference in precipitate population develops on solidification. Reheating to a high (~ 1225 - 1250 ºC) temperature causes complete dissolution of the precipitates regardless of the regions (dendritic or interdendritic) in which they are located removing all pinning particles and a coarse austenite grain size without bimodality is observed [14, 43, 44]. Commercial reheating can be carried out at lower temperatures, between 1150 ºC and 1250 ºC for HSLA steels [1, 12, 17, 88]. This temperature range may not give complete dissolution of the Nb-rich precipitates in the interdendritic regions so that some pinning may remain and a bimodal austenite grain structure prior to deformation may develop. Even for complete dissolution of Nb(C,N) the segregated Nb distribution that remains leads to spatially inhomogeneous solute drag forces and tendency to precipitate. These can influence the recrystallisation kinetics [200]. It is therefore important to understand the effect of rolling deformation on grain size development in a segregated structure compared with an homogenised one [198] as discussed the Chapter 6.

In Chapter 6, using a homogenised Slab 1 (0.045 wt% Nb), have shown that using the Dutta-Sellars equations with the mode grain size overestimates the degree of recrystallisation for deformation of 0.3 strain at temperatures above 1010 °C, whilst

modelling the behaviour for individual grain size classes (i.e. considering the whole grain size distribution) gave better agreement for the degree of recrystallisation [198]. This method also allowed prediction of the resulting grain size distributions using a simple halving of the original grain size values for grains that recrystallise; this is important for subsequent toughness prediction [198].

The present chapter is concerned with the applicability of the Dutta-Sellars model for predicting the amount of recrystallisation and grain size distributions in the presence of Nb segregation and with an initial unimodal or bimodal grain size distribution.

8.1 Inputs for modelling recrystallisation, precipitation in presence of segregation

It has been pointed out in the Chapter 3 that the inputs for Dutta-Sellars equations (equations 3.12, 3.16 and 3.17) are strain, mode grain size after reheating and available Nb in solution [98, 155].

In the as-cast condition, the presence of segregation will alter the stability of any precipitates. In this steel the precipitate population is dominated by (Nb,Ti,V)(C,N) and so the variation in [Nb] shown in Figure 5.4 (b), Chapter 5 is the most significant factor determining relative precipitate stability between solute-rich and solute-depleted regions (there is less Ti in the steel than Nb, and Ti does not segregate as strongly [14, 19, 22, 23, 43, 44]). Use of Thermo-Calc software to predict the compositions of solid (δ and/or γ) and liquid in equilibrium as a function of temperature gives a Nb content of 0.01 wt % for the first δ-ferrite to solidify, which is consistent with the SEM-EDS measurements for the dendrites, Figure 5.4 (b), Chapter 5. The composition of the last liquid present is predicted to have a niobium content of 0.15 wt % using Thermo-Calc.

Experimentally, Figure 5.4 (b), the interdendritic regions have a lower Nb content (0.095 wt % Nb) that's extends fairly uniformly throughout the 0.26 volume fraction of solute-rich material. Although of concern generally, and being addressed in current research, in the context of this work, however, this discrepancy is not important as, at both the reheat temperatures (Nb,Ti,V)(C,N) precipitates are predicted to be present in the solute-rich regions so that both values predict the same amount of Nb in solution, Table 8.1.

The difference between the predicted and measured Nb levels would be manifested as a variation in the amount of precipitate present; as pre-existing precipitates are assumed to not impede recrystallisation in this system only strain-induced ones [12, 99, 100, 112] then the appropriate solute compositions are being used. In the solute-depleted regions, then full dissolution is predicted at the higher reheating temperature with only a small amount of Nb precipitated at the lower reheating temperature, Table 8.1. The experimentally determined [Nb] profile, Figure 5.4 (b), Chapter 5, shows a very steep rise from solute-depleted to solute-rich with flat profiles within each region and so the compositions of each region were treated as constant with a step-change at the interface between them.

Reheating the homogenised material for 1 hour at 1225 °C resulted in a unimodal grain distribution with a mode of 280 μm and a maximum grain size of 600 μm (Figure 5.8, Chapter 5). The same reheating schedule applied to the as-cast material without the intervening 4 days at 1225 °C, still gave a unimodal distribution, but with smaller values for mode (160 – 180 μm) and the maximum grain size 300 μm, Figure 5.5 (b), Chapter 5. Although these distributions could be represented by a log-normal function, they do not show the 3:1 ratio of coarsest to mode used by Rodriquez-Ibabe and co-

workers [118] to successfully model thin slab direct rolling (TSDR) steels (~ 4 % discrepancy between predicted and measured recrystallisation fractions) and their processing. Although there are similarities in the approaches adopted in dealing with grain size distributions, the issues of segregation and bimodal starting grain distributions have not been covered. The processing of TSDR steels involves fewer rolling stages with larger strains, whilst greater supersaturation of [Nb] would be expected than in the thicker continuously cast and reheated steel considered in this study. Hence, the grain size class approach that proved successful for the homogenised material (Chapter 6, [198]) has been used in this part of the study.

Whilst reheating at 1225 °C resulted in a unimodal grain size distribution, use of a lower reheating temperature (1150 °C) for 1 hour resulted in a bimodal prior austenite grain size distribution, Figure 5.6 (b), Chapter 5. For this reheating schedule, the maximum grain size is only 300 μm, whilst the two mode values are 40 – 60 and 220 – 240 μm for the fine and coarse parts of the distribution respectively. The distribution shown in Figure 5.6 (b), Chapter 5 qualitatively agrees with the stability of (Nb,Ti,V)(C,N) precipitates summarised in Table 8.1. The prediction of some precipitation in the solute-depleted as well as in the solute-rich regions, coupled with the lower driving force for grain coarsening at the lower reheating temperature, is consistent with the smaller coarsest grain size. The bimodal grain size distribution is consistent with the presence of far fewer (Nb,Ti,V)(C,N) precipitates in the solute-depleted regions resulting in reduced grain boundary pinning in these regions, whereas the grain boundaries in the solute-rich regions are still pinned by (Nb,Ti,V)(C,N) particles. In this instance (grain size control during reheating) pre-existing precipitates exert an influence, unlike the prevention of recrystallisation (noted above) where their influence is negligible.

The uncertainties about the precise degree of precipitation (level of [Nb] in solute-rich regions principally) would lead to errors if these reheated grain size distributions were to be predicted and so the experimentally determined ones were used for modelling with the Dutta –Sellars equations for comparison to the thermo-mechanical simulations. As in the previous chapter no stereological corrections were applied as both deformed (elongated) and recrystallised (equiaxed) grains will be present in some of the distributions. Single correction factors for both elongated and equiaxed grains are not available and so area (and equivalent circle diameter, ECD) values have been used throughout. Although the distributions are consistent qualitatively, this is not the case quantitatively. In Figure 5.6 (b), Chapter 5 the area % of fine grains is ~ 69 %; if the fine grained part of the distribution was entirely composed of solute-rich regions where greater amounts of grain boundary pinning was present then this would only be 26 %. Thus some of the fine grains in the distribution are present in solute-depleted regions, which has an impact on the modified use of the Dutta-Sellars equations as considered below.

8.2 Prediction of recrystallisation-precipitation-temperature - time (RPTT) diagrams

The parameters in the Dutta-Sellars equations for recrystallisation and precipitation (strain-induced) in Nb-alloyed steels are summarised in Table 8.2 and involve a number of constants, empirical values and exponents. It has been discussed in the Chapter 6 that a number of groups [125-128, 134, 147, 148, 150-152, 158-161, 169, 176, 177] have produced modifications of these original equations, such as modifying the strain, grain size exponents or varying values for the activation energy for deformation. The aim of this study was to compare the applicability of the basic equations to homogenised and segregated conditions for a commercial microalloyed steel. The

equations in Table 8.2 were found to give predictions that agreed well with experimentally determined grain distributions in the homogenised case with the modification that the mode or average grain size, D_0, is replaced by each class of grain size (such as those in Figure 5.8, Chapter 5 [198] and so these values have been used in this part of the study. In the homogenised case [Nb] was constant for each class of grains and strain was also assumed to be constant. In the segregated case considered here strain was still assumed to be constant throughout all grain classes, but the value of [Nb] will differ depending on whether a grain is present in a solute-rich or solute-depleted region. This has been recognised by other researchers [118], but so far no attempt to link the grain distribution to local composition has been reported.

Initially, the Dutta-Sellars equations, Table 8.2, were used with the mode grain size and composition values, Table 8.1, in order to predict regimes for full, partial and no recrystallisation. These will only be guidelines as they do not incorporate grain size distributions (see below), but are the basis for deformation temperature selection for subsequent grain size distribution modelling. The RPTT plots for reheating at 1225 and 1150 °C, Figures 8.1 (a) and (b) respectively, were produced. These show the recrystallisation start and finish times for solute-rich and solute-depleted regions as well as the precipitation start time for the solute-rich regions (strain-induced precipitation is not predicted to occur in the solute-depleted regions for the conditions studied) as a function of deformation temperature (10 s hold after straining to 0.3 at a rate of 10 s^{-1}). The recrystallisation temperature range in the solute-rich regions in presence and absence of precipitation is listed in Table 8.3. In original Dutta-Sellars approach it has been assumed that 5 % strain-induced precipitation ceases recrystallisation, although no effect of precipitation at this level was noted in the homogenised case.

Reheating at 1225 °C, Figure 8.1 (a), shows four predicted recrystallisation regimes neglecting any retardation effects of strain-induced precipitation:

- Below 890 °C there is no recrystallisation in either solute-rich or solute-depleted regions.
- Above 1020 °C there is complete recrystallisation in both solute-rich and solute-depleted regions.
- Between 890 and 975 °C the solute-rich regions show no recrystallisation with the solute-depleted regions showing partial recrystallisation.
- Between 975 and 1020 °C there is complete recrystallisation in the solute-depleted regions, but only partial recrystallisation in the solute-rich regions.

The very wide partial recrystallisation region (c.f. 1010 – 1040 °C in the homogenised case for the same grain size distribution) reflects the effects of increased Nb level in the solute-rich regions in retarding recrystallisation through solute drag as the grain size distributions are taken to be the same in both regions. For deformation and holding in the partial recrystallisation region the initially unimodal grain structure could develop a bimodal distribution [88, 198]. If strain-induced precipitation does stop recrystallisation (as in the original Dutta-Sellars approach, then the partial recrystallisation range would be very narrow (1060 – 1070 °C) so that any effect would be readily apparent.

The effect of segregation would be predicted to be offset by the bimodal grain size distribution for reheating at the lower temperature of 1150 °C (in this case a finer mode grain size for solute-rich compared with solute-depleted), Figure 8.1 (b). The predicted

full, partial and no recrystallisation region in presence of strain-induced precipitation in the solute-rich regions is listed in Table 8.3.

The temperature ranges for partial recrystallisation of solute-rich (875 – 925 °C) and solute-depleted (860 – 925 °C) are similar and at lower temperatures than for the higher reheat temperature, which represents the effects of the refined grain structure in promoting recrystallisation, presumably through increased nucleation site density in the finer structure. For deformation and holding above 925 °C complete recrystallisation in both regions is predicted whilst no recrystallisation in either region is predicted at temperatures below 860 °C.

In order to examine the effects of segregation on recrystallisation behaviour the grain size distributions in the solute-rich and solute depleted regions in the reheated material prior to deformation are required. The two reheating schedules used in this study represent two forms of assumed relationship between composition and prior austenite grain size. On reheating, at a relatively slow rate, Figure 4.2 (b), Chapter 4, austenite will initially reform in the interdendritic regions growing to impingement there before spreading out into the prior dendritic regions. Reheating to 1225 °C and holding for one hour gives precipitate dissolution in solute-depleted regions and almost complete dissolution in solute-rich, Table 8.1. This behaviour has been confirmed by SEM [14, 43] investigation of the precipitates present in the reheated microstructure. The degree of Zener pinning is, therefore, low in both regions, although solute drag would be expected to be greater in the solute-rich region compared with solute-depleted given the low diffusivity (4.60×10^{-10} cm^2 s^{-1} [12, 185, 199]) of Nb in austenite so that redistribution throughout the steel at 1225 °C is limited within one hour. The low

overall grain boundary pinning allows austenite grain growth to occur so that grains extend up to 300 μm ECD.

Given that the mode austenite grain size is close to the secondary dendrite arm spacing in this steel then it is likely that all grain classes contain solute-rich and solute-depleted material. Whilst it may be expected that there is a higher proportion of the finer grains in solute-rich regions (greater pinning / drag force) and that the larger grains might encompass both solute-rich and solute-depleted regions in the same grain, this level of characterisation has not been carried out. Hence, it is assumed that each class in the unimodal grain size distribution, Figure 5.5 (b), Chapter 5, has a fraction of 0.26 in solute-rich material ([Nb] of 0.086 wt %) and 0.74 in solute-depleted material ([Nb] of 0.01 wt %). The grain size distribution in the solute-rich and in the solute-depleted regions after reheating at 1225 °C is shown in Figure 8.2 (a). It is recognised that this may not be strictly accurate, but given the original assumptions of the Dutta-Sellars analysis and the errors inherent in optical determination of both the as-cast solute-rich fraction as well as recrystallised fractions, this is unlikely to noticeably affect the results.

Reheating to 1150 °C causes less dissolution of precipitates in the solute-rich regions than at the higher reheat temperature resulting in increased Zener pinning so that the prior austenite grain size in the solute-rich regions should be finer. In the solute-depleted regions the grain boundary pinning forces will be more similar to those acting at the higher reheat temperature although the boundary mobility is lower and the coarsest grain class is similar (300 μm). The difference in grain boundary pinning forces between solute-rich and solute-depleted regions leads to a bimodal grain size distribution, Figure 5.6 (b), Chapter 5. In this case, it is more likely that the finer

grained part of the distribution (0 – 160 μm) is associated with the solute-rich material, whilst the coarser grained part (160 – 300 μm) is exclusively associated with solute-depleted regions. As noted above the fraction of finer and coarser grains in the distribution do not match with those for solute-rich and solute-depleted regions, so that, whilst the coarser grains are exclusively in solute-depleted material, the finer grained part of the distribution is composed of both solute-rich and solute-depleted material. The distribution, as for the higher reheating temperature, has not been characterised to any greater detail than this and so each class in the finer part of the distribution was taken to be 0.377 solute-rich and 0.623 solute-depleted with each class in the coarser part being 100 % solute-depleted. The grain size distribution in the solute-rich and in the solute-depleted regions after reheating at 1150 °C is shown in Figure 8.2 (b).

These grain size and composition values were then used to predict the grain size distribution after deformation by determining the recrystallised fraction for each individual grain size class using the same approach as for the homogenised slab material in Chapter 6; this approach is summarised here. The grain size after deformation was predicted, assuming that the strain is uniformly distributed throughout all the grains, by halving the initial grain size for the grains in that class that recrystallised, i.e. a class centred on 280 μm recrystallises to one centred on 140 μm. In the previous study on the homogenised Slab 1 it has been shown that the equations in the literature for recrystallised grain size could not reproduce the experimentally determined grain size distributions as well as this simplified approach based on halving the grain size values in the original reheated distribution. For each grain class the recrystallised fraction for the solute-rich (0, 0.26 or 0.377) and solute-depleted (1.0, 0.74 or 0.623) proportion are calculated and then summed to give an overall recrystallised fraction for that grain class (now at half the ECD value) for comparison

with optical measurements. The same approach has been used here to predict grain size distribution.

The percent recrystallised in terms of area was determined assuming a linear progression between the 5% (time for 5% recrystallisation, R_s) and 85% (time for 85% recrystallisation, R_f) curves in the Dutta-Sellars relationship and without considering any influence of precipitation on recrystallisation. The use of plane strain compression means that unrecrystallised grains have the same area and ECD values after deformation as before allowing them to be distinguished easily in the predicted distributions. Figure 8.3 gives a summary of the results obtained after deformation for the homogenised steel showing that there is better agreement between prediction and experiment when using the grain size class-based approach than when using the mode-based approach (as originally proposed in the Dutta-Sellars approach) for these sets of conditions as discussed in Chapter 6. For the conditions studied precipitation is predicted to start during the hold period at deformation temperatures below 1025 ^{o}C (Chapter 6). If precipitation had an effect then the measured recrystallised fraction should be less than the predicted value, which is not the case for either class- or mode-based predictions. TEM investigation discussed in Chapter 6 has also confirmed that there is no effect of strain induced precipitation after deformation at 0.3 strain in the homogenised Slab 1 (0.045 wt % Nb) for the range of deformation temperatures studied. The procedure followed to determine the grain size distribution after deformation is summarised by the flow diagram shown in Figure 8.4.

8.3 Thermo-mechanical simulations

The initial segregated RPTT plots (using mode grain sizes for the solute-rich and solute-depleted regions), Figure 8.1, indicated, for the reheat temperatures used, that

deformation at 880 °C (1225 °C reheat) would give no recrystallisation; 870 and 910 °C (1150 °C reheat) and 925, 975 and 1025 °C (1225 °C reheat) would give various amounts of partial recrystallisation, whilst 950 and 990 °C (1150 °C reheat) should give complete recrystallisation. Incorporating the grain size distributions discussed above for solute-rich and solute-depleted regions causes slight changes to these in that a small amount (5.90 – 6.93 %) of recrystallisation is predicted for deformation at 880 °C (1225 °C reheat) and 870 °C (after an 1150 °C reheat) with deformation at 950 and 990 °C after reheating at 1150 °C giving partial rather than full recrystallisation.

The optically determined proportions of recrystallised grains are presented in Figure 8.5 and Table 8.4 along with the predicted proportions using the experimentally determined grain size distributions with average composition and with solute-rich and solute-depleted compositions (experimentally the grains were not characterised as solute-rich and solute-depleted only recrystallised or not based on size and shape). The use of the average composition notably underestimates the recrystallised proportion, Figure 8.5, which would be consistent with the greater proportion (74 %) of solute-depleted material in the actual samples. In practice these would have less solute drag (and strain-induced precipitation) than predicted for the bulk composition so that recrystallisation would occur more rapidly in practice than predicted by the model for the solute-depleted material, an effect that more than offsets the slower recrystallisation (experimentally) in the solute-rich regions. The discrepancy between experiment and prediction is greater for partially recrystallised samples after reheating at 1150 °C than at 1225 °C, which would fit with the assumptions made above regarding the grain size distributions for solute-rich and solute-depleted. The assumption that the coarse part of the bimodal distribution is entirely solute-depleted in the experimental samples would

lead to a larger difference in recrystallisation behaviour compared with the prediction using the average composition than in the unimodal distribution, where both the slower recrystallising coarse grain classes are both solute-rich and solute-depleted.

When the segregated compositions are used with the respective bimodal or unimodal grain distributions (discussed above) then the agreement between experiment and prediction is much improved; 3.9 – 7.0 % discrepancy for the samples reheated at 1150 °C and 5.9 – 13.9 % for those reheated at 1225 °C, Figure 8.5 and Table 8.4. In the case of the samples reheated at 1150 °C, the predictions overestimate the proportion recrystallised, except for the highest deformation temperature, with the discrepancy between the two values increasing with decreasing deformation temperatures. For the lower deformation temperatures the discrepancy between predicted and experimental recrystallisation behaviour is slightly non-linear for the initially bimodal grain size distribution, but the non-linearity is much greater for samples reheated at 1225 °C, and the over prediction increases with increasing deformation temperature from 880 to 975 °C, before sharply changing to an under prediction for deformation at 1025 °C. The differences between prediction and experiment are generally greater than in the previous model for grain size distributions in TSDR processing [118] although for different strains and grain size ranges. Although the qualitative behaviour is reasonable, quantitatively the errors are too high for use in multi-pass rolling where they would be summative. Hence, probable causes for this behaviour need to be determined, based on consideration of the post-deformation grain size distributions.

8.4 Prediction of grain size distribution after deformation in Slab 1 with a starting unimodal grain size distribution

The mode and maximum grain sizes of the grain size distributions for the four experimental and modelled conditions with staring unimodal grain size distribution (generated after reheating at 1225 °C for 1 hour) are summarised in Table 8.5.

The highest deformation temperature i.e. 1025 °C gave 100 % recrystallisation experimentally (the microstructure shown in Figure 8.6 (a) is consists of fine recrystallised grains), whilst the predictions underestimated the amount of recrystallisation, Table 8.4. This was associated with incomplete recrystallisation of the solute-rich regions, Table 8.5, which causes the initially unimodal (1225 °C reheat) grain structure to remain unimodal, but to be heavily skewed so that the mode and maximum grain sizes are larger in the prediction compared with experiment, Figure 8.6 (b) and Table 8.5.

The deformation simulations studied at 925 and 975 °C after 1225 °C reheat gave bimodal distributions as in Figure 8.7 (b) (after deformation at 975 °C); the initially unimodal distributions became bimodal (both experimentally and predicted) after deformation and holding in the partial recrystallisation regime. The microstructure observed does indeed consist of mixed fine recrystallised and coarse non-recrystallised grains (Figure 8.7 (a)) with a bimodal distribution (Figure 8.7 (b)). The distributions for these conditions gave good agreement for the fine and coarse mode and maximum grain sizes, Table 8.5, with any differences in the modes being in the adjacent class, which could represent scatter in the grain size measurements. The distributions for different conditions differed in the proportions of the grain area contributed by each size class, whilst the discrepancy between experiment and prediction for each

simulation resulted from an overprediction of the degree of recrystallisation for solute-depleted grains in the 160 – 300 μm size classes, Tables 8.4 and 8.5 and Figure 8.7 (b).

The grain size distribution type was shown for the lowest deformation temperature (880 °C) after a 1225 °C reheat, which shows a unimodal distribution, Figure 8.8 (within the error for each class) for this small amount of (predicted) recrystallisation. In this case, however, as for the simulations represented by Figure 8.7 (b), the discrepancy between experiment and prediction is due to overestimation of the amount of recrystallisation in the solute-depleted material in the coarser grain classes (120 – 260 μm).

8.5 Prediction of grain size distribution after deformation in Slab 1 with a starting bimodal grain size distribution

Reheating to 1150 ^{o}C results in the formation of a bimodal grain structure. Deformation at 990 ^{o}C gave 100 % recrystallisation experimentally, whilst the predictions underestimated the amount of recrystallisation, Figure 8.9, Table 8.4. This represents the behaviour similar to the deformation simulation at 1025 ^{o}C after reheating at 1225 ^{o}C. The initially bimodal grain distribution (1150 °C reheat) remains bimodal, Figure 8.9, but, because the solute-rich material is assumed to be entirely within the finer grained part of the distribution there is no difference between the predicted and measured maximum grain sizes, Table 8.5. The mode of the coarse grained fraction, however, is greater for the prediction than experiment as the coarser solute-rich grains are not predicted to recrystallise.

Recrystallisation is not expected to be completed in either of the regions after deformation at 950 ^{o}C; the predicted recrystallised fraction based on individual grain size class using the homogenised composition is 16 %, whilst using the segregated

composition 8.72 % recrystallisation in the solute-rich region and 52.74 % in solute-depleted regions is predicted. The measured and predicted grain size distributions using the segregated composition (Figure 8.10) are bimodal consisting of fine recrystallised grains (57.59 %) and coarse unrecrystallised grains. The measured recrystallised fraction is therefore less than the predicted amount although the discrepancy is 3.87 %, Table 8.3. This suggests the precipitation which is predicted to start after 0.3 s in the solute-rich regions might have an effect and /or resulted from an overprediction of the degree of recrystallisation for solute-depleted grains. It was shown in the Chapter 7 that there is an effect of precipitation on the recrystallisation kinetics at 0.3 strain in a homogenised 0.094 wt % Nb steel. In the solute-rich regions the average Nb in solution is 0.08 wt %. Deformation-induced precipitation of Nb(C,N) might have an effect in slowing down recrystallisation. In the solute depleted regions the available Nb in solution is 0.0095 wt %. Therefore it is expected that precipitation might not have an effect on recrystallisation in the solute depleted regions as it has been discussed in the Chapter 6 that deformation induced precipitates of Nb(C,N) is not having an effect on slowing down recrystallisation in a homogenised Slab 1.

When the deformation temperature is reduced to 910 °C 2.28 % recrystallisation is predicted in the solute-rich regions and 35.31 % in the solute-depleted regions. The grain size distribution (Figure 8.11) contains fine recrystallised grains and coarse deformed grains with approximately 31.92 % recrystallised grains measured experimentally. This is again consistent with 950 °C and may indicate precipitation which precedes recrystallisation in the solute-rich regions having an effect in slowing down the amount of recrysallisation or could be due to inaccuracies in the equations in predicting the amount of recrystallisation.

No recrystallisation has been found out experimentally and 6.93 % recrystallisation is predicted in the solute-depleted regions based on individual grain size class approach after deformation at 870 ^{o}C. From the predicted and measured grain size distribution (Figure 8.12) it can be seen that there is an increase in area % of 0-40 μm grain size class. This is attributed to the 6.93 % recrystallisation in the solute depleted region. This result clearly indicates that the equations are not accurately predicting the amount of recrystallisation in the solute-depleted regions. It has been pointed out in the Chapter 6 that there is a discrepancy between predicted and measured amount of recrystallisation in a 0.02 wt % Nb steel and that is not due to deformation induced precipitation of Nb(C,N).

The possible cause for discrepancy between the measured and predicted amount of recrystallisation will be discussed in the next section.

8.6 Potential causes for over- and under-prediction

The proposed modification in the use of the Dutta-Sellars equations for single hit deformation gives reasonable agreement with experiment for the grain size distributions, but, as industrial implementation would probably involve multi-pass rolling, then the quantitative discrepancies need to be addressed without the need for excessive characterisation. In particular the high temperature behaviour needs to be accurate as errors in these stages will grow with subsequent passes. Analysis of the predictions and experimental results shows two main effects that need to be addressed, namely:

- underestimation of the amount of recrystallisation of solute-rich material at high deformation temperatures, and

- overestimation of the degree of recrystallisation of solute-depleted material at lower deformation temperatures.

The greater agreement between experiment and prediction for deformation after 1150 °C reheating might indicate that the assumptions made regarding the grain class / solute-rich / solute-depleted relationship may be in error and that the solute-rich should be confined to finer grain size classes. This would help address the discrepancy at higher deformation temperatures, but would increase the differences between experiment and prediction at lower deformation temperatures and so is not the complete solution. Indeed, the general agreement for mode and maximum grain sizes suggests that the assumptions about grain classes and solute-rich and solute-depleted as well as the simple approach of halving the grain size for classes that recrystallise are not significantly in error for the conditions studied here.

As mentioned above, there are a number of parameters and exponents in the Dutta-Sellars equations that have been used and are summarised in Table 8.2. The potential effects of these will be considered here.

In estimating the Zener-Hollomon parameter, Z, in Nb-bearing steels a range of activation energies has been used [125-128] for deformation, Q_{def}, with a value of 400 kJ/mol being utilised here. Variation of the Z parameter would affect the start time for strain-induced precipitation, which would not account for both high and low temperature effects. As an example, if Z was decreased to increase the time for 5 % precipitation at the highest deformation temperatures used, then the degree of recrystallisation in solute-rich material could increase, but that would only increase the discrepancy at lower deformation temperatures.

The solubility product, K_s, could have a greater temperature dependence, but its form has been established over the range of deformation temperatures used in this study [57, 98] and Thermo-Calc calculations [14, 198, 200] have confirmed the equilibrium variation with temperature, which is consistent with the form of K_s used in this study.

Strain-induced precipitation was shown to have little effect during hot deformation and holding in homogenised samples of this alloy (Chapter 6). The much greater [Nb] levels in the solute-rich material could be expected to give rise to greater amounts of strain-induced precipitation, particularly at lower deformation temperatures. It has been shown in Chapter 7 that in a homogenised 0.094 wt % Nb steel strain-induced precipitates are having an effect in slowing down recrystsllisation at temperature below 1090 °C. However, the model would need to account for the opposite behaviour, i.e. slowing of recrystallisation in solute-depleted material at lower deformation temperatures and acceleration of recrystallisation of solute-rich material at higher deformation temperatures. That indicates towards the fact that there is no effect of deformation-induced precipitates in the solute-rich regions. Given the low [Nb] level in the solute-depleted regions precipitation is unlikely to give sufficient Zener pinning to account for the lower levels of recrystallisation seen experimentally for the conditions studied as it has been shown in the Chapter 6 that deformation induced precipitates of Nb(C,N) are not effective in slowing down recrystallisation at 0.3 strain.

The recrystallisation finish time, R_f, is a function of the start time, R_s, and so variation in the latter will have an effect on the former. The form used here, Table 8.2, fitted the homogenised case [98] and in order to account for effects noted in this study a greater temperature and/ or composition dependence would be needed. R_f would need to be reduced for solute-rich material at high deformation temperatures, whilst being

increased for solute-depleted material at lower deformation temperatures. This is possible, but may arise naturally from other effects in terms of driving force (stored energy) and mobility (solute drag).

Thus, the term most likely to account for the experimental behaviour is that for R_s, which is composed of a number of parameters. The effect of prior austenite grain size has been dealt with through use of a class-based calculation, which leaves strain, ε; activation of recrystallisation, $\exp\left(\frac{300{,}000}{RT}\right)$; and solute drag, $\exp\left(\left(\frac{2.75x10^5}{T}-185\right)[Nb]\right)$. Medina and Quipse [125] has measured the activation energy of recrystallisation for 0.1 wt % C and 0.041 wt % Nb to be 252 kJ/mol. If this value is used in R_s equation then R_s shifts to shorter time, in other words it would predict more recrystallisation increasing the discrepancy between predicted and measured amount of recrystallisation. The value of 300 kJ/mol was also appropriate in the homogenised case over similar reheating and deformation temperatures and so is unlikely to account for the discrepancies here.

The equations as used assume uniform strain throughout all grain size classes, but, in unimodal, single phase metals [98], this condition is not achieved for strains below 0.4 – 0.5. Below that strain range, greater stored energy is observed for finer grains. The previous research [99, 100, 112] has been for pure metals and so the effects of solid solution strengthening are not included. The greater solid solution strengthening in the solute-rich grains compared with solute-depleted would raise the local yield stress resulting in reduced strain, although greater work hardening [201] may cause increased levels of stored energy for similar plastic strains. Overall, it is therefore likely that there are differences in stored energy between coarse and fine grains in the

distributions. The net effect of reduced stored energy and work hardening in the solute-depleted grains would be to reduce the effective force, i.e. to increase the $\varepsilon^{-4}\exp\left(\frac{300{,}000}{RT}\right)$ term in the expression for R_s in Table 8.2, for solute-depleted regions compared with solute-rich. This would account for the over-prediction of the degree of recrystallisation for solute-depleted material in the 160 – 300 μm class for the lower deformation temperatures. The maximum discrepancy between predicted and measured amount of recrystallisation is 13.9 % after deformation at 975 °C in 1225 °C reheated sample, Table 8.4. In the expression for R_s if 0.25 strain is used instead of 0.3 then 41 % recrystallization is predicted in the solute-depleted regions at 975 °C. That would bring the predicted amount of recrystallisation close to the measured value at this temperature. Therefore, only ~ 0.05 strain difference between solute-rich and solute-depleted regions would be needed to account for the discrepancy.

If local differences in stored energy occurs, then the effect would be expected to be seen in the homogenised case, but to a lesser extent as the difference in work hardening arises from grain size differences without composition differences. Further examination of the partial recrystallisation grain distributions, e.g. Figure 6.20 in Chapter 6, shows the same trends as observed in the segregated case, but the discrepancies between prediction and experiment are less. The reduced discrepancy may arise from the homogenised grain size distribution, which is heavily skewed to the higher (300 – 600 μm) grain sizes. Stored energy difference effects decrease as the grain sizes involved increase [186] so this effect in the homogenised case would be less than in either of the segregated cases.

Stored energy differences would increase the rate of recrystallisation in solute-rich material, which would offset the reduced recrystallisation rate for solute-depleted material at lower deformation temperatures, although would address some of the discrepancy at the highest deformation temperatures. The level of [Nb] (0.01 wt %) present in the solute-depleted material is very low so that solute drag effects will be limited and the strain partition discussed above would dominate to give an overall reduction in the amount of recrystallisation; incorporating stored energy differences into the equations would improve the agreement at lower deformation temperatures. The same assumption will not hold for the solute-rich material, where the higher [Nb] levels should provide increased amounts of solute drag. Studies on solute drag have not been extensive, although recently a more systematic approach in other systems [185, 199] has been adopted and so the uncertainty in this part of the expression for R_s is large. It is possible that the temperature dependence of solute drag is greater than that given in Table 8.2 with the result that, at lower deformation temperatures solute drag offsets the increased stored energies in the finer grained solute-rich material. If the level of solute drag decreases more rapidly with increasing deformation temperatures recrystallisation would still be retarded in the solute-rich material at lower deformation temperatures. The increased stored energy would, however, provide greater recrystallisation in the solute-rich material at the highest deformation temperatures, which would bring the predictions into line with experimental data.

8.7 Conclusions

A 0.045 wt% Nb-containing continuously-cast HSLA steel slab, which has a segregated structure (interdendritic segregation giving Nb-rich and Nb-depleted

regions), has been used to examine the influence of simulated rolling deformation on grain size development after reheating. The major findings are as follows:

1. The presence of segregated solute (Nb) content increases the partial recrystallisation temperature range compared to an homogeneous composition.

2. The Dutta-Sellars model using an individual grain size class input (rather than mode grain size) can be used to predict the austenite grain structure developed after deformation in the presence of segregation and with a starting bimodal grain size distribution provided that the initial (after reheat) grain size distribution, segregated levels of Nb and area fraction of solute-rich area are used as input.

3. There is generally good agreement between predicted and measured mode and maximum grain sizes using the class-based modification of the Dutta-Sellars equations, although the predicted and measured amounts of recrystallisation do differ with under-prediction of the amount of recrystallisation in solute-rich material at the highest deformation temperatures and overestimation of the amount of recrystallisation in the solute-depleted material at lower deformation temperatures for both unimodal and bimodal starting (reheated) grain structures.

4. Analysis of the parameters and assumptions used in the predictions indicates that the assumed relationships between grain distributions and solute-rich / solute-depleted materials are reasonable as is the approach of halving the original grain size distribution on recrystallisation. The discrepancies between prediction and measurement are most readily accounted by invoking strain partition between fine and coarse grained material and a greater temperature dependence for solute drag.

5. The degree of differences in stored energy needs to be verified, which could be achieved through in-situ synchrotron experiments, whilst the temperature dependence of solute drag needs to be determined in order to verify the conclusion above.

Tables and Figures

Table 8.1. Variables used to construct the recrystallisation precipitation diagrams used in this study.

Reheat temperature (°C)	Grain structure	Mode grain size (μm)		Nb in solution (wt%)		True strain
		Solute-rich	Solute-depleted	Solute - rich	Solute-depleted	
1225	unimodal	160	160	0.086	0.01	0.3
1150	bimodal	40	100	0.08	0.0095	0.3

Table 8.2. Summary of Dutta-Sellars equations and values used in this study. [*Nb*], [*C*] and [*N*] are the concentrations of Nb, C and N in solution (wt %); *T* is temperature (K); D_0 is austenite grain size (mode in original formulation; μm); ε is strain (using single dot for strain rate, s^{-1}); and Q_{def} is activation energy for deformation at the deformation temperature.

Feature	Equation	Values used
Start time (5 %) of precipitation (P_s)	$P_5 = 3x10^{-6}[Nb]^{-1}\varepsilon^{-1}Z^{-0.5}\exp\left(\frac{270{,}000}{RT}\right)\exp\left(\frac{2.5x10^{10}}{T^3(\ln K_s)^2}\right)$	
Start time (5 %) of recrystallisation (R_s)	$R_s = 6.75x10^{-20}D_0^2\varepsilon^{-4}\exp\left(\frac{300{,}000}{RT}\right)\exp\left(\left(\frac{2.75x10^5}{T}-185\right)[Nb]\right)$	
Finish time (85 %) of recrystallisation (R_f)	$0.85 = 1-\exp\left(\ln(0.95)\frac{R_f}{R_s}\right)^2$	
Zener-Hollomon, Z	$Z = \dot{\varepsilon}\exp\left(\frac{Q_{def}}{RT_{def}}\right)$	Q_{def} = 400 kJ/mol
Solubility product, K_s	$K_s = \frac{[Nb]\left[C+\frac{12N}{14}\right]}{10^{2.26-\frac{6770}{T}}}$	

Table 8.3. Predicted recrystallisation precipitation behaviour in the solute-rich regions after reheating at 1225 and 1150 °C.

Region	Temperature range (°C) in solute-rich region after reheating at 1225 °C		Temperature range (°C) in solute-rich region after reheating at 1150 °C	
	In absence of precipitation	In presence of precipitation	In absence of precipitation	In presence of precipitation
Full recrystallisation within 10 s after strain to 0.3	T > 1020	T > 1070	T > 920	T > 1010
Partial recrystallisation within 10 s after strain to 0.3	975 < T <1020	1060<T<1070	860 < T < 920	960 < T < 1010
No recrystallisation within 10 s after strain to 0.3	T < 975	T < 1060	T < 860	T < 960

Table 8.4. Summary of proportions of recrystallised grains predicted using a class- based approach and experimentally measured.

Reheat temperature (°C)	Deformation temperature (°C)	Predicted percentage of recrystallisation (%)			Experimentally measured percentage recrystallised	% difference between prediction and measurement
		Solute-rich	Solute-depleted	Total		
1150	990	19.10	73.87	92.97	100	-7.03
	950	8.72	52.74	61.46	57.59	+3.87
	910	2.28	35.31	37.59	31.92	+5.67
	870	0	6.93	6.93	0	+6.93
1225	1025	15.65	74.00	89.65	100	-10.35
	975	4.85	49.68	54.53	40.65	+13.88
	925	0	25.75	25.75	16.95	+8.80
	880	0	5.90	5.90	0	+5.90

Table 8.5. Summary of experimentally determined and predicted (grain class-based) grain size distributions.

Reheat temperature (°C)	Deformation temperature (°C)	Predicted mode grain size (μm)		Experimental mode grain size (μm)		Predicted maximum grain size (μm)	Experimental maximum grain size (μm)
		Fine	Coarse	Fine	Coarse		
1150	990	20-40	100 - 120	20-40	80-100	160	160
	950	20-40	220 - 240	20 - 40	220 - 240	300	300
	910	40-60	220 - 240	20 - 40	220 - 240	300	300
	870	20-40	220 - 240	40 - 60	220 - 240	300	300
1225	1025	80-100	-	40 - 60	-	300	180
	975	60-80	200-220	60 - 80	180 - 200	300	300
	925	40 - 60	160-180	40 - 60	160 - 180	300	300
	880	160 - 180	-	160 - 180	-	300	300

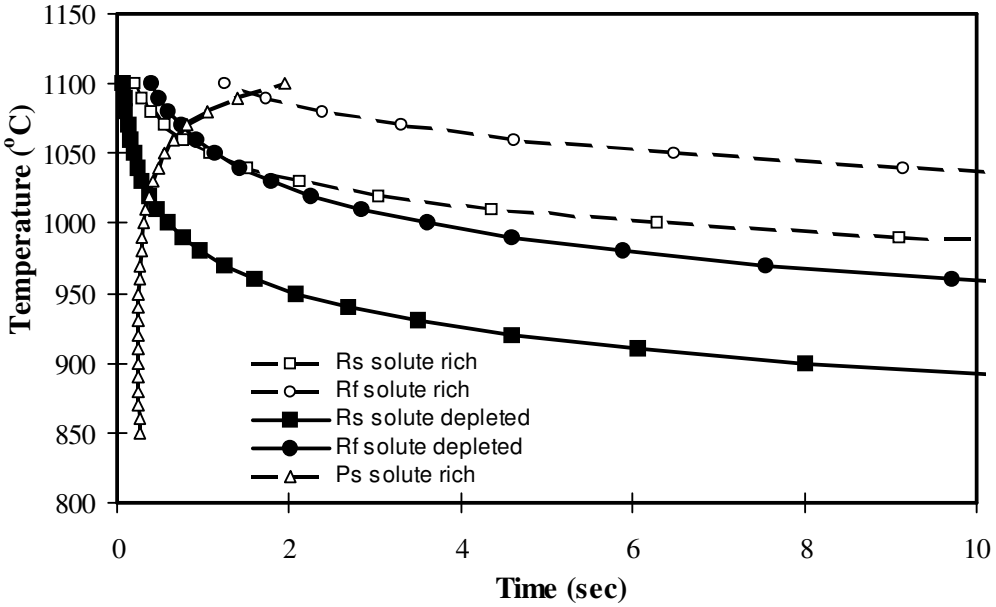

(a)

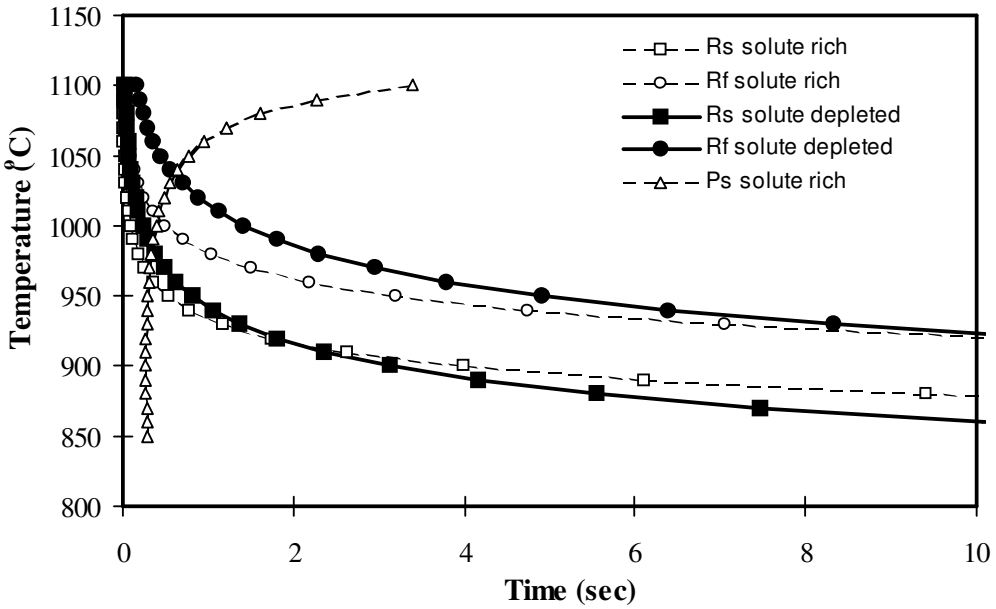

(b)

Figure 8.1. Recrystallisation – precipitation – time diagram for non-homogenised samples reheated to (a) 1225 °C with a unimodal grain size distribution and (b) 1150 °C with a bimodal austenite grain size distribution.

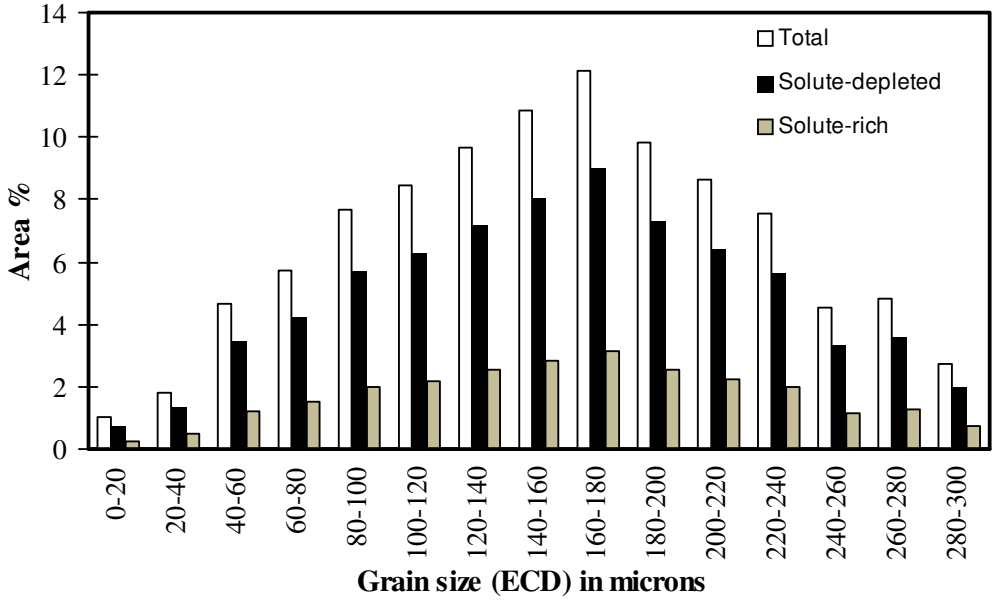

(a)

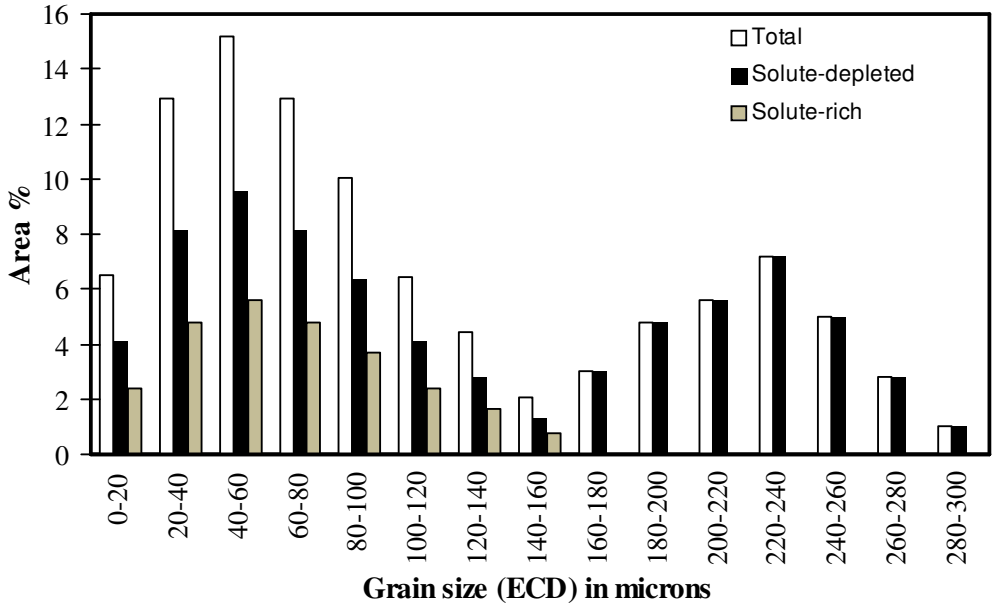

(b)

Figure 8.2. Solute-depleted and solute-rich grain size distribution after reheating at (a) 1225 °C and (b) 1150 °C.

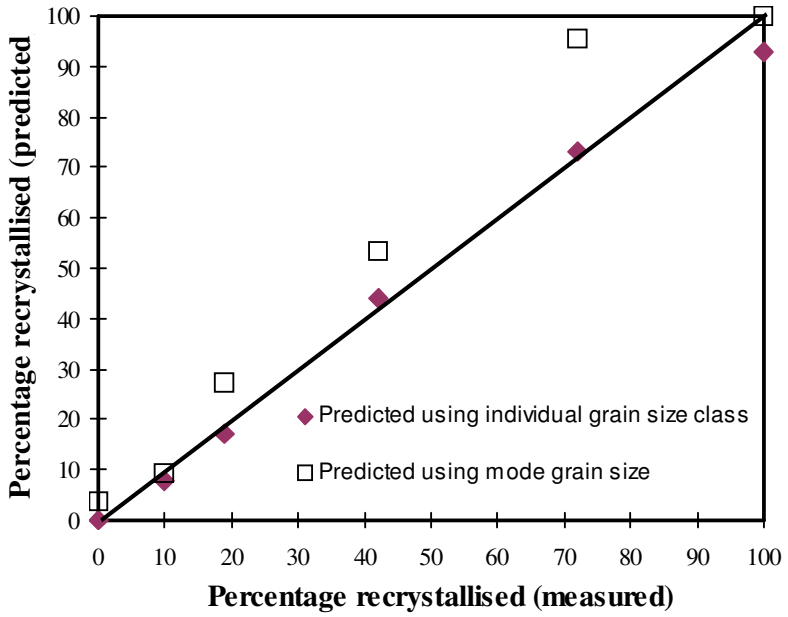

Figure 8.3. variation of predicted percentage recrystallised vs measured amount at 0.3 strain. The prediction was carried out using the mode grain size and using the starting grain size distribution.

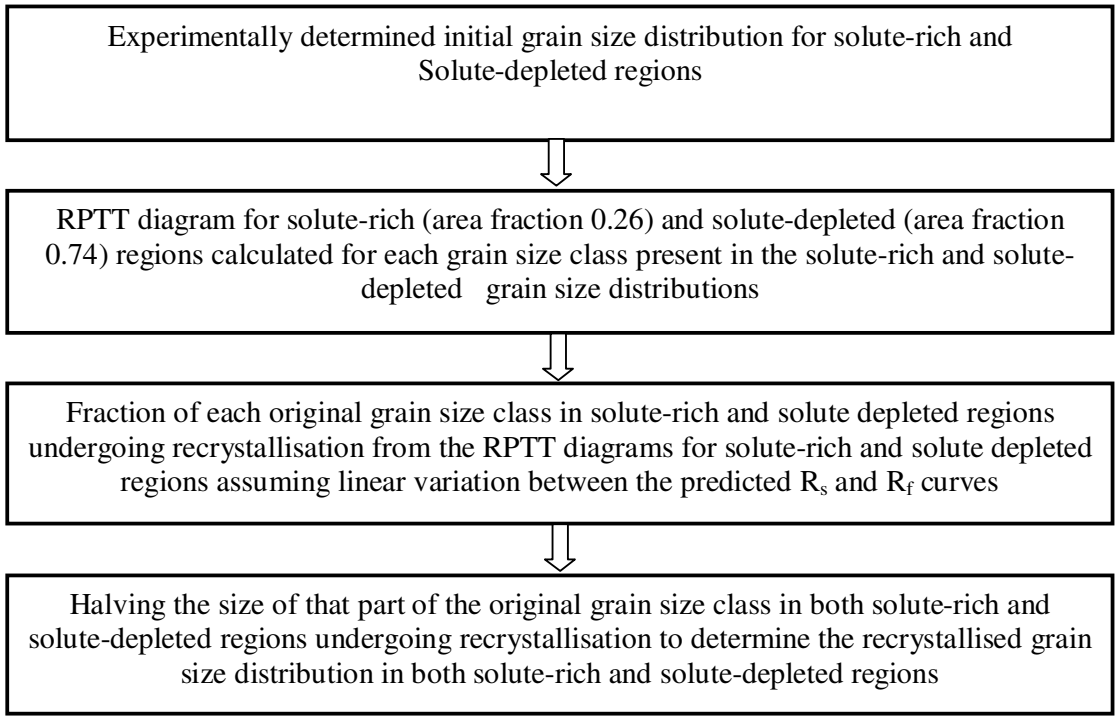

Figure 8.4. Flow diagram showing the modelling approach ('class' prediction) to predict the grain size distribution after deformation in a steel with Nb segregation.

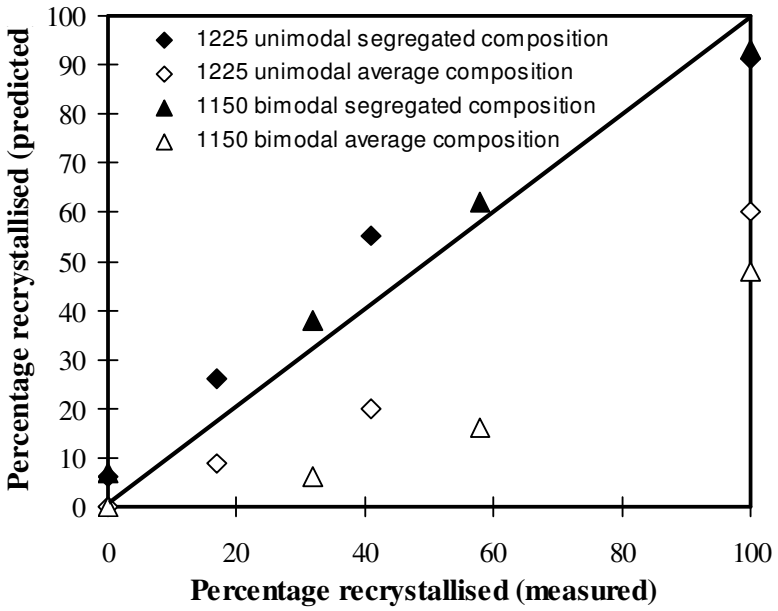

Figure 8.5. Variation of predicted percentage recrystallised vs the measured amount at 0.3 strain using a segregated and average Nb content.

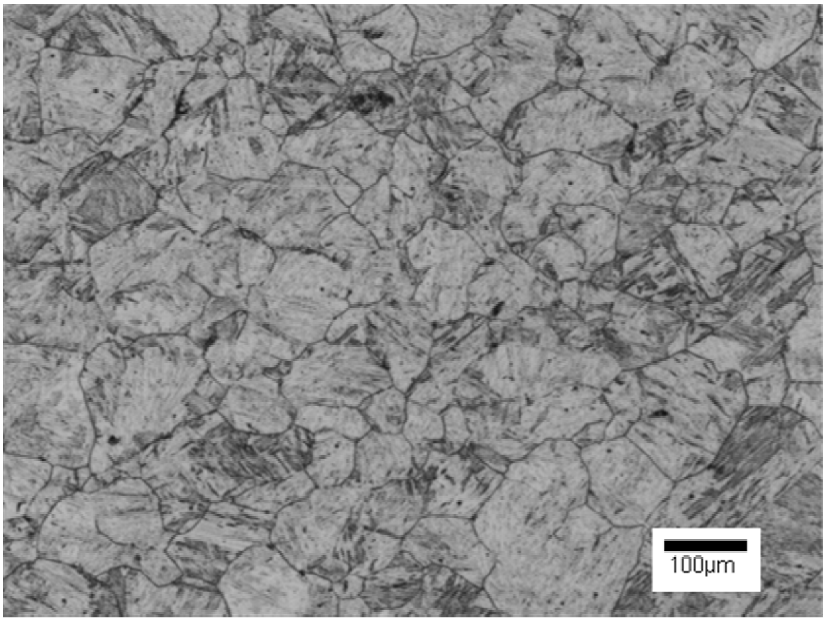

(a)

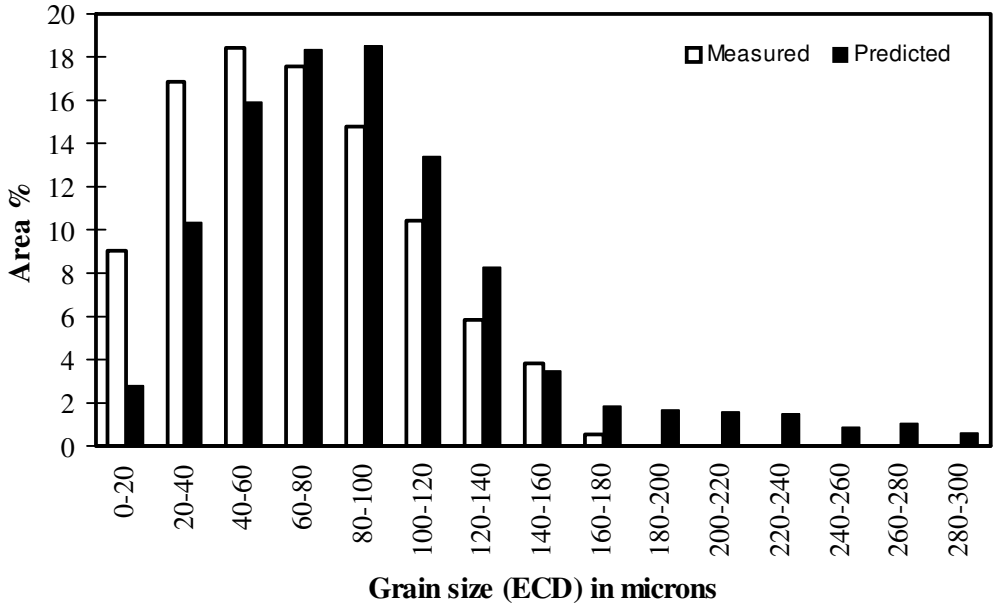

(b)

Figure 8.6. (a) Microstructure (as-quenched) and **(b)** grain size distributions (measured and predicted) for samples deformed to a strain of 0.3 and held for 10 s at 1025 °C after reheating at 1225 °C.

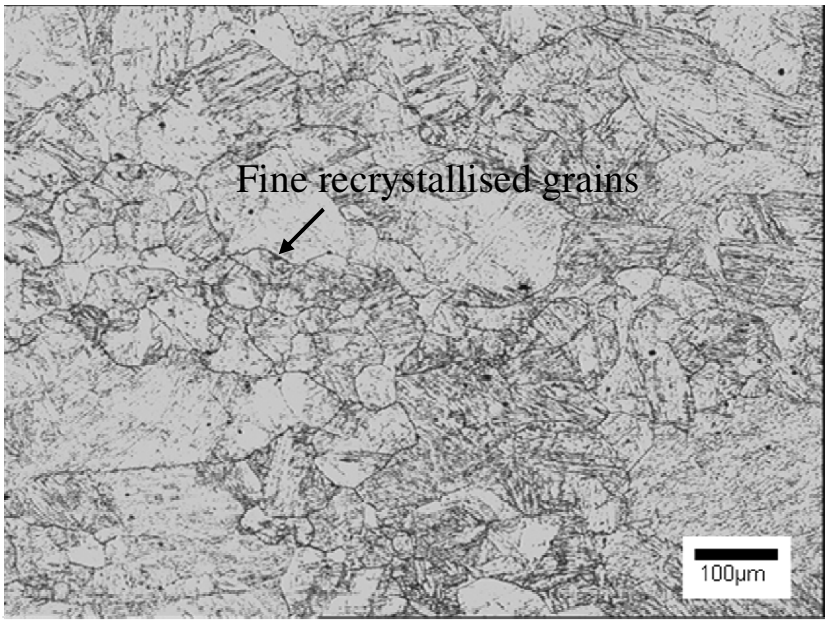

(a)

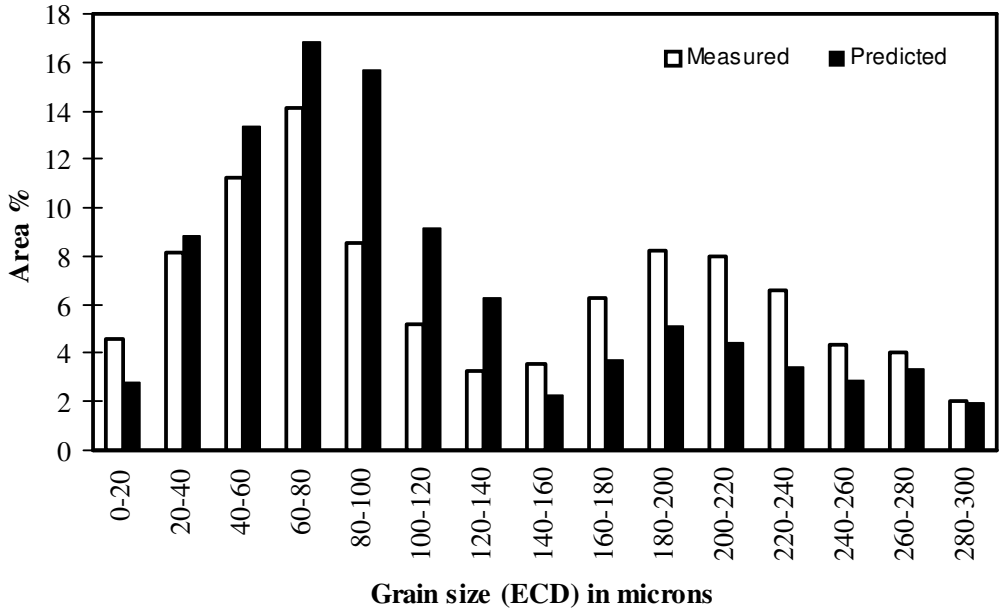

(b)

Figure 8.7. (a) Microstructure and (b) grain size distributions (measured and predicted) for samples deformed to a strain of 0.3 and held for 10 s at 975 °C after reheating at 1225 °C.

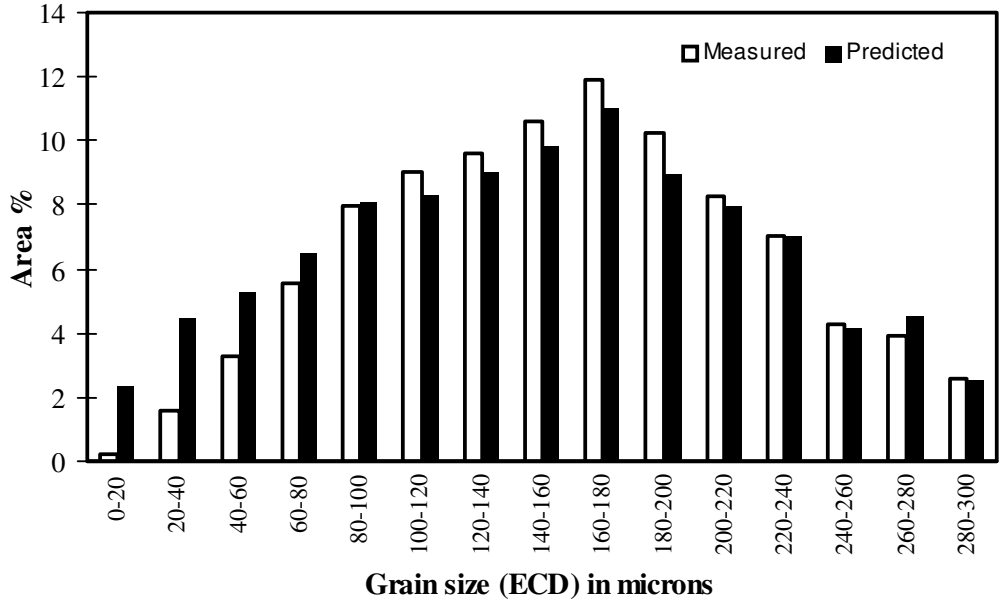

Figure 8.8. Grain size distribution (measured and predicted) for the reheated (1225 °C) as-cast sample deformed to a strain of 0.3 at 880 °C.

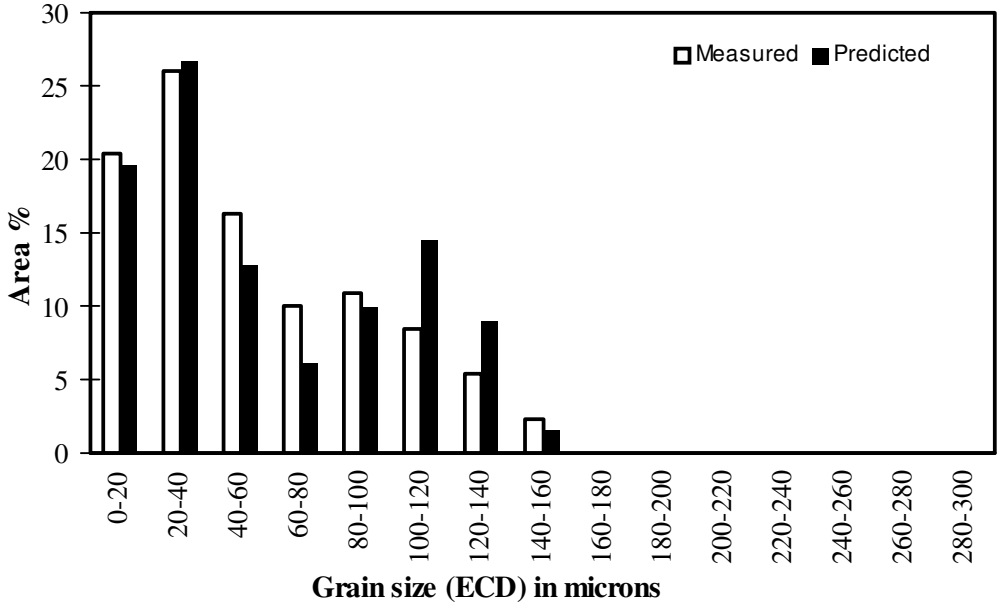

Figure 8.9. Grain size distribution (measured and predicted) for reheated (1150 °C) sample deformed to a strain of 0.3 at 990 °C.

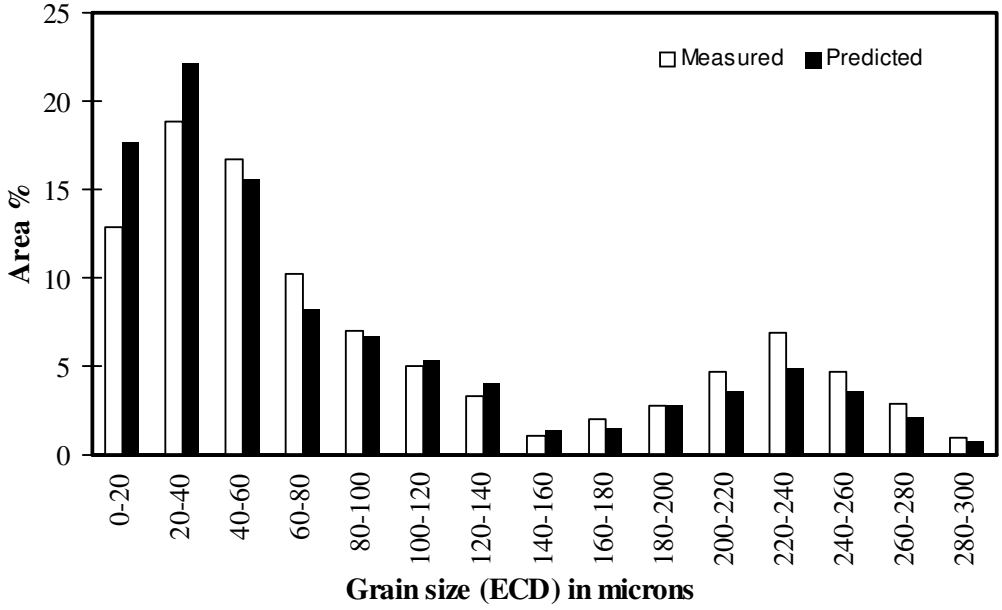

Figure 8.10. Grain size distribution (measured and predicted) for reheated (1150 °C) sample deformed to a strain of 0.3 at 950 °C.

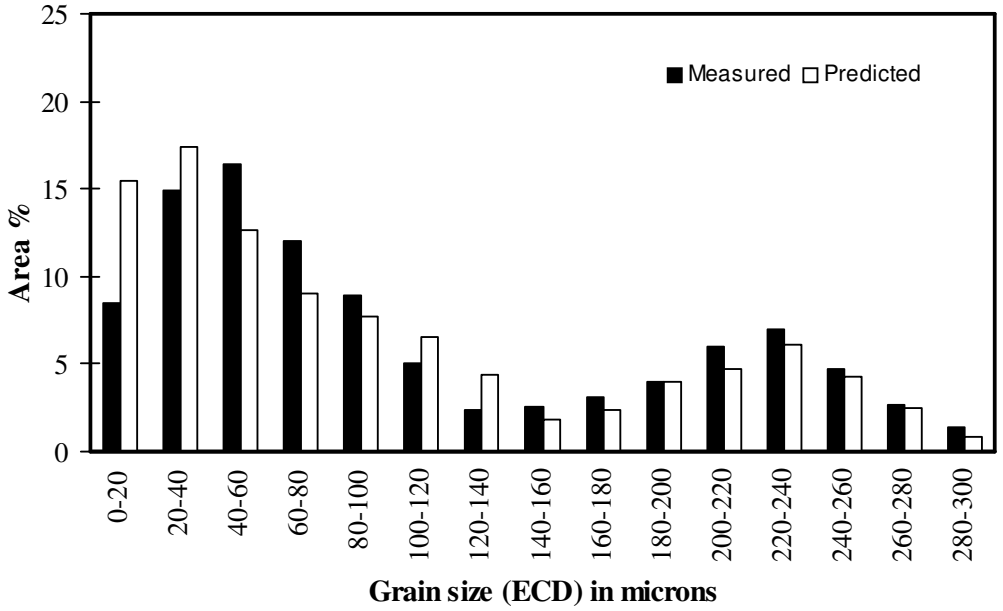

Figure 8.11. Grain size distribution (measured and predicted) for reheated (1150 °C) sample deformed to a strain of 0.3 at 910 °C.

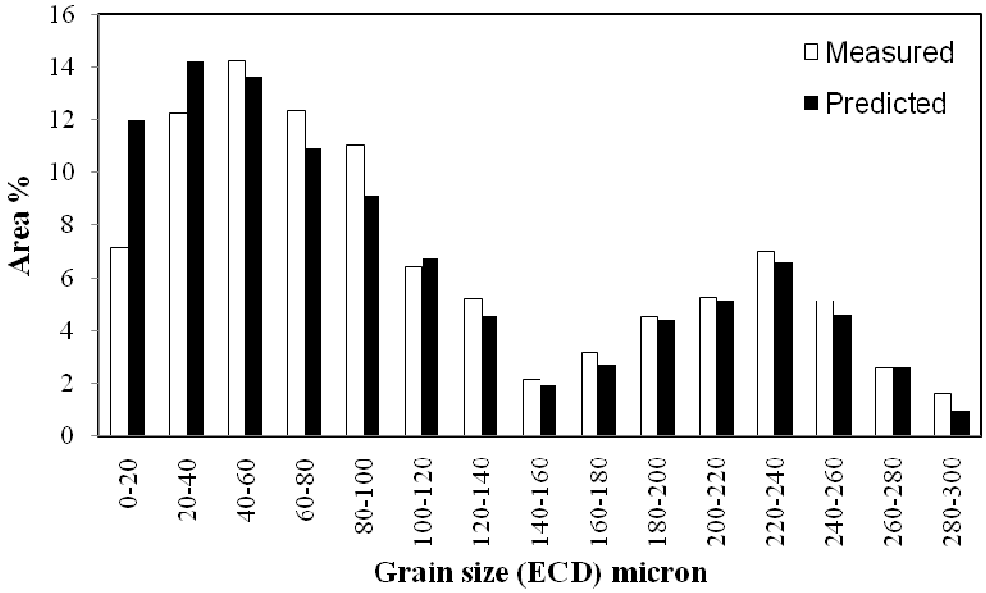

Figure 8.12. Grain size distribution (measured and predicted) for reheated (1150 °C) sample deformed to a strain of 0.3 at 870 °C.

CHAPTER – 9

Effect of strain on recrystallisation kinetics

In Chapter 6 the Dutta-Sellars equations were assessed in terms of their accuracy in predicting the amount of recrystallisation for 0.3 strain for steels with a range of Nb contents and starting grain sizes. It was found that by considering the complete grain size range, through the individual grain classes present in the distribution, the equations predicted the amount of recrystallisation more accurately. In this Chapter the equations have also been assessed in terms of their accuracy over a range of deformation strains from 0.1-0.6. Low strains i.e., 0.1-0.2 are often used in conventional rolling mills and higher strains are used in new generation rolling mills such as thin slab direct rolling (TSDR).

Figure 9.1 presents the results for the original Dutta-Sellars equations using literature data (given in Table 6.1) for the predicted percentage recrystallised vs measured over a range of strains (0.1-0.6). Comparing Figures 6.1 and 6.2 from Chapter 6 showing predicted vs measured percentage recrystallised for a range of grain size and composition at 0.3 strain with Figure 9.1 it can be seen that a greater discrepancy exists in predicting the percentage of recrystallised grains over a range of strain compared to what was shown at 0.3 strain. The black data points in Figure 9.1 are for low strain i.e. strain < 0.3 and the red data points are for high strain i.e. strain > 0.3. Generally it would appear that at low strain (i.e. strain < 0.3) the amount of recrystallisation is under predicted whilst at high strain (i.e. strain > 0.3) it is over predicted. Greater discrepancy exists between predicted and measured amount of recrystallisation at higher strain range. The root mean square (RMS) error between

predicted and measured amount of recrystallisation at higher strain range is 44 compared to that of at lower strain range is 20.

It was shown in the Chapter 6 that by considering the total grain size distribution it is possible to predict amount of recrystallisation more accurately at 0.3 strain. Applying this approach to the literature data at different strains (again using the same assumptions as before, given in section 6.3, Chapter 6, to generate the initial grain size distribution) generates Figure 9.2. From Figure 9.2 it can be seen that at higher strain range recrystallisation is over predicted whereas at lower strain range it is under predicted with a reduced discrepancy compared to Figure 9.1. The RMS error at higher strain range is 30 and at lower strain range is 12. In the section 6.3, Chapter 6 it has been shown that the average error at 0.3 strain is 10 % when taking into account the grain size distribution at 0.3 strain (The dashed line on the figure shows the mean error that can occur even after considering the grain size distribution). From Figure 9.2, considering the range of strains, greater discrepancy exists between predicted and measured amount of recrystallisation especially at higher strain range i.e. there is an effect due to strain in addition to the error that may be introduced due to grain size distribution.

The predictions presented in Figure 9.2 do not take into account strain-induced precipitation and any effect that might have on recrystallisation. It was shown in Chapter 7 that strain-induced precipitation has an effect on slowing down recrystallisation at temperature below 1090 °C in a homogenised 0.094 wt % Nb steel at 0.3 strain resulting in a greater discrepancy between the predicted and measured amount of recrystallisation. It was shown in Chapter 6 that there is no effect of strain-induced Nb(C,N) precipitates on slowing down recrystallisation in a homogenised Slab

1 (0.045 wt % Nb) steel deformed at 0.3 strain. However, increased deformation strain is expected to increase the amount of strain-induced precipitation that can occur [12]. Therefore experiments were carried out in this work using a range of strains on homogenised 0.045 and 0.094 wt % Nb steels and TEM investigations were performed to determine to what extent strain-induced precipitation could occur and its effect on recrystalisation kinetics.

9.1 Deformation simulation for a range of strains (0.15, 0.225, 0.375 and 0.45)

Deformation simulations were carried out across a strain range from 0.15 to 0.45 using homogenised Slab 1 and 0.094 wt% Nb steels. The deformation temperatures ranges between 1125-975 °C covering full, partial and no recrystallisation regions for both the steels. The predicted, compared to measured, amount of recrystallisation is shown in Figure 9.3 (a) and (b) for homogenised Slab 1 and 0.094 wt % Nb steels respectively, using the Dutta-Sellars equations modified to include the starting grain size distribution. From these two figures it can be seen that greater discrepancy exists at higher strain range for both the steel. The RMS errors at higher strain range for homogenised Slab 1 and 0.094 wt% Nb steels were 30 and 39 respectively. The RMS error is consistent with the error that was shown to exist using the literature data. At lower strain range the error is 10 for homogenised Slab 1 and 11 for 0.094 wt% Nb steels. At both higher and lower strain range greater discrepancy is seen for 0.094 wt% Nb steel compared to homogenised Slab 1 and that is consistent with the results discussed in Chapter 6 and 7 at 0.3 strain. It can be seen that for homogenised Slab 1 the agreement is not as good as at 0.3 strain, and that the additional discrepancy occurs at higher and lower strains.

At higher strain the greater discrepancy could be due to deformation induced precipitation of Nb(C,N) slowing down recrystallisation. TEM investigation has been carried out on both the steels to see whether this discrepancy is due to deformation-induced Nb(C,N) slowing down recrystallisation kinetics. At lower strain the predicted amount of recrystallisation is less than that is measured. Therefore that may indicate that deformation induced precipitates cannot be the cause of discrepancy. Additionally it has also been shown in Chapter 6 that strain-induced precipitates of Nb(C,N) are not having an effect on slowing down recrystallisation kinetics in homogenised Slab 1 steel at 0.3 strain. But if precipitation of Nb(C,N) takes place during deformation simulations that may remove Nb from solution reducing solute drag. That may enhance the recrystallisation kinetics resulting in more amount of recrystallisation to take place experimentally. TEM investigation has been carried out to see whether there is any presence of precipitates in the samples deformed at low strain range.

9.2 Discussion on the cause of the discrepancy at high (i.e. strain > 0.3) strain range

Deformation-induced precipitates were identified following the same procedure described in Chapter 6: TEM was carried out after quenching following the reheat furnace treatment and 5 minutes hold in the Gleeble to determine if any precipitates were present in the samples prior to deformation. A small volume fraction (0.000001) of undissolved (Ti,Nb)(C,N) precipitates were identified with a size (diameter) range of 20-120 nm; this precipitate distribution was subsequently discarded from analysis of any strain-induced precipitates imaged. The details of precipitate quantification for 0.094 wt % and 0.045 wt % steel are given in Table 9.1 and Table 9.2.

It has been shown in Chapter 7 that strain-induced particles of Nb(C,N) have an effect on slowing down recrystallisation at 0.3 strain in the 0.094 wt % Nb steel at temperature below 1090 °C. Therefore, it is likely that at higher strains recrystallisation will be slowed down by strain-induced Nb(C,N) as the amount of precipitation should increase with increased strain at a constant temperature [12]. Deformation simulations were carried out using the 0.094 wt% Nb steel at 1090 °C and 0.45 strain with 6, 8 and 10 s hold periods after deformation. At 1090 °C strain-induced precipitation precedes recrystallisation. Figure 9.4 shows the variation of recrystallised percentage with hold period. The discrepancy between the measured and predicted amount of recrystallisation increases with the increase in hold period similar to the behaviour shown in Figure 7.10, Chapter 7. The volume fraction of deformation-induced precipitates after the 6 s hold period is 0.000081, with average size (diameter) 5 nm, which increased to 0.00009 after 8 s, with a similar average size. After 10 s the volume fraction of particles is 0.00012 with average diameter 4 nm. The volume fractions of the precipitates are higher at 0.45 strain compared to that at 0.3 strain (Table 7.2, Chapter 7) with similar average size.

A TEM image of the deformation-induced Nb(C,N) particles that formed after the 6 s hold period at 1090 °C is shown in Figure 9.5. The variation of percentage measured recrystallised and volume fraction of deformation-induced particles as function of hold period is shown in Figure 9.6. From Figure 9.6 it can be seen that the rate of increase in percentage recrystallised reduced with time whereas there is an increase in the rate of precipitate volume fraction. This suggests that with increase in volume fraction of precipitates the Zener drag [75] increases as the average particle size remains the same. That leads to greater discrepancy between measured and predicted amount of recrystallisation with longer hold period after deformation at 1090 °C. It

should also be noted here that the discrepancy between predicted and measured amount of recrystallisation at 0.3 strain at 1090 °C after 10 s is 17 (Chapter 7) and the volume fraction of deformation-induced Nb(C,N) is 0.000094. Therefore the greater discrepancy (47 %) at 0.45 strain in this steel is associated with greater amount of deformation-induced Nb(C,N) present (particle volume fraction 0.00012) at this temperature after 10 s hold.

The use of 0.45 strain over a range of deformation temperatures (1050-1125 °C) gave a range of volume fractions of deformation-induced precipitates (0-0.00027) for the same size range (average diameter 3.9-5.0 nm) along with different discrepancies between predicted and measured recrystallised amounts. For no deformation-induced precipitates the discrepancy (21 %) was greater than that noted for the grain size effect (10 %) discussed in section 6.3, Chapter 6, Figure 9.7, but, beyond that, an approximately linear relationship exists between the volume fraction of deformation-induced precipitates and discrepancy, Figure 9.8. Given little difference in precipitate size, this linear relationship would be consistent with a variation in Zener drag.

Unlike in the 0.094 wt % Nb steel there is no effect of deformation-induced precipitates of Nb(C,N) on slowing down recrystallisation at 0.3 strain in homogenised Slab 1, discussed in Chapter 6. Deformation simulations were carried out at 975, 990, 1025, 1050 and 1075 ^{o}C with 0.45 strain. At 1025 ^{o}C precipitation precedes recrystallisation. Deformation simulations were carried out at 1025 ^{o}C with a strain of 0.45, and 6, 8 and 10 s hold to investigate whether there is any influence of strain-induced particles on recrystallisation kinetics. The variation of measured and predicted (using individual grain size class) amount of recrystallisation as a function of hold period after deformation is shown in Figure 9.8. Straining to 0.45 at 1025 ^{o}C results in

over-prediction on the amount of recrystallisation that increases markedly between 8 and 10 s hold time, Figure 9.8, opposite to the behaviour shown in Chapter 6 where predicted amount of recrystallisations are in good agreement with the measured values. TEM examination revealed that a 0.00005 volume fraction of strain-induced Nb(C,N) (average diameter 3.6 nm) had formed after 6 s hold, which increased to 0.00007 after 8 s, Figure 9.9. The greater driving force for recrystallisation at 0.45 strain than at 0.3 means that deformation-induced precipitates does not retard recrystallisation significantly until the large increase in volume fraction (up to 0.00014) between 8 and 10 s hold when recrystallisation is effectively stopped, Figure 9.9, and the largest discrepancy between predicted and measured recrystallisation amounts occurs.

At 1050 ^{o}C after 0.45 strain, 5 % precipitation is expected to start after 2 s of the 10 s hold period. The predicted recrystallised fraction without any influence of precipitation is 99 %. The measured recrystallised fraction at that strain and temperature is 79 %. This discrepancy (20 %) could be due to deformation-induced precipitates of Nb(C,N) slowing down recrystallisation. TEM investigation has revealed the presence of deformation-induced Nb(C,N) and the measured volume fraction is 0.000045. With the 0.094 wt % Nb steel the discrepancy between predicted and measured amount of recrystallisation is 54 % and the volume fraction of precipitates measured is 0.00027 at 1050 ^{o}C. This implies that with higher amount of Nb greater amount of precipitation has occurred during deformation leading to greater discrepancy between predicted and measured amount of recrystallisation at this temperature.

Deformation simulations in homogenised Slab 1 have also been carried out at 990 and 975 ^{o}C with 0.45 strain and 10 s hold period after deformation. At 990 ^{o}C the discrepancy between predicted and measured amount of recrystallisation is 49 % (37 %

at 1025 ^{o}C) and the measured volume fraction of strain-induced precipitates is 0.00019. Therefore a greater volume fraction of deformation induced precipitates generates greater Zener drag (average particles size is same, Table 9.2) leads to a greater amount of discrepancy between predicted and measured amount of recrystallisation.

Figure 9.10 shows the variation of discrepancy between predicted and measured amount of recrystallisation with the measured volume fraction of strain-induced precipitates showing that the discrepancy between the measured and predicted amount of recrystallisation increases with an increase in volume fraction of deformation-induced precipitates due to increased Zener drag [75] as there is no change in the particle size distribution. The discrepancy due to the grain size effect (superimposed on the Figure 9.10) is less than the discrepancy due to strain. Deformation-induced precipitates therefore increases the discrepancy. The effect of which is more pronounced at lower deformation temperature where the greater volume fraction of deformation-induced precipitates provides greater Zener drag.

Comparing the volume fraction of the precipitates that form in 0.094 wt % Nb steel with homogenised Slab 1 and Figure 9.7 and 9.10 it can be said that the greater discrepancy that exists between predicted and measured amount of recrystallisation in 0.094 wt % Nb steel is due to greater volume fraction of the deformation-induced Nb(C,N) particles (average particles size is same, Table 9.1 and 9.2) generating greater Zener drag and causing greater discrepancy.

It should be noted from Figure 9.7 and 9.10 that in absence of any deformation-induced precipitates 21 and 17 % discrepancy could occur in 0.094 wt % Nb steel and homogenised Slab 1 respectively. Therefore at 0.45 strain the discrepancy between predicted and measured amount of recrystallisation is not only due to the deformation-

induced precipitates but may indicate towards the inaccuracies present in the equation in predicting R_s. It has been discussed in the Chapter 7 that 14 % discrepancy between predicted and measured amount of recrystallisation can be caused due to under predicted solute-drag in 0.094 wt % Nb steel at 0.3 strain. This could be a cause of discrepancy in 0.094 wt % Nb steel at 0.45 strain. However, it has also been shown in Chapter 6 that Dutta-Sellars equations based on individual grain size class accurately predicted amount of recrystallisation in homogenised Slab 1 steel. Therefore, the discrepancy due to solute drag of Nb will not be applicable to homogenised Slab 1 (0.045 wt % Nb). With change in strain the driving force part, i.e. $\varepsilon^{-4}\exp\left(\frac{300{,}000}{RT}\right)$ present in R_s will change. Very few data points exist with poor agreement with the experimentally measured value at strain > 0.3 in Sellars original paper [98]. This suggests that strain exponent 4 is not predicting the amount of recrystallisation accurately at higher strain range. Therefore the discrepancy that exists at higher strain range could be due to three factors such as deformation induced precipitates of Nb(C,N), under predicted solute drag and inaccurate strain exponent present in the equation of R_s.

9.3 Discussion on the cause of the discrepancy at low (i.e. strain < 0.3) strain range

The discrepancy between the predicted and measured amount of recrystsllisation is highest at 0.15 strain (13 %) compared to that at 0.225 strain (12 %) in the homogenised Slab 1 and 0.094 wt % Nb steel, Figure 9.3 (a) and the measured amount of recrystallisation is more than predicted. In order to see whether there is any precipitation during deformation simulation removing Nb from solution and causing enhanced recrystallisation TEM investigation has been carried out.

Deformation simulations were carried out at 1025 ^{o}C for the 0.045 wt % Nb steel and 1090 ^{o}C in 0.094 wt % Nb steel with a strain of 0.15 and hold times of 6, 8 and 10 s. 1025 and 1090 ^{o}C were the lowest deformation temperatures used in this study for Slab 1 homogenised and 0.094 wt % Nb steels. Effect of strain-induced precipitation should be expected to be more at lowest deformation temperatures at constant strain. Interrupted deformation simulations with 6, 8 and 10 s hold period after deformation were carried out at these two temperatures to see how recrystallisation and strain-induced precipitation progresses with time. The variation of measured and predicted (using individual grain size class) amount of recrystallisation as a function of hold period after deformation is shown in Figure 9.11 for the homogenised Slab 1 steel and Figure 9.12 for the 0.094 wt % Nb steel. At 0.15 strain the discrepancy between the predicted and measured amount of recrystallisation increases with an increase in the hold period (RMS errors 4.5 %, in homogenised Slab 1 steel, Figure 9.11 and 5 % 0.094 wt % Nb steel, Figure 9.12). Under these deformation conditions no precipitation is predicted in the homogenised Slab 1 (0.045 wt % Nb) and precipitation is predicted to start after 2 s in the 0.094 wt % Nb steel. TEM investigation has not revealed the presence of any deformation induced Nb(C,N) in both the steels.

It has been pointed out in the literature that at low pass strain, i.e. strain ranging from 0.1 to 0.25, solute drag of Nb is the controlling factor on recrystallisation kinetics [12, 17, 131, 132, 185, 199] in the Nb bearing microalloyed steels. Zurob et al. [199] has discussed the interaction of solute drag and deformation induced precipitation of Nb(C,N) on recrystallisation kinetics. In their physically based model they have shown that recrystallisation is first retarded by Nb solute drag before Nb(C,N) precipitates start to nucleate on the dislocation structures after deformation for a 0.1 wt % Nb steel.

Once precipitates start to nucleate that will reduce the solute Nb in solution and there will be gradual reduction of solute drag and then recrystallisation kinetics would be governed by the strain induced precipitation. The nucleation time for Nb(C,N) precipitates is predicted to be 20 s in their model. In their model they used dislocation density as an input parameter for the nucleation time for strain induced precipitation instead of strain. In the present study, as no precipitates were revealed using TEM, then recrystallisation should be controlled by the solute drag of Nb at low pass strain, according to, and in agreement with the model.

Figure 9.13 and 9.14 shows the predicted vs. measured amount of recrystallisation after taking out the data points where the cause of discrepancy is due to deformation-induced precipitates in Slab1 homogenised and in 0.094 wt % Nb steel respectively with RMS errors of 14 and 18 % respectively. The RMS error present in the literature data after taking out the data points where the cause of discrepancy could be due to strain-induced precipitates is 20 %, Figure 9.15. This is greater than the error (10 %) that could be introduced due to grain size effect.

The removal of strain-induced precipitates effects leaves the remaining discrepancy (grain size and strain) as most likely due to the equation for R_s, which is not predicting the time for recrystallisation accurately. The effect of prior austenite grain size has been dealt with through the use of a class-based prediction and that leaves the terms ε; activation energy of recrystallisation, $\exp\left(\frac{300{,}000}{RT}\right)$; and solute drag, $\exp\left(\left(\frac{2.75x10^5}{T}-185\right)[Nb]\right)$. The variation of stored energy as a function of grain size has been shown in Figure 6.12, Chapter 6. At the lower strain range there is expected to be greater strain partitioning [99, 100, 107, 112] leading to greater stored energy

gradient between the grains. That may enhance the recrystallisation kinetics at lower strain range. It has also been pointed out in the Chapter 7 14 % discrepancy between predicted and measured amount of recrystallisation could be there as the solute-drag of Nb is not being predicted accurately in 0.094 wt % Nb steel. As in the lower strain range recrystallisation kinetics is controlled by solute drag of Nb it is likely that this will introduce error in the case of 0.094 wt % Nb steel. Although at 0.3 strain solute drag is accurately predicted in Slab 1 homogenised steel but at lower strain range that may not be the case. Therefore driving force and solute drag expressions need to be dealt with along with strain partition (particularly when bimodal distributions are considered, as discussed in Chapter 8 and at low strain range).

9.4 Conclusions

The validity of the original and modified (taking into account the grain size distribution through the individual grain class approach) Dutta-Sellars equations in quantifying the amount of recrystallisation has been reviewed for a larger range of strains than used in the original work. The major findings are as follows:

1. The original Dutta-Sellars equation does not predict the amount of recrystallisation well over a large strain range (0.1-0.6, shown using experimental data in this work and literature data (both under- and over-predictions are seen)). When the starting grain size distribution is taken into account there is an over-prediction of recrystallisation at higher strain range and under prediction at lower strain range.

2. The greater discrepancy that exists in the higher strain range can be accounted for by strain-induced precipitates of Nb(C,N) reducing the recrystallised

fraction, particularly for high Nb steels (literature data and from the present study) and at high strains (results presented here).

3. Improvement in prediction can be made in future by addressing the issues of accurate prediction of solute drag especially for the steel that contains 0.094 wt % Nb, strain partitioning and correct strain exponent values at lower and higher strain range.

Tables and Figures

Table 9.1. Summary of quantification of deformation induced Nb(C,N) precipitate after deformation at 0.45 strain in 0.094 wt % Nb steel.

Deformation temperature (^oC)	Hold period after deformation (s)	Average particle size (nm)	Volume fraction (F_v) (deformed)	Volume fraction (F_v) (without deformation)	Volume fraction (F_v) (predicted using Thermo-Calc)
1090	10	4	0.00012	0.000001	0.00024
	8	4.2	0.00009		
	6	5	0.000081		
1075	10	4	0.00021	0.0000029	0.00031
1050	10	3.9	0.00027	0.0000051	0.00039

Table 9.2. Summary of quantification of deformation induced Nb(C,N) precipitate after deformation at 0.45 strain in 0.046 wt % Nb steel.

Deformation temperature (^oC)	Hold period after deformation (s)	Average particle size, nm	Volume fraction, F_v (deformed)	Volume fraction, F_v (without deformation)	Volume fraction, F_v (predicted using Thermo-Calc)
1050	10	4.2	0.000045	0.000002	0.00016
1025	10	4	0.00014	0.0000035	0.00024
	8	4.2	0.00007		
	6	3.6	0.00005		
990	10	3.9	0.00019	0.000005	0.0003

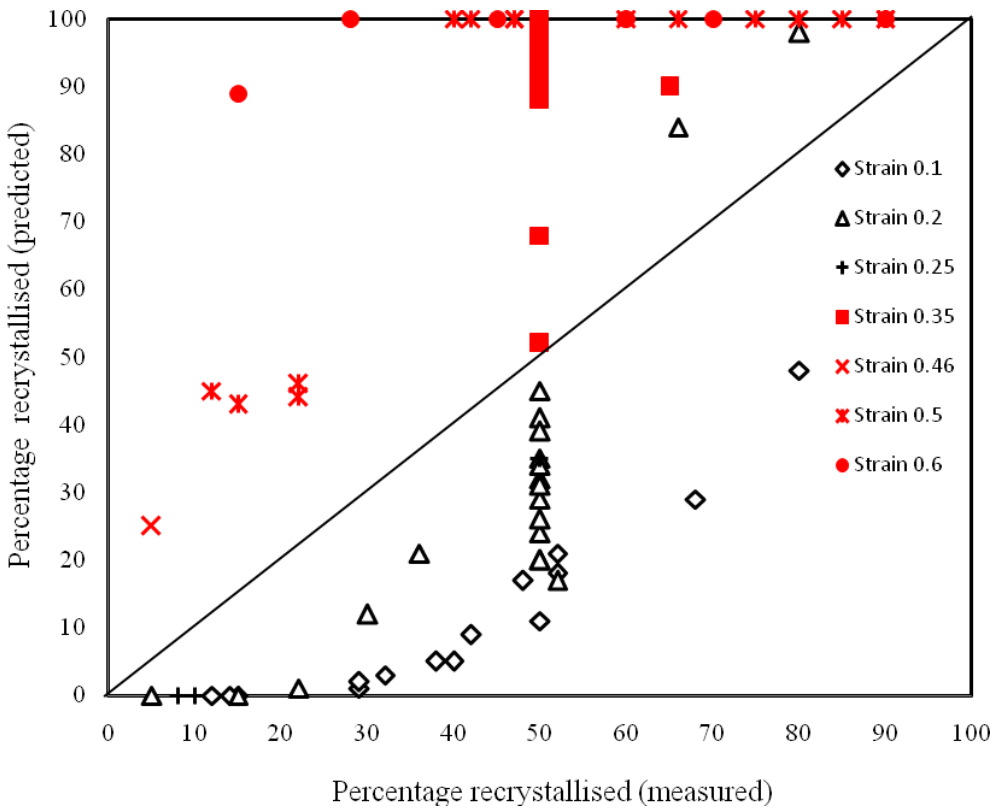

Figure 9.1. The amount (%) of predicted compared to measured recrystallised grains for a range of deformation strains using the literature data mentioned in Table 6.1 in Chapter 6.

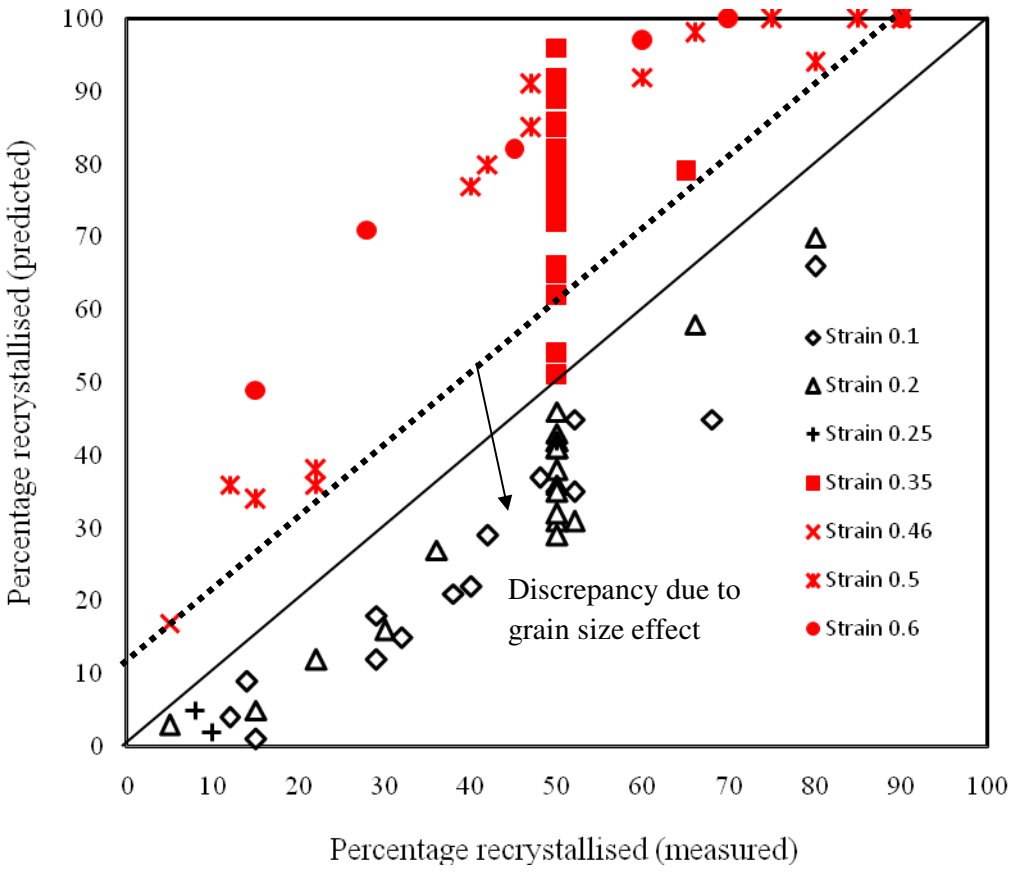

Figure 9.2. The variation of predicted % recrystallised vs the measured amount for range of deformation strains using the literature data and the modified Dutta-Sellars equations considering individual grain size classes.

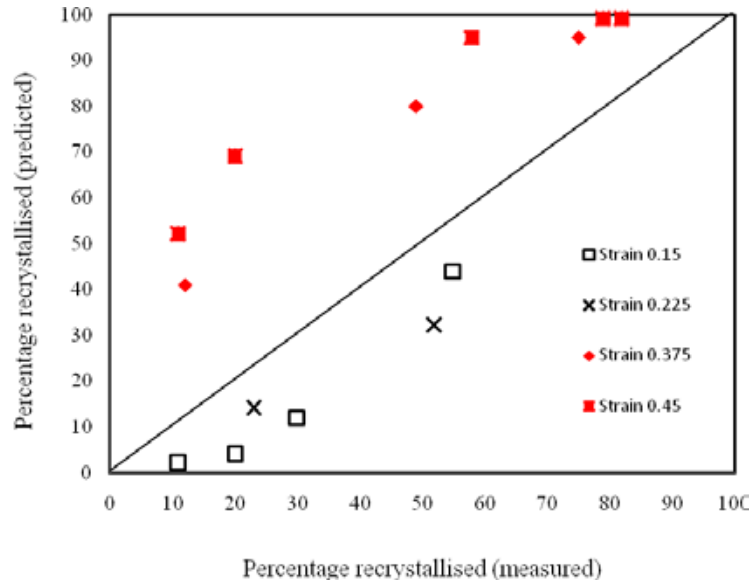

(a)

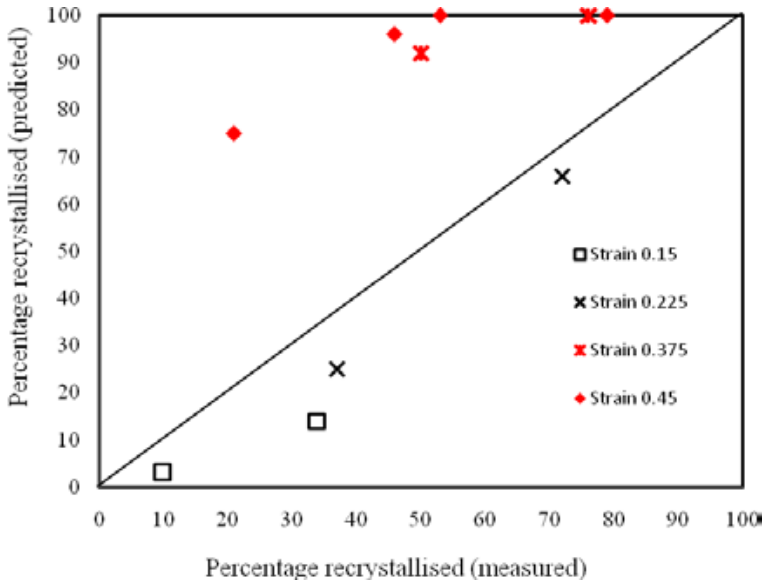

(b)

Figure 9.3. The variation of predicted % recrystallised vs the measured amount for a range of deformation strains from the present study using the Dutta-Sellars equations modified by the individual grain size class approach (a) homogenised Slab 1 (0.045 wt % Nb), (b) 0.094 wt % Nb steel.

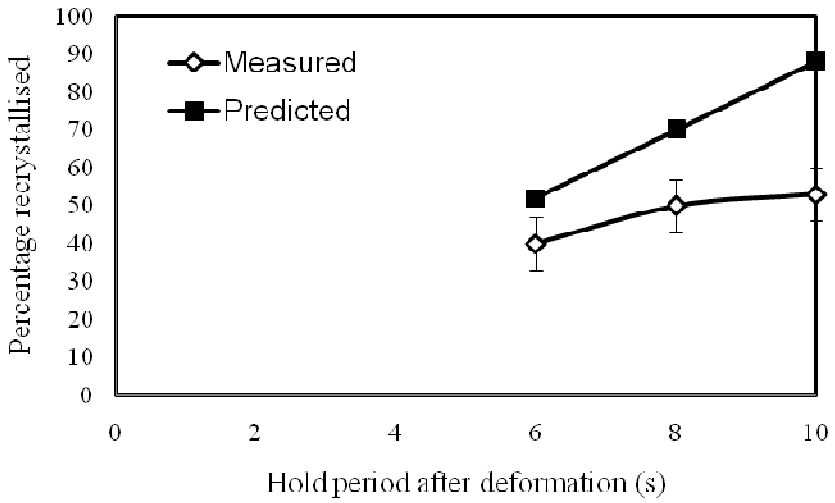

Figure 9.4. Variation of predicted and measured amount of recrystallisation with time for the 0.094 wt% Nb steel after deformation at 1090 ^{o}C to a strain of 0.45.

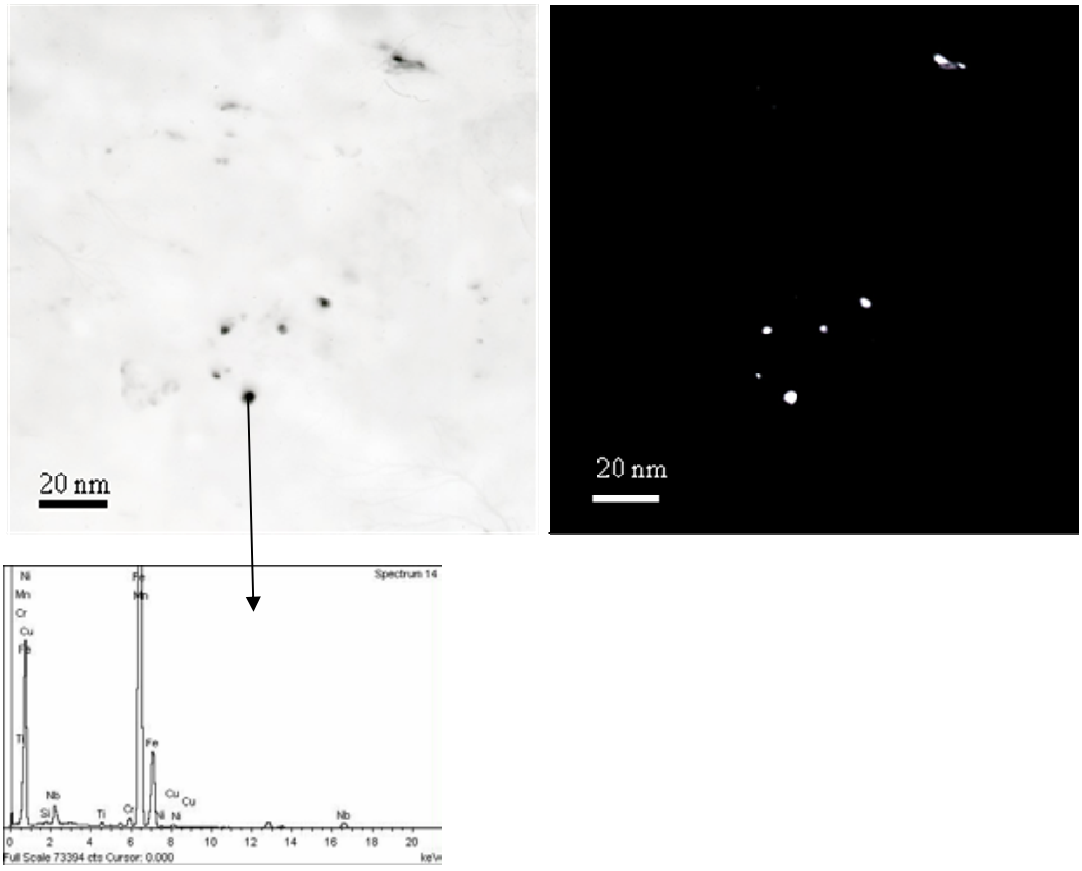

Figure 9.5. Bright field and dark field TEM images and EDS trace, showing Nb-rich precipitates, probably Nb(C,N), taken from a 0.094 wt% Nb sample deformed at 1090°C with 0.45 strain and 6 seconds hold. Nb(C,N) particles were identified using a <220> pole for the fcc phase.

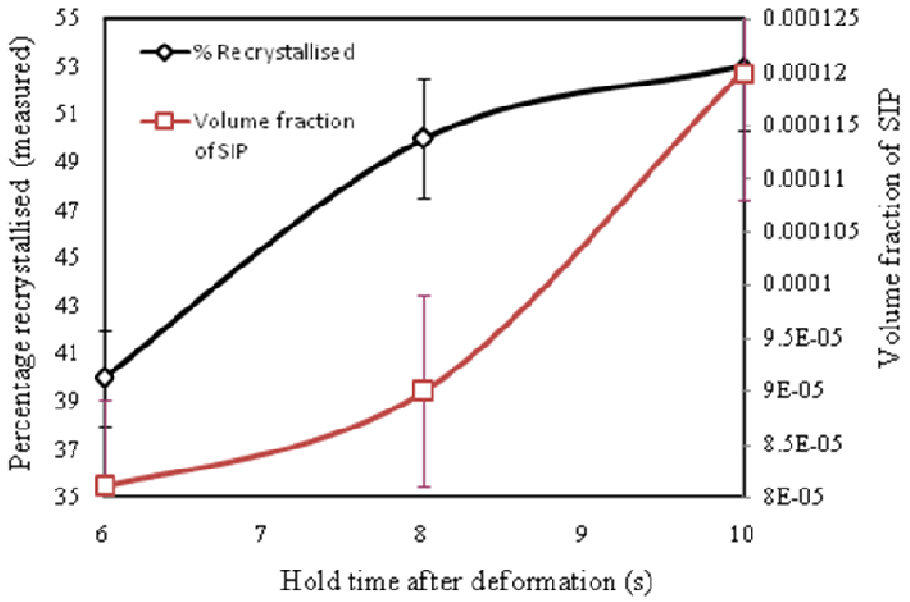

Figure 9.6. The variation of measured % recrystallised and volume fraction of strain-induced Nb(C,N) precipitates (SIP) as a function of hold period after deformation to 0.45 strain at 1090 °C, for the 0.094 wt% Nb sample.

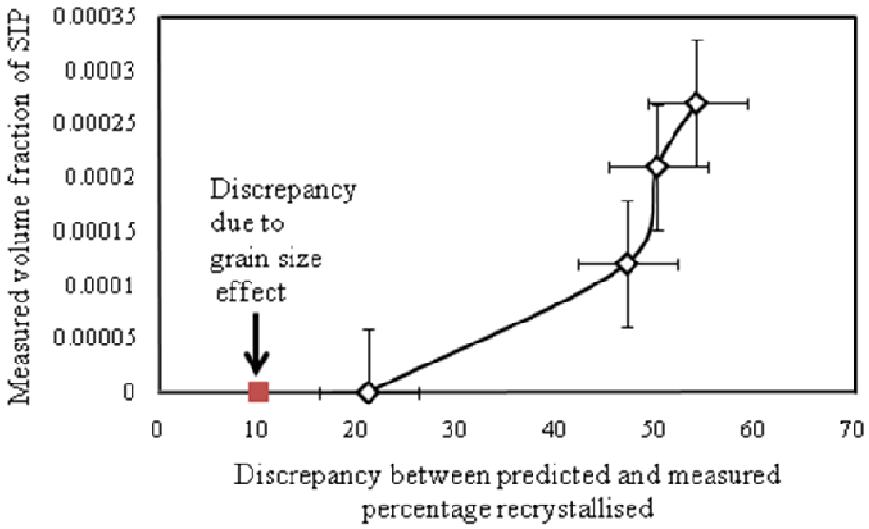

Figure 9.7. Variation of measured volume % of SIPs with discrepancy between predicted and measured amount of recrystallisation at 0.45 strain for 10 s hold at a range of deformation temperatures in 0.094 wt % Nb steel.

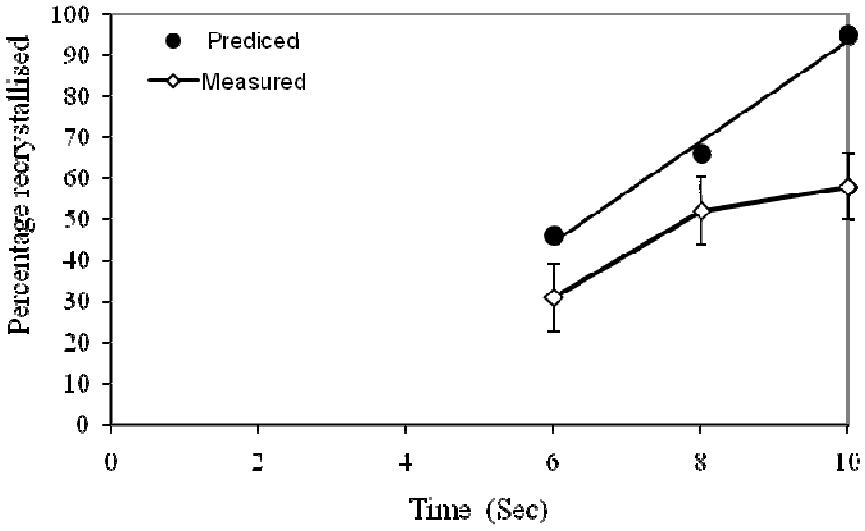

Figure 9.8. Variation of predicted and measured amount of recrystallisation with time after deformation at 1025 ^{o}C and 0.45 strain in the Slab 1 homogenised (0.045 wt % Nb) steel.

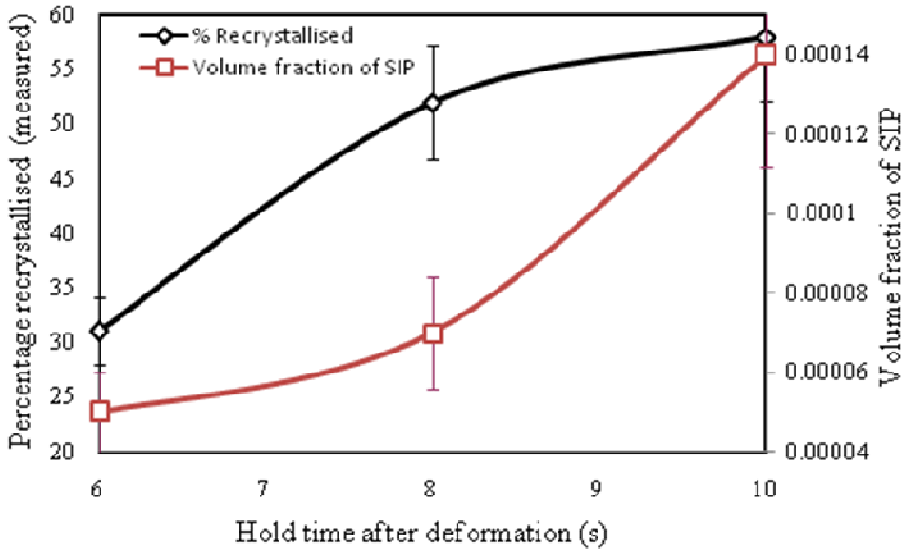

Figure 9.9. The variation measured % recrystallised and volume fraction of strain-induced Nb(C,N) precipitates as a function of hold period after deformation to 0.45 strain at 1025 °C in the Slab 1 homogenised (0.045 wt % Nb) steel.

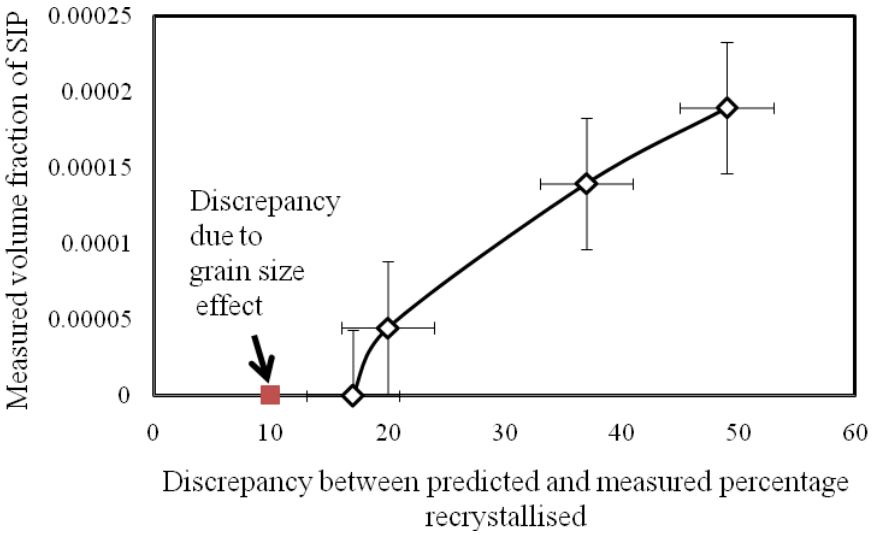

Figure 9.10. Variation of measured volume % of SIPs with discrepancy between predicted and measured amount of recrystallisation at 0.45 strain for 10 s hold at a range of deformation temperatures in the Slab 1 homogenised (0.045 wt % Nb) steel.

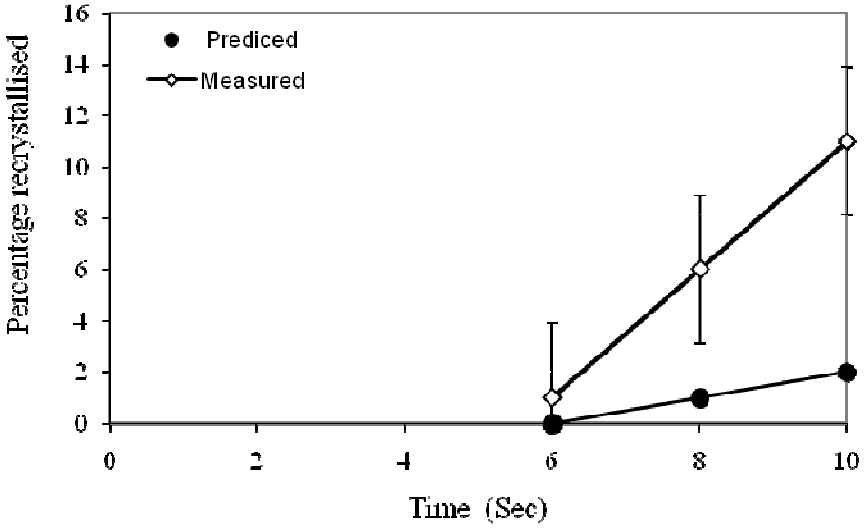

Figure 9.11. Variation of predicted and measured amount of recrystallisation with time after deformation at 1025 ^{o}C and 0.15 strain in Slab 1 homogenised (0.045 wt % Nb) steel.

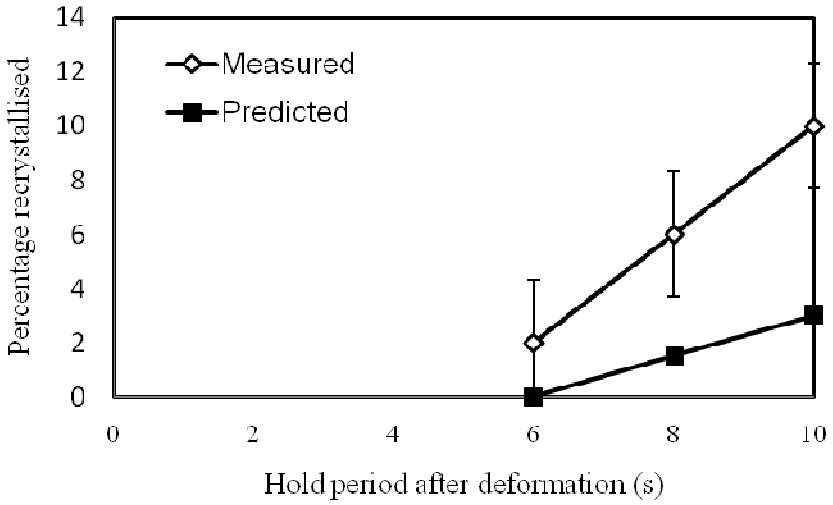

Figure 9.12. Variation of predicted and measured amount of recrystallisation with time after deformation at 1025 ^{o}C and 0.15 strain in 0.094 wt % Nb bearing steel.

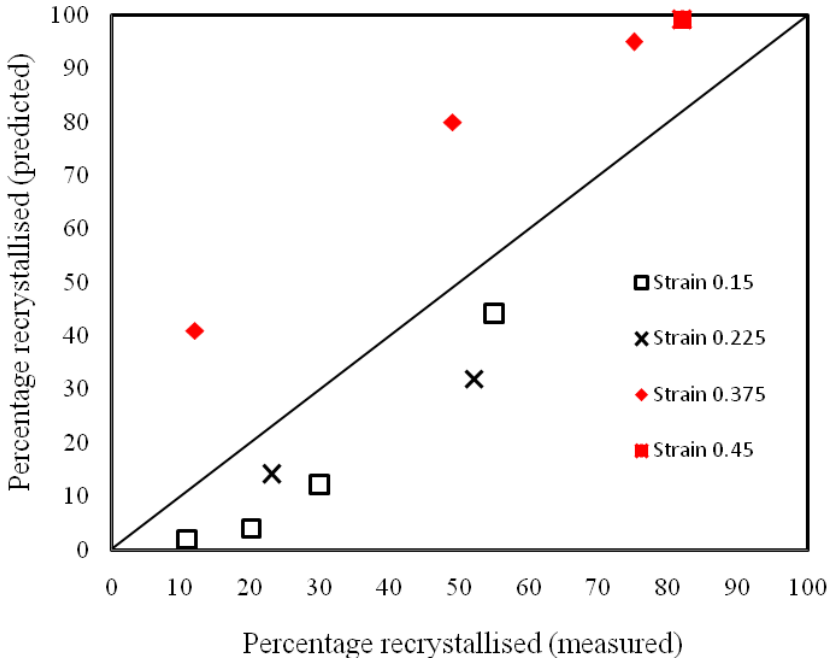

Figure 9.13. Variation of predicted and measured amount of recrystallisation after removing the data where discrepancy is caused by deformation induced precipitates in the homogenised Slab 1 steel.

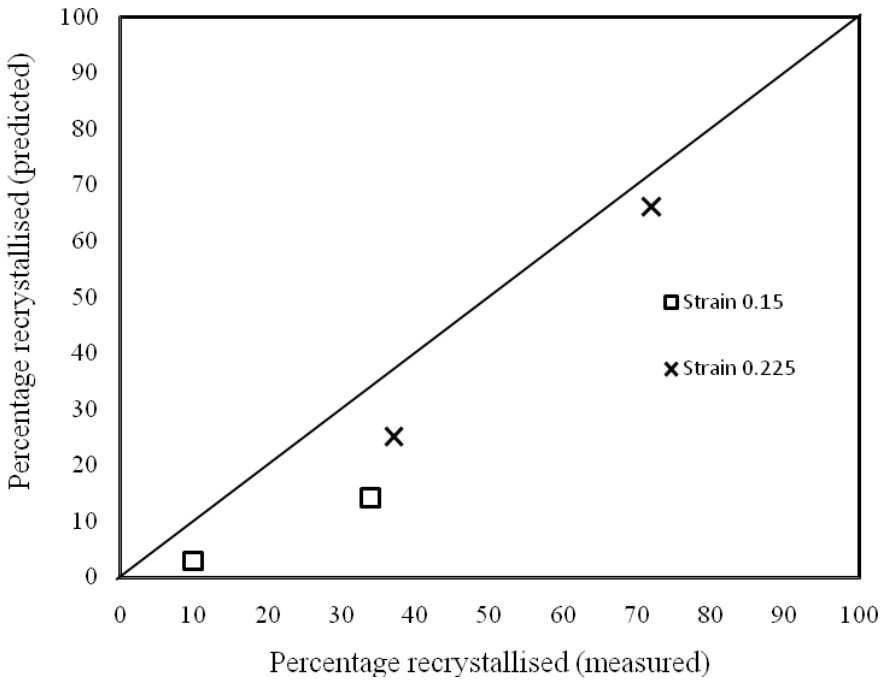

Figure 9.14. Variation of predicted and measured amount of recrystallisation after removing the data where the discrepancy was caused by deformation induced precipitates in the 0.094 wt % Nb bearing steel.

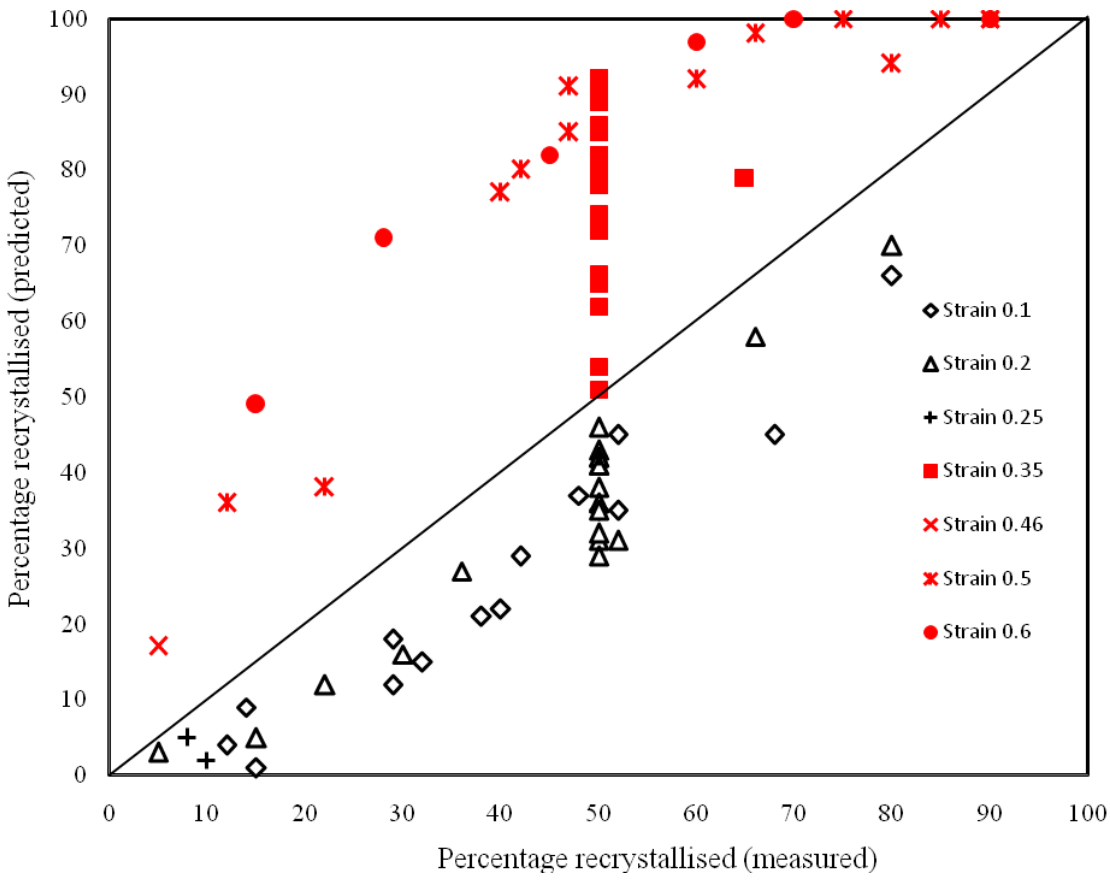

Figure 9.15. Variation of predicted and measured amount of recrystallisation using literature data after removing the data where discrepancy is caused by deformation induced precipitates.

CHAPTER – 10

Pinning of austenite grain boundaries by mixed AlN and Nb(C,N) precipitates

It was discussed in section 2.7.5 in Chapter 2 that the development of a bimodal grain structure can be associated with the microsegregation of microalloying elements, particularly Nb, during solidification [14, 22, 23, 43, 44]. It was shown in Chapter 5 that reheating Slab 1 (0.045 wt % Nb) to 1150 ºC for 1 hour leads to the formation of a bimodal grain structure and that this was linked to dissolution of Nb(C,N) particles in the solute-depleted regions and subsequent grain growth in this region, whilst the Nb(C,N) particles in the solute-rich regions did not dissolve and pinned the grain boundaries. In this work it was proposed that instead of Nb(C,N) particles, AlN particles are used to pin the grain boundaries during reheating, as the segregation tendency is low in the case of Al, the precipitate stability is expected to be similar in the solute-rich and solute-depleted regions. This would be expected to lead to the formation of a unimodal grain structure on reheating. This chapter discusses the dissolution and coarsening of AlN and Nb(C,N) precipitates in solute-rich and solute-depleted regions and the final development of the grain structure after reheating in a steel that contains 0.057 wt % Al and 0.019 wt % Nb.

10.1 As-cast microstructure

Thermo-Calc software was used to predict the solidification sequence of the steel using average composition of the steel as an input. The slab starts to solidify as δ ferrite at 1520 ºC, and completes solidification as δ ferrite (Figure 10.1). The solute-rich last liquid will be present at the δ/δ grain boundaries, which would gradually transform to austenite (starts forming at 1440 ºC). The complex carbo-nitride particles

(i.e. (Nb,Ti,V)(C,N)) are predicted to start forming in austenite at 1320 ºC and the AlN particles are predicted to form at 1250 ºC. The as-cast microstructure from the quarter thickness position and the ferrite grain size distribution are shown in Figure 10.2. The area percent of second phase (predominantly pearlite and enclosed ferrite within the pearlite colony) is 16±2 %. It has been discussed in Chapter 5 that the area % of second phase is approximately the amount of solute-rich material present in the structure when solidification completed as δ ferrite. The C content in this steel (0.1 wt %) is the same as in Slab 1 and solidification in both the steels completed as δ ferrite. Therefore the area % of second phase can be considered as the total amount of solute-rich material present in the structure. The Thermo-Calc predicted partition ratio (i.e. solute content ratio in the last liquid and first solid) for Nb is 4.72 and for Al is 0.8 in this steel.

Figure 10.3 (a) shows an array of Nb rich precipitates decorating a prior boundary (δ ferrite or austenite) in the as-cast structure. The Nb-rich precipitate size distributions in the solute-rich and in the solute-depleted regions show that Nb-rich precipitates were present in the size range ~ 0-300 nm (Figure 10.3 (b)) in both regions. The extent of inhomogeneity in the distribution of Nb-rich precipitates has been quantified in terms of the average (local) precipitate number density (number / mm^2) in the solute-rich and solute-depleted regions, Table 10.1. The overall average number density was also measured by considering the solute-rich and solute-depleted regions over continuous fields of view. The number density and area fraction of Nb-rich particles are ~ 4.2-4.6 times higher in the solute-rich regions compared to that in the solute-depleted regions, which is consistent with the segregation tendency of Nb. Previous studies on a 0.045 wt % Nb steel containing same amount of C and N has also shown that at the quarter-

thickness position the average precipitate number density in the solute-rich regions was ~ 3.8-5.0 times higher than that in the solute-depleted regions [14, 22, 23, 43, 44].

AlN particles were observed using SEM and are faceted and irregular in shape, Figure 10.4 (a), they were identified from their dark appearance in the back scattered electron (BSE) image and from the presence of the Al peak in the EDS spectrum. The size distribution of AlN particles at the quarter-thickness position of the slab (mean particle size of 150 nm) is shown in Figure 10.4 (b). AlN particles were found randomly distributed throughout the matrix. As Al shows limited segregation tendency compared to Nb the number density of the particles should be similar in the solute-rich and in the solute-depleted regions. However a slightly higher number density of AlN particles was found in the solute-depleted regions and that is associated with the greater availability of nitrogen in the solute-depleted regions. The Thermo-Calc predicted mass % of nitrogen and Nb in the solute-depleted regions is 0.008 and 0.0039 and that in the solute-rich regions is 0.014 and 0.019 respectively. Nb has a greater affinity to nitrogen compared to Al [1]. Therefore more amount of nitrogen should be free in the solute-depleted regions to combine with Al as available Nb content is less due to partition of Nb to the solute-rich regions. The mass % of available nitrogen in solution at 1250 ºC, the temperature at which AlN starts to nucleate is 0.003. The area fraction of AlN particles is higher in the solute-depleted regions compared to the Nb rich particles and in solute-rich regions it is one third of that of the Nb rich particles, Table 10.1. The lower number density of AlN particles in the solute-depleted regions as compared to Nb(C,N) particles is due to the larger size of AlN particles compared to Nb(C,N). Although the area fraction of AlN particles is higher. The larger size of the

AlN particles is due to the faster diffusivity of Al (Table 2.4, Chapter 2) leading to faster growth compared to Nb(C,N).

The total number density of the particles present in this steel (i.e. Nb(C,N) and AlN) in the solute-depleted regions is $22.4X10^4$ mm^{-2}, greater than that is present in Slab 1 in the solute-depleted regions [14, 43]. The number density of the particles present in the Slab 1 in the solute-depleted regions is $16X10^4$ mm^{-2} [14, 43]. Due to the higher number density and area fraction of Nb(C,N) and AlN in the solute-depleted regions greater pinning is expected during reheating compared to Slab 1 where Nb(C,N) is only the pinning particle and due to the strong segregation tendency of Nb to solute-rich regions there is less pinning is available in the solute-depleted regions leading to formation of bimodal grain size distribution during reheating.

10.2 Thermo-Calc predicted precipitate stability

The Thermo-Calc predicted stability of (Nb,Ti,V)(C,N) and AlN in the solute-rich and solute-depleted areas is shown in Figure 10.5. The compositions of the last liquid and first solid were used as input to predict the precipitate stability in the solute-rich and solute-depleted regions respectively. The reheat temperatures were selected based on this diagram. Commercial reheating is usually carried out at temperatures of 1100 to 1200 °C [1, 12, 13, 17]. Reheating in the temperature range of approximately 1100-1200 °C would result in near complete dissolution of the (Nb,Ti,V)(C,N) precipitates in the solute-depleted regions but retention of the majority of those in the solute-rich regions. Dissolution of the AlN particles occurs over a small temperature range (1200-1250 °C) for the solute-depleted and solute-rich regions.

The higher dissolution temperature of AlN in the solute-depleted regions is due to the fact that Al partitions to solute-depleted regions (partition ratio 0.8) and there is a

higher N content in solution in this region (N in solute rich region preferentially combines with Nb); therefore a greater amount of AlN is predicted to be stable in the solute-depleted regions as compared to solute-rich regions. Figure 10.5 shows that a bimodal grain structure would be predicted for reheating below 1200 °C based on the Nb(C,N) particles alone, the presence of AlN in the solute-depleted region mean that below ~ 1250 °C a unimodal structure is predicted if the AlN are effective in pinning the grain boundaries. Above ~ 1300 °C dissolution of pinning precipitates in both regions would give a coarse, but still unimodal, grain structure. In the present study reheating was carried out at 1150 and 1125 °C (i.e. in the commercial reheat temperature range) to see whether the presence of AlN particles in the solute-depleted regions would give sufficient pinning to stop grain growth and hence avoid the formation of bimodal grain size distribution.

10.3 Reheated microstructures

The marked difference in (Nb,Ti,V)(C,N) stability between the solute-rich and solute-depleted regions, Figure 10.5, should result in a strongly bimodal grain structure for reheating at 1150 °C. However, the presence of AlN in both solute-depleted and solute-rich regions at 1150 °C should offset this to give reduced levels of bimodality. Chakrabarti et al. [43] has reported Thermo-Calc predicted precipitate stability in a 0.045 wt % Nb steel (Figure 2.23, Chapter 2) considering segregation of Nb and Al. There is predicted to no particles present in the solute-depleted regions at 1150 °C. Bimodal grain structures forms after reheating at 1150 °C due to loss of pinning in the solute-depleted regions leading to grain growth [14, 43]. Detailed SEM investigation has shown that there is no particles present in the solute-depleted regions [14, 43]. In the present study the total volume fraction (i.e. volume fraction of AlN and Nb(C,N))

of particles predicted to be present in the solute-depleted regions is 0.000108 at 1150 °C. If this amount of particles is sufficient to give pinning in the solute-depleted regions then formation of bimodal grain structure can be avoided or bimodality can be reduced.

The microstructure and prior austenite grain size distribution after reheating at 1150 °C is shown in Figure 10.6. The grain size distribution is bimodal with 29 % coarse grains by area, which is less than the total amount of solute-depleted material present in the microstructure (~ 84 %) suggesting that some pinning is available in the solute-depleted regions. In the present study reheating has been carried out on Slab 1 at 1150 °C (Chapter 5, Figure 5.4 (d)). The area % of the coarse grains present in the distribution is 35 % and the maximum grain size present in the distribution is 300 µm, ~ twice that shown in Figure 10.6. This also suggests some pinning is available in the solute-depleted regions compared to Slab 1.

The number density distributions of Nb- and Al-rich particles in the solute-rich and solute-depleted regions after reheating at 1150 °C are shown in Figure 10.7 (a and b) and Table 10.2 and 10.3. As mentioned in section 2.7.2, Chapter 2, the stability of precipitates is not the same everywhere in a slab and is proportional to the local solute levels. In the presence of micro-segregation the stability of Nb(C,N), therefore, is expected to be higher within the solute-rich regions compared to the solute-depleted dendrite centre regions. However AlN should have greater stability in the solute-depleted regions compared to solute-rich regions as Al partition to solute-depleted regions (Thermo-Calc predicted partition ratio of Al is 0.8). Around 90 % of the Nb-rich particles in the solute-depleted regions have dissolved after reheating to 1150 °C (compared to that in the as-cast condition) whilst the remaining ones have coarsened to

a mean size of 300 nm. The area fraction of the Nb(C,N) particles measured in the solute-depleted regions is 0.000009 which is less than predicted by Thermo-Calc (0.000018). Chakrabarti [14] has also found that the measured area fraction of particles using SEM is less than that predicted by Thermo-Calc. This disagreement could be due to the fact that SEM quantification of the precipitates is an average for the measurement area used, which is typically 480 μm^2 in this case. The composition of first solid and last liquid has been used to predict the precipitate stability in Thermo-Calc, which will relate to a smaller area of material. It has been shown in Chapter 2 and Chapter 5 that the SEM measured partition ratio is less than that predicted using Thermo-Calc. This may also lead to a greater predicted volume fraction of particles using Thermo-Calc than measured using SEM.

Fine particles of Nb(C,N), with a greater area fraction and number density, are present in the solute-rich regions, compared to the solute-depleted regions, to provide grain boundary pinning there. The area fraction of Nb(C,N) particles in the solute-rich regions is 0.000076 with a mean size of 175 nm. The higher solvus temperature of the precipitates in the solute-rich regions leads to less dissolution and coarsening of the particles. The measured area fraction of Al-rich particles in the solute-depleted regions is 0.000027 (0.000096 in the as-cast condition) and the mean size of the particles present is 350 nm. In the solute-rich regions the mean size of the Al-rich particles is 350 nm with a reduced area fraction of 0.0000042 (0.00006 in the as-cast condition). The greater dissolution of the AlN particles in the solute-rich regions as compared to those in the solute-depleted regions is due to the reduced stability of AlN in the solute-rich regions. The Thermo-Calc predicted volume fraction of AlN particles in the solute-rich and solute-depleted regions are respectively 0.000019 and 0.00009, higher

than that measured, which is consistent with the area fraction result of Nb(C,N) discussed earlier.

During reheating austenite nucleation occurs first in the solute-rich regions as the solute-rich region is associated with the second phases, which is predominantly pearlite. During reheating pearlite will undergo transformation first. The austenite that nucleates in the solute-rich regions will inherit the precipitate distribution and pinning dominated by Nb rich particles as a greater number density and area fraction of Nb(C,N) particles are present in the solute-rich regions compared to AlN due to partition of Nb. The solute-depleted regions transform later and have reduced grain boundary pinning as the number density and area fraction of Nb(C,N) and AlN is less as compared to solute-rich regions. The nucleation in the solute-depleted regions will initially be at the prior α ferrite grain boundaries where Nb and Al rich particles are observed. The total area fraction of Nb(C,N) and AlN particles in the solute-depleted regions in the as-cast condition is 0.000102 with average size 125 nm. This should pin the austenite nuclei nucleated at the ferrite grain boundaries at the start of reheating. Couch [44] and Chakrabarti [14] has reported that a volume fraction of 0.00009 with mean size 150 nm of Nb(C,N) particles are able to pin the grain boundary in 0.045 wt % Nb steel. So, despite the slow heating rate (3 °C/min), the nucleation is expected to be displaced from grain boundaries to grain interiors. The inclusions such as MnS, complex oxide particles present within the grains can act as nucleation sites for the austenite [30]. The number density of the inclusions i.e. MnS, Al_2O_3, SiO_2, MgO present in this steel at quarter thickness position is 25-45 /mm^2. The formation of austenite in the solute-depleted regions then proceeds accompanied by more growth until complete transformation occurs. At this stage all solute-rich regions consist of fine austenite grains whereas solute depleted regions show a range of grain sizes as the

austenite that nucleates at the ferrite grain boundaries will be finer but the austenite that nucleates within the grains would be able to grow. Further reheating above the complete austenite transformation temperature (912 °C, predicted by Thermo-Calc in this case) would lead to dissolution of Nb-rich precipitates first in the solute-depleted regions then in the solute-rich regions. Al-rich precipitates should undergo dissolution in the solute-rich regions first and then in the solute-depleted regions, due to the higher precipitate stability in the solute-depleted regions. At 1150 °C, the combined area fraction value of Nb(C,N) and AlN in the solute-depleted regions is 0.000029, which is only 28 % of the particles present in the as-cast condition (area fraction of AlN and Nb(C,N) in solute-depleted regions in the as-cast condition is 0.000102) with a mean size of 350 nm. The dissolution and coarsening of precipitates leads to growth in the bulk solute-depleted regions first and then gradually in the grains which are present at the prior ferrite/ferrite grain boundaries. Therefore the coarse grain part of the grain size distribution after reheating is associated with the solute-depleted material.

The much smaller proportion of coarse-grained material (29 %) compared with solute-depleted material (84 %) indicates that the increased amount of AlN particles are able to offset some difference in pinning in the solute-depleted regions which was absent in the case of Slab 1 and results in reduced bimodality as compared to Slab 1. In order to investigate the difference in pinning between solute-rich and solute-depleted regions the relative Zener drag value in both regions needs to be quantified.

As discussed in section 2.7.5, Chapter 2 the average grain diameter (D) can be related to the average diameter (d) of the pinning particles and to the volume fraction (f) of particles by the following equation:

$$D = \xi . \frac{d}{f} \qquad (10.1)$$

where, ξ is a constant and, in the current investigation the austenite grains grow in the presence of similar particles and over a similar temperature range (1050 - 1250 ºC) to that studied by Gladman [76] hence $\xi = \frac{\pi}{6}\left(\frac{3}{2} - \frac{2}{Z}\right)$ where Z is in the range 1.41 - 2.0. Gladman [76] pointed out that Zener's model overestimates the driving force for grain growth and, therefore, could overestimate the equilibrium grain size. Hillert [197] and Gladman [76] considered the inhomogeneity in grain size distribution and introduced the grain size heterogeneity factor, Z. Gladman [76] suggested, $\xi = \frac{\pi}{6}\left(\frac{3}{2} - \frac{2}{Z}\right)$, and compared his model with the experimental studies on the growth of austenite grains in the presence of NbC and AlN particles [76]. For the normally observed range of Z values (1.41 - 2.00) excellent agreement was reported between Gladman's model and experimental data [76]. Considering Z=2, for which ξ=0.26, and using the experimentally measured volume fractions and average precipitate sizes, the limiting grain sizes can be predicted in the solute-rich and solute-depleted regions of the reheated samples. Limiting grain size values represent the average grain sizes at which grain growth stops in a particular region. The limiting grain size values after reheating at 1150 ºC using the measured area fractions and average size of Nb(C,N) and AlN in the solute-rich and solute-depleted regions are listed in Table 10.4 and suggest that grain growth is expected more in the solute-depleted regions.

The relative Zener drag in the solute-rich and solute-depleted regions has been calculated by taking the ratio of the limiting grain size in the solute-rich and solute-depleted regions. Zener drag results from the combined area fractions and sizes of Nb-

and Al-rich particles and the relative levels of Zener drag in the solute-rich and solute-depleted regions are shown in Table 10.5. During reheating full re-formation of austenite occurs first after which grain growth takes place. The large difference in Zener drag between solute-rich and solute-depleted regions results in faster coarsening in the solute-depleted regions. The average particles size (both AlN and Nb(C,N)) present in the solute-depleted regions are in excess of 300 nm. These few coarse particles are not able to pin the grain boundaries in the solute-depleted regions, hence bimodal grain size distribution develops.

The total measured volume fraction of the particles (i.e. volume fraction of AlN and Nb(C,N)) present in the solute-rich and solute-depleted regions are 0.0000802 and 0.000029 respectively. No grain growth was seen in the solute-rich regions. Therefore it can be said that 0.0000802 area fraction of particles with an average size of 175 nm can provide sufficient pinning to retard grain growth at this temperature.

Using a lower reheat temperature of 1125 °C retains a greater volume fraction of AlN (0.00019 predicted) in the solute-depleted regions compared to 1150 °C (0.00009) with approximately the same amount of (Nb,Ti,V)(C,N) in that region (0.000019 at 1125 °C and 0.000018 at 1150 °C). At 1125 °C the total volume fraction of particles is predicted to be 0.000209 in the solute-depleted regions and 0.00021 in the solute-rich regions. Assuming similar particle size distributions as seen in the as-cast condition then the grain boundary pinning should be more uniform between the solute-rich and solute-depleted regions and that should result in less coarsening of the particles. The grain size distribution should be unimodal if AlN, with greater volume fraction and number density are as effective in pinning in solute-depleted regions as Nb-rich particles are in solute-rich regions.

Figure 10.8 shows that the microstructure and prior austenite grain size distribution after reheating for 1 hour is bimodal with ~ 12 % coarse grains by area. This is less bimodality than at 1150 °C indicating that the volume fraction of Al-rich particles are providing grain boundary pinning in the solute-depleted regions, but not completely as expected from equilibrium volume fraction values. From the number density distribution of Nb-rich particles it can be seen (Figure 10.9 (a)) that there is almost no change in number density of the Nb(C,N) particles in the solute-depleted regions compared to 1150 °C as predicted by Thermo-Calc. However, a greater number of finer particles of AlN are present in the solute-depleted regions as compared to reheating at 1150 °C (Figure 10.9 (b)). Therefore AlN particles should dominate grain boundary pinning in solute-depleted regions as there is no change in area fraction of Nb(C,N) particles at 1125 °C as compared to 1150 °C, whereas AlN and Nb(C,N) should both act in solute-rich regions.

The coarsening of AlN at 1125 °C in the solute-depleted regions is also less as compared to 1150 °C. The average AlN particle size after 1125 °C is 175 nm, finer than that at 1150 °C (350 nm). Using measured particle area fraction and mean size values the limiting grain size values have been determined (Table 10.4). From the limiting grain size values it can also be seen that less grain growth is expected in the solute-depleted regions as compared to at 1150 °C. Relative grain boundary pinning forces in solute-rich and in solute-depleted regions were also determined (Table 10.6). The smaller difference in Zener drag between solute-rich and solute-depleted regions results in more even grain boundary movement i.e. reduced bimodality. Although Al-rich particles are providing greater grain boundary pinning in solute-depleted regions, parity between solute-rich and solute-depleted is not achieved as the particles

distributions are not equilibrium ones after 1 hour holding at the reheating temperatures.

Extended holding for 2 and 8 hours at 1125 ^{o}C caused further dissolution of both Nb- and Al-rich particles, Table 10.2 and 10.3. Figure 10.10 (a) shows the variation of number density distribution of AlN particles, which is associated with increased grain growth, initially increasing then reducing bimodality, Figure 10.10 (b). The degree of bimodality is increased at 2 hours (17 % coarse grains in the distribution) reheating at 1125 ^{o}C. The area fraction of the AlN particles in the solute-depleted regions after 2 hours holding is 0.000012 and after 1 hour holding it was 0.000031. Therefore this increase in area % of coarse grains is associated with the ~ 60 % dissolution of the AlN particles within an hour (Table 10.3).

After 8 hours holding at 1125 ^{o}C the grain size distribution is a skewed unimodal distribution. This is consistent with the gradual dissolution of AlN particles in the solute-depleted regions. After 8 hours the area fraction of the particles present in the solute-depleted regions is 0.0000048 which is only 4 % of the particles present in the as-cast condition in the solute-depleted regions. The mean size of the particles is 350 nm. Therefore the small numbers of coarse particles do not provide any significant pinning in the solute-depleted regions leading to ~ 84 % coarse grains present in the distribution. This would suggest that pinning for the equilibrium particle distributions in solute-rich and solute-depleted regions should be uniform, but that, in practice, the pinning is greater due to undissolved particles in the solute-rich region resulting in differences in pinning between solute-rich and solute-depleted regions. Thus, formation of bimodal grain size distribution is consistent with Al-rich particles being present during reheating then gradually being dissolved to release grain boundaries and

give a proportion of coarse-grained closer to 84 %, i.e. the total solute-depleted materials present in the structure.

10.4 Conclusions

A 0.057 wt % Al, 0.019 wt % Nb steel has been investigated to see whether AlN particles are effective in pinning grain boundaries during reheating to offset difference in grain boundary pinning between solute-rich and solute-depleted regions due to segregation of Nb. The major findings are as follows:

1. Grain bimodality is due to the difference in grain boundary pinning between solute-rich and solute-depleted regions.

2. Increased amounts of AlN particles can offset difference in pinning behaviour due to Nb segregation.

3. Quantitative correlation of coarse and fine grains with solute-depleted and solute-rich regions is not seen for shorter heating times due to incomplete dissolution of particles to equilibrium levels.

4. Prolonged holding times give greater particle dissolution and grain boundary pinning closer to that expected.

Tables and Figures

Table 10.1. The area fraction number density and average size of the Nb and Al rich particles in the solute-rich and in the solute-depleted regions of the as-cast slab.

As-cast	Area fraction (Measured)		Area fraction (Average)	Number density (mm^{-2})			Average size (nm)	
	Solute - rich	Solute - depleted		Average	Solute – rich	Solute – depleted	Solute - rich	Solute - depleted
AlN	0.000096	0.00006	0.000085	$3.8X10^4$	$3X10^4$	$4X10^4$	200	150
Nb(C,N)	0.00018	0.000042	0.000080	$3.23\ X10^5$	$8.47X10^5$	$1.84X10^5$	125	125

Table 10.2. Area fraction and number density of Nb(C,N) particles in the solute-rich and solute-depleted regions.

Reheat temperature (°C)	Area fraction (Measured)		Area fraction (Measured)	Number density		
	Solute – rich	Solute – depleted		Total	Solute – rich	Solute – depleted
1125 - 1 hour	0.0001	0.0000028	0.00007	2.41 $X10^5$	6.04$X10^5$	0.14$X10^5$
1125 - 2 hour	0.00009	0.000002	0.000039	1.28$X10^5$	3.4$X10^5$	0.07$X10^5$
1125 - 8 hour	0.000006	0.0000007	0.000006	0.39$X10^5$	0.82$X10^5$	0.01$X10^5$
1150 - 1 hour	0.000076	0.000002	0.000032	1.1 $X10^5$	2.92$X10^5$	0.12$X10^5$

Table 10.3. Area fraction and number density of AlN particles in the solute-rich and solute-depleted regions.

Reheat temperature (°C)	Area fraction (Measured)		Area fraction (Measured)	Number density		
	Solute – depleted	Solute – rich		Total	Solute – depleted	Solute – rich
1125 - 1 hour	0.000078	0.000031	0.000071	1.59 $X10^4$	1.71$X10^4$	0.87$X10^4$
1125 - 2 hour	0.00005	0.000012	0.000045	0.97$X10^4$	1.06$X10^4$	0.52$X10^4$
1125 - 8 hour	0.0000041	0.000001	0.0000024	0.3$X10^4$	0.31$X10^4$	0.14$X10^4$
1150 - 1 hour	0.000027	0.0000042	0.000023	0.54 $X10^4$	0.62$X10^4$	0.1$X10^4$

Table 10.4. Limiting grain size in the solute-rich and solute-depleted regions at 1150 and 1125 °C.

Temperature (°C)	Predicted limiting grain size based on measured area fraction of Nb(C,N) and AlN in solute-rich area (μm)	Predicted limiting grainsize based on measured area fraction of Nb(C,N) and AlN in solute-depleted area (μm)
1150	567	3137
1125	297	482

Table 10.5. Zener drag in the solute-rich and solute-depleted regions at 1150 °C.

Relative grain boundary particle pinning	
Solute – depleted regions	Solute – rich regions
1	5.5

Table 10.6. Zener drag in the solute-rich and solute-depleted regions at 1125 °C.

Relative grain boundary particle pinning	
Solute – depleted regions	Solute – rich regions
1	1.6

$$L \longrightarrow L+\delta \longrightarrow \delta + \gamma \longrightarrow \gamma + NbTiV(CN)$$

1520 °C 1440 °C 1320 °C

Figure 10.1. Thermo-Calc predicted solidification sequence.

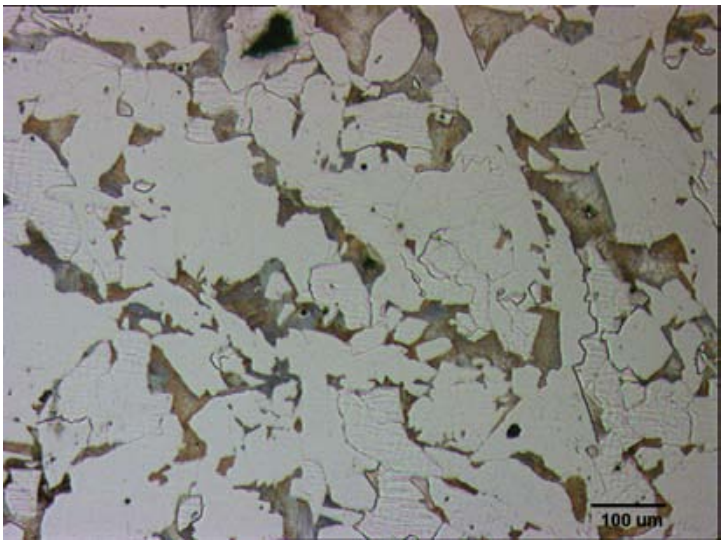

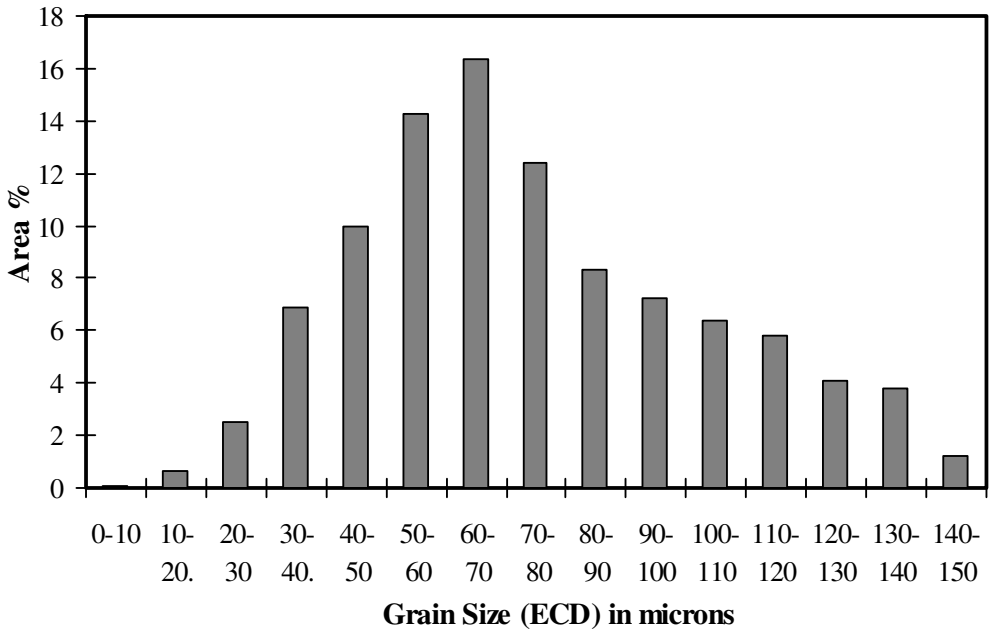

Figure 10.2. Microstructure from the quarter thickness position of the as-cast slab and the ferrite grain size distribution

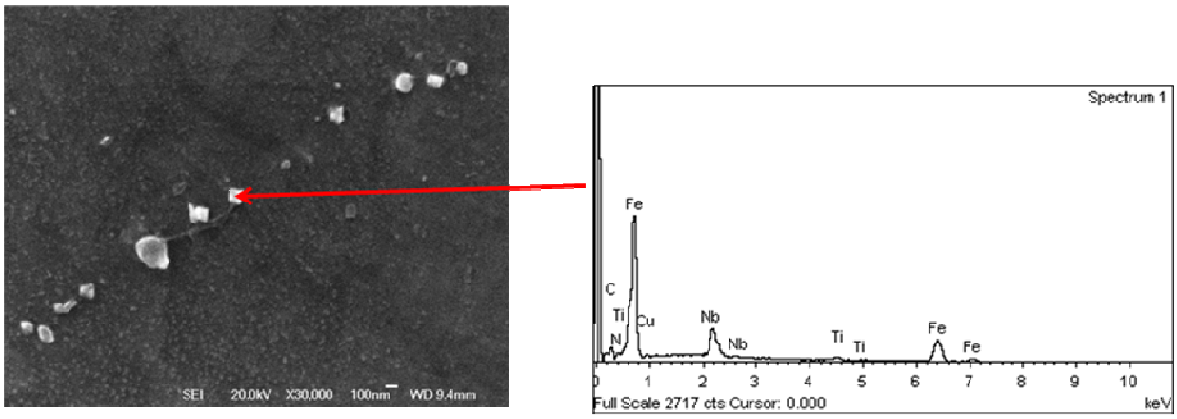

(a)

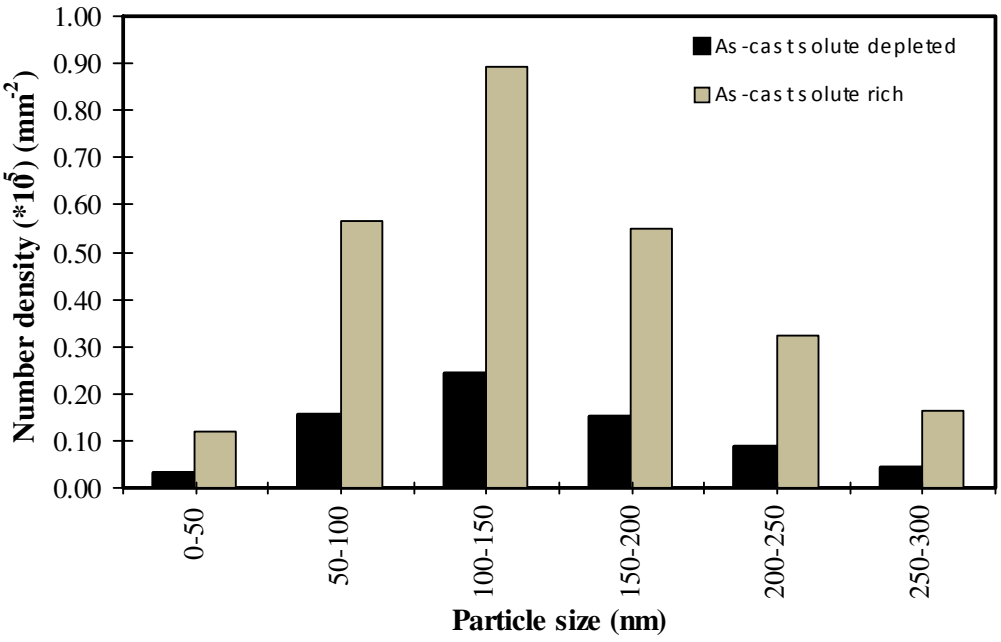

(b)

Figure 10.3. (a) Array of Nb-rich particles, probably Nb(C,N), with EDS trace showing the Nb peak, and (b) number density distribution of Nb-rich particles in the solute-rich and solute-depleted regions in the as-cast slab.

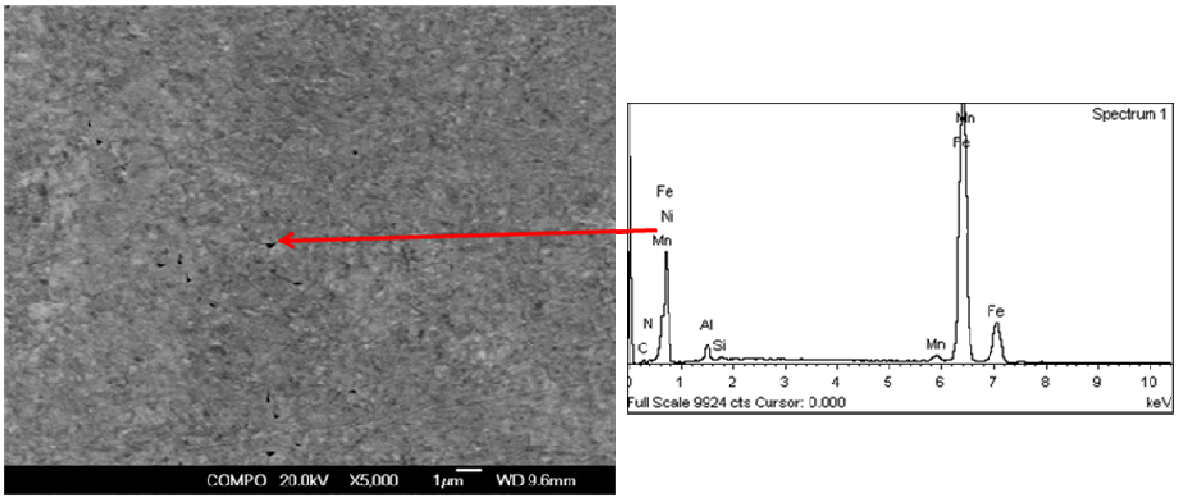

(a)

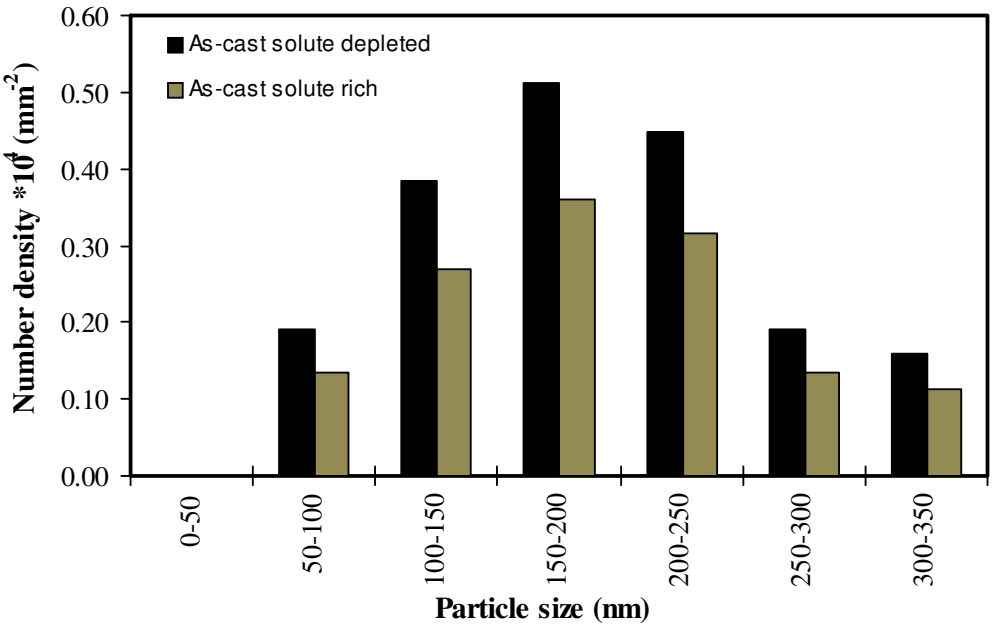

(b)

Figure 10.4. (a) Array of Al-rich particles, expected to be AlN, with EDS trace showing the Al peak, and (b) number density distribution of Al-rich particles in solute-rich and solute-depleted regions in the as-cast slab.

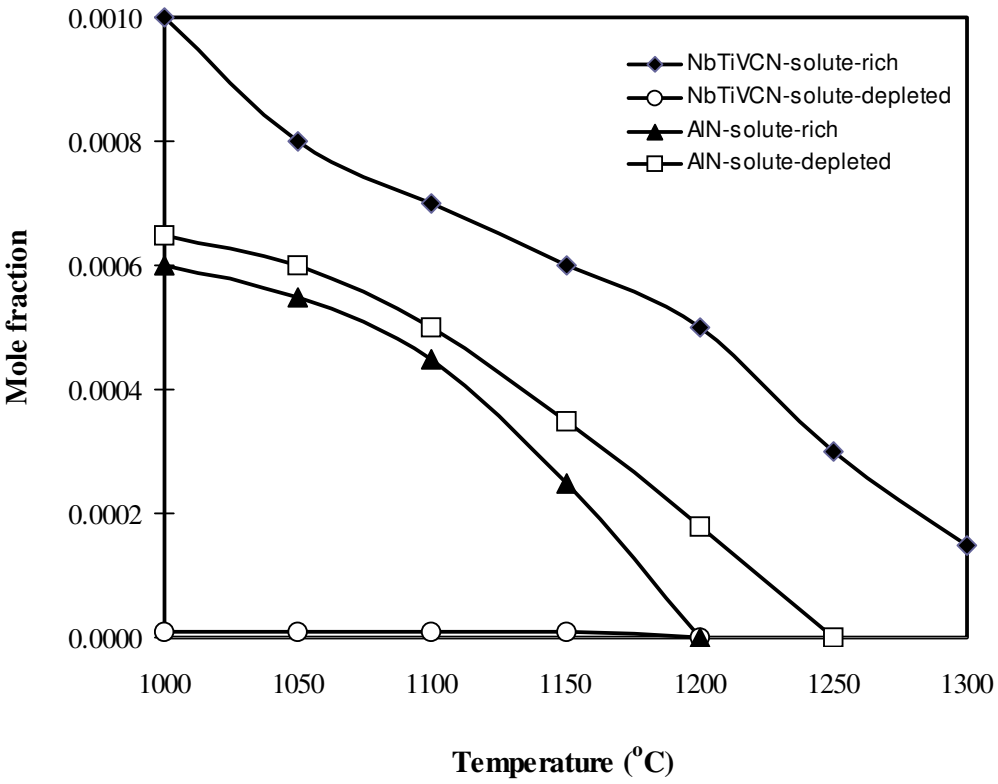

Figure 10.5. Thermo-Calc predicted stability of (Nb,Ti,V)(C,N) and AlN in the solute-rich and solute-depleted regions.

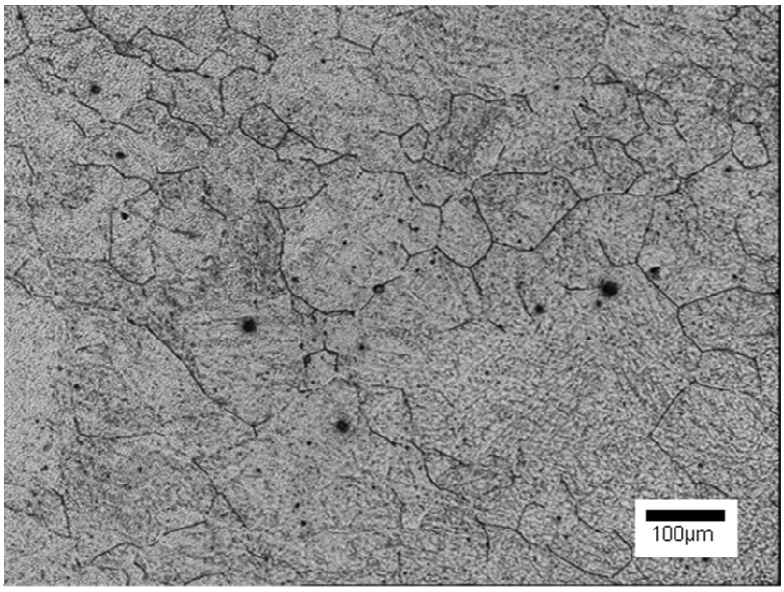

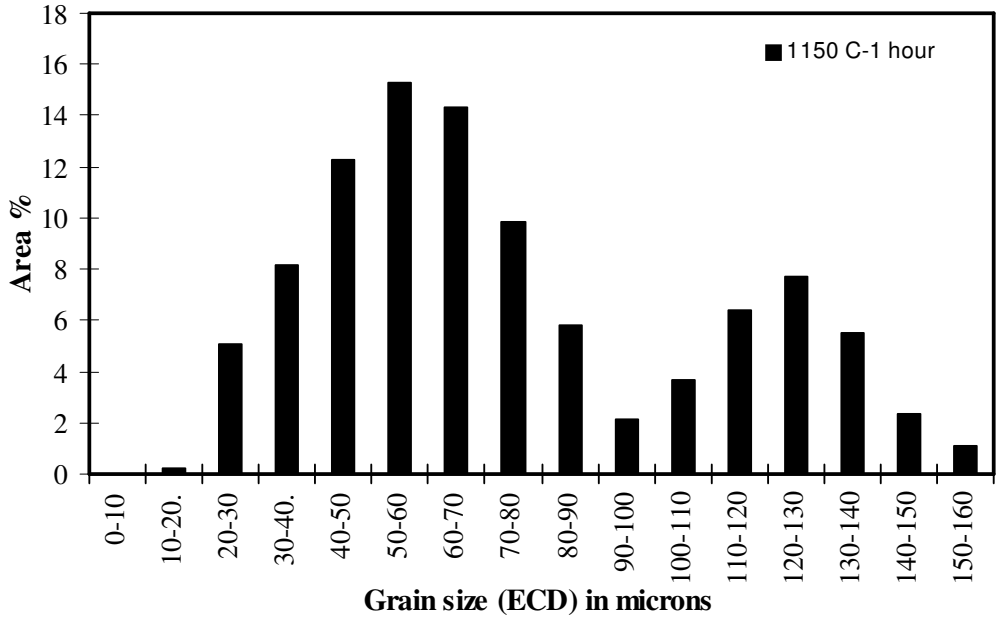

Figure 10.6. Microstructure and prior austenite grain size distribution after reheating at 1150 ℃.

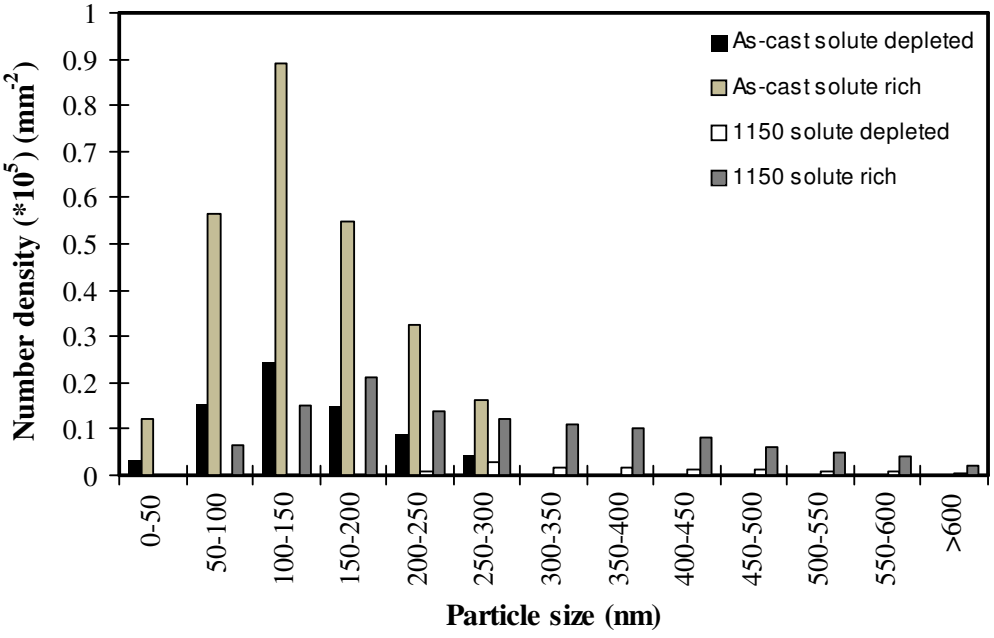

(a)

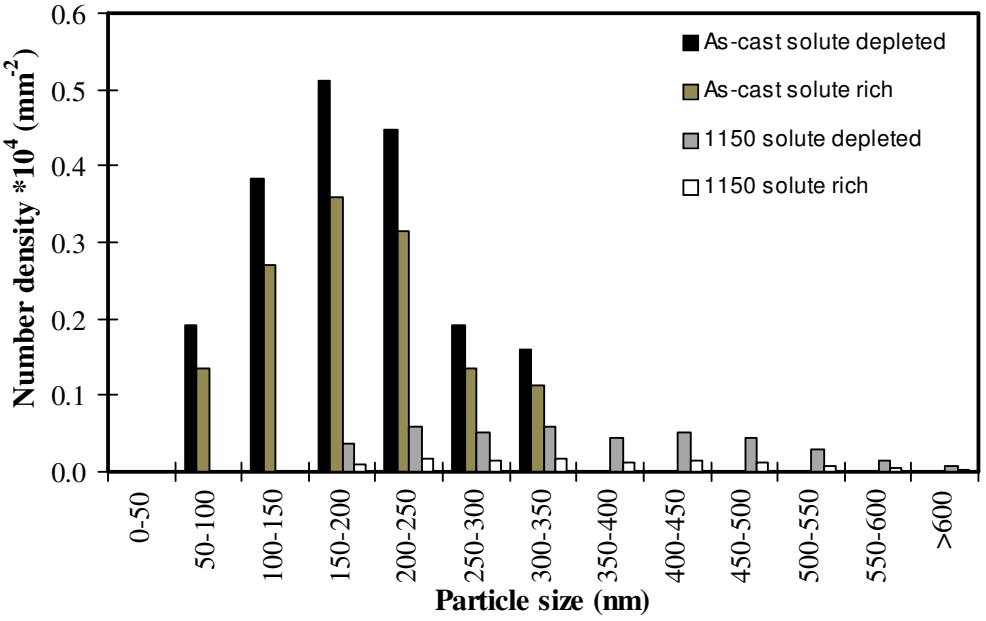

(b)

Figure 10.7. Number density distributions of (a) Nb(C,N) and (b) AlN particles in the solute-rich and solute-depleted regions after reheating at 1150 °C, compared to that present in the as-cast slab.

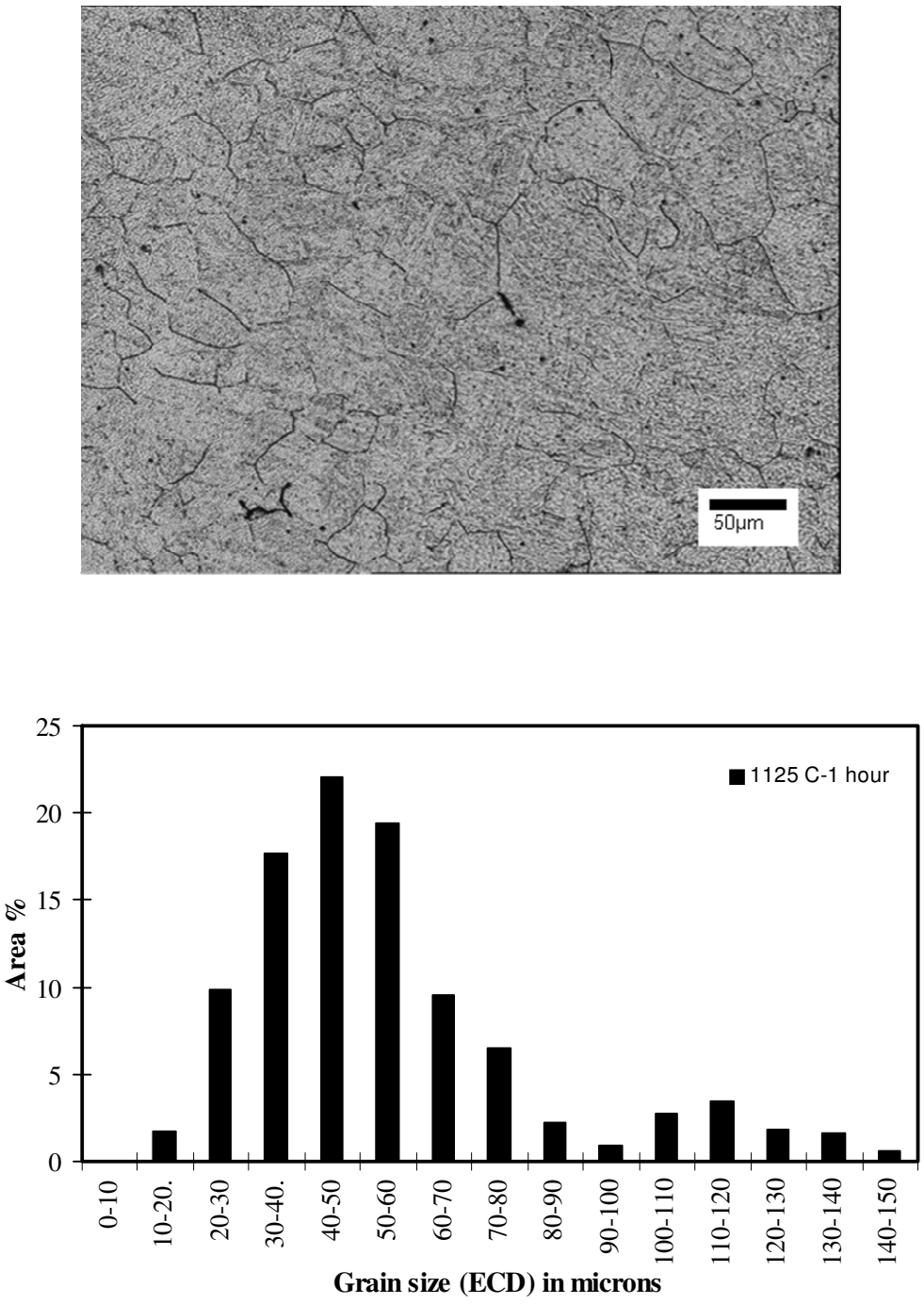

Figure 10.8. Microstructure and prior austenite grain size distribution after reheating at 1125 °C.

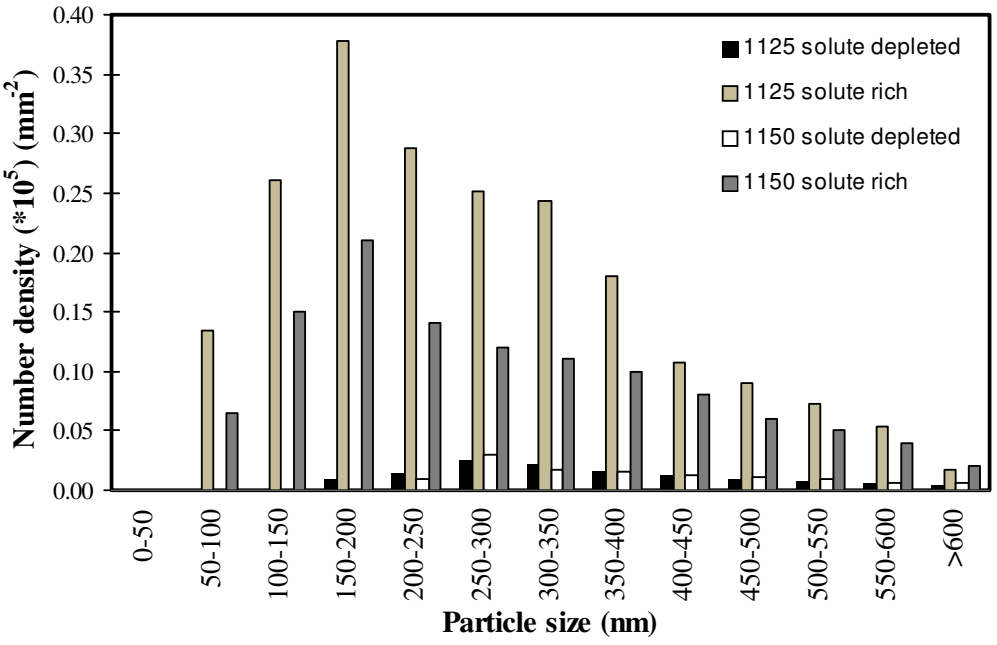

(a)

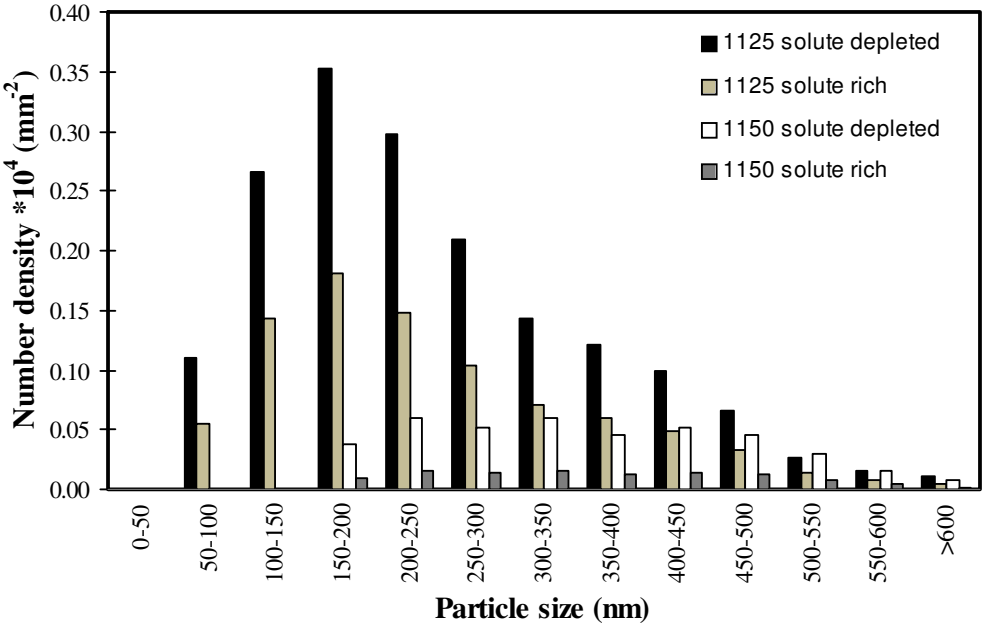

(b)

Figure 10.9. Number density distributions of (a) Nb(C,N) and (b) AlN particles in the solute-rich and solute-depleted regions after reheating at 1125 °C.

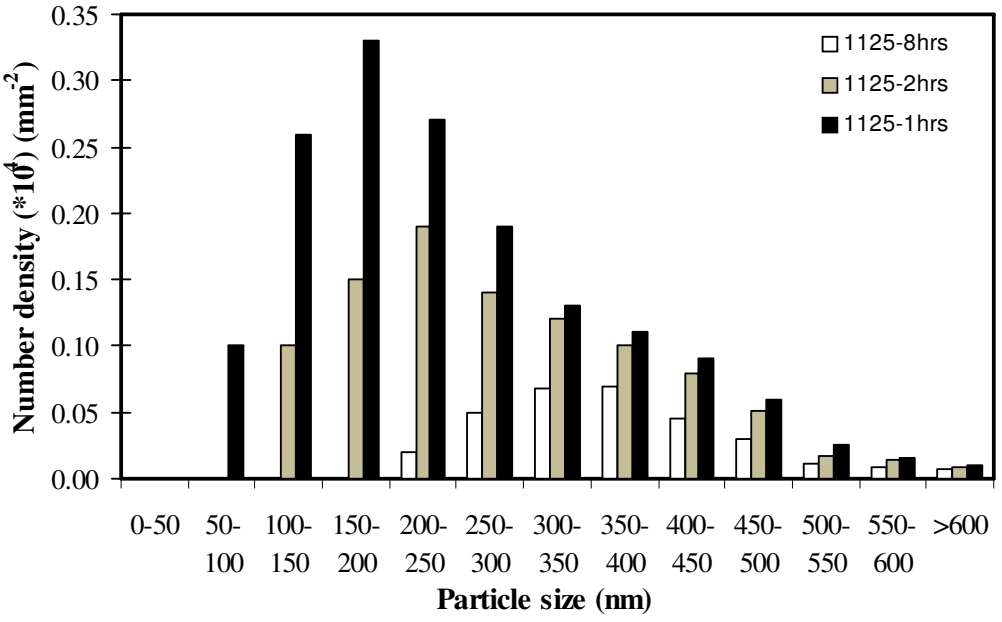

(a)

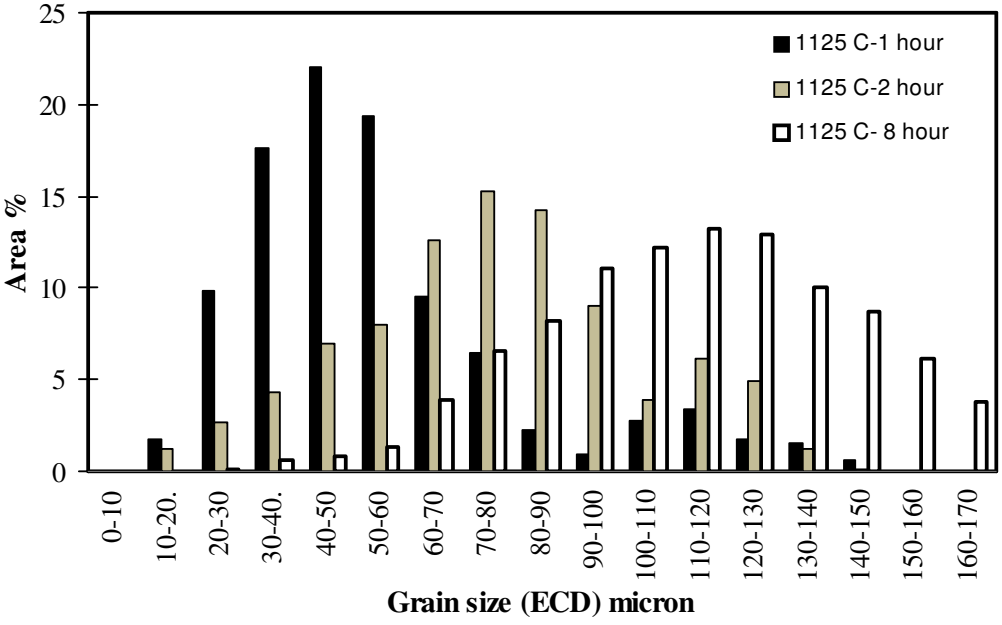

(b)

Figure 10.10. (a) Number density distributions of Al-rich particles (b) prior austenite grain size distribution after reheating at 1125 °C for 1, 2 and 8 hours.

CHAPTER – 11

Conclusions

In this thesis studies have been carried out in three major areas:

(i) Limits of validity of Dutta-Sellars equations; effect of grain size, strain and Nb content on recrystallisation kinetics.

(ii) Modelling grain size distribution after deformation on homogenised Slab 1 (0.045 wt % Nb) and extending that approach to take into account Nb segregation and starting bimodal grain size distribution.

(iii) Investigating the effect of AlN, to replace Nb(C,N), on pinning the austenite grain boundaries during reheating, as the segregation tendency of Al is much less compared with Nb.

Limits of validity of Dutta-Sellars equations, effect of grain size, strain and Nb content on recrystallisation kinetics:

1. The original Dutta-Sellars equations over predicts the amount of recrystallisation for steels with greater range grain sizes and Nb content than used to develop the original equation.

2. Modified Dutta-Sellars equations proposed by Fernandez et al. and Medina et al. do not predict the amount of recrystallisation well for the range of data available in the literature.

3. Using the original Dutta-Sellars equations but taking into account the starting grain size range via an individual grain size class approach more accurately

predicts deformation behaviour in terms of percent recrystallised for all literature data (assuming a log-normal starting grain size distribution) at 0.3 strain.

4. The original Dutta-Sellars equations do not predict the amount of recrystallisation well over a large strain range (0.1 - 0.6) using the literature data (both under and over predictions are seen). When the starting grain size distribution is taken into account there is an over prediction of recrystallisation at higher strain range (i.e. strain > 0.3) and an under prediction at lower strain range with reduced discrepancy.

5. Some of the over prediction of recrystallisation can be accounted for by strain induced precipitates reducing the recrystallised fraction, particularly for high Nb steels (literature data and deformation simulation on homogenised 0.094 wt % Nb steel) and at high strains (results presented in Chapter 7 and 9).

Modelling grain size distribution after deformation in homogenised and segregated Slab 1 (0.045 wt % Nb):

1. Grain size distributions following deformation (based on the amount recrystallised) were determined using the Dutta-Sellars equations for the individual grain size class present in the reheated grain size range. The equation in the literature for recrystallised grain size gave poorer agreement to the experimental values than a simplified approach based on halving the grain size values in the original reheated distribution.

2. Good agreement between the measured grain size distributions and predicted grain size distributions was obtained for deformation in the partial and no

recrystallisation regimes. The prediction underestimated the proportion of the fine grain classes.

3. No significant effect of precipitation on recrystallisation was observed for homogenised Slab 1 and the deformation strain and temperature ranges studied.

4. Equilibrium thermodynamics can be used to predict amount of microsegregation present in Slab 1. This is used to quantify the amount of segregated material present after reheating and amount of recrystallisation after deformation in the solute-rich and solute-depleted regions.

5. The presence of segregated solute (Nb) content increases the partial recrystallisation temperature range compared to an homogeneous composition.

6. The Dutta-Sellars model using an individual grain size class input can be used to predict the austenite grain structure developed after deformation in the presence of segregation and with a starting bimodal grain size distribution provided that the initial (after reheat) grain size distribution, segregated levels of Nb and area fraction of solute-rich area are used as input.

7. There is generally good agreement between predicted and measured mode and maximum grain sizes using the class-based modification of the Dutta-Sellars equations, although the predicted and measured amounts of recrystallisation do differ with under-prediction of the amount of recrystallisation in solute-rich material at the highest deformation temperatures and overestimation of the amount of recrystallisation in the solute-depleted material at lower deformation temperatures for both unimodal and bimodal starting (reheated) grain structures.

8. Analysis of the parameters and assumptions used in the predictions indicates that the assumed relationships between grain distributions and solute-rich / solute-depleted materials are reasonable as is the approach of halving the original grain size distribution on recrystallisation. The discrepancies between prediction and measurement are most readily accounted by invoking strain partition between fine and coarse grained material and a greater temperature dependence for solute drag.

Pinning of Austenite Grain Boundaries by Mixed AlN and Nb(C,N) Precipitates:

1. Grain bimodality is due to the difference in grain boundary pinning between solute-rich and solute-depleted regions. Increased numbers of Al-rich particles more uniformly distributed can offset difference in pinning behaviour due to Nb segregation in a 0.057 wt % Al and 0.019 wt % Nb steel.

2. Quantitative correlation of coarse and fine grains with solute-depleted and solute-rich regions is not seen for shorter heating times due to incomplete dissolution of particles to equilibrium levels. Prolonged holding times give greater particle dissolution and grain boundary pinning closer to that expected.

CHAPTER – 12

Further work

From this investigation the following suggestions for further research can be made:

1. The simple equilibrium model used in Chapter 5 to quantify the amount of segregated material present in the steel needs to be verified for a range of compositions, casting parameters and complex solidification mode. It can be expected that different casting conditions may result in different levels of segregation and different spacings between solute-rich and solute-depleted regions – indeed whether solidification progresses with dendritic or cellular fronts. The simple analysis may not be valid for different solidification modes. In those situations more complex modelling such as a phase field approach would be required.

2. The discrepancy that has been shown to occur when using the Dutta-Sellars equations, incorporating the individual grain size class modification, in predicting the amount of recrystallisation across a range of strains (0.15 – 0.45) and composition (0.045 – 0.94 wt% Nb) can be addressed by invoking issues such as strain partitioning and a temperature dependence of solute drag. In-situ synchrotron studies could be used to measure dislocation density before and after deformation. That can be used to quantify the driving force of recrystallisation. This method would also allow the generation of an accurate variation of driving force with grain size. Based on this relationship the strain exponent in the Dutta-Sellars equation could be modified to achieve better agreement across the entire strain range. With the knowledge of the driving force for recrystallisation, any discrepancy due to strain-induced precipitation of Nb(C,N) can be determined from a comparison with the precipitate pinning force.

This is important in steel containing a high amount of Nb and in multipass deformation schedules where the effect of deformation-induced precipitates on recrystallisation kinetics would be more obvious.

3. In the present study the Dutta-Sellars model, modified with an individual grain size class approach, has been used to quantify the deformation behaviour during a single stage deformation process. However commercial rolling is a multistage deformation process. Addressing the above modifications and taking the grain structure developed from single hit deformation, the Dutta-Sellars's model can then be used for double hit tests to check its suitability. To model recrystalisation kinetics in the subsequent deformation stages deformation-induced precipitates need to be quantified in each stage of deformation to determine the available Nb in solution after each deformation stage. Once the amount of recrystallisation in each stage of deformation has been quantified then the simple approach used in the present study to model the grain size distribution after deformation can be extended to the multistage process to check its applicability. The simple approach of predicting grain size distribution after deformation needs to be validated across the wide range of compositions and strain level.

4. It has been shown in Chapter 6 that there is a discrepancy in predicting the amount of recrystallisation in a 0.02 wt % Nb steel (present in the literature data). The cause of the discrepancy is not evident from the original paper. A low Nb steel could be investigated across the entire strain and temperature range in this thesis to determine the cause of the disagreement. It has also been shown, using the literature data, that a greater discrepancy, between the predicted and measured amounts of recrystallisation, exists in steels containing a higher amount of nitrogen (>0.024 wt %). Whether the

presence of a greater amount of nitrogen increases the volume fraction of strain-induced Nb(C,N) and causes the discrepancy needs to be established.

5. It has been shown that using AlN can offset the difference in pinning between the solute-rich and solute-depleted regions due to Nb segregation in a 0.057 wt % Al and 0.019 wt % Nb steel at 1125 °C. Thermo-Calc can be used to predict the wt % of Al and N required in a steel with a given Nb content to provide sufficient AlN to give complete pinning in the solute-depleted regions. Hence, it can be determined if the formation of a bimodal grain size distribution due to dissolution of Nb(C,N) particles in the solute-depleted regions can be avoided. Once grain boundary pinning during reheating is established then deformation simulations can be carried out to see if there is an influence of AlN on recrystallisaion kinetics. Influence of Al as a solute on recrystallisation kinetics can also be studied.

6. A greater amount of Nb(C,N) is expected to be stable in the solute-depleted regions in a steel that contains a high Nb content. Therefore using a higher Nb content may be used to avoid the formation of a bimodal grain size distribution during reheating. A sufficient amount of precipitates are predicted to be stable even after reheating above 1400 °C in both the solute-rich and solute-depleted regions in a steel that contains 0.094 wt % Nb, which will result in the formation of a unimodal grain structure upon reheating. Precipitate quantification after reheating would give an accurate estimation of solute Nb that would influence recrystallisation kinetics. In has been shown in the present thesis that there is an influence of deformation-induced Nb(C,N) on recrystallisation kinetics in a homogenised 0.094 wt % Nb steel at temperatures below 1090 °C. Deformation simulations using the as-cast and reheated 0.094 wt % Nb steel (i.e with segregation) would give an insight into whether there is any influence

of deformation-induced precipitates on recrystallisation kinetics in the solute-rich and solute-depleted regions.

References

1. Gladman T; “The Physical Metallurgy of Microalloyed Steels”; Book 615, The Institute of Materials, London, (1997).
2. Morrison W B; “Microalloy steels – the begining”; Materials Science and Technology, v 25, n 9, (2009), pp. 1066-1073.
3. Korchynsky M; “Role of microalloying in achieving a sustainable growth rate of steel usage”; Proceedings International Conference on Microalloyed Steels: Emerging Technologies and Applications, Kolkata, India, 9-11 March 2007.
4. DeArdo A J, Hua M J, Cho K G and Garcia C I; “On strength of microalloyed steels: an interpretive review”; Materials Science and Technology, v 25, n 9, (2009), pp. 1074-1082.
5. Cuddy L J; “Microstructures developed during thermomechanical treatment of HSLA steels”; Metallurgical Transactions A, v 12A, n 7, (1981), pp. 1313-1320.
6. Cuddy L J; “Grain refinement of Nb steels by control of recrystallisation during hot-rolling”;Metallurgical and Materials Transactions A, v 15A, n 1, (1984), pp. 87-98.
7. Wu S J, Davis C L; “Effect of duplex ferrite grain size distribution on local fracture stresses of Nb-microalloyed steels”; Materials Science and Engineering A, v 387-389, n 1-2, (2004), pp. 456-460.
8. Knott J F; “Microstructural heterogeneity in high strength structural steels and effects on scatter in toughness values”; Proceedings International Conference on Microalloyed Steels: Emerging Technologies and Applications, Kolkata, India, 9-11 March 2007.
9. Talbot D, Davis C L, Strangwood M; “The effects of different plate rolling processes on microstructure and mechanical properties in a Nb-containing HSLA steel”; Proc. of 32nd Annual IMS Convention on ‘Understanding Processing / Structure / Property / Behaviour Correlations’, Pub ASM Intl ISBN 0-87170-687-3 (2000), in Microstructural Science, v 27, n 4, pp. 56-65.
10. Talbot D, Davis C L and Strangwood M; Proc ‘Thermomechanical Processing of Steels', London, pub. IoM Communications ISBN I-86125-122-X, (2000), pp. 681-691.

11. Talbot D; "The effects of plate processing parameters on the microstructure, mechanical properties and precipitation characteristics of niobium containing high strength low alloy steels"; Thesis submitted to University of Birmingham, (2002).
12. DeArdo A J; "Niobium in modern steels"; International Materials Reviews, v 48, n 6, (2003), pp. 371-402.
13. Tither G; "The development and applications of niobium-containing HSLA steels"; Proc. 2nd Int. Conf. On 'HSLA steels: processing, properties and applications', (ed. G. Tither et al.), Baijing, China, TMS, Warrendale, (1992), pp. 61-80.
14. Chakrabarti D; "Development of bimodal grain structures and their effect on toughness in HSLA steel" ; Ph.D. Thesis, University of Birmingham, (2007).
15. Irving W R; "Continuous casting of steel";Book 584, The Institute of materials, London, (1993).
16. Gray R J, Irving W R, Baker R; "Steel making, casting, and rolling of pipeline steels in BSC"; Ironmaking and Steelmaking, v 10, n 4, (1983), pp. 185-192.
17. Tanaka T; "Controlled rolling of steel plate and strip";International Metals Reviews, v 26, n 4, (1981), pp. 185-212.
18. Bhadeshia H K D H and Sellars C M; "Changes in grain structure subjected to complex deformation"; Proceedings International Conference on Microalloyed Steels: Emerging Technologies and Applications, Kolkata, India, 9-11 March 2007.
19. Bhattacharjee D, Davis C L and Knott J F; "Predictability of Charpy impact toughness in thermomechanically control rolled (TMCR) microalloyed steels"; v 30, n 3, (2003), pp. 249-255.
20. Sellars C M, Whiteman J A; "Recrystallisation and grain growth in hot working"; Metal Science, v 13, n 3-4, (1979), pp. 187-193.
21. Cai S, Boyd J D; "Mechanism of microstructural banding in hot rolled microalloyed steels"; Materials Science Forum, v 500-501, (2005), pp. 171-178.
22. Davis C L, Strangwood M; "Preliminary study of the inhomogeneous precipitate distributions in Nb-microalloyed plate steels"; Journal of materials Science, v 37, (2002), pp. 1083-1090.
23. Davis C L; "The effect of microalloy precipitates on final products mechanical properties"; Transaction Indian Institute of Metals, v 59, n 5, (2006), pp. 1-16.
24. Shehata M T, Boyd J D; "Quantitative correlations between toughness and microstructure for commercial line pipe steel"; Proc. Conf. On 'Advances in the

Physical Metallurgy and Applications of Steels', Liverpool, Metals Soc (Book 284), London, (1982), pp. 229-236.

25. Cuddy L J; "Effects of microalloy concentration on the recrystallization of austenite during hot deformation"; Proc. Conf. on 'Thermomechanical Processing of Microalloyed Austenite', Metallurgical Soc of AIME, Warrendale, Pa, USA, (1982), pp. 129-140.
26. Reed-Hill R E; "Physical Metallurgy principles"; 2nd edition, D Van Nostrand Company, New York, (1973).
27. Flemings M C; "Solidification Processing"; McGraw-Hill, New York, (1974).
28. Zhang L P, Davis C L, Strangwood M; "Assessment of microstructural development during continuous casting of microalloyed bars"; Proc. Conf. On 'Thermomechanical processing of steels', published by IoM Communications, ISBN I-86125-122-X, London, (2000), pp. 764-775.
29. He J Z, Liu Y Z, Shi B H, Liu Q Y, Wang X L, Li D G; "Effect of microstructure of continuous cast slab on formation of mixed grain in rolled producer";Kang T'ian / Iron and Steel (Peking), v 40, n 2, (2005), pp. 69-71.
30. Porter D A, Easterling K E; "Phase transformations in metals and alloys"; 2nd edition, Chapman and Hall, London, (1992).
31. Bower T F, Flemings M C; "Formation of chill zone in ingot solidification"; Transactions Metallurgical Society of American Institute of Mining, Metallurgical and Petroleum Engineers, v 239, n 2, (1967), pp. 216-219.
32. Flemings M C, Nereo G E; "Macrosegregation-1"; Transactions AIME, v 239, n 9, (1967), pp. 1449-1461.
33. Krauss G; "Solidification, segregation and banding in carbon and alloy steels"; Metallurgical and Materials Transactions B, v 34B, (2003), pp. 781-792.
34. Davis C L, Strangwood M; "Segregation behaviour in Nb microalloyed steels"; Materials Science and Technology, v 25, n 9, (2009), pp. 1126-1133.
35. Ghosh A; "Segregation in cast products"; Sadhana, v 26, n 1 and 2, (2001), pp. 5-24.
36. Priestler R, Li P H, Zhou C, Ibraheem A K; "Microally precipitation in HSLA steel austenite"; Microstructural Science, v 26, (1998) Ottawa, Canada, pp. 447-454.
37. Chen Z, Loretto M H, Cochrane R C; "Nature of large precipitates in titanium-containing HSLA steels"; Materials Science and Technology, v 3, n 10, (1987), pp. 836-844.

38. El-Bealy M, Thomas B G; “Production of dendritic arm spacing for low alloy steel casting processes; Metallurgical and Materials Transactions B, v 27B, (1996), pp. 689-693.
39. Haggart J E, Hardie A W, Bruce D W; “Control of segregation in continuously cast slabs for high quality plate applications at British Steel, Ravenscraig Works”; Ironmaking and Steelmaking, v 17, n 2, (1990), pp. 130-134.
40. Lasoult G; “Macrosegregation in steel strands and ingots”, Characterisation formation and consequences”; Materials Science and Engineering A, v 413-414, (2005), pp. 19-29.
41. Moore J J; “Review of axial segregation in continuous cast steel”; Continuous casting, Iron and Steel Society, v 3, (1984), pp. 11-20.
42. Lee P D, Yuan L, Ramirez-Lopez P and Mills KC; “Solidification defect prediction using multiscale modelling”; Proc. of Corus-Academia Symposium, London, (2010).
43. Chakrabarti D, Davis C L and Strangwood M; “Development of bimodal grain structures in Nb containing high strength low alloy steels during slab reheating”; Metallurgical and Materials Transactions A, v 39A, (2008), pp. 1963-1977.
44. Couch A J; “Grain growth and dissolution kinetics in high strength low alloy (HSLA) steels”; Ph.D Thesis, The University of Leeds, (2001).
45. Presslinger H, Mayr M, Tragl E, Bernhard C; “Assessment of the primary structure of slabs and the influence on hot- and cold-rolled strip structures”; Steel Research Int., v 77, n 2, (2006), pp. 107-115.
46. Pottore N S, Garcia C I and DeArdo A J; “Interrupted and isothermal solidification studies of low and medium carbon steels”; Metallurgical and Materials Transactions A, v 22, n 8, (1991), pp. 1971-1980.
47. Kneissi A C, Garcia C I, DeArdo A J; “Characterisation of precipitates in HSLA steels”;Proc. 2nd Int. Conf. On ‘HSLA steels: processing, properties and applications’, (ed. G. Tither et al.), Baijing, China, TMS, Warrendale, (1992), pp. 99-105.
48. Crowther D N, Morrison W B; “The influence of hypo-stoichiometric additions of titanium on the properties of microalloyed structural steels”;‘Titanium technology in microalloyed steels’, (Proc. of Conf. in Sheffield, 1994), edited by T. N. Baker, Book 662, The Institute of materials, London, (1997), pp. 44-64.

49. Craven A J, He K, Garvie L A J, Baker T N; “Complex heterogeneous precipitation in titanium-niobium microalloyed Al-killed HSLA steels - II. Non-titanium based particles”;Acta Materialia, v 48, n 15, (2000), pp. 3869-3878.
50. Craven A J, He K, Garvie L A J, Baker T N; “Complex heterogeneous precipitation in titanium-niobium microalloyed Al-killed HSLA steels - I. (Ti,Nb)(C,N) particles”; Acta Materialia, v 48, n 15, (2000), pp. 3857-3868.
51. Shanmugam S, Tanniru M, Misra R D K, Panda D, Jansto S; “Precipitation in v bearing microalloyed steel containing low concentrations of Ti and Nb”;Materials Science and Technology, v 21, n 8, (2005), pp. 883-892.
52. Morales E V, Gallego J, Kestenbach H J; “On coherent carbonitride precipitation in commercial microalloyed steels”; Philosophical Magazine Letters, v 83, n 2, (2003), pp. 79-87.
53. Leap M J, Brown E L; “Crystallography of duplex AlN-Nb(C, N) precipitates in 0.2 % C steel”; Scripta Materialia, v 47, (2002), pp 793-797.
54. Mintz B, Crowther D N; “The influence of small additions of Ti on the hot ductility of steel”;‘Titanium technology in microalloyed steels’, (Proc. of Conf. in Sheffield, 1994), edited by T. N. Baker, Book 662, The Institute of materials, London, (1997), pp. 98-114.
55. Mintz B, Morrison W B, Cochrane R C; “Influence of grain boundary carbide thickness and grain size on the impact properties of steels”.Proc. Conf. on ‘Advances in the Physical Metallurgy and Applications of Steels’, Liverpool, Metals Soc (Book 284), London, (1982), pp. 222-228.
56. Mintz B, Wilcox J R, Crowther D N; “Hot ductility of directly cast C-Mn-Nb-Al steel”;Materials Science and Technology, v 2, (1986), pp. 589-594.
57. Irvine K J, Pickering F B, Gladman T; “Grain-refined C-Mn steels”; Iron and Steel Institute - Journal, v 205, n 2, (1967), pp. 161-182.
58. Wagner C: “Thermodynamics of Alloys”; Addison-Wesley Press, Reading, (1952).
59. Palmiere E J, Garcia C I, DeArdo A J; “Compositional and microstructural changes which attend reheating and grain coarsening in steels containing niobium”; Metallurgical and Materials Transactions A, v 25A, n 2, (1994), pp. 277-286.
60. Jansson B, Schalin M, Selleby M, Sundman B; “The Thermo-Calc database system”; Proc. of 2nd Int. Symp. on ‘Computer software in chemical and extractive metallurgy’, (ed. C. W. Bale, G. A. Irons) Quebec City, Montreal, (1993), pp. 57-71.

61. Hong S G, Jun H J, Kang K B, Park C G; “Evolution of precipitates in the Nb-Ti-V microalloyed HSLA steels during reheating”; Scripta Materialia, v 48, (2003), pp. 1201-1206.
62. Rose A J, Howe A A; “Precipitation in niobium treated HSLA steels”; Report number SL / PM / R / S 2924 / 5 / 96 / A, British Steel Internal Report, Swinden, UK, (1996).
63. Rose A J, Gladman T, ‘referred in “The Physical Metallurgy of Microalloyed Steels” by T. Gladman; Book 615, The Institute of Materials, London, (1997).
64. Ardell A J; “On the coarsening of grain boundary precipitates”; Acta Metallurgica, v 20, (1972), pp. 601-609.
65. Lifshitz I M, Slyozov V V; “The kinetics of precipitation from supersaturated solid solutions”;Journal of Phys. Chem. Solids, v 19, (1961), pp. 35-50.
66. Speer J G, Michael J R, Hansen S S; “Carbonitride precipitation in niobium / vanadium microalloyed steels”; Metallurgical and Materials Transactions A, v 18A, n 2, (1987), pp. 211-222.
67. Gladman T, Pickering F B; “Grain coarsening of austenite”; Journal of Iron and Steel Institute, v 205, (1967), pp. 653-664.
68. Coladas R, Masounave J, Guerin G, Bailon J P; “Austenite grain growth in medium- and high-carbon steels microalloyed with niobium”; Metal Science, v 11, n 11, (1977), pp. 509-516.
69. Cheng L M, Hawbolt E B, Meadowcroft T R; “Dissolution and coarsening of aluminium nitride precipitates in low carbon steel-distribution, size, morphology”; Canadian Metallurgical Quarterly, v 39, (2000), pp. 73-86.
70. San Martin D, Caballero F G, Capdevila C, Garcia de Anders C; “Discussion of the rate controlling process of coarsening of niobium corbonitride in a niobium microalloyed steel”; Materials Science Forum, v 500-501, (2005), pp. 703-710.
71. Smithells Metal Refernce book, 6th edition, (edited by E. A. Brandes), Butterworths, London, (1983).
72. Sarian S J; “Diffusion of Ti in TiCx”;Journal of Applied Physics, v 40, (1969), pp. 3515-3520.
73. Shewmon P G; “Diffusion in solids”, McGraw-Hill, New York, (1963).
74. Faulkner R G, Song S H, Flewitt P E J; “Combined quenching and tempering induced phosphorus segregation to grain boundaries in 2.25Cr-1Mo steel”; Materials Science and Technology, v 12, n 10, (1996), pp. 818-822.

75. Zener C; quoted by Smith C S; “Grains, phases and interphases, an interpretation of microstructure”;Transactions of Metallurgical Society of AIME; v 175, (1948), pp. 47.
76. T Gladman; “On the theory of the effect of precipitate particles on grain growth in metals”; Proceedings of Royal Society of London; v 294, (1966), pp. 298-309.
77. Gladman T, Pickering F B; “Grain coarsening of austenite”; Journal of Iron and Steel Institute, v 205, (1967), pp. 653-664.
78. Gladman, T; “Second phase particle distribution and secondary recrystallisation”; Scripta Metallurgica et Materialia, v 27, n 11, (1992), pp. 1569-1573.
79. Doherty R D, Srolovitz D J, Rollett A D, Anderson M P; “On the volume fraction dependence of particle limited grain growth”.Scripta Metallurgica, v 21, n 5, (1987), pp. 675-679.
80. Dogan O N, Michal G M, Kwon H W; “Pinning of austenite grain boundaries by AIN precipitates and abnormal grain growth”; Metallurgical Transactions A, v 23A, n 8, (1992), pp. 2121-2129.
81. Cuddy L J, Raley J C; “Austenite grain coarsening in microalloyed steels”; Metallurgical Transactions A, v 14A, n 10, (1983), pp. 1989-1995.
82. Cabrera J M, Flores E, Al Omar A, Prado J M; “Abnormal grain growth in medium carbon V-Ti-Al microalloyed steels”; Proc 1996 Symp Fundam Appl Microalloying Forging Steels, Golden, CO, USA, Minerals, Metals & Materials Soc (TMS), (1996), pp. 173-186.
83. Arieta F G, Sellars C M; “Precipitation kinetics of Nb (C, N) in austenite for the low C high Nb HSLA steels”;Proc. International Symposium on Low-Carbon Steels for the 90's, (eds. R. Asfahani and G. Tither), pub. TMS, Pittsburg, PA, USA, (1993), pp. 101-112.
84. Pickering F B, Gladman T; “Investigation into some factors which control strength of carbon steels”; Iron and Steel Institute - Special Report No. 81, (1963), pp. 10-25.
85. Speer J G, Hansen S S; “Austenite recrystallization and carbonitride precipitation in niobium microalloyed steels”; Metallurgical Transactions A, v 20A, n 1, (1989), pp. 25-38.
86. Hodgson P D, Beladi H, Barnet M R; “Grain refinement in steels through thermomechanical processing”; Materials Science Forum, v 500-501, (2005), pp. 39-48.

87. Ali Bepari M; “Effect of second phase particles on coarsening of austenite in 0.15 % C steel”; Metallurgical Transactions A, v 20A, n 1, (1989), pp. 13-16.
88. Palmiere E J, Garcia C I, DeArdo A J; “Influence of niobium supersaturation in austenite on the static recrystallization behavior of low carbon microalloyed steels”; Metallurgical and Materials Transactions A, v 27A, n 4, (1996), pp. 951-960.
89. Dutta B, Palmiere E J; “Effect of prestrain and deformation temperature on the recrystallization behavior of steels microalloyed with niobium”; Metallurgical and Materials Transactions A, v 34 A, n 6, (2003), pp. 1237-1247.
90. Bakkaloglu A; “Effect of processing parameters on the microstructure and properties of an Nb microalloyed steel”; Materials letters, v 56, n 3, (2002), pp. 200-209.
91. Gunduz S, Cochrane R C; “Influence of cooling rate and tempering on precipitation and hardness of Vanadium microalloyed steels”; Materials and Design, v 26, (2005), pp. 486-492.
92. Ubhi H S, Baker T N; “The influence of Manganese and Silicon on the precipitation of Vanadium Carbide in Steel”; Materials Science and Engineering A, v 111, (1989), pp. 189-199.
93. Zajac S; “Precipitation of microalloy carbo-nitrides prior, during and after g / a transformation”; Materials Science Forum, v 500-501, (2005), pp. 75-86.
94. Iparraguirre C, Fernandez A I, Lopez B, Scott C, Rose A, Kraendonk W, Soenen B and Paul G; “Characterisation of strain induced precipitation of Nb in microalloyed austenite ”; Materials Science Forum, v 500-501, (2005), pp.677-684.
95. Courtois E, Epicier T and Scott C; “Characterisation of Niobium carbide and carbonitride evolution within ferrite: contribution of transmission electron microscopy and advanced associated techniques”; Materials Science Forum, v 500-501, (2005), pp.669-677.
96. Baker T N; “Process microstructure and properties of V microalloyed steels”; Materials Science and Technology, v 25, n 9, (2009), pp. 1083-1107.
97. Roberts W and Ahlblom B; “A nucleation criterion for dynamic recrystallisation during hot working”; Acta Metallurgica, v 26, Issue 5, (1978), pp. 801-813.
98. Sellars C M; “The physical metallurgy of hot working”; Proc. Conf. on ‘Hot working and forming processes’, (eds. C. M. Sellars, G. L. Davies), Book 264, The Metals Society, London, (1980), pp. 3-15.
99. Martin J W, Doherty R D; “Stability of microstructures in metallic systems”; Cambridge University Press, Cambridge, United Kingdom, 1976, pp. 40.

100. Doherty R D, Hughes D A, Humphreys F J, Jonas J J, Juul Jensen D, Kassner M E, King W E, McNelley T R, McQueen H J, Rollett A D; "Current issues in recrystallization: a review"; Materials Science and Engineering A, v 238, (1997), pp. 219-274.

101. le Bon A, Rofes-Vernis J, Rossard C; "Recrystallization and precipitation during hot working of a Nb-bearing HSLA steel"; Metal Science Journal, v 9, n 1, (1975), pp. 36-40.

102. le Bon A, Rofes-Vernis J, Rossard C; Mem. Sci. Rev. Metall., v 57, (1973), pp. 577.

103. Burke J E and Turnbull D; Prog Met Phys, v 3, (1952), pp. 220.

104. Cahn R W; "Recrystallisation, Grain Growth and Textures"; New York, NY, H.Margolin, ed. ASM, Metal Park, OH, 1966, pp. 99.

105. Beck P A and Sperry P R; Trans. AIME, 1949, v 185, pp. 240.

106. Beck P A and Sperry P R; Journal of Applied Physics, 1950, v 21, pp. 150.

107. Honeycombe R W K; "The plastic deformation of metals"; 2nd edition, ASM, Metal Park, OH, 1984, pp. 287.

108. Bailey J E and Hirsch P B; Proc. R. Soc. (London), 1962, v A 267, pp. 11.

109. Keh A S and Weissman S; "The impact of transmission electron microscopy on theories of the strength of crystals"; 231, (1963), New York, Wiley.

110. Kelly A and Groves G W; "Crystallography and crystal defects", Addison-Wesley publishing company, Reading, MA, 1970, pp. 198.

111. Verhoeven J D; "Fundamentals of Physical Metallurgy", John Willy and Sons, New York, NY, 1975, p. 15.

112. Humphreys F J; "Modelling mechanism and microstructures of recrystallisation"; Materials Science and Technology, v 8, n 2, (1992), pp. 135-144.

113. Sellars C M; "Hot deformation processing"; Materials Science and Technology, v 8, n 2, (1992), pp. 134.

114. Kozasu I, Ouchi C, Sampei T and Okita T; Microalloying 75, v 1, (1975), pp.120.

115. Miller O O; Transactions of the American Society for Metals, v 43, (1951), pp. 260.

116. Foster S R: Ph.D Thesis, University of Sheffield, 1975.

117. Korchynsky M and Stuart H: Symposium 'Low alloy and high strength steels', 1970, 17.

118. Uranga P, Lopez B and Rodriguez-Ibabe J M; "Role of carbon and nitrogen content on microstructural homogeneity in thin slab direct rolled microalloyed steels"; Iron Making and Steel Making, v 36, n 3, (2009), pp.162-169.

119. Cahn J W; "The impurity-drag effect in grain boundary motion"; Acta Metallurgica, v 10, Issue 9, (1962), pp. 789-798.

120. Hillert M and Sundman B; "A treatment of solute drag on moving grain boundaries and phase interfaces in binary alloys"; Acta Metallurgica, v 24, Issue 8, (1976), pp. 731-743.

121. Luton M J, Dorvel R, Petkovic R; "Interaction between deformation, recrystallization and precipitation in niobium steels"; Metallurgical Transactions A, v 11A, n 3, (1980), pp. 411-420.

122. White M J and Owen W S;" Effects of vanadium and nitrogen on recovery and recrystallization during and after hot-working some HSLA steels"; Metallurgical Transactions A, v 11A, n 4, (1980), pp. 597-604.

123. Pearson W B; "The crystal chemistry and the physics of metals and alloys"; (1972), 152, Wiley, New york.

124. Akben M G, Weiss I and Jonas J J; "Dynamic precipitation and solute hardening in a V microalloyed steel and two Nb steels containing high levels of Mn"; Acta Metallurgica, v 29, Issue 1, (1981), pp. 111-121.

125. Medina S F, Quispe A; "Improved model for static recrystallization kinetics of hot deformed austenite in low alloy and Nb/V microalloyed steels"; ISIJ International, v 41, (2001), pp. 774-781.

126. Somani M C, Karjalainen L P, Porter D A and Morgridge R A; Proc. International Conference on Thermomechanical Processing: Mechanisms, Microstructure and Control, edited by E.J. Palmiere, M. Mahfouf and C. Pinna, The University of Sheffield, UK (2003), pp. 436.

127. Somani M C and Karjalainen L P; Materials Science Forum, v 467-470, (2004), pp. 335.

128. Karjalainen L P, Somani M C and Porter D A ; Materials Science Forum, v 426-432, (2003), pp. 1121.

129. Andrade H L, Akben M G and Jonas J J; "Effect of molybdenum, niobium, and vanadium on static recovery and recrystallization and on solute strengthening in microalloyed steels"; Metallurgical Transactions A, v 14A, n 10, (1983), pp. 1967-1977.

130. Akben M G and Jonas J J; Proc. International Conference 'HSLA Steel, Technology & Applications', ASM, Metals Park, OH (1983), pp. 149.

131. Yamamoto S, Ouchi C, Osuka T; "Effect of microalloying elements on the recovery and recrystallisation in deformed austenite"; Proc. International Conference Thermomechanical processing of microalloyed austenite, 1982, Warrendale, PA, pp.613-639.

132. Abad R, Fernandez A I, Lopez B and Rodriguez-Ibabe J M; "Interaction between recrystallization and precipitation during multipass rolling in a low carbon niobium microalloyed steel"; ISIJ International, v 41, n 11, (2001), pp. 1373-1382.

133. Hornbogen E and Koster U; "Recrystallisation of metallic materials"; (1978), 159.

134. Kwon O, DeArdo A J; "Interactions between recrystallization and precipitation in hot-deformed microalloyed steels"; Acta Metallurgica et Materialia, v 39, n 4, (1991), pp. 529-538.

135. Wilber G A, Bell J R, Bucher J H, and Childs W J; Trans. Metall. Soc. A. I. M. E. , v 242, (1968), pp. 2305-2308.

136. Hansen S S, Vander Sande J B, Cohen M; "Niobium carbonitride precipitation and austenite recrystallization in hot-rolled microalloyed steels"; Metallurgical Transactions A, v 11A, n 3, (1980), pp. 387-402.

137. Hong S G, Kang K B, Park C G; "Strain-induced precipitation of NbC in Nb and Nb-Ti microalloyed HSLA steels"; Scripta Materialia, v 46, n 2, (2002), pp. 163-168.

138. Klinkenberg C and Hensger K E; "Processing of Nb microalloyed API grade steel"; Materials Science Forum, v 500-501, (2005), pp.253-260.

139. DeArdo A J; Proc. International Conference 'Microalloying 1995', Warrendale, PA, pp.15-34.

140. Narita K; Trans iron steel inst., Japan, v 15, 1975, pp.145.

141. Jack D H and Jack K H; Material Science Engineering, v 11, n 1, (1973), pp. 1-27.

142. Davenport A T and Honeycombe R W K; Material Science, v 9, (1975), pp. 201-208.

143. Silcock J M; Journal of Iron and Steel Institute, v 201, (1963), pp. 409-421.

144. Silcock J M; "Precipitation of vanadium carbide"; Acta Metallurgica, v 14, Issue 5, (1966), pp. 687-692.

145. Baker R G and Nutting J; “Precipitation processes in steels”; ISI Special Report 64, v 1, (1959), London, The Iron and Steel Institute.

146. G. Kurdjumov and G. Sachs; Z. Phys., v 62, (1930), pp. 592.

147. Li G, Maccagno T M, Bai D Q and Jonas J J; “Effect of initial grain size on the static recrystallisation kinetics of Nb microalloyed steels”; ISIJ International, v 36, (1996), pp. 1479-1485.

148. Fernandez A I, Uranga P A, Lopez B and Rodriguez-Ibabe J M; “Static recrystallization behaviour of a wide range of austenite grain sizes in microalloyed steels”; ISIJ International, v 40, (2000), pp. 893-901.

149. Medina S F, Mancilla J E; “Static recrystallisation modelling of hot deformed steel containing several alloying elements”; ISIJ International, v 36, (1996), pp. 1070-1076.

150. Karjalailen L P and Perttula J S: Proc. 3rd International Conference. on recrystallisation and related phenomena, Rex 96, Monterry, 1996, 413.

151. K. Airaksinen, L. P. Karjalailen, D. Porter and J. S. Perttula: Proc. International Conference ‘Microalloying in steels’, 1998, 119, Switzerland, Trans Tech Publication.

152. Medina S F, Mancilla J E; “Influence of Alloying elements in solution on static recrystallisation kinetics of hot deformed steel”; ISIJ International, v 36, (1996), pp. 1063-1069.

153. Cordea J N and Hook R E; “Effect of molybdenum, niobium, and vanadium on static recovery and recrystallization and on solute strengthening in microalloyed steels”; Metallurgical Transactions A, v 1, (1970), pp. 111-121.

154. Ouchi C; “Hot deformation of austenite”; ed. J. B. Balance, (1977), New York, The metal society AIME.

155. Dutta B, Sellars C M; “Effect of composition and process variables on Nb(C,N) precipitation in niobium microalloyed austenite”; Materials Science and Technology, v 3, n 3, (1987), pp. 197-206.

156. Dutta B, Valdes E, Sellars C M; “Mechanism and kinetics of strain induced precipitation of Nb(C, N) in austenite”; Acta Metallurgica et Materialia, v 40, n 4, (1992), pp. 653-662.

157. Dutta B, Palmiere E J, Sellars C M; “Modelling the kinetics of strain induced precipitation in Nb microalloyed steels”; Acta Materialia, v 49, n 5, (2001), pp. 785-794.

158. Medina S F, Quispe A; “Influence of microalloy type and content on induced precipitation kinetics in microalloyed steels”;Steel research, v 67, (1996), pp. 257-262.

159. Medina S F, Fabregue P; “Activation energy in the static recrystallisation of austenite”; Journal of materials Science, v 26, (1991), pp. 5427-5432.

160. Medina S F, Mancilla J E; “Static recrystallization of austenite and strain induced precipitation kinetics in titanium microalloyed steels”;Acta Metallurgica et Materialia, v 42, n 12, (1994), pp. 3945-3951.

161. Medina S F; “Influence of niobium on the static recrystallization of hot deformed austenite and on strain induced precipitation kinetics”; Scripta Metallurgica et Materialia, v 32, n 1, (1995), pp. 43-48.

162. Zeng Y and Wang W; “Computer simulation of carbonitride precipitation during deformation in Nb-Ti microalloyed steels”; Journal of Material Science, v 43, (2008), pp. 874-882.

163. Akamatsu S, Senuma T and Yada H; Proc. of Int. Symp. On Mathematical Modelling of Hot Rolling of Steel, ed. S. Yue. Canadian Institute of Mining and Metallurgy, 1990, 467.

164. Nagarajan V, Palmiere E J and Sellars C M; “New approach for modelling strain induced precipitation of Nb(C,N) in HSLA steels during multipass hot deformation in austenite”; Materials Science and Technology, v 25, n 9, (2009), pp. 1168-1174.

165. Rainforth W M, Black M P, Higginson R L, Palmiere E J, Sellars C M, Prabst I, Warbichler P, Hofer F; “Precipitation of NbC in a model austenitic steel”;Acta Materialia, v 50, n 4, (2002), pp. 735-747.

166. Poths R M, Rainforth W M, Palmiere E J; Materials Science Forum, v 500-501, (2005), pp. 139-146.

167. Bai D Q, Yue S, Sun W P, Jonas J J; “Effect of test variables on the critical temperatures Tnr and Ar3 of high Nb - low C plate steel Ar3 of high Nb - low C plate steel”; Proc. of the Int. Conference on Processing, Microstructure and Properties of Microalloyed and Other Modern High Strength Low Alloy Steels, published by Iron & Steel Soc of AIME, Pittsburgh, PA, USA, (1992), pp. 165-173.

168. Sun W P, Militzer M, Bai D Q and Jonas J J; “Measurement and modelling of the effects of precipitation on recrystallization under multipass deformation conditions”; Acta Metallurgica et Materialia, v 41, n 12, (1993), pp. 3595-3604.

169. Hodgson P D, Gibbs R K; “A mathematical model to predict the mechanical properties of hot rolled C-Mn and microalloyed steels”; ISIJ international, v 32, n 12, (1992), pp. 1329-1338.

170. Whittaker H J: Proc. ICSTIS, Suppl. Trans iron steel inst., Japan, (1971), 11, 662.

171. Nagarajan V, Sellars C M and Palmiere E J; “Strain-induced precipitation of Nb(C,N) in microalloyed austenite during multipass hot deformation”; Proceedings International Conference on Microalloyed Steels: Emerging Technologies and Applications, Kolkata, India, 9-11 March 2007.

172. Sellars C M and Palmiere E J; “Modelling strain induced precipitation of Niobium carbonitride during multipass deformation of austenite”; Materials Science Forum, v 500-501, (2005), pp. 3-14.

173. Weiss H, Gittings A, Brown G G, McG Tegart W J; Journal of Iron and Steel Institute, v 211, (1973), pp. 703.

174. Watanabe H, Smith Y, Pehlke R D: “Precipitation kinetics of niobium varbonitride in austenite in high-strength low-alloy steels”; Proc. Int. Conf. on ‘The Hot Deformation of Austenite’, (ed. J B Balance), The Metallurgical Society of AIME, New York, (1977), pp. 140-168.

175. Janampa C S; “The role of nitrogen in the hot working of niobium microalloyed steels”; Ph.D. Theis, The University of Sheffield, (1982).

176. Williams J G, Kilmore C R and Harris G R; Proc. Int. Conf. on ‘Phys. Metallurgy of Thermomechanical Processing of Steels and Other Materials (Thermec 88)’, (ed. I. Tamura), ISIJ international, 1988, 232.

177. Siwecki T; Proc. Int. Conf. on Proc. Int. Conf. on ‘Phys. Metallurgy of Thermomechanical Processing of Steels and Other Materials (Thermec 88)’, (ed. I. Tamura), ISIJ international, 1988, 232.

178. Laasraoui A and Jonas J J; “Prediction of Steel Flow Stresses at High Temperatures and Strain Rates”; Metallurgical Transactions A, v 22 A, (1991), pp. 1545-1565.

179. Kwon O; “A technology for the prediction and control of microstructural changes and mechanical properties in steel”; ISIJ international, v 32, n 3, (1992), pp. 350-358.

180. Choquet P, Fabregue P, Giusti J, Chamont B, Pensant J N and Blanchet F: Proc. of Int.Symp. On Mathematical Modelling of Hot Rolling of Steel, ed. S. Yue. Canadian Institute of Mining and Metallurgy, 1990, 34.

181. www.x-raymicroanalysis.com.

182. Williams D and Carter C B; "Transmission electron microscopy, II – Diffraction"; Plenum Press, New York, (1996).

183. Miguad B; "The physical metallurgy of hot working";Proc. Conf. on 'Hot working and forming processes', (eds. C. M. Sellars, G. L. Davies), Book 264, The Metals Society, London, (1980), pp. 67-76.

184. J. P. Sah and C. M. Sellars; "The physical metallurgy of hot working";Proc. Conf. on 'Hot working and forming processes', (eds. C. M. Sellars, G. L. Davies), Book 264, The Metals Society, London, (1980), pp. 62-66.

185. Zurob H S, Hutchinson C R, Bréchet Y and Purdy G; "Modeling recrystallization of microalloyed austenite: effect of coupling recovery, precipitation and recrystallization"; Acta Materialia, v 50, (2002), pp. 3075-3092.

186. Oliferuk W, Swiatnicki W A, Grabski M W; "Effect of the grain size on the rate of energy storage during the tensile deformation of an austenitic steel"; Material Science Engineering A, v 197, (1995), pp. 49-58.

187. Clarebrough L M, Hargreaves M E and Loretto M H; "The influence of grain size on the stored energy and mechanical properties of copper"; Acta Metallurgica, v 6, (1958), pp. 725-735.

188. Ashby M F; "The deformation of plastically non-homogeneous materials"; Philosophical Magazine, v 21, (1970), 399-424.

189. Kwon O, DeArdo A J; "On the recovery and recrystallisation which attend static softening in hot deformed copper and aluminium"; Acta Metallurgica et Materialia, v 38, n 1, (1990), pp. 41-54.

190. Loretto M H and White A J; "The influence of grain size on the energy stored in deformed copper"; Acta Metallurgica, v 9, (1961), pp. 512-513.

191. Williams R O; "The stored energy in deformed copper: the effect of grain size and silver content"; Acta Metallurgica, v 9, (1961), pp. 949-957.

192. Williams R O; "The stored energy in deformed copper at 24 ^{o}C"; Acta Metallurgica, v 13, (1965), pp. 163-168.

193. I. Baker, L. Liu (Lee Louis) and D. Mandal; “The effect of grain size on the stored energy of cold work as a function of strain for polycrystalline Nickel”; Scripta Metallurgica et Materialia, v 32, n 2, (1995), pp. 167-171.

194. Kazeminezhad M; “On the modelling of static recrystallisation considering the initial grain size effect”; Material Science Engineering A, v 486, (2008), pp. 202-207.

195. Ghosh G , Olson G B; “The isotropic shear modulus of multicomponent Fe-base solid solutions”; Acta Materialia, v 50, (2002), pp. 2655-2675.

196. Titchener A L; “ The stored energy of cold work in relation to grain size and other variables”; Acta Metallurgica, v 9, (1961), pp. 379-382.

197. Hillert M; “on the theory of normal and abnormal grain growth”; Acta Metallurgica, v 13, (1965), pp. 227-238.

198. Kundu A, Davis C L, Strangwood M; “Modelling of Grain Size Distributions During Single Hit Deformation of a Nb-Containing Steel”; Metallurgical Transactions A, v 41A, (2010), pp. 994-1002.

199. Zurob H S, Bréchet Y and Purdy G; “A model for the competition of precipitation and recrystallisation in deformed austenite”; Acta Materialia, v 49, (2001), pp. 4183-4190.

200. Kundu A, Davis C L, Strangwood M; “Grain structure development during reheating and deformation in microalloyed steels”; Proc. of 3rd International conference on Thermomechanical processing of steel. Italy, 2008.

201. Schmidt C G, Miller A K; “The effect of solutes on the strength and strain hardening behavior of alloys ”; Acta Metallurgica, v 30, (1982), pp. 615-625.